Numerical methods for incompressible fluid-structure interaction

THÈSE DE DOCTORAT

Présentée par

Jimmy Mullaert

pour obtenir le grade de

DOCTEUR DE
L'UNIVERSITÉ PIERRE ET MARIE CURIE - Paris VI

Spécialité : Mathématiques Appliquées

Soutenue publiquement le 17 Décembre 2014 devant le jury composé de:

Miguel Ángel Fernández	Directeur de thèse
Yvon Maday	Directeur de thèse
Emmanuel Maitre	Rapporteur
Laurence Halpern	Examinateur
Élisabeth Longatte	Examinateur
Dominique Chapelle	Examinateur
Frédéric Hecht	Examinateur
Marina Vidrascu	Invité

Après avis favorables des rapporteurs: Suncica Canic et Emmanuel Maitre

Méthodes numériques de simulation de problèmes d'interaction fluide-structure

Résumé :

Cette thèse présente une famille de schémas explicites pour la résolution d'un problème couplé d'interaction entre un fluide visqueux incompressible et une structure élastique (avec possiblement un comportement visco-élastique et/ou non linéaire). La principale propriété de ces schémas est une condition de Robin consistante à l'interface, qui représente une caractéristique fondamentale du problème continu dans le cas où la structure est mince. Si le couplage s'effectue avec une structure épaisse, une condition de Robin généralisée peut être formulée pour le problème semi-discret en espace, à l'aide d'une condensation de la matrice de masse de la structure. Une deuxième caractéristique majeure de ces schémas est la capacité d'obtenir une condition de Robin qui intègre à la fois des extrapolations de la vitesse et des efforts du solide (donnant lieu à un schéma de couplage explicite), mais également un traitement implicite de l'inertie de la structure, qui rend le schéma stable quelle que soit l'intensité de l'effet de masse ajoutée. Un résultat général de stabilité et de convergence est présenté pour tous les ordres d'extrapolations dans un cadre linéaire représentatif. On montre, en particulier, que les propriétés de stabilité se conservent lorsque le couplage s'effectue avec une structure mince ou épaisse. En revanche, la précision optimale obtenue dans le cas d'une structure mince n'est pas retrouvée avec une structure épaisse. L'erreur introduite par le schéma de couplage comporte en effet une non-uniformité en espace, qui provient de la non-uniformité des reconstructions discrètes des opérateurs visco-élastiques. L'approximation induite par la condensation de la matrice de masse solide n'est pas responsable de cette non-uniformité. À partir de ce schéma, on propose également des méthodes itératives pour la résolution du schéma fortement couplé. La convergence de cette méthode est démontrée dans un cadre linéaire et ne montre pas de sensibilité à l'effet de masse ajoutée. Finalement, les résultats théoriques obtenus sont illustrés par des exemples numériques variés, dans les cas linéaire et non linéaire.

Mots-clés : interaction fluide-structure, fluide incompressible, structure viscoélastique, schéma de couplage, préconditionnement, résolution partitionnée, méthodes Robin-Neumann.

NUMERICAL METHODS FOR INCOMPRESSIBLE FLUID-STRUCTURE INTERACTION

Abstract:

This thesis introduces a class of explicit coupling schemes for the numerical solution of fluid-structure interaction problems involving a viscous incompressible fluid and a general elastic structure (thin-walled or thick-walled, viscoelastic and non-linear). The first fundamental ingredient of these methods is the notion of interface Robin-consistency on the interface. This is an intrinsic (parameter free) feature of the continuous problem, in the case of the coupling with thin-walled solids. For thick-walled structures, we show that an intrinsic interface Robin consistency can also be recovered at the space semi-discrete level, using a lumped-mass approximation in the structure. The second key ingredient of the methods proposed consists in deriving an explicit Robin interface condition for the fluid, which combines extrapolations of the solid velocity and stresses with an implicit treatment of the solid inertia. The former enables explicit coupling, while the latter guarantees added-mass free stability. Stability and error estimates are provided for all the variants (depending on the extrapolations), using energy arguments within a representative linear setting. We show, in particular, that the stability properties do not depend on the thin- or thick-walled nature of the structure. The optimal first-order accuracy obtained in the case of the coupling with thin-walled structures is, however, not preserved when the structure is thick-walled, due to the spatial non-uniformity of the splitting error. The genesis of this problem is the non-uniformity of the discrete viscoelastic operators, related to the thick-walled character of the structure, and not to the mass-lumping approximation. Based on these splitting schemes, new, parameter-free, Robin-Neumann iterative procedures for the partitioned solution of strong coupling are also proposed and analyzed. A comprehensive numerical study, involving linear and nonlinear models, confirms the theoretical findings reported in this thesis.

Keywords: fluid-structure interaction, incompressible fluid, viscoelastic structure, thin-walled structure, splitting scheme, preconditioning, partitioned procedure, Robin-Neumann methods.

Remerciements

Il est d'usage de commencer un manuscrit de thèse par un message de remerciements à destination de tous ceux qui ont contribué à rendre possible sa réalisation. Je cède ici bien volontiers à cette coutume tant le travail décrit dans ce manuscrit dépend des nombreuses interactions que j'ai pu avoir avec les personnes remerciées ici.

Mes premiers remerciements vont naturellement à mes deux directeurs de thèse. Yvon Maday m'impressionne régulièrement par la pertinence et la précision de ses remarques. Quant à Miguel Fernandez, sa disponibilité et son investissement en tant que directeur de thèse vont bien au delà de ce que peut imaginer n'importe quel étudiant en doctorat.

J'ai également une pensée pour les nombreuses personnes que j'ai eu l'occasion de croiser dans les deux laboratoires. Au Laboratoire Jacques-Louis Lions, je pense particulièrement à Albert Cohen, Laurent Boudin, Jean-François Babadjian et Frédérique Charles, avec qui j'ai participé à des enseignements de L2 et L3 à l'UPMC au début de ma thèse. Dans l'équipe-projet REO à Inria, Jean-Frédéric Gerbeau, Céline Grandmont, Irène Vignon-Clementel m'ont marqué par leur conseils bienveillants. Merci également à Marina Vidrascu d'avoir apporté son expertise sur le couplage avec des modèles solides non linéaires et qui a permis la publication de plusieurs articles.

Préparer une thèse en parallèle d'un emploi à plein temps n'est pas sans générer un certain nombre de difficultés. Ainsi, ce travail n'aurait très probablement jamais vu le jour sans l'indulgence sans limite des personnes avec lesquelles j'ai travaillé au cours de mon internat de Santé Publique. Il s'agit, en particulier, du Dr Anne Castot-Villepelet (ARS Île-de-France), des professeurs Joël Coste (Hôtel-Dieu), Bruno Falissard (Maison des Adolescents), Nathalie Pelletier-Fleury (CERMES3) et, plus récemment, Laurent Abel (Institut Imagine) ainsi que de toutes leurs équipes respectives.

Merci également aux deux rapporteurs de ce manuscrit Suncica Canic et Emmanuel Maitre pour leur travail attentif de relecture. Relire en six semaines un travail qui a mis plusieurs années à être élaboré est une performance qui mérite d'être soulignée. Les échanges avec un rapporteur, même s'il sont redoutés, incitent à se remettre en question et sont toujours enrichissants. J'en profite aussi pour remercier tous les membre du jury de ma soutenance qui ont accepté de lire le manuscrit et de se déplacer pour assister à la soutenance.

Enfin, j'adresse mes remerciements à mes amis et proches qui, depuis plusieurs années, ont régulièrement pris des nouvelles de cette aventure.

Contents

Introduction and main results **1**

1 Partitioned solution of a strong coupling scheme **9**
1.1 Introduction . . . 9
1.2 Problem setting . . . 10
1.2.1 The coupled problem . . . 10
1.2.2 Time discretization . . . 12
1.2.3 The defect-correction method . . . 15
1.3 Preconditionning strategies . . . 16
1.3.1 Algorithm 1: Robin-Neumann iteration . . . 16
1.3.2 Algorithm 2: Projection scheme . . . 17
1.3.3 Algorithm 3: Artificial compressibility . . . 20
1.4 Study of Algorithm 3 in a linear framework . . . 21
1.4.1 Interface artifical compressibility . . . 30
1.5 Numerical results . . . 32
1.6 Conclusion . . . 33

2 Robin-Neumann explicit coupling schemes for the coupling with a thin-walled structure **35**
2.1 Introduction . . . 36
2.2 A linear model problem . . . 38
2.3 Robin-Neumann methods . . . 39
2.3.1 Explicit coupling schemes . . . 40
2.4 Stability analysis . . . 44
2.4.1 Notation and weak formulation . . . 44
2.4.2 Space discretization: fully discrete schemes . . . 45
2.4.3 Kinematic perturbation of implicit coupling . . . 46
2.4.4 A priori energy estimates . . . 47
2.4.5 Proof of Theorem 2.4.1 . . . 50
2.5 Iterative partitioned solution of implicit coupling . . . 54
2.5.1 Convergence of the iterative solution procedure . . . 55
2.6 A priori error estimates . . . 57
2.6.1 Preliminaries and main result . . . 57
2.6.2 Proof of Theorem 4.3.3 . . . 60
2.7 Formulation in the non-linear case . . . 67
2.7.1 The non-linear coupled problem . . . 67
2.7.2 Explicit Robin-Neumann schemes . . . 68
2.8 Numerical experiments . . . 69
2.8.1 Convergence study in a two-dimensional test-case . . . 70

2.8.2 Pressure wave propagation in a straight tube 72
2.8.3 Blood flow in an abdominal aortic aneurysm 74
2.8.4 Lid-driven cavity with flexible bottom 76
2.8.5 Damped structural instability 78
2.9 Conclusion 80

3 Generalized Robin-Neumann explicit coupling schemes for the coupling with general thick-walled structures 81
3.1 Introduction 82
3.2 Problem setting 83
3.3 Generalized Robin-Neumann methods 84
3.3.1 Space semi-discretization 84
3.3.2 Generalized interface Robin consistency 86
3.3.3 Time discretization: explicit coupling schemes 88
3.3.3.1 Computer implementation 91
3.3.4 Partitioned solution of implicit coupling 93
3.4 Numerical analysis 94
3.4.1 Preliminaries 95
3.4.2 Stability analysis of the explicit coupling schemes 97
3.4.3 Convergence of the iterative solution procedure 101
3.5 The non-linear case 103
3.5.1 The non-linear coupled problem 103
3.5.2 Explicit coupling schemes 104
3.6 Numerical experiments 105
3.6.1 Numerical study in a two-dimensional test-case 105
3.6.1.1 Accuracy of the explicit coupled schemes 105
3.6.1.2 Partitioned solution of implicit coupling 109
3.6.2 Pressure wave propagation in a straight tube 111
3.6.3 Cantilever test problem 112
3.6.4 Damped structural instability 115
3.7 Conclusion 116

4 Convergence analysis of the generalized Robin-Neuman explicit coupling schemes 119
4.1 Introduction 119
4.2 Numerical methods 120
4.2.1 Spatial semi-discrete approximation 120
4.2.2 Time discretization: coupling schemes 122
4.2.2.1 Generalized Robin-Neumann explicit coupling schemes 122
4.2.2.2 Alternative splitting scheme 127
4.3 Convergence Analysis 128
4.3.1 Preliminaries 128
4.3.2 Projection operators and error decomposition 129

4.3.3 Discrete error estimation 131
4.3.4 A priori error estimates 135
4.3.5 Anlaysis of the fluid-solid hydrodynamic projector 136
4.3.6 Proof of Theorem 4.3.1 140
4.3.7 Proof of Theorem 4.3.2 148
4.4 Numerical experiments 149
4.5 Conclusion 151

General conclusion and perspectives **153**

Bibliography **157**

Introduction and main results

This thesis is devoted to the numerical simulation of mechanical systems involving the interaction of an incompressible fluid and an elastic structure. These problems arise in a wide range of engineering fields, from aeroelasticity of bridge decks and parachute to naval hydrodynamics and the bio-mechanics of airflow and blood (see, e.g., [87, 110, 99, 41, 90, 72]). Computer based simulation of blood flow in large arteries can be used, for instance, in the design of medical devices (see, e.g.,[82, 107]) and the understanding of some pathologies (e.g., aortic coarctation in [109, 9]). Besides, the resolution of inverse problems from patient-specific imaging is particularly relevant for diagnosis and prognosis (see, e.g., [101, 9]). This examples illustrates the need for the development of efficient numerical methods for incompressible fluid-structure interaction, which is one of the main objectives of this thesis.

The fluid will be described by the incompressible Navier-Stokes equations (in a moving domain) and the structure by the non-linear (visco-)elastodynamic equations, coupled on the fluid-structure interface Σ via the kinematic/kinetic relations

$$\begin{cases} \boldsymbol{u}^{\mathrm{f}} = \boldsymbol{u}^{\mathrm{s}} & \text{on} \quad \Sigma, \\ \boldsymbol{\sigma}^{\mathrm{s}}\boldsymbol{n}^{\mathrm{s}} = -\boldsymbol{\sigma}^{\mathrm{f}}\boldsymbol{n}^{\mathrm{f}} & \text{on} \quad \Sigma. \end{cases} \tag{1}$$

Here, $\boldsymbol{u}^{\mathrm{f}}$ and $\boldsymbol{u}^{\mathrm{s}}$ stand for the fluid and solid velocity, and $\boldsymbol{\sigma}^{\mathrm{f}}\boldsymbol{n}^{\mathrm{f}}$ and $\boldsymbol{\sigma}^{\mathrm{s}}\boldsymbol{n}^{\mathrm{s}}$ for the fluid and solidtraction forces on the interface[1]. In most applications, the displacement of the structure cannot be considered infinitesimal. Thus, the position of the interface and, as a result, the computational fluid domain are unknowns of the problem, leading to an additional geometrical compatibility constraint on Σ.

The separate simulation of either an incompressible fluid or an elastic structure are rather well known. The efficient simulation of their interaction through the interface relations (1) is, however, more difficult. Over the last fifteen years, the development of efficient numerical methods for the solution of the coupled problem has been an extremely active field of research (see, e.g., [43, 75] for recent reviews).

In general, the time discretization exploits the heterogeneous structure of the coupled problem. For instance, the fluid and the solid are discretized by different implicit time-marching schemes, tailored by their different mathematical properties. The way the interface coupling conditions (1) are treated at the discrete level (i.e., after space and time discretization) defines the so-called *coupling scheme*. Three different kinds of coupling schemes are traditionally referred to in the literature as: implicit, semi-implicit and explicit coupling schemes.

[1] It should be noted that, in the case of the coupling with a thin-walled structure, the notation $\boldsymbol{\sigma}^{\mathrm{s}}\boldsymbol{n}^{\mathrm{s}}$ represents the left-hand side of the solid momentum conservation equation (see Chapter 2).

A priori, the most efficient way to solve these coupled problems is to consider an **explicit coupling scheme** (or *loosely coupled* scheme, see [100, 103, 42]), that only involves the solution of the fluid and of the structure once per time step with an explicit treatment of the fluid domain motion and of (1). For instance, we can consider the standard Dirichlet-Neumann explicit coupling scheme:

$$\begin{cases} \boldsymbol{u}^{\mathrm{f,n}} = \boldsymbol{u}^{\mathrm{s,n-1}} & \text{on} \quad \Sigma, \\ \boldsymbol{\sigma}^{\mathrm{s,n}}\boldsymbol{n}^{\mathrm{s,n}} = -\boldsymbol{\sigma}^{\mathrm{f,n}}\boldsymbol{n}^{\mathrm{f,n}} & \text{on} \quad \Sigma. \end{cases}$$

Clearly, the resulting solution procedure is genuinely *partitioned*, in the sense that it facilitates the (re-)use of independent fluid and solid solvers, that have been specifically developed for each sub-system (fluid and solid) separately. Unfortunately, the stability of this scheme is dictated by the amount of added-mass in the system (see, e.g., [25, 61]). More precisely, the method suffers from unconditional instability in a physical regime whenever

$$\frac{\rho^{\mathrm{s}}\epsilon}{\rho^{\mathrm{f}}\lambda} < 1, \tag{2}$$

where ρ^{s} and ρ^{f} stand for the solid and fluid density respectively, ϵ is the solid thickness and λ the largest eigenvalue of the so-called added-mass operator, related to the domain geometry. Blood flow in large arteries is a widespread example in which (2) holds. It should be noted that (2) only involves purely physical quantities and, therefore, tuning the time or spatial grid discretization parameters does not cure the problem.

This failure explains why explicit coupling schemes have been practically ruled out for the simulation of incompressible fluid-structure interaction problems and, in part, it has motivated the tremendous amount of work devoted to improve efficiency via alternative methods, based on the more computationally onerous implicit and semi-implicit coupling paradigms (see, e.g., [88, 85, 64, 71, 53, 37, 36, 48, 104, 7, 81, 3, 67, 63, 31, 98, 92, 6]).

For an **implicit coupling scheme** the coupling conditions are exactly enforced at each time step, providing unconditional stability and optimal accuracy. The coupling condition for the implicit coupling scheme reads:

$$\begin{cases} \boldsymbol{u}^{\mathrm{f,n}} = \boldsymbol{u}^{\mathrm{s,n}} & \text{on} \quad \Sigma, \\ \boldsymbol{\sigma}^{\mathrm{s,n}}\boldsymbol{n}^{\mathrm{s,n}} = -\boldsymbol{\sigma}^{\mathrm{f,n}}\boldsymbol{n}^{\mathrm{f,n}} & \text{on} \quad \Sigma, \end{cases} \tag{3}$$

together with an implicit treatment of the geometric compatibility on the interface. Schemes for which (3) holds are often referred to in the literature as *strongly coupled*. The payoff of this enhanced stability is the resolution of a highly-coupled nonlinear problem (at each time-step), which often is computationally demanding. The *monolithic* approach consists in solving the whole coupled problem using specific global solvers and appropriate preconditioners (see, e.g., [111, 58, 63, 31, 37, 62, 71, 92]). On the contrary, *partitioned* methods are modular algorithms using sub-iterations within

each time step ([85, 64, 37, 81, 3, 36, 33, 34]), where the fluid and solid problems are alternatively solved with appropriate interface conditions. As mentioned above, the main advantage of a partitioned resolution is that it enables the use of separate solvers for the fluid and the solid. Such an advantage comes however at a price, computational efficiency over a monolithic approach is not necessarily guaranteed (see, e.g., [4, 63]). In fact, strong added-mass effect not only causes instability of Dirichlet-Neumann explicit coupling schemes, but it also harms the convergence of Dirichlet-Neumann partitioned methods (see, e.g., [25]). Partitioned procedures that overcome this issue through Robin interface conditions have been reported in [3], at the expense of introducing free algorithmic parameters that can be hard to tune.

In a **semi-implicit coupling scheme**, the geometry is treated explicitly. The fluid domain is updated using the interface displacement from previous time-steps, whereas the conditions (3) are enforced on the interface. This does not compromise numerical stability (see, e.g., [96, 108, 94]) and is less computationally onerous than the above discussed (fully) implicit schemes. It should be noted, however, that since the fluid and solid problems remain strongly coupled via (3), the computational complexity at each time-step is still high. Further computational cost reduction can be obtained by reducing the implicit part of the coupling scheme. Typically, this has been achieved by using a fractional-step time-marching in the fluid [48, 104, 5, 1] or in the structure [67, 15, 88, 14].

Stable explicit coupling schemes, circumventing the aforementioned infamous numerical instabilities, have only recently been proposed in the literature. In [16, 18, 20], added-mass free stability is achieved through a specific Robin-Robin treatment of the interface coupling conditions, derived from Nitsche's interface method (see, e.g., [69, 95]) and a stabilization of the interface pressure fluctuations in time (weakly consistent interface compressibility). The price to pay is deterioration of the accuracy, which demands restrictive constraints on the discretization parameters (parabolic-CFL condition), unless enough correction iterations and appropriate extrapolations are performed (see [20, 18, 43]). Numerical evidence suggests that optimal first-order accuracy can be achieved by using a non-symmetric penalty-free formulation (see [20, Section 4.3]). The stability analysis of the resulting schemes remains, however, an open issue.

For a linear coupled problem involving the Stokes equations and an undamped elastic thin-solid model (string or membrane), added-mass free stability and optimal (first-order) accuracy are obtained with the Robin-Neumann explicit coupling schemes introduced in [45, 44]. In short, these methods are incremental displacement-correction fractional-step schemes which introduce optimally consistent perturbations of the interface kinematic constraint $(1)_1$. The non-incremental variant corresponds to the so-called kinematically coupled scheme, reported in [67], which is known to yield poor accuracy (see [45, 44]). Numerical evidence suggests that enhanced accuracy can be obtained with the variants recently introduced in [15, 88, 14]. It should be noted that,

if physical damping is present in the structure equations, the kinematically coupled scheme [67] and its variants [15, 88, 14] are no longer explicit coupling schemes, since the solid viscous contribution must be integrated within the fluid solver (semi-implicit coupling scheme).

To summarize, a challenge remains in the design and the analysis of stable explicit coupling schemes for the coupling with general solid models (thin- and thick-walled, including damping and non-linear behavior) and which deliver optimal accuracy without restrictive constraints on the discretization parameters. This will be addressed in Chapters 2-4 by building on the ideas introduced in [45].

Outline and main results of this thesis

This thesis focuses on the design and analysis of iterative solution procedures of strong coupling (Chapter 1 and Sections 2.5 and 3.4.3) and of Robin-Neumann explicit coupling schemes (Chapters 2-4). We summarize below the contributions of the thesis chapter by chapter. These contributions are recalled in the introduction of each chapter.

Chapter 1 is an introductory chapter in which we consider the iterative solution of a semi-implicit coupling scheme in the case of a non-linear incompressible fluid governed by the Navier-Stokes equation in ALE formalism and a general elastic structure, described by a black-box Neumann-to-Dirichlet map. In this framework, the objective is to investigate iterative solution procedures that are insensitive to the added-mass effect and that are computationally less demanding than standard Dirichlet-Neumann iterations. In the framework of defect-correction iterations, we recover the procedures already reported in [3] and in [34], and propose a new algorithm.

Basically, all the discussed algorithms involve a relaxation of the Dirichlet condition for the fluid and/or the incompressibility constraint, leading to a relative insensitivity to the added mass effect. In addition, some of the methods proposed allow a separate resolution of the fluid velocity and pressure. This specific feature yields additional computational savings.

The three iterative procedures involve a free parameter that has to be properly chosen since the global performances of the scheme highly depend on it. We propose an extensive study of an algorithm based on the artificial compressibility method (see [35]) to investigate the role played by the parameter and how the convergence speed depends on it. At last, a short numerical study is presented.

In **Chapter 2**, we introduce a class of Robin-Neumann explicit coupling schemes for the numerical solution of fluid-structure interaction problems involving a viscous incompressible fluid and a general thin-walled structure (e.g., including damping and non-linear behavior). The methods proposed build on the ideas introduced in [45] by proposing new developments.

It is well known that much materials exhibit viscoelastic behavior and this is, in particular, the case of biological tissue (see, e.g., [79, 24, 115]). Since viscoelastic constitutive laws introduce hydrodynamic effects within the solid equation, one can think of implicitly embeddeding this contributions within the fluid, trough a non-standard Robin condition, and then solve for the solid with the remaining purely elastic contributions (see [67, 44, 88, 15]). As mentioned above, this strategy yields a coupling scheme which is not explicit and the corresponding solution procedure is not partitioned, since part of the solid constitutive behavior must be transferred to the fluid solver. On the other hand, if we keep the whole viscoelastic contribution in the solid solver, the parabolic part of coupled system is not fully implicitly treated and, hence, one could argue that this might yield restrictive stability time-step restrictions. In this chapter, we consider the latter approach, the whole solid viscoelastic contribution is explicitly coupled with the fluid using the inherent Robin consistency of the interface coupling.

The second contribution has to do with the formulation of the explicit coupling schemes. We propose a new Robin-Neumann coupling paradigm which enables the fluid-solid splitting exclusively in terms of the solid velocity and fluid stress on the interface. An interesting feature of this new formulation is its intrinsic character, in the sense that it avoids the annoying extrapolations of the solid viscoelastic terms within the fluid. Hence, the resulting solution procedures are genuinely partitioned. This is, in particular, essential for the coupling with *Reissner-Mindlin* shell models, commonly used in engineering practice (see, e.g, [26, 10]), and that include transverse shear strain effects via rotation surface vectors (independent of the mid-surface displacements). Indeed, the intrinsic Robin interface condition removes the ambiguity in the extrapolation of rotation unknowns and of non-linear terms. The explicit coupling schemes are then formulated in a fully non-linear setting, involving the incompressible Navier-Stokes equations (ALE formalism) and a non-linear viscoelastic shell model.

The third development concerns the numerical analysis of the methods within a representative linear setting, involving a Stokesian fluid and a viscoelastic thin-walled solid (string or membrane). By generalizing the arguments reported in [45], a priori energy and error estimates are provided for all the variants. The analysis shows that the sole implicit treatment of the solid inertia is enough to guarantee (added-mass free) stability. Sub-optimal time-convergence is expected for the variant without extrapolation and optimal accuracy is obtained for the schemes with first- and second-order extrapolations. In particular, the method with first-order extrapolation is (to our knowledge) the first explicit coupling scheme which guaranties unconditional stability and optimal (first-order) accuracy for the considered model problem.

The fourth development deals with the partitioned solution of implicit coupling, via the iterative Robin-Neumann procedures introduced in [3]. So far the convergence analysis of these methods has been addressed in specific simplified models (e.g., inviscid fluid) and in particular geometrical configurations (e.g., a rectangle), using modal analysis (see [3]). In this work, we show that the the stability analysis of the explicit

Robin-Neumann coupling schemes can be reshaped to derive, using energy arguments, a general result on the (added-mass free) convergence of these iterative methods. To the best of our knowledge, the error estimate proposed is the first which yields convergence towards the implicit coupling solution in such a general setting.

Finally, the theoretical results are confirmed by a comprehensive numerical study based on both linear and non-linear models.

In **Chapter 3**, we propose an extension (the first, to the best of our knowledge) of the explicit coupling schemes introduce in Chapter 2 and [45] to the case of the coupling with thick-walled structures: linear and non-linear (possibly damped) elasticity. We show that an intrinsic (parameter free) interface Robin consistency can be recovered at the space semi-discrete level, using a lumped-mass approximation in the structure. Instead of the usual identity operator, the generalized Robin condition involves a new interface operator which consistently accounts for the solid inertial effects within the fluid. The fluid-solid splitting is hence performed through appropriate extrapolations of the solid velocity and stress on the interface. A priori energy estimates, guaranteeing (added-mass) free stability, are derived for all the extrapolations considered within a representative linear framework.

The second contribution of this chapter deals with the partitioned solution of implicit coupling. In fact, the proposed explicit coupling schemes can be interpreted as a single iteration (with appropriate initialization) of a new Robin-Neumann iterative method. Unlike traditional Robin based procedures (see, e.g., [3]), these iterations are parameter free. Using energy arguments, we demonstrate the (added-mass free) convergence of this iterative procedure towards the implicit coupling solution. To the best of our knowledge, the error estimate proposed is the first which yields convergence of a Robin-Neumann procedure in the framework of the coupling with a thick-walled structure (linear viscoelasticity).

Several numerical experiments, based on different linear and non-linear fluid-structure interaction examples from the literature, illustrate the accuracy and performance of the methods proposed. Though the proposed extension retains the main stability properties of the original explicit Robin-Neumann schemes, numerical evidence suggests that their optimal (first-order) accuracy is not necessarily preserved. Indeed, the order of the kinematic perturbation induced by the splitting is expected to be $\mathcal{O}((\tau/h)^{\frac{1}{2}})$, $\mathcal{O}(\tau/h^{\frac{1}{2}})$ or $\mathcal{O}(\tau^2/h^{\frac{1}{2}})$, depending on the order of the extrapolations and with τ, h respectively denoting the time and space discretization parameters.

Finally, **Chapter 4** is devoted to the a priori error analysis of the generalized Robin-Neumann methods introduced in Chapter 3. We show that these schemes can be seen as a lumped-mass approximation of a semi-implicit (fractional-step) coupling scheme with the same stability properties as the original explicit coupling.

A priori error estimates are derived for all the variants (including the case without mass-lumping in the structure) using energy arguments. The analysis proposed represents, to the best of our knowledge, the first theoretical convergence result for a explicit

coupling scheme with a thick-walled structure. Though the proof of the error estimates follows the main steps of thin-walled case (Chapter 2), the thick-walled nature of the solid and the mass-lumping approximation make the analysis more intricate.

The analysis predicts an $\mathcal{O}(h^{-\frac{1}{2}})$ perturbation in the splitting error, confirming the numerical results reported in Chapter 3. The analysis shows that this perturbation is exclusively related to the thick-walled character of the structure, through the non-uniformity of the discrete viscoelastic operator, and not to the mass-lumping approximation in the solid. This point is also evidenced via numerical experiments. We show, in addition, that alternative splitting methods that have been recently reported in the literature (e.g., [14]) suffer from this issue.

Chapter 1

Partitioned solution of a strong coupling scheme

The results presented in this chapter lead to the conference proceedings paper [55]: M.A. Fernández, Y. Maday, J. Mullaert. **Preconditioning of a partitioned fluid-structure interaction Algorithm**. *CSMA 2011, 10ème Colloque National en Calcul des Structures*, May 9-13, 2011, Giens, France.

Contents

1.1 Introduction **9**
1.2 Problem setting **10**
1.2.1 The coupled problem 10
1.2.2 Time discretization 12
1.2.3 The defect-correction method 15
1.3 Preconditionning strategies **16**
1.3.1 Algorithm 1: Robin-Neumann iteration 16
1.3.2 Algorithm 2: Projection scheme 17
1.3.3 Algorithm 3: Artificial compressibility 20
1.4 Study of Algorithm 3 in a linear framework **21**
1.4.1 Interface artifical compressibility 30
1.5 Numerical results **32**
1.6 Conclusion **33**

1.1 Introduction

In this Chapter, we consider the numerical simulation of the interaction between an incompressible fluid and an elastic structure describing, for instance, blood flow in a large artery (see, e.g., [60]). For this kind of problem, the fluid-solid density ratio is close to 1 and the computational domain has a slender shape. These two particularities lead to a large added-mass effect ([25, 61]) that has three major consequences:

- Dirichlet-Neumann iterative solutions procedures need strong relaxation to guarantee convergence;
- The convergence rate of this method is low and dictated by the amount of added-mass in the system;

- Explicit coupling schemes based on Dirichlet-Neumann coupling conditions are unstable.

In this chapter, the fluid is described by incompressible Navier-Stokes equations in ALE (arbitrary Lagrangian Eulerian) formulation. The solid model is described in an abstract form as a general Neumann-to-Dirichlet map, allowing the use of a wide range of solvers. We consider a semi-implicit coupling scheme in which the motion of the fluid domain is treated explicitly.

The general objective is to investigate iterative solution procedures that are insensitive to the added-mass effect, using appropriate (non-linear) preconditioners of the coupled problem. Multiple choices are discussed, some of them leading to already existing strategies and other to a new one. As we shall see in the following, added-mass free preconditioners are mainly obtained by simplified fluid-structure coupled models where one of the following ingredients are used:

- The solid acts as a spring, leading to Robin condition for the fluid. As it is discussed in [3], the compliance of the spring plays the role of a relaxation parameter for the Dirichlet boundary condition;

- The incompressibility of the fluid is relaxed, either by using a Chorin-Temam projection scheme or by introducing artificial compressibility (see, e.g., [35]).

The rest of this chapter is organized as follows. Section 1.2 recalls the coupled problem and its time discretization. Then three iterative procedures are briefly presented in Section 1.3. The analysis of the third method in a linear setting is done in Section 1.4. At last, a short numerical study are presented in Section 1.5.

1.2 Problem setting

1.2.1 The coupled problem

We consider a reference domain $\Omega = \Omega^{\mathrm{f}} \cup \Omega^{\mathrm{s}}$ for the fluid-structure interaction problem and we denote by $\Sigma \stackrel{\mathrm{def}}{=} \partial\Omega^{\mathrm{f}} \cap \partial\Omega^{\mathrm{s}}$ the fluid-structure interface in this reference configuration. The fluid border $\partial\Omega^{\mathrm{f}} = \Sigma \cup \Gamma$ is composed of the fluid-structure interface Σ and of the inlet/outlet boundary $\Gamma \stackrel{\mathrm{def}}{=} \Gamma^{\mathrm{in}} \cup \Gamma^{\mathrm{out}}$ (see Figure 1.1). The solid border $\partial\Omega^{\mathrm{s}}$ is split into Σ, Γ^{d} and Γ^{n}. The symbols $\boldsymbol{n}^{\mathrm{f}}$ and $\boldsymbol{n}^{\mathrm{s}}$ denote the outward unit normal to the fluid and the solid, respectively. At time $t > 0$, the current configuration of the fluid domain, $\Omega^{\mathrm{f}}(t)$, is parametrized by the ALE map $\boldsymbol{\mathcal{A}} \stackrel{\mathrm{def}}{=} \boldsymbol{I}_{\Omega_{\mathrm{f}}} + \boldsymbol{d}_{\mathrm{f}}$ as $\Omega^{\mathrm{f}}(t) = \boldsymbol{\mathcal{A}}(\Omega^{\mathrm{f}}, t)$, where $\boldsymbol{d}^{\mathrm{f}} : \Omega^{\mathrm{f}} \times \mathbb{R}^+ \to \mathbb{R}^d$ stands for the displacement of the fluid domain. In practice, $\boldsymbol{d}^{\mathrm{f}} = \mathrm{Ext}(\boldsymbol{d}|_\Sigma)$, where $\mathrm{Ext}(\cdot)$ denotes any reasonable lifting operator from the (reference) interface Σ into the (reference) fluid domain Ω^{f}, which vanishes on Γ.

The strong form of the non-linear fluid-structure problem reads therefore as follows: find the fluid velocity $\boldsymbol{u} : \Omega^{\mathrm{f}} \times \mathbb{R}^+ \to \mathbb{R}^d$, $(d = 2, 3)$ the fluid pressure $p : \Omega^{\mathrm{f}} \times \mathbb{R}^+ \to \mathbb{R}$,

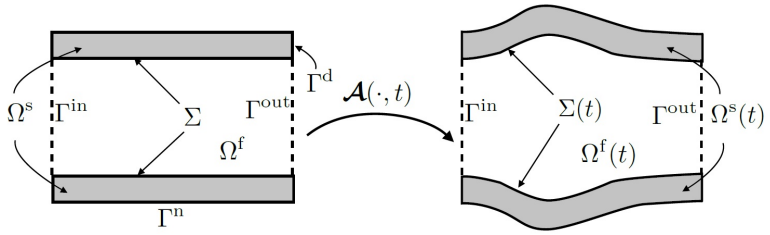

Figure 1.1: Geometrical description

the structure displacement $\boldsymbol{d} : \Omega^{\mathrm{s}} \times \mathbb{R}^+ \to \mathbb{R}^d$ and the structure velocity $\dot{\boldsymbol{d}} : \Omega^{\mathrm{s}} \times \mathbb{R}^+ \to \mathbb{R}^d$ such that

$$\text{(Fluid)} \begin{cases} \rho^{\mathrm{f}} \partial_t|_{\mathcal{A}} \boldsymbol{u} + \rho^{\mathrm{f}}(\boldsymbol{u} - \boldsymbol{w}) \cdot \boldsymbol{\nabla} \boldsymbol{u} - \boldsymbol{\nabla} \cdot \boldsymbol{\sigma}^{\mathrm{f}}(\boldsymbol{u}, p) = \boldsymbol{0} & \text{in} \quad \Omega^{\mathrm{f}}(t), \\ \mathrm{div} \boldsymbol{u} = 0 & \text{in} \quad \Omega^{\mathrm{f}}(t), \\ \boldsymbol{\sigma}^{\mathrm{f}}(\boldsymbol{u}, p) \boldsymbol{n}^{\mathrm{f}} = -\bar{p} \boldsymbol{n}^{\mathrm{f}} & \text{on} \quad \Gamma, \end{cases} \tag{1.1}$$

$$\text{(Solid)} \begin{cases} \rho^{\mathrm{s}} \partial_t \dot{\boldsymbol{d}} - \mathbf{div}\, \boldsymbol{\Pi}(\boldsymbol{d}) = \boldsymbol{0} & \text{in} \quad \Omega^{\mathrm{s}}, \\ \dot{\boldsymbol{d}} = \partial_t \boldsymbol{d} & \text{in} \quad \Omega^{\mathrm{s}}, \\ \boldsymbol{d} = \boldsymbol{0} & \text{on} \quad \Gamma^{\mathrm{d}}, \\ \boldsymbol{\Pi}(\boldsymbol{d}) \boldsymbol{n}^{\mathrm{s}} = \boldsymbol{0} & \text{on} \quad \Gamma^{\mathrm{n}}, \end{cases} \tag{1.2}$$

$$\text{(Coupling)} \begin{cases} \boldsymbol{d}^{\mathrm{f}} = \mathrm{Ext}(\boldsymbol{d}|_{\Sigma}), \quad \boldsymbol{w} = \partial_{\mathrm{t}} \boldsymbol{d}^{\mathrm{f}} & \text{on} \quad \Omega^{\mathrm{f}}, \\ \boldsymbol{u} = \boldsymbol{w} & \text{on} \quad \Sigma(t), \\ \boldsymbol{\Pi}(\boldsymbol{d}) \boldsymbol{n}^{\mathrm{s}} = -J \boldsymbol{\sigma}^{\mathrm{f}}(\boldsymbol{u}, p) \boldsymbol{F}^{-\mathrm{T}} \boldsymbol{n}^{\mathrm{f}} & \text{on} \quad \Sigma, \end{cases} \tag{1.3}$$

complemented with the initial conditions

$$\boldsymbol{u}(0) = \boldsymbol{u}^0, \quad \boldsymbol{d}(0) = \boldsymbol{d}^0, \quad \dot{\boldsymbol{d}}(0) = \dot{\boldsymbol{d}}^0.$$

Here $\partial_t|_{\boldsymbol{\mathcal{A}}}$ represents the ALE time derivative, $\boldsymbol{F} \overset{\mathrm{def}}{=} \boldsymbol{\nabla} \boldsymbol{\mathcal{A}}$ the fluid domain gradient of deformation and $J \overset{\mathrm{def}}{=} \det \boldsymbol{F}$ the Jacobian.

Remark 1.2.1. *Note that the physical quantities $\boldsymbol{u}$, p and $\boldsymbol{w}$ are defined in the reference fluid domain Ω^{f}. In (1.1) and $(1.3)_2$ they are evaluated in the current fluid domain, $\Omega^{\mathrm{f}}(t)$, by composition with $\boldsymbol{\mathcal{A}}^{-1}(\cdot, t)$. In order to ease the presentation, this change of variable is not specified in the equations.*

The quantity $\bar{p}$ represents a pressure enforced at the inlet/outlet interface Γ. The constants ρ^{f} and ρ^{s} stand for the fluid and solid densities, respectively. The Cauchy stress tensor is denoted by $\boldsymbol{\sigma}^{\mathrm{f}}(\boldsymbol{u}, p) \overset{\mathrm{def}}{=} -p\boldsymbol{I} + 2\mu \boldsymbol{\epsilon}(\boldsymbol{u})$ with the dynamic viscosity μ and $\boldsymbol{\epsilon}(\boldsymbol{u}) \overset{\mathrm{def}}{=} \frac{1}{2}\left(\boldsymbol{\nabla} \boldsymbol{u} + \boldsymbol{\nabla} \boldsymbol{u}^{\mathrm{T}}\right)$. At last, $\boldsymbol{\Pi}(\boldsymbol{d})$ denotes the first Piola-Kirchhoff tensor, $\boldsymbol{F}^{\mathrm{f}} \overset{\mathrm{def}}{=} \boldsymbol{\nabla} \boldsymbol{\mathcal{A}}$ the gradient of the fluid domain deformation and $J \overset{\mathrm{def}}{=} \det \boldsymbol{F}^{\mathrm{f}}$ its Jacobian.

The coupled problem (1.1)-(1.2) and (1.3) is the root problem in this thesis. A review of the mathematical analysis for this type of problem can be found in [89]. In particular, the next result (from [91] and [46]) states an energy inequality.

Lemma 1.2.1. *Assume that the structure is hyper-elastic (with energy density function W) and that the coupled fluid-structure system is isolated, (i.e. $\boldsymbol{u} = 0$ on Γ). Let*

$$E(t) \stackrel{\text{def}}{=} \int_{\Omega^{\mathrm{f}}(t)} \frac{\rho^{\mathrm{f}}}{2}|\boldsymbol{u}|^2 + \int_{\Omega^{\mathrm{s}}} \frac{\rho^{\mathrm{s}}}{2}|\dot{\boldsymbol{d}}|^2 + \int_{\Omega^{\mathrm{s}}} W\big(\boldsymbol{d}\big)$$

be the total mechanical energy of the fluid-structure system described by (1.1)-(1.2) *and* (1.3)*. Then, the following energy identity holds:*

$$E(t) = E(0) - \int_0^t \int_{\Omega^{\mathrm{f}}(t)} 2\mu|\boldsymbol{\epsilon}(\boldsymbol{u})|^2.$$

1.2.2 Time discretization

In what follows, $\tau > 0$ denotes the time step, $\partial_\tau X^n \stackrel{\text{def}}{=} (X^n - X^{n-1})/\tau$ the discrete backward difference derivative and $X^{n-\frac{1}{2}} \stackrel{\text{def}}{=} (X^n + X^{n-1})/2$ the mid-point approximation. We use a standard semi-implicit time discretization of (1.1) and a mid-point (energy-preserving) scheme for the structure (1.2). For a positive integer m, $H^m(\Omega^{\mathrm{f}})$ denotes the standard Sobolev space and we define $\boldsymbol{H}^m(\Omega^{\mathrm{f}}) \stackrel{\text{def}}{=} \big[H^m(\Omega^{\mathrm{f}})\big]^d$. The space $\boldsymbol{H}^m_\Sigma(\Omega^{\mathrm{f}})$ stands for the closed subspace of functions of $\boldsymbol{H}^m(\Omega^{\mathrm{f}})$ with zero trace on Σ.

For the sake of simplicity, we reduce the solid model to a Neumann-to-Dirichlet map $\boldsymbol{S} : \boldsymbol{H}^1(\Omega^{\mathrm{f}}) \times L^2(\Omega^{\mathrm{f}}) \to \boldsymbol{H}^{\frac{1}{2}}(\Sigma)$, that maps the couple of fluid unknowns $(\boldsymbol{u}, p)$ to the interface restriction $\boldsymbol{\lambda} = \boldsymbol{S}(\boldsymbol{u}, p) \stackrel{\text{def}}{=} \boldsymbol{d}|_\Sigma$, where $\boldsymbol{d}$ is the solution of the following problem:

$$\begin{cases} \dfrac{\rho^{\mathrm{s}}}{\tau}\big(\dot{\boldsymbol{d}} - \dot{\boldsymbol{d}}^{n-1}\big) - \boldsymbol{\nabla}\cdot\boldsymbol{\Pi}\big((\boldsymbol{d} + \boldsymbol{d}^{n-1})/2\big) = \boldsymbol{0}, & \text{in} \quad \Omega^{\mathrm{s}}, \\ \dfrac{1}{\tau}(\boldsymbol{d} - \boldsymbol{d}^{n-1}) = \dfrac{1}{2}\big(\dot{\boldsymbol{d}} + \dot{\boldsymbol{d}}^{n-1}\big), & \text{in} \quad \Omega^{\mathrm{s}}, \\ \boldsymbol{d} = \boldsymbol{0} & \text{on} \quad \Gamma^{\mathrm{d}}, \\ \boldsymbol{\Pi}\big((\boldsymbol{d} + \boldsymbol{d}^{n-1})/2\big)\boldsymbol{n}^{\mathrm{s}} = \boldsymbol{0}, & \text{on} \quad \Gamma^{\mathrm{n}}, \\ \boldsymbol{\Pi}\big((\boldsymbol{d} + \boldsymbol{d}^{n-1})/2\big)\boldsymbol{n}^{\mathrm{s}} = -J^{\mathrm{f,n}}\boldsymbol{\sigma}^{\mathrm{f}}(\boldsymbol{u}, p)\big(\boldsymbol{F}^{\mathrm{f,n}}\big)^{-T}\boldsymbol{n}^{\mathrm{s}}, & \text{on} \quad \Sigma. \end{cases}$$

Remark 1.2.2. *From now on, the time discretized solid model will be embedded into this black-box abstract operator $\boldsymbol{S}$.*

The time semi-discretized formulation of the coupled problem (1.1)-(1.3) with an implicit treatment of the coupling conditions reads therefore as follows: for $n > 0$, find the domain displacement $\boldsymbol{d}^{\mathrm{f,n}} : \Omega^{\mathrm{f}} \to \mathbb{R}^d$ and the fluid unknowns $\boldsymbol{u}^n : \Omega^{\mathrm{f}} \to \mathbb{R}^d$ and $p^n : \Omega^{\mathrm{f}} \to \mathbb{R}$ such that

1. Geometry update (explicit step):

$$\begin{cases} \boldsymbol{d}^{\mathrm{f,n}} = \mathrm{Ext}(\boldsymbol{d}^{\mathrm{n}-1}|_{\Sigma}), \\ \boldsymbol{w}^n = \partial_\tau \boldsymbol{d}^{\mathrm{f},n}, \\ \Omega^{\mathrm{f,n}} = (\boldsymbol{I}_{\Omega^{\mathrm{f}}} + \boldsymbol{d}^{\mathrm{f},n})(\Omega^{\mathrm{f}}). \end{cases}$$

2. Fluid-structure interaction step (implicit coupling):

$$\begin{cases} \dfrac{\rho^{\mathrm{f}}}{\tau}(\boldsymbol{u}^n - \boldsymbol{u}^{n-1})|_{\mathcal{A}} + \rho^{\mathrm{f}}(\boldsymbol{u}^{n-1} - \boldsymbol{w}^n)\cdot\boldsymbol{\nabla}\boldsymbol{u}^n - \boldsymbol{\nabla}\cdot\boldsymbol{\sigma}^{\mathrm{f}}(\boldsymbol{u}^n, p^n) = \boldsymbol{0} \quad \text{in} \quad \Omega^{\mathrm{f,n}}, \\ \qquad\qquad \mathrm{div}\,\boldsymbol{u}^n = 0 \quad \text{in} \quad \Omega^{\mathrm{f,n}}, \\ \qquad\qquad \boldsymbol{\sigma}^{\mathrm{f}}(\boldsymbol{u}^n, p^n)\boldsymbol{n}^{\mathrm{f}} = -\bar{p}^n\boldsymbol{n}^{\mathrm{f}} \quad \text{on} \quad \Gamma, \\ \qquad\qquad \boldsymbol{u}^n = \dfrac{\boldsymbol{S}(\boldsymbol{u}^n, p^n) - \boldsymbol{d}^{n-1}_{|\Sigma}}{\tau} \quad \text{on} \quad \Sigma^n, \end{cases} \tag{1.4}$$

3. Update the interface displacement

$$\boldsymbol{d}^n_{|\Sigma} = \boldsymbol{S}(\boldsymbol{u}^n, p^n).$$

Remark 1.2.3. *Note that, by definition, all the time semi-discrete fluid fields* $\{\boldsymbol{u}^n\}_{n\geq 0}$, $\{p^n\}_{n\geq 1}$ *and* $\{\boldsymbol{w}\}_{n\geq 1}$ *are defined in the reference configuration* Ω^{f}. *In* (1.4) *these fields are transported to* $\Omega^{\mathrm{f},n}$ *by composition with* $(\boldsymbol{\mathcal{A}}^n)^{-1}$, *where* $\boldsymbol{\mathcal{A}}^n \overset{\mathrm{def}}{=} \boldsymbol{I}_{\Omega^{\mathrm{f}}} + \boldsymbol{d}^{\mathrm{f},n}$. *This also applies to the solid quantities appearing in the right-hand side of* $(1.4)_4$.

The variational form of (1.4) reads as follows: for $n \geq 0$, find $\boldsymbol{u}^n \in \boldsymbol{H}^1(\Omega^{\mathrm{f}})$ and $p^n \in L^2(\Omega^{\mathrm{f}})$ such that

$$\begin{aligned} \frac{\rho^{\mathrm{f}}}{\tau}\left(\int_{\Omega^{\mathrm{f},n}} \boldsymbol{u}^n\cdot\boldsymbol{v}^{\mathrm{f}} - \int_{\Omega^{\mathrm{f},n-1}} \boldsymbol{u}^{n-1}\cdot\boldsymbol{v}^{\mathrm{f}}\right) + \rho^{\mathrm{f}}\int_{\Omega^{\mathrm{f},n}} \big(\boldsymbol{u}^{n-1} - \boldsymbol{w}^n\big)\cdot\boldsymbol{\nabla}\boldsymbol{u}^n\cdot\boldsymbol{v}^{\mathrm{f}} \\ - \rho^{\mathrm{f}}\int_{\Omega^{\mathrm{f},n}} \big(\boldsymbol{\nabla}\cdot\boldsymbol{w}^n\big)\boldsymbol{u}^n\cdot\boldsymbol{v}^{\mathrm{f}} + \int_{\Omega^{\mathrm{f},n}} \boldsymbol{\sigma}(\boldsymbol{u}^n, p^n) : \boldsymbol{\nabla}\boldsymbol{v}^{\mathrm{f}} + \int_{\Omega^{\mathrm{f},n}} q\,\mathrm{div}\boldsymbol{u}^n \\ + \int_{\Sigma^n}\left(\boldsymbol{u}^n - \frac{\boldsymbol{S}(\boldsymbol{u}^n, p^n) - \boldsymbol{d}^{n-1}_{|\Sigma}}{\tau}\right)\cdot\boldsymbol{\xi} = -\int_{\Gamma}\bar{p}(t_n)\boldsymbol{v}^{\mathrm{f}}\cdot\boldsymbol{n} \end{aligned} \tag{1.5}$$

for all $(\boldsymbol{v}^{\mathrm{f}}, q, \boldsymbol{\xi}) \in \boldsymbol{H}^1_{\Sigma}(\Omega^{\mathrm{f}}) \times L^2(\Omega^{\mathrm{f}}) \times \boldsymbol{L}^2(\Sigma)$. Note that, or the sake of simplicity, we have integrated the Dirichlet boundary condition on Σ^n in the variational formulation.

Remark 1.2.4. *The test functions and the time-semidiscrete quantities are defined in the reference configuration (see Remark 1.2.3 above). Hence, each appearance of these fields within the integrals* $\int_{\Omega^{\mathrm{f},n}}$ *and* $\int_{\Omega^{\mathrm{f},n-1}}$ *of* (1.5) *implicitly includes a composition with* $(\boldsymbol{\mathcal{A}}^n)^{-1}$ *and* $(\boldsymbol{\mathcal{A}}^{n-1})^{-1}$, *respectively. The same applies to the boundary integral on* Σ^n.

The standard Dirichlet-Neumann iteration to solve problem (1.4) consists in setting the initial values $\boldsymbol{u}_0 = \boldsymbol{u}^{n-1}$, $p_0 = p^{n-1}$, $\boldsymbol{\lambda}_0 = \boldsymbol{d}_{|\Sigma}^{n-1}$ and performing the following iteration, until convergence:

1. Fluid step (Dirichlet): find $(\boldsymbol{u}_k, p_k) \in \boldsymbol{H}^1(\Omega^{\mathrm{f}}) \times L^2(\Omega^{\mathrm{f}})$, such that

$$\left\{\begin{array}{rll} \dfrac{\rho^{\mathrm{f}}}{\tau}(\boldsymbol{u}_k - \boldsymbol{u}^{n-1})|_{\mathcal{A}} + \rho^{\mathrm{f}}(\boldsymbol{u}^{n-1} - \boldsymbol{w}^n)\cdot\boldsymbol{\nabla}\boldsymbol{u}_k - \boldsymbol{\nabla}\cdot\boldsymbol{\sigma}^{\mathrm{f}}(\boldsymbol{u}_k, p_k) = \boldsymbol{0} & \text{in} & \Omega^{\mathrm{f,n}}, \\ \mathrm{div}\,\boldsymbol{u}_k = 0 & \text{in} & \Omega^{\mathrm{f,n}}, \\ \boldsymbol{\sigma}^{\mathrm{f}}(\boldsymbol{u}_k, p_k)\boldsymbol{n}^{\mathrm{f}} = -\bar{p}^n\boldsymbol{n}^{\mathrm{f}} & \text{on} & \Gamma, \\ \boldsymbol{u}_k = \dfrac{\boldsymbol{\lambda}_{k-1} - \boldsymbol{d}_{|\Sigma}^{n-1}}{\tau} & \text{on} & \Sigma^n, \end{array}\right. \tag{1.6}$$

2. Solid step (Neumann): find $\boldsymbol{\lambda}_k \in \boldsymbol{H}^{\frac{1}{2}}(\Sigma)$ such that

$$\boldsymbol{\lambda}_k = \boldsymbol{S}(\boldsymbol{u}_k, p_k). \tag{1.7}$$

Unfortunately, added-mass issues make this iteration unconditionally unstable when dealing with the simulation of blood flow in large arteries because the fluid-solid density ratio is close to 1 and the domain is lengthy (see [25]). One solution to overcome this difficulty is to introduce a relaxation step at the end of the algorithm. Practically, the iteration in the case of a static relaxation with parameter ω becomes:

1. Fluid step (Dirichlet): find $(\boldsymbol{u}_k, p_k) \in \boldsymbol{H}^1(\Omega^{\mathrm{f}}) \times L^2(\Omega^{\mathrm{f}})$, such that

$$\left\{\begin{array}{rll} \dfrac{\rho^{\mathrm{f}}}{\tau}(\boldsymbol{u}_k - \boldsymbol{u}^{n-1})|_{\mathcal{A}} + \rho^{\mathrm{f}}(\boldsymbol{u}^{n-1} - \boldsymbol{w}^n)\cdot\boldsymbol{\nabla}\boldsymbol{u}_k - \boldsymbol{\nabla}\cdot\boldsymbol{\sigma}^{\mathrm{f}}(\boldsymbol{u}_k, p_k) = \boldsymbol{0} & \text{in} & \Omega^{\mathrm{f,n}}, \\ \mathrm{div}\,\boldsymbol{u}_k = 0 & \text{in} & \Omega^{\mathrm{f,n}}, \\ \boldsymbol{\sigma}^{\mathrm{f}}(\boldsymbol{u}_k, p_k)\boldsymbol{n}^{\mathrm{f}} = -\bar{p}^n\boldsymbol{n}^{\mathrm{f}} & \text{on} & \Gamma, \\ \boldsymbol{u}_k = \dfrac{\boldsymbol{\lambda}_{k-1} - \boldsymbol{d}_{|\Sigma}^{n-1}}{\tau} & \text{on} & \Sigma^n, \end{array}\right. \tag{1.8}$$

2. Solid step (Neumann): find $\widetilde{\boldsymbol{\lambda}}_k \in \boldsymbol{H}^{\frac{1}{2}}(\Sigma)$ such that

$$\widetilde{\boldsymbol{\lambda}}_k = \boldsymbol{S}(\boldsymbol{u}_k, p_k). \tag{1.9}$$

3. Relaxation step: set

$$\boldsymbol{\lambda}_k = \omega\widetilde{\boldsymbol{\lambda}}_k + (1-\omega)\boldsymbol{\lambda}_{k-1}. \tag{1.10}$$

Of course, the parameter ω has to be properly chosen and the iteration may fail to converge if ω is to large (see [3]). A possible improvement is to use dynamic relaxation with, for example, Aitken's formula (see [81, 85]). Nevertheless, this method still yields very slow convergence rate and high computational costs. In this context, the purpose of this chapter is to propose an alternative generic formulation in order to derive iterative procedures with better numerical properties.

1.2.3 The defect-correction method

We first introduce some notations. Let $\boldsymbol{V}$ be the space

$$\boldsymbol{V} \stackrel{\text{def}}{=} \boldsymbol{H}^1_{\Sigma}(\Omega^{\mathrm{f}}) \times L^2(\Omega^{\mathrm{f}}) \times \boldsymbol{L}^2(\Sigma),$$

and $\boldsymbol{A} : \boldsymbol{H}^1(\Omega^{\mathrm{f}}) \times L^2(\Omega^{\mathrm{f}}) \times \boldsymbol{L}^2(\Sigma) \to \boldsymbol{V}'$, the fluid linear operator taken from (1.5) and defined for all $\big(\boldsymbol{v}, q, \boldsymbol{\xi}\big) \in \boldsymbol{V}$ by

$$\begin{aligned}\big\langle \boldsymbol{A}\big(\boldsymbol{u}, p, \boldsymbol{\lambda}\big), \big(\boldsymbol{v}, q, \boldsymbol{\xi}\big)\big\rangle_{\boldsymbol{V}',\boldsymbol{V}} \stackrel{\text{def}}{=} \frac{\rho^{\mathrm{f}}}{\tau}\left(\int_{\Omega^{\mathrm{f,n}}} \boldsymbol{u}\cdot\boldsymbol{v} - \int_{\Omega^{\mathrm{f,n-1}}} \boldsymbol{u}^{n-1}\cdot\boldsymbol{v}\right) - \rho^{\mathrm{f}}\int_{\Omega^{\mathrm{f,n}}} (\boldsymbol{\nabla}\cdot\boldsymbol{w}^n)\boldsymbol{u}\cdot\boldsymbol{v} \\ + \rho^{\mathrm{f}}\int_{\Omega^{\mathrm{f,n}}} (\boldsymbol{u}^{n-1}-\boldsymbol{w}^n)\cdot\boldsymbol{\nabla}\boldsymbol{u}\cdot\boldsymbol{v} + \int_{\Omega^{\mathrm{f,n}}} \boldsymbol{\sigma}(\boldsymbol{u},p) : \boldsymbol{\epsilon}(\boldsymbol{v}) \\ + \int_{\Omega^{\mathrm{f},n}} q\,\mathrm{div}\boldsymbol{u} + \int_{\Gamma} \bar{p}(t_n)\,\boldsymbol{v}\cdot\boldsymbol{n}^{\mathrm{f}} \\ + \int_{\Sigma^n}\left(\boldsymbol{u} - \frac{\boldsymbol{\lambda} - \boldsymbol{d}^{n-1}_{|\Sigma}}{\tau}\right)\cdot\boldsymbol{\xi}.\end{aligned} \tag{1.11}$$

Whith this notation, problem (1.4) reduces to the determination of

$$(\boldsymbol{u}^n, p^n) \in \boldsymbol{H}^1(\Omega^{\mathrm{f}}) \times L^2(\Omega^{\mathrm{f}}),$$

such that the following residual vanishes in $\boldsymbol{V}'$:

$$\boldsymbol{R}\big(\boldsymbol{u}^n, p^n\big) \stackrel{\text{def}}{=} \boldsymbol{A}\big(\boldsymbol{u}^n, p^n, \boldsymbol{S}(\boldsymbol{u}^n, p^n)\big) = \boldsymbol{0}. \tag{1.12}$$

In this chapter, we use the defect-correction method (see e.g. [106]) to build a sequence $(\boldsymbol{u}_k, p_k)$ that converges towards the solution $\big(\boldsymbol{u}^n, p^n\big)$ of (1.12). To this aim, we introduce a variety of simplified residuals denoted by $\widetilde{\boldsymbol{R}}$ as preconditioner for the implicit coupling problem and we study the numerical properties of the following sequence:

$$\begin{cases} (\boldsymbol{u}_0, p_0) = (\boldsymbol{u}^{n-1}, p^{n-1}) \\ \widetilde{\boldsymbol{R}}(\boldsymbol{u}_k, p_k) = \widetilde{\boldsymbol{R}}(\boldsymbol{u}_{k-1}, p_{k-1}) - \boldsymbol{R}(\boldsymbol{u}_{k-1}, p_{k-1}) \quad \forall k \geq 1, \end{cases} \tag{1.13}$$

From (1.13), we infer that the limit of the sequence $(\boldsymbol{u}_k, p_k)$ (if it exists) provides a solution of (1.12). Moreover, the computation of $(\boldsymbol{u}_k, p_k)$ only requires the evaluation $\boldsymbol{R}(\boldsymbol{u}_{k-1}, p_{k-1})$ of the full residual and not the resolution of the full problem $\boldsymbol{R}(\boldsymbol{u}_k, p_k) = 0$. The contribution of this chapter therefore consist in proposing simplified residuals $\widetilde{\boldsymbol{R}}$ that are easy to inverse and studying the convergence speed of the resulting iterative procedure.

Remark 1.2.5. *Iteration* (1.13) *has clear connections with the stationary Richardson iterative method in the case where the residual* $\widetilde{\boldsymbol{R}}$ *is a linear operator. Indeed, in this case, iteration* (1.13) *reduces to*

$$\begin{pmatrix}\boldsymbol{u}_k \\ p_k\end{pmatrix} = \begin{pmatrix}\boldsymbol{u}_{k-1} \\ p_{k-1}\end{pmatrix} - \widetilde{\boldsymbol{R}}^{-1}\boldsymbol{R}(\boldsymbol{u}_{k-1}, p_{k-1})$$

Hence, we call the simplified residual $\widetilde{\boldsymbol{R}}$ *a preconditioner in the following.*

Remark 1.2.6. *The original Dirichlet-Neumann iteration* (1.6)-(1.7) *can also be seen as a defect-correction iteration with the choice*

$$\widetilde{\boldsymbol{R}}(\boldsymbol{u},p) = \boldsymbol{A}\big(\boldsymbol{u},p,\boldsymbol{0}\big),$$

which illustrate that defect-correction iteration are a convenient framework for deriving iterative solution algorithms of problem (1.4).

1.3 Preconditionning strategies

In this section, we present four algorithms based on defect-correction iteration to solve problem (1.5).

1.3.1 Algorithm 1: Robin-Neumann iteration

We first propose to use a simplified solid model $\widetilde{S}$ which is linear and reacts proportionally to the stress applied to it. Namely, for all $(\boldsymbol{u},p) \in \boldsymbol{H}^1(\Omega^{\mathrm{f}}) \times L^2(\Omega^{\mathrm{f}})$, we set

$$\widetilde{\boldsymbol{S}}(\boldsymbol{u},p) \stackrel{\text{def}}{=} -\alpha\, \boldsymbol{\sigma}(\boldsymbol{u},p)\, \boldsymbol{n}^{\mathrm{f}}, \tag{1.14}$$

for a positive parameter α. With this model, the solid acts as a coil spring without mass and with rigidity $1/\alpha$. The corresponding residual $\widetilde{\boldsymbol{R}}$ reads

$$\widetilde{\boldsymbol{R}}_1\big(\boldsymbol{u},p\big) \stackrel{\text{def}}{=} \boldsymbol{A}\big(\boldsymbol{u},p,\widetilde{\boldsymbol{S}}(\boldsymbol{u},p)\big).$$

With this choice of the preconditioner, iteration $(1.13)_2$ writes

$$\Big\langle \widetilde{\boldsymbol{R}}_1\big(\boldsymbol{u}_k,p_k\big), (\boldsymbol{v},q,\boldsymbol{\xi})\Big\rangle_{\boldsymbol{V}',\boldsymbol{V}} = \frac{1}{\tau}\int_{\Sigma^n} \Big(\boldsymbol{S}(\boldsymbol{u}_{k-1},p_{k-1}) - \widetilde{\boldsymbol{S}}(\boldsymbol{u}_{k-1},p_{k-1})\Big)\cdot\boldsymbol{\xi}$$

and leads to the following defect-correction iteration based on a Robin interface condition for the fluid:

$$\left\{\begin{aligned}
\rho^{\mathrm{f}}\,\frac{\boldsymbol{u}_k-\boldsymbol{u}^n}{\tau}\Big|_{\boldsymbol{\mathcal{A}}} + \rho^{\mathrm{f}}(\boldsymbol{u}^{n-1}-\boldsymbol{w}^n)\cdot\boldsymbol{\nabla}\boldsymbol{u}_k - \boldsymbol{\nabla}\cdot\boldsymbol{\sigma}^{\mathrm{f}}(\boldsymbol{u}_k,p_k) &= \boldsymbol{0} \quad \text{in} \quad \Omega^{\mathrm{f,n}},\\
\boldsymbol{\nabla}\cdot\boldsymbol{u}_k &= 0 \quad \text{in} \quad \Omega^{\mathrm{f,n}},\\
\boldsymbol{\sigma}^{\mathrm{f}}(\boldsymbol{u}_k,p_k)\boldsymbol{n}^{\mathrm{f}} + \frac{\tau}{\alpha}\boldsymbol{u}_k = \frac{\tau}{\alpha}\frac{\boldsymbol{S}(\boldsymbol{u}_{k-1},p_{k-1}) - \boldsymbol{d}^{n-1}_{|\Sigma}}{\tau} + \boldsymbol{\sigma}^{\mathrm{f}}(\boldsymbol{u}_{k-1},p_{k-1})\,\boldsymbol{n}^{\mathrm{f}} &\quad \text{on} \quad \Sigma^n,\\
\boldsymbol{\sigma}(\boldsymbol{u}_k,p_k)\,\boldsymbol{n}^{\mathrm{f}} = -\bar{p}\,\boldsymbol{n}^{\mathrm{f}} &\quad \text{on} \quad \Gamma.
\end{aligned}\right. \tag{1.15}$$

Iteration (1.15) is similar to the family of Robin-Neumann iterations proposed in [3], with the correspondence $\tau/\alpha \stackrel{\text{def}}{=} \alpha_{\mathrm{f}}$. In addition, the main difference between iteration (1.15) and the original Dirichlet-Neumann iteration (1.8)-(1.9) is the relaxation of

the Dirichlet boundary condition $(1.6)_4$. Indeed, the boundary condition $(1.15)_3$ also writes:

$$\boldsymbol{u}_k = \frac{\boldsymbol{S}(\boldsymbol{u}_{k-1}, p_{k-1}) - \boldsymbol{d}^n}{\tau} - \frac{\alpha}{\tau}\left(\boldsymbol{\sigma}^{\mathrm{f}}(\boldsymbol{u}_k, p_k)\boldsymbol{n}^{\mathrm{f}} - \boldsymbol{\sigma}^{\mathrm{f}}(\boldsymbol{u}_{k-1}, p_{k-1})\boldsymbol{n}^{\mathrm{f}}\right)$$

Thus, apart from its physical interpretation, the parameter α also plays the role of a relaxation parameter. At the limit $\alpha \to 0$, the relaxation vanishes and the Dirichlet condition $(1.6)_4$ is recovered. As for the relaxed Dirichlet-Neumann iteration (1.8)-(1.10), numerical evidences suggests that iteration (1.15) does not converge if the amount of relaxation α is to small and the solid model is thick-walled.

Remark 1.3.1. *Since algorithm* 1 *introduces a free parameter* α*, the choice its value is critical. In a two-dimensional linear framework involving an inviscid incompressible fluid and the membrane model*

$$\frac{\rho^{\mathrm{s}}\epsilon}{\tau^2}\left(\boldsymbol{d}_k - 2\boldsymbol{d}^{n-1} + \boldsymbol{d}^{n-2}\right) + \beta\boldsymbol{d} = -\boldsymbol{\sigma}^{\mathrm{f}}(\boldsymbol{u}_k, p_k)\boldsymbol{n}^{\mathrm{f}} \quad \textit{on} \quad \Sigma,$$

for the solid, a study from [3] suggests that the optimal choice is

$$\alpha = \rho^{\mathrm{s}}\epsilon + \beta\tau^2, \tag{1.16}$$

where ρ^{s}*,* ϵ *stand for the density and thickness of the solid, respectively, and* β *the zero-th order term in the solid model. In this case, the iteration always converges without the need of relaxation step on the solid interface displacement. This optimal value, derived from a simplified problem, will be systematically chosen for the numerical experiments in Section 1.5. However, for more complex fluid and solid models, the convergence of* (1.15) *with the value of the parameter given by* (1.16)*, the convergence is not guaranteed.*

1.3.2 Algorithm 2: Projection scheme

In this section, we propose to use a semi-implicit coupling scheme proposed in [48] (see also [5, Section 3.3]) as preconditioner for the coupled problem (1.4). This semi-implicit coupling scheme implicitly couples the fluid pressure with solid unknowns while leaving the treatment of the viscous effects in the fluid explicit. In strong form, this coupling scheme reads as follows:

1. Fluid advection-diffusion step (explicit): find $\widetilde{\boldsymbol{u}}^n \in \boldsymbol{H}^1(\Omega^{\mathrm{f}})$ such that

$$\left\{\begin{array}{rl} \rho^{\mathrm{f}}\left.\dfrac{\widetilde{\boldsymbol{u}}^n - \boldsymbol{u}^{n-1}}{\tau}\right|_{\boldsymbol{\mathcal{A}}} + \rho^{\mathrm{f}}(\widetilde{\boldsymbol{u}}^{n-1} - \boldsymbol{w}^n)\cdot\boldsymbol{\nabla}\widetilde{\boldsymbol{u}}^n - 2\mu\boldsymbol{\nabla}\cdot\boldsymbol{\epsilon}(\widetilde{\boldsymbol{u}}^n) = \boldsymbol{0} & \text{in} \quad \Omega^{\mathrm{f,n}}, \\ 2\mu\,\boldsymbol{\epsilon}(\widetilde{\boldsymbol{u}}^n) = \boldsymbol{0} & \text{on} \quad \Gamma, \\ \widetilde{\boldsymbol{u}}^n = \partial_\tau \boldsymbol{d}^{n-1}_{|\Sigma} & \text{on} \quad \Sigma^n. \end{array}\right. \tag{1.17}$$

2. Projection step (implicit coupling): find $(\boldsymbol{u}^n, p^n) \in \boldsymbol{H}^1(\Omega^{\mathrm{f}}) \times L^2(\Omega^{\mathrm{f}})$ such that

$$\left\{\begin{array}{rll} \rho^{\mathrm{f}} \left.\dfrac{\boldsymbol{u}^n - \widetilde{\boldsymbol{u}}^n}{\tau}\right|_{\boldsymbol{\mathcal{A}}} + \boldsymbol{\nabla} p^n = \boldsymbol{0} & \text{in} & \Omega^{\mathrm{f,n}}, \\ \boldsymbol{\nabla} \cdot \boldsymbol{u}^n = 0 & \text{in} & \Omega^{\mathrm{f,n}}, \\ p^n = \bar{p}(t_n) & \text{on} & \Gamma, \\ \boldsymbol{u}^n \cdot \boldsymbol{n}^{\mathrm{f}} = \boldsymbol{S}(\widetilde{\boldsymbol{u}}^n, p^n) \cdot \boldsymbol{n}^{\mathrm{f}} & \text{on} & \Sigma^n. \end{array}\right. \tag{1.18}$$

Here, we reformulate the coupling scheme (1.17)-(1.18). We add equation $(1.18)_1$ written at time t_{n-1} to $(1.17)_1$ and we reformulate problem (1.18) into a pure Poisson problem. The resulting coupling scheme reads as follows:

1. Fluid viscous advection-diffusion step (explicit): find $\widetilde{\boldsymbol{u}}^n \in \boldsymbol{H}^1(\Omega^{\mathrm{f}})$ such that

$$\left\{\begin{array}{rll} \rho^{\mathrm{f}} \left.\dfrac{\widetilde{\boldsymbol{u}}^n - \widetilde{\boldsymbol{u}}^{n-1}}{\tau}\right|_{\boldsymbol{\mathcal{A}}} + \rho^{\mathrm{f}}(\widetilde{\boldsymbol{u}}^{n-1} - \boldsymbol{w}^n) \cdot \boldsymbol{\nabla} \widetilde{\boldsymbol{u}}^n - 2\mu \boldsymbol{\nabla} \cdot \boldsymbol{\epsilon}(\widetilde{\boldsymbol{u}}^n) = -\boldsymbol{\nabla} p^{n-1} & \text{in} & \Omega^{\mathrm{f,n}}, \\ \widetilde{\boldsymbol{u}}^n = \partial_\tau \boldsymbol{d}^{n-1}_{|\Sigma} & \text{on} & \Sigma^n, \\ 2\mu\, \boldsymbol{\epsilon}(\widetilde{\boldsymbol{u}}^n) \boldsymbol{n}^{\mathrm{f}} = \boldsymbol{0} & \text{on} & \Gamma. \end{array}\right. \tag{1.19}$$

2. Fluid projection step (implicit): find $p^n \in L^2(\Omega^{\mathrm{f}})$ such that

$$\left\{\begin{array}{rll} \dfrac{\tau}{\rho^{\mathrm{f}}} \Delta p^n = \boldsymbol{\nabla} \cdot \widetilde{\boldsymbol{u}}^n & \text{in} & \Omega^{\mathrm{f,n}}, \\ \dfrac{\tau}{\rho^{\mathrm{f}}} \dfrac{\partial p^n}{\partial \boldsymbol{n}} = -\left(\dfrac{\boldsymbol{S}(\widetilde{\boldsymbol{u}}^n, p^n) - 2\boldsymbol{d}^{n-1}_{|\Sigma} + \boldsymbol{d}^{n-2}_{|\Sigma}}{\tau} \right) \cdot \boldsymbol{n}^{\mathrm{f}} & \text{on} & \Sigma^n, \\ p^n = \bar{p}(t_n) & \text{on} & \Gamma. \end{array}\right. \tag{1.20}$$

Inspired from (1.19)-(1.20), we propose to use the following preconditioner:

$$\begin{aligned} \left\langle \widetilde{\boldsymbol{R}}_2(\boldsymbol{u}, p), (\boldsymbol{v}, q, \boldsymbol{\xi}) \right\rangle_{\boldsymbol{V}', \boldsymbol{V}} \overset{\text{def}}{=} & \frac{\rho^{\mathrm{f}}}{\tau} \left(\int_{\Omega^{\mathrm{f,n}}} \boldsymbol{u} \cdot \boldsymbol{v} - \int_{\Omega^{\mathrm{f,n-1}}} \boldsymbol{u}^{n-1} \cdot \boldsymbol{v} \right) - \rho^{\mathrm{f}} \int_{\Omega^{\mathrm{f,n}}} (\boldsymbol{\nabla} \cdot \boldsymbol{w}^n) \boldsymbol{u} \cdot \boldsymbol{v} \\ & + \rho^{\mathrm{f}} \int_{\Omega^{\mathrm{f,n}}} (\boldsymbol{u}^{n-1} - \boldsymbol{w}^n) \cdot \boldsymbol{\nabla} \boldsymbol{u} \cdot \boldsymbol{v} + \int_{\Omega^{\mathrm{f,n}}} \boldsymbol{\sigma}(\boldsymbol{u}, p^{n-1}) : \boldsymbol{\epsilon}(\boldsymbol{v}) \\ & + \int_{\Omega^{\mathrm{f},n}} q \, \mathrm{div} \boldsymbol{u} + \frac{\tau}{\rho^{\mathrm{s}}} \int_{\Omega^{\mathrm{f},n}} \boldsymbol{\nabla} p \cdot \boldsymbol{\nabla} q - \int_\Gamma \gamma \left(p - \bar{p}(t_n) \right) q \\ & + \int_{\Sigma^n} \frac{\widetilde{\boldsymbol{S}}(\boldsymbol{u}^{n-1}, p) - 2\boldsymbol{d}^{n-1}_{|\Sigma} + \boldsymbol{d}^{n-2}_{|\Sigma}}{\tau} \cdot \boldsymbol{n}^{\mathrm{f}} q \\ & + \int_{\Sigma^n} \left(\boldsymbol{u} - \frac{\boldsymbol{d}^{n-1}_{|\Sigma} - \boldsymbol{d}^{n-2}_{|\Sigma}}{\tau} \right) \cdot \boldsymbol{\xi}. \end{aligned} \tag{1.21}$$

Note that we did not enforce $p^n = \bar{p}$ as a standard Dirichlet condition in (1.21) as it is done for the pressure problem (1.20). Indeed, $\bar{p}\,\boldsymbol{n}^{\mathrm{f}}$ represents the full stress applied on the interface Γ and not only the pressure p^n. However, we recall that this problem will only be used as preconditioner. Therefore we wrote a Robin condition on the pressure for the projection step, involving a free parameter γ. Numerical experiments shows that the value of this parameter does not have a big influence on the convergence properties of the resulting iteration.

Another key difference between the preconditioner (1.21) and problem (1.19)-(1.20) is the introduction of the simplified solid operator (1.14). The implicit coupling with the simplified structure is thus embedded into the pressure problem as a Robin condition for the pressure.

The defect-correction method yields the following iteration: find $(\boldsymbol{u}_k, p_k) \in \boldsymbol{H}^1(\Omega^{\mathrm{f}}) \times L^2(\Omega^{\mathrm{f}})$, such that

$$\begin{aligned}
&\frac{\rho^{\mathrm{f}}}{\tau}\left(\int_{\Omega^{\mathrm{f,n}}} \boldsymbol{u}_k \cdot \boldsymbol{v} - \int_{\Omega^{\mathrm{f,n-1}}} \boldsymbol{u}^{n-1} \cdot \boldsymbol{v}\right) - \rho^{\mathrm{f}} \int_{\Omega^{\mathrm{f,n}}} (\boldsymbol{\nabla} \cdot \boldsymbol{w}^n)\boldsymbol{u}_k \cdot \boldsymbol{v} \\
&+ \rho^{\mathrm{f}} \int_{\Omega^{\mathrm{f,n}}} (\boldsymbol{u}^{n-1} - \boldsymbol{w}^n) \cdot \boldsymbol{\nabla}\boldsymbol{u}_k \cdot \boldsymbol{v} + \int_{\Omega^{\mathrm{f,n}}} \boldsymbol{\sigma}(\boldsymbol{u}_k, p_{k-1}) : \boldsymbol{\epsilon}(\boldsymbol{v}) \\
&+ \int_{\Omega^{\mathrm{f},n}} q\,\mathrm{div}\boldsymbol{u}_k + \frac{\tau}{\rho^{\mathrm{s}}} \int_{\Omega^{\mathrm{f},n}} \boldsymbol{\nabla}(p_k - p_{k-1}) \cdot \boldsymbol{\nabla} q - \int_{\Gamma} \gamma(p_k - p_{k-1}) q \\
&+ \int_{\Sigma^n} \frac{\widetilde{\boldsymbol{S}}(\boldsymbol{u}_{k-1}, p_k) - \widetilde{\boldsymbol{S}}(\boldsymbol{u}_{k-1}, p_{k-1})}{\tau} \cdot \boldsymbol{n}^{\mathrm{f}} q \\
&+ \int_{\Sigma^n} \left(\boldsymbol{u} - \frac{\boldsymbol{S}(\boldsymbol{u}_{k-1}, p_{k-1}) - \boldsymbol{d}^{n-1}_{|\Sigma}}{\tau}\right) \cdot \boldsymbol{\xi} + \int_{\Gamma} \bar{p}(t_n)\, \boldsymbol{v} \cdot \boldsymbol{n}^{\mathrm{f}} = 0.
\end{aligned} \tag{1.22}$$

for all $(\boldsymbol{v}, q, \boldsymbol{\xi}) \in \boldsymbol{V}$.

For the sake of clarity, we also present the strong form of problem (1.22):

1. Fluid step: find $\boldsymbol{u}_k \in \boldsymbol{H}^1(\Omega^{\mathrm{f}})$ such that

$$\begin{cases}
\rho^{\mathrm{f}} \left.\dfrac{\widetilde{\boldsymbol{u}}^n - \widetilde{\boldsymbol{u}}^{n-1}}{\tau}\right|_{\boldsymbol{\mathcal{A}}} + \rho^{\mathrm{f}}(\boldsymbol{u}^{n-1} - \boldsymbol{w}^n) \cdot \boldsymbol{\nabla}\boldsymbol{u}_k - 2\mu\boldsymbol{\nabla} \cdot \boldsymbol{\epsilon}(\boldsymbol{u}_k) = -\boldsymbol{\nabla} p_{k-1} & \text{in} \quad \Omega^{\mathrm{f,n}}, \\
\boldsymbol{u}_k = \dfrac{\boldsymbol{S}(\boldsymbol{u}_{k-1}, p_{k-1}) - \boldsymbol{d}^{n-1}_{|\Sigma}}{\tau} & \text{on} \quad \Sigma^n, \\
2\mu\,\boldsymbol{\epsilon}(\boldsymbol{u}_k)\boldsymbol{n}^{\mathrm{f}} = (p_{k-1} - \bar{p})\,\boldsymbol{n}^{\mathrm{f}} & \text{on} \quad \Gamma,
\end{cases} \tag{1.23}$$

2. Projection step: find $p_k \in L^2(\Omega^{\mathrm{f}})$ such that

$$\begin{cases}
\dfrac{\tau}{\rho^{\mathrm{f}}}\Delta p_k = \dfrac{\tau}{\rho^{\mathrm{f}}}\Delta p_{k-1} + \boldsymbol{\nabla} \cdot \boldsymbol{u}_k & \text{in} \quad \Omega^{\mathrm{f,n}}, \\
\dfrac{\tau}{\rho^{\mathrm{f}}}\dfrac{\partial p_k}{\partial \boldsymbol{n}} + \dfrac{\alpha}{\tau} p_k = \dfrac{\tau}{\rho^{\mathrm{f}}}\dfrac{\partial p_{k-1}}{\partial \boldsymbol{n}} + \dfrac{\alpha}{\tau} p_{k-1} & \text{on} \quad \Sigma^n, \\
\dfrac{\tau}{\rho^{\mathrm{f}}}\dfrac{\partial p_k}{\partial \boldsymbol{n}} + \gamma p_k = \dfrac{\tau}{\rho^{\mathrm{f}}}\dfrac{\partial p_{k-1}}{\partial \boldsymbol{n}} + \gamma p_{k-1} & \text{on} \quad \Gamma.
\end{cases} \tag{1.24}$$

Remark 1.3.2. *At the limit $k \to \infty$, the projection step $(1.24)_1$ simply reduces to $\nabla \cdot \boldsymbol{u} = 0$ and the boundary conditions $(1.24)_2$ and $(1.24)_3$ vanish. In the fluid step (1.23), the full Neumann condition $(1.4)_3$ on Γ is recovered from $(1.23)_3$.*

In addition to Algorithm (1.15), this iterative procedure has three remarkable features:

- It enables a separate resolution of the fluid velocity $\boldsymbol{u}_k$ and the fluid pressure p_k, leading to savings in terms of computational cost.
- The pressure step represents a relaxation of the incompressibility condition $(1.4)_2$, which was not present in Algorithm (1.15) . Besides, the Dirichlet condition from the Dirichlet-Neumann iteration (1.6)-(1.7) is preserved.
- Interestingly, the coupling between the solid model and the fluid pressure only reveals through the term $\boldsymbol{\nabla} \cdot \boldsymbol{u}_{k+1}$. As we shall see in numerical experiments below, it is sufficient to ensure added-mass insensitivity.

1.3.3 Algorithm 3: Artificial compressibility

The next preconditioner also involves a relaxation of the fluid incompressibility. It is inspired from [34] (see also [77]). The relaxation of the incompressibility condition is achieved through an artificial compressibility term, where the divergence of the fluid velocity is proportional to the time derivative of the pressure as follows:

$$\boldsymbol{\nabla} \cdot \boldsymbol{u} = -c\, \partial_t p, \tag{1.25}$$

with $c >$ a positive constant.

Remark 1.3.3. *For a compressible fluid, when there is an accumulation of mass somewhere ($\boldsymbol{\nabla} \cdot \boldsymbol{u} < 0$), then the pressure grows ($\partial_t p > 0$). Hence the sign of c is positive.*

In this case, our preconditioner writes

$$\begin{aligned}\Big\langle \widetilde{\boldsymbol{R}}_3\big(\boldsymbol{u},p\big),(\boldsymbol{v},q,\boldsymbol{\xi})\Big\rangle_{\boldsymbol{V}',\boldsymbol{V}} \overset{\text{def}}{=} & \frac{\rho^{\mathrm{f}}}{\tau}\left(\int_{\Omega^{\mathrm{f,n}}} \boldsymbol{u}\cdot\boldsymbol{v} - \int_{\Omega^{\mathrm{f,n-1}}} \boldsymbol{u}^{n-1}\cdot\boldsymbol{v}\right) - \rho^{\mathrm{f}}\int_{\Omega^{\mathrm{f,n}}} (\boldsymbol{\nabla}\cdot\boldsymbol{w}^n)\boldsymbol{u}\cdot\boldsymbol{v} \\ & + \rho^{\mathrm{f}}\int_{\Omega^{\mathrm{f,n}}} (\boldsymbol{u}^{n-1}-\boldsymbol{w}^n)\cdot\boldsymbol{\nabla}\boldsymbol{u}\cdot\boldsymbol{v} + \int_{\Omega^{\mathrm{f,n}}} \boldsymbol{\sigma}(\boldsymbol{u},p):\boldsymbol{\epsilon}(\boldsymbol{v}) \\ & + \int_{\Omega^{\mathrm{f},n}} q\,\mathrm{div}\boldsymbol{u} - \frac{c}{\tau}\int_{\Omega^{\mathrm{f},n}} (p-p^{n-1})q \\ & + \int_{\Sigma^n}\left(\boldsymbol{u} - \frac{\boldsymbol{d}^{n-1}_{|\Sigma} - \boldsymbol{d}^{n-2}_{|\Sigma}}{\tau}\right)\cdot\boldsymbol{\xi},\end{aligned} \tag{1.26}$$

for all $(\boldsymbol{v}, q, \boldsymbol{\xi}) \in \boldsymbol{V}$, and the corresponding iterative procedure reads as follows: find $(\boldsymbol{u}_k, p_k) \in \boldsymbol{H}^1(\Omega^{\mathrm{f}}) \times L^2(\Omega^{\mathrm{f}})$, such that

$$\begin{aligned}
&\frac{\rho^{\mathrm{f}}}{\tau}\left(\int_{\Omega^{\mathrm{f,n}}} \boldsymbol{u}_k \cdot \boldsymbol{v} - \int_{\Omega^{\mathrm{f,n-1}}} \boldsymbol{u}^{n-1} \cdot \boldsymbol{v}\right) - \rho^{\mathrm{f}} \int_{\Omega^{\mathrm{f,n}}} (\boldsymbol{\nabla} \cdot \boldsymbol{w}^n)\boldsymbol{u}_k \cdot \boldsymbol{v} \\
&+ \rho^{\mathrm{f}} \int_{\Omega^{\mathrm{f,n}}} (\boldsymbol{u}^{n-1} - \boldsymbol{w}^n) \cdot \boldsymbol{\nabla}\boldsymbol{u}_k \cdot \boldsymbol{v} + \int_{\Omega^{\mathrm{f,n}}} \boldsymbol{\sigma}(\boldsymbol{u}_k, p_k) : \boldsymbol{\epsilon}(\boldsymbol{v}) \\
&+ \int_{\Omega^{\mathrm{f},n}} q \,\mathrm{div}\boldsymbol{u}_k - \frac{c}{\tau}\int_{\Omega^{\mathrm{f},n}} (p_k - p_{k-1})q \\
&+ \int_{\Sigma^n} \left(\boldsymbol{u} - \frac{\boldsymbol{S}(\boldsymbol{u}_{k-1}, p_{k-1}) - \boldsymbol{d}^{n-1}_{|\Sigma}}{\tau}\right) \cdot \boldsymbol{\xi} + \int_{\Gamma} \bar{p}(t_n)\, \boldsymbol{v} \cdot \boldsymbol{n}^{\mathrm{f}} = 0.
\end{aligned} \tag{1.27}$$

for all $(\boldsymbol{v}, q, \boldsymbol{\xi}) \in \boldsymbol{V}$. In strong form, iteration (1.27) writes: find $(\boldsymbol{u}_k, p_k) \in \boldsymbol{H}^1(\Omega^{\mathrm{f}}) \times L^2(\Omega^{\mathrm{f}})$, such that

$$\begin{cases}
\rho^{\mathrm{f}} \left.\dfrac{\boldsymbol{u}_k - \boldsymbol{u}^{n-1}}{\tau}\right|_{\boldsymbol{\mathcal{A}}} + \rho^{\mathrm{f}}(\boldsymbol{u}^{n-1} - \boldsymbol{w}^n) \cdot \boldsymbol{\nabla}\boldsymbol{u}_k - \boldsymbol{\nabla} \cdot \boldsymbol{\sigma}^{\mathrm{f}}(\boldsymbol{u}_k, p_k) = \boldsymbol{0} \quad \text{in} \quad \Omega^{\mathrm{f,n}}, \\
\boldsymbol{\nabla} \cdot \boldsymbol{u}_k = -c\,\dfrac{p_k - p_{k-1}}{\tau} \quad \text{in} \quad \Omega^{\mathrm{f,n}} \\
\boldsymbol{u}_k = \dfrac{\boldsymbol{S}(\boldsymbol{u}_{k-1}, p_{k-1}) - \boldsymbol{d}^{n-1}_{|\Sigma}}{\tau}\,\boldsymbol{n} \quad \text{on} \quad \Sigma^n
\end{cases} \tag{1.28}$$

Remark 1.3.4. *A variant of this scheme is to localize the artificial compressibility only on the interface (see [34]). In this case, equation* $(1.28)_2$ *becomes*

$$\boldsymbol{\nabla} \cdot \boldsymbol{u}_k = -c\,\frac{p_k - p_{k-1}}{\tau}\,\delta_{\Sigma},$$

where δ_{Σ} *stands for the Dirac distribution on the interface.*

In this scheme, the Dirichlet boundary condition $(1.28)_3$ is not modified with respect to the standard Dirichlet-Neumann procedure (1.6)-(1.7). However, the main ingredient in this iterative procedure is the relaxation of the divergence-free constraint $(1.28)_2$.

As Algorithm 1, problem (1.28) involves a free parameter c that acts as a relaxation parameter. Therefore we expect that the convergence properties of this iteration highly depend on its value. The mathematical properties of iteration (1.28) depending on the value of c in a simplified linear setting is the purpose of next section.

1.4 Study of Algorithm 3 in a linear framework

In this section, we consider a two-dimensional inviscid incompressible fluid in a fixed rectangular geometry such that $\Omega^{\mathrm{f}} = [0, L] \times [0, R]$. The solid is represented by membrane model on $\Sigma = [0, L] \times \{R\}$. The inlet and outlet boundaries are $\Gamma^{\mathrm{in}} = \{0\} \times [0, R]$

and $\Gamma^{\text{out}} = \{L\} \times [0, R]$ respectively. Symetry conditions are enforced at the boundary $\Gamma = [0, L] \times \{0\}$.

The solid, whose transverse displacement is denoted by d, is represented by a membrane equation on Σ, including a zero-th order term βd with $\beta > 0$.

This simplified model has been studied in [3] for the derivation of the optimal value of α in Robin-Neumann iterations (Algorithm 1). Here we propose to study the behavior of the iterative procedure given by Algorithm 3 (iteration (1.28)). In this framework, the coupled problem into consideration reads as follows: find $(\boldsymbol{u}_k, p_k) \in \boldsymbol{H}^1(\Omega^{\text{f}}) \times L^2(\Omega^{\text{f}})$ and $d_k \in H^{\frac{1}{2}}(\Sigma)$ such that

$$\left\{\begin{array}{rl} \rho^{\text{f}} \dfrac{\boldsymbol{u}_k - \boldsymbol{u}^{n-1}}{\tau} + \boldsymbol{\nabla} p_k = \boldsymbol{0} & \text{in} \quad \Omega^{\text{f}}, \\ \boldsymbol{\nabla} \cdot \boldsymbol{u}_k = -c \dfrac{p_k - p_{k-1}}{\tau} & \text{in} \quad \Omega^{\text{f}}, \\ \boldsymbol{u}_k = \dfrac{d_{k-1} - d^{n-1}}{\tau} \boldsymbol{n}^{\text{f}} & \text{on} \quad \Sigma, \\ p_k = \bar{p} & \text{on} \quad \Gamma^{\text{in}} \cup \Gamma^{\text{out}}, \\ \dfrac{\partial p_k}{\partial \boldsymbol{n}} = 0 & \text{on} \quad \Gamma, \\ \rho^{\text{s}} \epsilon \dfrac{d_k - 2d^{n-1} + d^{n-2}}{\tau^2} + \beta\, d_k = p_k & \text{on} \quad \Sigma. \end{array}\right. \tag{1.29}$$

If we take the divergence of $(1.29)_1$ and thanks to the relation $\boldsymbol{\nabla} \cdot \boldsymbol{u}^{n-1} = 0$, we can eliminate the fluid velocity and problem (1.29) reduces to the following pressure problem: find the pressure $p_k \in L^2(\Omega^{\text{f}})$ such that

$$\left\{\begin{array}{rl} \left(\Delta - \dfrac{\rho^{\text{f}}\, c}{\tau^2}\right) p_k = -\dfrac{\rho^{\text{f}}\, c}{\tau^2} p_{k-1} & \text{in} \quad \Omega^{\text{f}}, \\ \dfrac{\partial p_k}{\partial \boldsymbol{n}} = -\dfrac{\rho^{\text{f}}}{\rho^{\text{s}}\epsilon + \beta\tau^2}\, p_{k-1} + v_{n-1} & \text{on} \quad \Sigma, \\ \dfrac{\partial p_k}{\partial \boldsymbol{n}} = 0 & \text{on} \quad \Gamma, \\ p_k = \bar{p} & \text{on} \quad \Gamma^{\text{in}} \cup \Gamma^{\text{out}}. \end{array}\right. \tag{1.30}$$

with

$$v_{n-1} \stackrel{\text{def}}{=} \frac{\rho^{\text{f}}}{\tau} \boldsymbol{u}^{n-1} \cdot \boldsymbol{n}^{\text{f}} + \frac{\rho^{\text{f}}}{\tau^2}\, d^{n-1} - \frac{\rho^{\text{f}} \rho^{\text{s}} \epsilon}{\tau^2\, (\rho^{\text{s}}\epsilon + \beta\tau^2)} (2d^{n-1} - d^{n-2}).$$

The iterative procedure for the sequence p_k therefore reads:

$$p_k = M\, p_{k-1} + r_{n-1},$$

where r_{n-1} denotes the solution of

$$\begin{cases} \left(\Delta - \dfrac{\rho^{\mathrm{f}}\, c}{\tau^2}\right) r_{n-1} = 0 & \text{in} \quad \Omega^{\mathrm{f}}, \\ \dfrac{\partial r_{n-1}}{\partial \boldsymbol{n}} = v_{n-1} & \text{on} \quad \Sigma, \\ \dfrac{\partial r_{n-1}}{\partial \boldsymbol{n}} = 0 & \text{on} \quad \Gamma, \\ r_{n-1} = \bar{p} & \text{on} \quad \Gamma^{\mathrm{in}} \cup \Gamma^{\mathrm{out}}, \end{cases} \tag{1.31}$$

and M the automorphism of L^2 that maps p_{k-1} to the solution p of

$$\begin{cases} \left(\Delta - \dfrac{\rho^{\mathrm{f}}\, c}{\tau^2}\right) p = -\dfrac{\rho^{\mathrm{f}}\, c}{\tau^2} p_{k-1} & \text{in} \quad \Omega^{\mathrm{f}}, \\ \dfrac{\partial p}{\partial \boldsymbol{n}} = -\dfrac{\rho^{\mathrm{f}}}{\rho^{\mathrm{s}}\epsilon + \beta\tau^2}\, p_{k-1} & \text{on} \quad \Sigma, \\ \dfrac{\partial p}{\partial \boldsymbol{n}} = 0 & \text{on} \quad \Gamma, \\ p = 0 & \text{on} \quad \Gamma^{\mathrm{in}} \cup \Gamma^{\mathrm{out}}. \end{cases} \tag{1.32}$$

Hence the spectrum of M and more precisely its spectral radius governs the convergence speed of iteration (1.29). We now state the main result of this part:

Theorem 1.4.1. *The spectral radius $\rho(c)$ of the operator M has the following properties:*

- *If c is large, $\rho(c)$ is increasing and*

$$\lim_{c \to +\infty} \rho(c) = 1^{-}.$$

- *If c is small, $\rho(c)$ is decreasing and*

$$\lim_{c \to 0} \rho(c) = \frac{\rho^{\mathrm{f}} L}{\pi(\rho^{\mathrm{s}}\epsilon + \beta\tau^2)} \tanh^{-1}\left(\frac{\pi R}{L}\right).$$

Proof. We look for eigenfunctions of the operator M that writes $p(x,y) = p_1(x)\, p_2(y)$ for an (unknown) eigenvalue λ. Owing to (1.32), the relation $Mp = \lambda p$ yields the following problem:

$$\begin{cases} \Delta p = \dfrac{\rho^{\mathrm{f}}\, c}{\tau^2}\left(1 - \dfrac{1}{\lambda}\right) p & \text{in} \quad \Omega^{\mathrm{f}}, \\ \dfrac{\partial p}{\partial \boldsymbol{n}} = -\dfrac{\rho^{\mathrm{f}}}{\lambda\,(\rho^{\mathrm{s}}\epsilon + \beta\tau^2)}\, p & \text{on} \quad \Sigma, \\ \dfrac{\partial p}{\partial \boldsymbol{n}} = 0 & \text{on} \quad \Gamma, \\ p = 0 & \text{on} \quad \Gamma^{\mathrm{in}} \cup \Gamma^{\mathrm{out}}. \end{cases} \tag{1.33}$$

The Dirichlet condition on $\Gamma^{\text{in}} \cup \Gamma^{\text{out}}$ enforces

$$p_1(x) = \sin\left(\frac{k\,\pi\,x}{L}\right)$$

for some $k \in \mathbb{Z}$. Then, owing to $(1.33)_1$, the function p_2 is a solution of the following ODE:

$$\frac{p_2''(y)}{p_2(y)} = \frac{\rho^{\text{f}}\,c}{\tau^2}\left(1 - \frac{1}{\lambda}\right) + \frac{k^2\,\pi^2}{L^2} \tag{1.34}$$

Now we have to make an assumption for the sign of the right-hand side of (1.34). If we suppose that

$$\frac{\rho^{\text{f}}\,c}{\tau^2}\left(1 - \frac{1}{\lambda}\right) + \frac{k^2\,\pi^2}{L^2} = \xi^2 \geq 0, \tag{1.35}$$

then, thanks to $p_2'(0) = 0$, we have

$$p(x,y) = \sin\left(\frac{k\pi x}{L}\right)\cosh\left(\xi y\right).$$

Conversely, for all $k > 0$, the function defined above is an eigenfunction of the operator M if there exist a couple $(\lambda, \xi) \in \mathbb{R} \times \mathbb{R}^+$ such that the Neumann boundary condition $(1.33)_2$ on Σ and (1.35) hold. This leads to the following non-linear system:

$$\begin{cases} \xi\,\tanh\left(R\,\xi\right) = -\dfrac{\rho^{\text{f}}}{\lambda\left(\rho^{\text{s}}\epsilon + \beta\tau^2\right)}, \\ \lambda = \dfrac{1}{1 - \dfrac{\tau^2}{\rho^{\text{f}}\,c}\left(\xi^2 - \dfrac{k^2\,\pi^2}{L^2}\right)}. \end{cases} \tag{1.36}$$

We now introduce the notation $c_0 \overset{\text{def}}{=} \tau^2/(\rho^{\text{f}} R^2)$ and the following dimensionless quantities:

$$\begin{cases} z \overset{\text{def}}{=} R\xi, \\ \gamma_k \overset{\text{def}}{=} \dfrac{k\pi R}{L}, \\ \delta \overset{\text{def}}{=} \dfrac{\rho^{\text{s}}\epsilon + \beta\tau^2}{\rho^{\text{f}} R}, \\ \nu \overset{\text{def}}{=} \dfrac{c}{c_0}. \end{cases}$$

With these new definitions, system (1.36) reduces to

$$\begin{cases} 1 + \delta z\,\tanh z = \dfrac{1}{\nu}\left(z^2 - \gamma_k^2\right), \\ \lambda = -\dfrac{1}{\delta z\,\tanh z}. \end{cases} \tag{1.37}$$

We introduce the continuous functions $f : z \mapsto 1 + \delta z\,\tanh z$ and $g_k : z \mapsto \dfrac{1}{\nu}\left(z^2 - \gamma_k^2\right)$ over $\mathbb{R}^+$. The next lemma states some properties of the solutions of system (1.37).

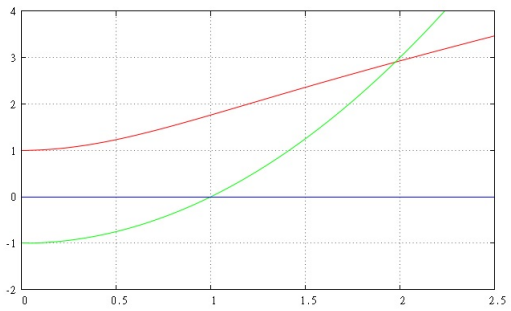

Figure 1.2: Plot of $f : z \mapsto 1 + \delta z \tanh z$ (red), plot of $g_k : z \mapsto (1/\nu)(z^2 - \gamma_k^2)$ (green).

Lemma 1.4.1. *Let k be given. Then there exist a unique solution $(z_k, \lambda_k) \in \mathbb{R}^+ \times \mathbb{R}$ of system* (1.37).

Proof. We first focus on the existence of z_k. We have

$$g_k(0) < 0 < f(0) = 1,$$

and, in the neighborhood of $+\infty$, we have $f(z) = \delta z + o(z)$ and $g_k(z) = z^2/\nu + o(z^2)$. Therefore, there exist at least one solution z_k of $(1.37)_1$. At last, the value λ_k is given by $(1.37)_2$. Figure 1.2 represents the functions f and g_k on the same plot.

We now prove that the solution (z_k, λ_k) is unique. Let $\phi : z \mapsto f(z) - g_k(z)$. We have that

$$\frac{1}{\delta}\phi'(z) = \tanh z + z\left(1 - \tanh^2 z\right) - \frac{2}{\delta\nu}z,$$

and

$$\frac{1}{2\delta}\phi''(z) = (1 - \tanh^2 z)(1 - z\tanh z) - \frac{1}{\delta\nu}$$

for all $z \in \mathbb{R}^+$. If we suppose that $\delta\nu \leq 1$ (see Figure 1.3, left), then ϕ'' is negative over $\mathbb{R}^+$, meaning that ϕ' is strictly decreasing. In addition, since $\phi'(0) = 0$, we have that ϕ' is strictly negative over $\mathbb{R}^{+*}$ and, finally, ϕ is strictly decreasing. Therefore, the solution z_k is unique in this case.

We now deal with the case $\delta\nu \geq 1$ (see Figure 1.3, right). We seek for the solutions of $\phi'(z) = 0$. We have

$$\phi'(z) = 0 \Leftrightarrow z = 0 \quad \text{or} \quad \frac{\tanh z}{z} + 1 - \tanh^2 z = \frac{2}{\delta\nu}.$$

Since the function $z \mapsto (\tanh z)/z + 1 - \tanh^2 z$ is a strictly decreasing bijection from $\mathbb{R}^+$ to $]0, 2]$ and that the right-hand side $2/\delta\nu$ lies in $]0, 2]$, we get that the function ϕ' has only two zeros in $\mathbb{R}^+$ and we denote by z_0 the strict positive one. Therefore, the function ϕ' is positive on $[0, z_0]$ and negative on $[z_0, +\infty[$. Finally, the solution z_k is still unique in this case. □

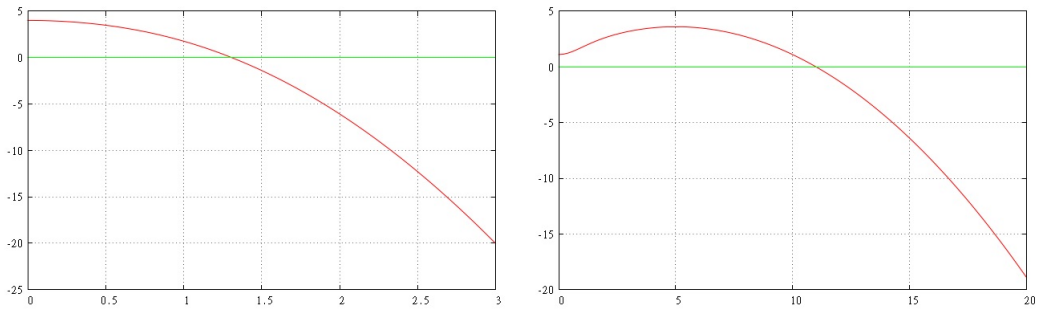

Figure 1.3: Shape of function ϕ. Left: $\delta\nu \leq 1$, Right: $\delta\nu > 1$

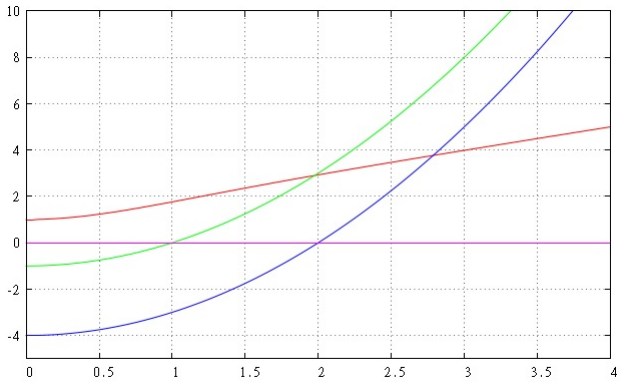

Figure 1.4: Plot of functions f (red), g_{k_1} (green) and g_{k_2} (blue) with $k_1 < k_2$.

Lemma 1.4.2. *The sequence z_k is increasing. Moreover, for all integer $k \geq 1$, we have*

$$\gamma_k < z_k < \frac{\delta\nu + \sqrt{(\delta\nu)^2 + 4(\nu + \gamma^2)}}{2}.$$

Proof. Let $(k_1, k_2) \in \mathbb{N}^* \times \mathbb{N}^*$ such that $k_1 < k_2$. Then we have that

$$f(z_{k_1}) = g_{k_1}(z_{k_1}) > g_{k_2}(z_{k_1}).$$

Therefore, $f(z_{k_1}) - g_{k_2}(z_{k_1}) > 0$ and $z_{k_2} > z_{k_1}$. This situation is detailed in Figure 1.4. Using the same argument, $g_k(\gamma_k) = 0 < f(\gamma_k)$ implies that $z_k > \gamma_k$ for all integer k.

Finally, we note that, for all $z > 0$, we have $f(z) < 1 + \delta z$. Since the solution z_k^+ of $g_k(z) = 1 + \delta z$ is the root of a second-order polynomial, we get

$$z_k < z_k^+ = \frac{\delta\nu + \sqrt{(\delta\nu)^2 + 4(\nu + \gamma^2)}}{2} \tag{1.38}$$

for all integer k. □

We resume to the mathematical study of system (1.37). Owing to $(1.37)_2$ and Lemmas 1.4.1 and 1.4.2, we have a first increasing family of negative eigenvalues.

Thus, the spectral radius of iteration is governed by $|\lambda_1|$. The next lemma is devoted to the study of the variations of $z_1(\nu)$, implicitly defined as a function of ν.

Lemma 1.4.3. *The function $\nu \mapsto z_1(\nu)$ is increasing and we have*

$$\begin{cases} z_1(\nu) = \delta\nu + o_{+\infty}(\nu) \\ z_1(\nu) = \gamma_1 + o_0(1) \end{cases} \tag{1.39}$$

Proof. Let $(\nu_1, \nu_2) \in \mathbb{R}^+ \times \mathbb{R}^+$ such that $\nu_1 < \nu_2$. Then for all $z > \gamma_1$, we have

$$\frac{1}{\nu_1}(z^2 - \gamma_1^2) > \frac{1}{\nu_2}(z^2 - \gamma_1^2)$$

Therefore, owing to the arguments developed in the proof of Lemma 1.4.2, we infer that the function $\nu \mapsto z_1(\nu)$ is increasing. For the sake of clearness, the situation is represented in Figure 1.5. Besides, from (1.38), we get that

$$\lim_{\nu \to 0} z_1(\nu) = \gamma_1$$

We now prove the first asymptotic result (1.39). We first infer that $\lim_{\nu \to +\infty} z_1(\nu) = +\infty$. Otherwise, if $z_1(\nu)$ were bounded, equation $(1.37)_1$ leads to a contradiction. Finally, since $1 + \delta z_1(\nu) \tanh z_1(\nu) = \delta z_1(\nu) + o_{+\infty}(z_1(\nu)$, $(1.39)_1$ follows from $(1.37)_1$. □

To sum up, owing to (1.37) and Lemma 1.4.3, the quantity $|\lambda_1(\nu)|$ is a decreasing function of ν and the following limits hold:

$$\begin{cases} \lim\limits_{\nu \to 0} |\lambda_1(\nu)| = \dfrac{1}{\delta\gamma_1 \tanh \gamma_1}, \\ \lim\limits_{\nu \to +\infty} |\lambda_1(\nu)| = 0. \end{cases} \tag{1.40}$$

Now we deal with the case where

$$\frac{\rho^{\mathrm{f}}\, c}{\tau^2}\left(1 - \frac{1}{\lambda}\right) + \frac{k^2\,\pi^2}{L^2} = -\xi^2 \leq 0.$$

The same arguments as above yield new eigenfunctions

$$p(x, y) = \sin\left(\frac{k\pi x}{L}\right)\cos\left(\xi y\right).$$

Thus, owing to condition $(1.33)_2$, we are now interested in the solutions (z, λ) of the following system:

$$\begin{cases} \delta z \, \tan z = 1 + \dfrac{1}{\nu}\left(z^2 + \gamma_k^2\right), \\ \lambda = \dfrac{1}{\delta z \, \tan z}. \end{cases} \tag{1.41}$$

We define the functions $h : z \mapsto \delta z \, \tan z$ and $\tilde{g}_k : z \mapsto \frac{1}{\nu}\left(z^2 + \gamma_k^2\right)$ over $\mathbb{R}^{+*}$. The next lemma is devoted to the mathematical study of system (1.41).

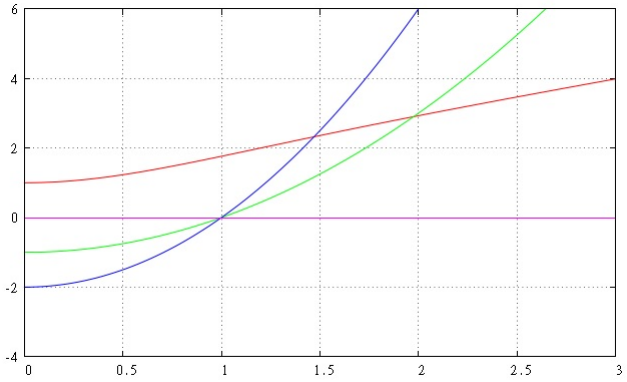

Figure 1.5: Plot of functions f (red), g_1 with $\nu = \nu_1$ (blue) and $\nu = \nu_2$ (green) with $\nu_1 < \nu_2$.

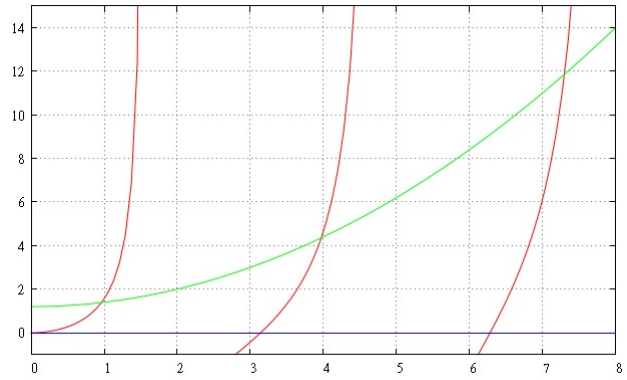

Figure 1.6: plot of functions h (red) and $\tilde{g}_k$ (green).

Lemma 1.4.4. *For all $k \in \mathbb{N}^*$, system 1.41 has an infinite number of solutions, denoted by $(z_{k,p}, \lambda_{k,p})$ for $p \in \mathbb{N}$. Moreover, the sequence $(z_{k,0})_{k\in\mathbb{N}^*}$ is increasing.*

Proof. Let $k \in \mathbb{N}^*$. The function $\tilde{g}_k$ is a bijection of every interval of the form $[p\pi, (p+\frac{1}{2})\pi[$ into $\mathbb{R}^+$. Thus, there exists a family $(z_{k,p})_{(k,p)\in\mathbb{N}^*\times\mathbb{N}}$ of solutions of $(1.41)_1$. The corresponding values $(\lambda_{k,p})_{(k,p)\in\mathbb{N}^*\times\mathbb{N}}$ are derived from $(1.36)_2$. For the sake of clarity, the situation is represented in Figure 1.6.

We now focus on the properties of the sequence $(z_{k,0})_{k\in\mathbb{N}^*}$. Let $(k_1, k_2) \in \mathbb{N}^* \times \mathbb{N}^*$ such that $k_1 < k_2$. Then we have that

$$\tilde{g}_{k_1}(z) < \tilde{g}_{k_2}(z)$$

for all $z > 0$ as shown in Figure 1.4. Thus, using arguments from Lemma 1.4.2, the sequence $(z_{k,0})_{k\in\mathbb{N}^*}$ is increasing and the lemma is proved. □

From (1.41) and Lemma 1.4.4, we infer that the largest eigenvalue of the family $(\lambda_{k,p})_{(k,p)\in\mathbb{N}^*\times\mathbb{N}}$ is $\lambda_{1,0}$. The next lemma is devoted to the study of the function $\nu \mapsto z_{1,0}(\nu)$.

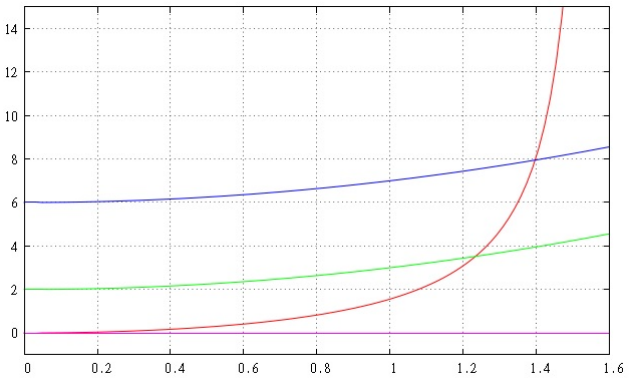

Figure 1.7: plot of functions h (red), $\tilde{g}_{k_1}$ (green) and $\tilde{g}_{k_2}$ (blue) with $k_1 < k_2$.

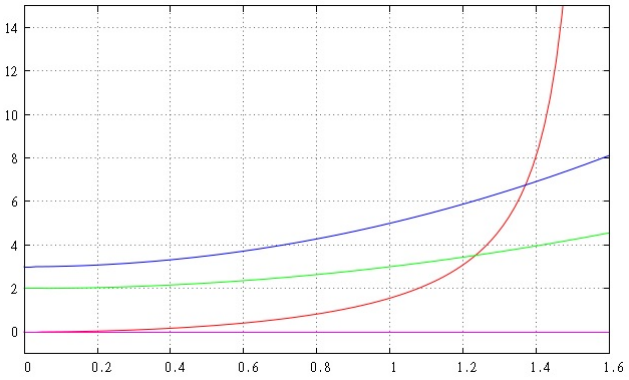

Figure 1.8: plot of functions h (red), $\tilde{g}_1$ with $\nu = \nu_1$ (blue) and $\nu = \nu_2$ (green) with $\nu_1 < \nu_2$.

Lemma 1.4.5. *The function $\nu \mapsto z_{1,0}(\nu)$ is decreasing. Moreover, we have the limits*

$$\begin{cases} \lim\limits_{\nu \to +\infty} z_{1,0}(\nu) = \dfrac{\pi}{2} \\ \lim\limits_{\nu \to 0} z_{1,0}(\nu) = z^- \end{cases} \tag{1.42}$$

where z^- is the unique solution in $[0, \pi/2[$ of $z^- \tan z^- = 1/\delta$.

Proof. Let $(\nu_1, \nu_2) \in \mathbb{R}^+ \times \mathbb{R}^+$ such that $\nu_1 < \nu_2$. Then for all $z > 0$, we have

$$1 + \frac{1}{\nu_1}(z^2 + \gamma_1^2) > 1 + \frac{1}{\nu_2}(z^2 + \gamma_1^2)$$

This situation is represented in Figure 1.4. Using arguments from Lemma 1.4.2, we conclude that the function $\nu \mapsto z_{1,0}(\nu)$ is decreasing. Finally, the inferred limits follow from $(1.41)_1$, where we make ν tend to 0 and $+\infty$. □

To sum up, owing to (1.41) and Lemma 1.4, the eigenvalue $\lambda_{1,0}(\nu)$ is an increasing function of ν and has the following limits:

$$\begin{cases} \lim\limits_{\nu\to 0} \lambda_{1,0}(\nu) = 0 \\ \lim\limits_{\nu\to+\infty} \lambda_{1,0}(\nu) = 1 \end{cases} \tag{1.43}$$

We conclude the proof of Theorem 1.4.1. Owing to (1.40) and (1.43), we have the following alternative:

- If ν is large (this is the case, in particular, when c tends to $+\infty$), the spectral radius is dictated by $\lambda_{1,0}(\nu)$. Therefore, $\rho(c)$ is increasing and tends to 1.

- If ν is small (this is the case, in particular, when c tends to 0), the spectral radius is dictated by $|\lambda_1(\nu)|$. Therefore, $\rho(c)$ is decreasing and

$$\lim_{c\to 0} \rho(c) = \frac{\rho^{\mathrm{f}} L}{\pi(\rho^{\mathrm{s}}\epsilon + \beta\tau^2)} \tanh^{-1}\left(\frac{\pi R}{L}\right).$$

□

Roughly speaking, Theorem 1.4.1 explains the low convergence speed if c is large and the possible lack of convergence if c is small and

$$\frac{\rho^{\mathrm{f}} L}{\pi(\rho^{\mathrm{s}}\epsilon + \beta\tau^2)} \tanh^{-1}\left(\frac{\pi R}{L}\right) > 1$$

However, the optimal value of c is hard to derive in this framework. Indeed, the implicit relation

$$|\lambda_1(\nu)| = \lambda_{1,0}(\nu).$$

has to be solved. As we shall see in the next section, the localization of the artificial incompressibility on the interface makes the analysis easier.

1.4.1 Interface artifical compressibility

A variant of the iterative procedure (1.29) is to localize the compressibility only on the interface. We now consider the following iteration: find $(\boldsymbol{u}_k, p_k) \in \boldsymbol{H}^1(\Omega^{\mathrm{f}}) \times L^2(\Omega^{\mathrm{f}})$

and $d_k \in H^{\frac{1}{2}}(\Sigma)$ such that

$$\left\{\begin{array}{rcl} \rho^{\mathrm{f}}\,\dfrac{\boldsymbol{u}_k-\boldsymbol{u}^{n-1}}{\tau}+\nabla p_k=0 & \text{in} & \Omega^{\mathrm{f}},\\ \boldsymbol{\nabla}\cdot\boldsymbol{u}_k=-c\,\dfrac{p_k-p_{k-1}}{\tau}\delta_\Sigma & \text{in} & \Omega^{\mathrm{f}},\\ \boldsymbol{u}_k=\dfrac{d_{k-1}-d^{n-1}}{\tau}\,\boldsymbol{n} & \text{on} & \Sigma\\ p_k=\bar{p} & \text{on} & \Gamma^{\mathrm{in}}\cup\Gamma^{\mathrm{out}},\\ \dfrac{\partial p_k}{\partial \boldsymbol{n}}=0 & \text{on} & \Gamma,\\ \rho^{\mathrm{s}}\epsilon\dfrac{d_k-2d^{n-1}+d^{n-2}}{\tau^2}+\beta\,d_k=p_k & \text{on} & \Sigma. \end{array}\right. \tag{1.44}$$

The next theorem gives an explicit form for the spectral radius of iteration (1.44):

Theorem 1.4.2. *The spectral radius $\rho(c)$ of this iteration writes*

$$\rho(c)=\left|\frac{c-\dfrac{\tau^2}{\rho^{\mathrm{s}}\epsilon+\beta\tau^2}}{c+\dfrac{\pi\tau^2}{\rho^{\mathrm{f}}\,L}\,\tanh\left(\dfrac{\pi\,R}{L}\right)}\right|.$$

Proof. The outline of the proof is similar to the one of Theorem 1.4.1. The reduction of problem (1.44) into a pure pressure problem writes:

$$\left\{\begin{array}{rcl} \Delta p_k=0 & & \text{in}\quad \Omega^{\mathrm{f}},\\ \dfrac{\partial p_k}{\partial \boldsymbol{n}}+\dfrac{\rho^{\mathrm{f}}\,c}{\tau^2}p_k=-\dfrac{\rho^{\mathrm{f}}}{(\rho^{\mathrm{s}}\epsilon+\beta\tau^2)}\,p_{k-1}+\dfrac{\rho^{\mathrm{f}}\,c}{\tau^2}p_{k-1}+v_{n-1} & & \text{on}\quad \Sigma,\\ p_k=\bar{p} & \text{on} & \Gamma^{\mathrm{in}}\cup\Gamma^{\mathrm{out}}\\ \dfrac{dp_k}{d\boldsymbol{n}}=0 & & \text{on}\quad \Gamma, \end{array}\right. \tag{1.45}$$

with

$$v_{n-1}\overset{\text{def}}{=}\frac{\rho^{\mathrm{f}}}{\tau}\,\boldsymbol{u}^{n-1}\cdot\boldsymbol{n}^{\mathrm{f}}+\frac{\rho^{\mathrm{f}}}{\tau^2}\,d^{n-1}-\frac{\rho^{\mathrm{f}}\rho^{\mathrm{s}}\epsilon}{\tau^2\,(\rho^{\mathrm{s}}\epsilon+\beta\tau^2)}\,(2d^{n-1}-d^{n-2}).$$

Therefore, we are interested in the following eigenvalue problem: find (λ,p) such that

$$\cdot\left\{\begin{array}{rcl} \Delta p=0 & \text{in} & \Omega^{\mathrm{f}}\\ \dfrac{\partial p}{\partial \boldsymbol{n}}+\dfrac{\rho^{\mathrm{f}}}{\lambda\,(\rho^{\mathrm{s}}\epsilon+\beta\tau^2)}\,p+\dfrac{\rho^{\mathrm{f}}\,c}{\tau^2}(1-\dfrac{1}{\lambda})\,p=0 & \text{on} & \Sigma\\ p=0 & \text{on} & \Gamma^{\mathrm{in}}\cup\Gamma^{\mathrm{out}}\\ \dfrac{\partial p_k}{\partial \boldsymbol{n}}=0 & \text{on} & \Gamma \end{array}\right. \tag{1.46}$$

The analysis of problem is much simpler than problem (1.33). Indeed, owing to $(1.46)_1$ and to the boundary conditions $(1.46)_3$ and $(1.46)_4$, we get eigenfunctions that write

$$p(x,y) = \sin\left(\frac{k\pi\, x}{L}\right) \cosh\left(\frac{k\pi\, y}{L}\right)$$

and the corresponding eigenvalue satisfies:

$$\frac{k\pi}{L} \tanh\left(\frac{k\pi\, R}{L}\right) + \frac{\rho^{\mathrm{f}}\, c}{\tau^2}(1 - \frac{1}{\lambda}) + \frac{\rho^{\mathrm{f}}}{\lambda} \frac{1}{\rho^{\mathrm{s}}\epsilon + \beta\tau^2},$$

which leads to

$$\lambda_k = \frac{c - \dfrac{\tau^2}{\rho^{\mathrm{s}}\epsilon + \beta\tau^2}}{c + \dfrac{k\pi\tau^2}{\rho^{\mathrm{f}}\, L} \tanh\left(\dfrac{k\pi\, R}{L}\right)}.$$

Since $c > 0$, we infer that $|\lambda_k|$ is a decreasing sequence. We conclude that the spectral radius $\rho(c)$ of the iteration is equal to $|\lambda_1|$ and the theorem is proved. □

Remark 1.4.1. *The optimal value of c in this case is $\frac{\tau^2}{\rho^{\mathrm{s}}\epsilon+\beta\tau^2}$ coinciding with the optimal value of $\alpha = \tau/\alpha_{\mathrm{f}}$ (see Remark 1.3.1). This is somehow not surprising since a certain similarity can be demonstrated between Algorithm* 1 *and Algorithm* 3 *as shown in [32].*

1.5 Numerical results

The numerical experiments are made with FreeFEM++ [70] in a two-dimensional rectangular 2D geometry with $L = 10$, $R = 0.5$ and $\epsilon = 0.1$ (all units are given in the CGS system). Boundary conditions are $\bar{p} = 0$ on the outlet boundary ($x = L$) and $\bar{p} = 10^4$ during $T_i = 5 \times 10^{-3}$ at the inlet boundary ($x = 0$). The fluid and solid densities are $\rho^{\mathrm{f}} = 1$ and $\rho^{\mathrm{s}} = 1.1$, respectively. The fluid viscosity is set to $\mu = 0.035$ and the structure has a Young modulus of $E = 3 \times 10^8$ and a Poisson coefficient of $\nu = 0.3$. The time step is $\tau = 10^{-4}$ and the final time is $T = 15 \times 10^{-3}$. We use a space discretization based on $\mathbb{P}2/\mathbb{P}1$ finite elements with a mesh size of $h = 0.1$.

The three algorithms presented in section 1.3 are compared to the standard Dirichlet-Neumann iterations with Aitken's dynamic relaxation (see [81, 85]). They all require the specification of a free parameter. We choose to set it at its optimal value (derived in the case of a linear simplified model), namely

$$c = \alpha = \frac{\tau^2}{\rho^{\mathrm{s}}\epsilon + \beta\tau^2}.$$

Figure 1.9 (Left) presents the mean number of iteration needed per time step for different values of the domain length. We clearly see that the Dirichlet-Neumann iterations are sensitive to a variation of the domain length. The performances deteriorates

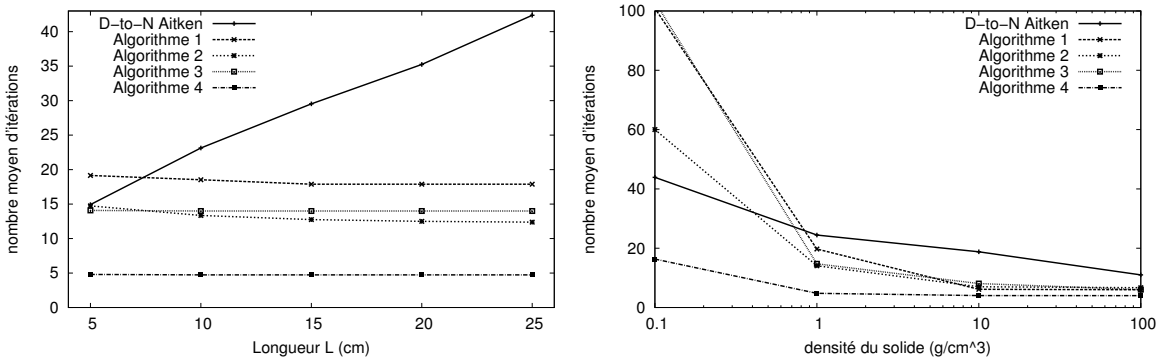

Figure 1.9: Mean number of iteration per time step.

when the domain in lengthy. This is a well-known illustration of the added-mass effect. The three preconditioned algorithms are rather insensitive to this effect and provide better performances. Note that Algorithm 3 yields better performances than the other algorithms.

Figure 1.9 (Right) presents the mean number of iteration needed per time step for different values of the domain solid density. We see that algorithms 1-3 are still sensitive to the solid density. However, for physiological values of ρ^s, the performances are better than the standard Dirichlet-Neumann iterations. Algorithm 3 still represents the best alternative in this test-case.

Table 1.1 presents the CPU time needed to compute 20 time steps (in adimensional units). Algorithm 2 becomes faster as the mesh size h tends to 0 since it allows a separate resolution of the fluid velocity and pressure.

h	0.04	0.05	0.08	0.1	0.2
Algorithm 1	34	22,6	9,4	6,5	1,8
Algorithm 2	21,2	14,5	5,5	3,8	1
Algorithm 3	49	32	12	7,6	1,5

Table 1.1: Elapsed CPU time to compute 20 time steps (adimentionnal units)

1.6 Conclusion

In this chapter, we discussed three algorithms for the solution of semi-implicit coupling (geometrical ALE non-linearities are treated explicitly) in incompressible fluid-structure iteration. Although some of them (Algorithms 1 and 3) have already been proposed in the literature, we present them in the framework of defect-correction iterations. The main ingredient of these algorithms is the relaxation of either the velocity

continuity constraint or the fluid incompressibility. Algorithm 2 enables a separate resolution of the fluid velocity and pressure which can be interesting from the computational and implementation standpoints.

We have also provided a comprehensive study of Algorithm 3 (artificial compressibility) and a major variant where the artificial compressibility is only located on the interface in a representative linear setting. This study shows that the iteration may fail to converge when the parameter c that relaxes the incompressibility constraint is too small. In addition, the optimal value of c, derived from the interface artificial compressibility model in a simplified linear setting, coincides with the optimal value of α for Algorithm 1, suggesting some similarities between Robin-Neuman iterations and the artificial compressibility (see [32]).

Numerical evidences has shown that the methods discussed are less sensitive to the added-mass effect that the standard Dirichlet-Neumann iterations, especially concerning the domain length.

All these methods involve a free parameter whose value has to be properly chosen. In the next chapters, we will propose alternative iterative procedures that congerge without the need of tuning any free parameter (see Sections 2.5 and 3.3.4).

Chapter 2

Robin-Neumann explicit coupling schemes for the coupling with a thin-walled structure

The results presented in this chapter lead to the paper [56]: M.A. Fernández, J. Mullaert, M. Vidrascu. **Explicit Robin-Neumann schemes for the coupling of incompressible fluids with thin-walled structures**. *Comput. Methods Appl. Mech. Engrg.*, 267:566–593, 2013.

Contents

2.1 Introduction 36
2.2 A linear model problem 38
2.3 Robin-Neumann methods 39
2.3.1 Explicit coupling schemes 40
2.4 Stability analysis 44
2.4.1 Notation and weak formulation 44
2.4.2 Space discretization: fully discrete schemes 45
2.4.3 Kinematic perturbation of implicit coupling 46
2.4.4 A priori energy estimates 47
2.4.5 Proof of Theorem 2.4.1 50
2.5 Iterative partitioned solution of implicit coupling 54
2.5.1 Convergence of the iterative solution procedure 55
2.6 A priori error estimates 57
2.6.1 Preliminaries and main result 57
2.6.2 Proof of Theorem 4.3.3 60
2.7 Formulation in the non-linear case 67
2.7.1 The non-linear coupled problem 67
2.7.2 Explicit Robin-Neumann schemes 68
2.8 Numerical experiments 69
2.8.1 Convergence study in a two-dimensional test-case 70
2.8.2 Pressure wave propagation in a straight tube 72
2.8.3 Blood flow in an abdominal aortic aneurysm 74
2.8.4 Lid-driven cavity with flexible bottom 76
2.8.5 Damped structural instability 78
2.9 Conclusion 80

2.1 Introduction

In this Chapter, we introduce a class of explicit coupling schemes for the numerical solution of fluid-structure interaction problems involving a viscous incompressible fluid and a general thin-walled structure (e.g., including damping and non-linear behavior). The methods proposed build on the Robin-Neumann splitting paradigm introduced [45] for the coupling of a linear purely elastic thin-solid model (string or membrane) and a Stokesian flow.

The first novelty of this chapter concerns the presence of physical dissipation (damping) in the thin-solid model. It is well known that much materials exhibit viscoelastic behavior and this is, in particular, the case of biological tissue (see, e.g., [79, 24, 115]). Since viscoelastic constitutive laws (e.g., *Kelvin-Voigt model*) introduce hydrodynamic effects within the solid equation, one can think of implicitly embeddeding this contributions within the fluid, trough a non-standard Robin condition, and then solve for the solid with the remaining purely elastic contributions (see [67, 44, 88, 15] and Remarks 2.3.1 and 2.3.2 below). Unfortunately, this strategy yields a coupling scheme which is not explicit and the corresponding solution procedure is not partitioned, since the solid viscous contribution must be integrated within the fluid solver. On the other hand, if we keep the whole viscoelastic contribution in the solid solver, the parabolic part of coupled system is not fully implicitly treated and, hence, one could argue that this might yield restrictive stability time-step restrictions (see below). In this chapter, we consider the latter approach, the whole solid viscoelastic contribution is explicitly coupled with the fluid using the inherent Robin consistency of the interface coupling.

The second contribution of this chapter has to do with the formulation of the explicit coupling schemes. We propose a new Robin-Neumann coupling paradigm which enables the fluid-solid splitting exclusively in terms of the solid velocity and fluid stress on the interface. A remarkable feature of this new formulation is its intrinsic character, in the sense that it avoids the extrapolations of the solid viscoelastic terms within the fluid. Hence, the resulting solution procedures are genuinely partitioned. This is, in particular, essential for the coupling with *Reissner-Mindlin* shell models, commonly used in engineering practice (see, e.g, [26, 10]), and that include transverse shear strain effects via rotation surface vectors (independent of the mid-surface displacements). Indeed, the intrinsic Robin interface condition removes the ambiguity in the extrapolation of rotation unknowns and of non-linear terms. The explicit coupling schemes are then formulated in a fully non-linear setting, involving the incompressible Navier-Stokes equations (ALE formalism) and a non-linear viscoelastic shell model. The main idea consists in combining the Robin-Neumann splitting proposed with a explicit treatment of the fluid domain motion.

The third novelty concerns the numerical analysis of the methods within a representative linear setting, involving a Stokesian fluid and a viscoelastic thin-walled solid (string or membrane). By generalizing the arguments reported in [45], a priori energy and error estimates are provided for all the variants (i.e., with and without

extrapolations). The analysis shows, in particular, that the sole implicit treatment of the solid inertia within the fluid is enough to guarantee (added-mass free) stability. In the case of the coupling with a purely elastic structure, this stabilization mechanism has been originally demonstrated in [67] (and in [93] in a non-linear setting) for the kinematically coupled scheme (i.e., without extrapolation), and then in [45] for optimally accurate first-order schemes (i.e., with extrapolation). The present analysis shows that, in the case of the coupling with a viscoelastic structure, the explicit treatment of the solid viscous contribution in the fluid does not perturb the overall stability of the variants without extrapolation and with first-order extrapolation. For the scheme with second-order extrapolation, however, a 2-CFL (parabolic CFL) condition is required for stability, instead of the mild 6/5-CFL (quasi-hyperbolic CFL) condition derived in [45] without solid damping, or in [44] with an implicit treatment of the solid damping in the fluid. As regards accuracy, sub-optimal time-convergence is obtained for the variant without extrapolation and optimal accuracy is expected for the schemes with first- and second-order extrapolations. In particular, the method with first-order extrapolation is (to our knowledge) the first explicit coupling scheme which guaranties unconditional stability and optimal (first-order) accuracy for the considered model problem.

The fourth contribution of this chapter deals with the partitioned solution of implicit coupling, via the iterative Robin-Neumann procedures introduced in [3]. So far the convergence analysis of these methods has been addressed in specific simplified models (e.g., inviscid fluid) and in particular geometrical configurations (e.g., a rectangle), using modal analysis (see [3]). In this work, we show that the the stability analysis of the explicit Robin-Neumann coupling schemes can be reshaped to derive, using energy arguments, a general result on the (added-mass free) convergence of these iterative methods. To the best of our knowledge, the error estimate proposed is the first which yields convergence towards the implicit coupling solution in such a general setting. The key argument consists in interpreting the explicit coupling schemes as single iterations of a parameter free Robin-Neumann iterative procedure for the solution of implicit coupling.

Finally, a comprehensive list of numerical experiments, based on different linear and non-linear fluid-structure interaction examples from the literature, supports the above findings.

This chapter is organized as follows. In Section 2.2, we present the linear continuous setting which serves as model coupled problem. In Section 2.3, we introduce the Robin-Neumann explicit coupling schemes and their different formulations within a linear time semi-discrete framework. We also discuss the connections with the partitioned solution of implicit coupling in section 2.5. Section 2.4 and 2.6 are devoted to the stability and convergence analysis of the methods. In Section 2.7, we present the generalization of the schemes to the non-linear case. The numerical experiments are reported in Section 2.8. Finally, Section 2.9 draws the conclusions.

2.2 A linear model problem

Let Ω be a domain of $\mathbb{R}^d$ ($d = 2, 3$) and $\partial\Omega = \Gamma^{\mathrm{d}} \cup \Gamma^{\mathrm{n}} \cup \Sigma$ a given partition of its boundary. In what follows, the symbol Σ stands for the fluid-structure interface. We consider a low Reynolds regime and assume that the structure undergoes infinitesimal displacements. The fluid is described by the Stokes equations in Ω, and the structure is assumed to behave as a linear thin-solid (e.g., plate, membrane or shell) represented by the $(d-1)$-manifold Σ. Our coupled model problem reads therefore as follows: find the fluid velocity $\boldsymbol{u} : \Omega \times \mathbb{R}^+ \to \mathbb{R}^d$, the fluid pressure $p : \Omega \times \mathbb{R}^+ \to \mathbb{R}$, the solid displacement $\boldsymbol{d} : \Sigma \times \mathbb{R}^+ \to \mathbb{R}^d$ and the solid velocity $\dot{\boldsymbol{d}} : \Sigma \times \mathbb{R}^+ \to \mathbb{R}^d$ such that

$$\begin{cases} \rho^{\mathrm{f}} \partial_t \boldsymbol{u} - \mathbf{div}\boldsymbol{\sigma}(\boldsymbol{u}, p) = \mathbf{0} & \text{in} \quad \Omega, \\ \mathrm{div}\boldsymbol{u} = 0 & \text{in} \quad \Omega, \\ \boldsymbol{u} = \mathbf{0} & \text{on} \quad \Gamma^{\mathrm{d}}, \\ \boldsymbol{\sigma}(\boldsymbol{u}, p)\boldsymbol{n} = \boldsymbol{h} & \text{on} \quad \Gamma^{\mathrm{n}}, \end{cases} \tag{2.1}$$

$$\begin{cases} \boldsymbol{u} = \dot{\boldsymbol{d}} & \text{on} \quad \Sigma, \\ \rho^{\mathrm{s}} \epsilon \partial_t \dot{\boldsymbol{d}} + \boldsymbol{L}^{\mathrm{e}} \boldsymbol{d} + \boldsymbol{L}^{\mathrm{v}} \dot{\boldsymbol{d}} = -\boldsymbol{\sigma}(\boldsymbol{u}, p)\boldsymbol{n} & \text{on} \quad \Sigma, \\ \dot{\boldsymbol{d}} = \partial_t \boldsymbol{d} & \text{on} \quad \Sigma, \\ \boldsymbol{d} = \mathbf{0} & \text{on} \quad \partial\Sigma, \end{cases} \tag{2.2}$$

complemented with the initial conditions

$$\boldsymbol{u}(0) = \boldsymbol{u}^0, \quad \boldsymbol{d}(0) = \boldsymbol{d}^0, \quad \dot{\boldsymbol{d}}(0) = \dot{\boldsymbol{d}}^0.$$

Here, ρ^{f} and ρ^{s} respectively denote the fluid and solid densities and ϵ the solid thickness. The fluid Cauchy-stress tensor is given by

$$\boldsymbol{\sigma}(\boldsymbol{u}, p) \stackrel{\mathrm{def}}{=} -p\boldsymbol{I} + 2\mu\boldsymbol{\epsilon}(\boldsymbol{u}), \quad \boldsymbol{\epsilon}(\boldsymbol{u}) \stackrel{\mathrm{def}}{=} \frac{1}{2}\left(\boldsymbol{\nabla}\boldsymbol{u} + \boldsymbol{\nabla}\boldsymbol{u}^{\mathrm{T}}\right),$$

where μ stands for the fluid dynamic viscosity. The exterior unit-vector normal to $\partial\Omega$ is denoted by $\boldsymbol{n}$ and $\boldsymbol{h}$ represents a given surface force on Γ^{n}. The strong formulation of the thin-solid elastic and viscous contributions are supposed to be given in terms of the surface differential operators $\boldsymbol{L}^{\mathrm{e}}$ and $\boldsymbol{L}^{\mathrm{v}}$, respectively.

The relations $(2.2)_1$ and $(2.2)_2$ enforce the kinematic and kinetic interface coupling conditions, respectively. It should be noted that the latter represents also the momentum equation of the structure. Though simplified, problem (2.1)-(2.2) features some of the main numerical issues that appear in complex nonlinear fluid-structure interaction problems involving an incompressible fluid (see, e.g., [25, 43]).

Remark 2.2.1. *A widely used form of the viscous operator $\boldsymbol{L}^{\mathrm{v}}$ is given by the so-called* Rayleigh damping*:*

$$\boldsymbol{L}^{\mathrm{v}} \dot{\boldsymbol{d}} \stackrel{\mathrm{def}}{=} \alpha_0 \rho^{\mathrm{s}} \epsilon \dot{\boldsymbol{d}} + \alpha_1 \boldsymbol{L}^{\mathrm{e}} \dot{\boldsymbol{d}}, \tag{2.3}$$

where $\alpha_0, \alpha_1 \geq 0$ *are given parameters (see, e.g., [76]). For instance, the expression* (2.3) *is often used in artery wall modeling, where the second term corresponds to the* Kelvin-Voigt *model (see, e.g., [79, 24, 115]), and the first takes into account the dissipative effects of external tissue on blood vessels (see [90]).* $\diamond$

Examples of thin-walled solid models entering the abstract form of $(2.2)_2$ are plate models and shell models derived under the *Kirchhoff-Love* kinematic assumption, the so-called *membrane-bending* shell models (see, e.g., [26, Section 4.2.3]). Richer shell models, such that the widespread *Reissner-Mindlin* shell models (see, e.g., [26, Sections 4.2.1-4.2.2]) which include transverse shear strain effects, will be considered in this work. In this case, the relations (2.2) have to be replaced by

$$\begin{cases} \boldsymbol{u} = \dot{\boldsymbol{d}} & \text{on} \quad \Sigma, \\ \rho^{\mathrm{s}}\epsilon\partial_t\dot{\boldsymbol{d}} + \boldsymbol{L}^{\mathrm{e}}_{\boldsymbol{d}}(\boldsymbol{d},\boldsymbol{\theta}) + \boldsymbol{L}^{\mathrm{v}}_{\boldsymbol{d}}(\dot{\boldsymbol{d}},\dot{\boldsymbol{\theta}}) = -\boldsymbol{\sigma}(\boldsymbol{u},p)\boldsymbol{n} & \text{on} \quad \Sigma, \\ \boldsymbol{L}^{\mathrm{e}}_{\boldsymbol{\theta}}(\boldsymbol{d},\boldsymbol{\theta}) + \boldsymbol{L}^{\mathrm{v}}_{\boldsymbol{\theta}}(\dot{\boldsymbol{d}},\dot{\boldsymbol{\theta}}) = \boldsymbol{0} & \text{on} \quad \Sigma, \\ \dot{\boldsymbol{d}} = \partial_t\boldsymbol{d}, \quad \dot{\boldsymbol{\theta}} = \partial_t\boldsymbol{\theta} & \text{on} \quad \Sigma, \\ \boldsymbol{d} = \boldsymbol{\theta} = \boldsymbol{0} & \text{on} \quad \partial\Sigma, \end{cases} \tag{2.4}$$

where the surface vector $\boldsymbol{\theta} : \Sigma \times \mathbb{R}^+ \to \mathbb{R}^3$ (satisfying the *Reissner-Mindlin* kinematic assumption) describes the rotation around the normal to the mid-surface. The elastic and viscous contributions are now given in terms of the surface operators $(\boldsymbol{L}^{\mathrm{e}}_{\boldsymbol{d}}, \boldsymbol{L}^{\mathrm{e}}_{\boldsymbol{\theta}})$ and $(\boldsymbol{L}^{\mathrm{v}}_{\boldsymbol{d}}, \boldsymbol{L}^{\mathrm{v}}_{\boldsymbol{\theta}})$. In particular, the quasi-static relation $(2.4)_3$ represents the additional equation for the rotations.

It should be noted that the kinematic and kinetic interface coupling $(2.4)_{1,2}$ are enforced only in terms of the mid-surface displacement. This approach, which amounts to neglect the effect of the thickness of the shell across the interface, is a widespread modeling assumption when coupling thin-solids with three-dimensional materials (see, e.g., [27]).

For the sake of clarity, we will consider (2.1)-(2.2) as model problem for the derivation of the explicit coupling schemes in Section 2.3. We briefly discuss their extension to the case of the coupling with the general shell model (2.4) in Remark 2.3.7. The stability and convergence analysis reported in Sections 2.4 and 2.6 focuses entirely on the linear coupled problem (2.1)-(2.2). In Section 2.8, numerical results are presented in the case of the coupling with (2.2), (2.4) and the non-linear version of (2.4) (see Section 2.7).

2.3 Robin-Neumann methods

A fundamental feature of the coupled problem (2.1)-(2.2) is its underlying Robin consistency on the interface. Indeed, by inserting $(2.2)_1$ into $(2.2)_2$ we get the expression

$$\boldsymbol{\sigma}(\boldsymbol{u},p)\boldsymbol{n} + \rho^{\mathrm{s}}\epsilon\partial_t\boldsymbol{u} = -\boldsymbol{L}^{\mathrm{e}}\boldsymbol{d} - \boldsymbol{L}^{\mathrm{v}}\dot{\boldsymbol{d}} \quad \text{on} \quad \Sigma, \tag{2.5}$$

which yields a Robin-like interface condition for the fluid (see, e.g., [97, 67]). Instead of formulating the fluid-solid time-splitting from the original Dirichlet-Neumann coupling $(2.2)_1$ and $(2.2)_2$ (see, e.g., [25, 61]), in this work we consider the Robin-Neumann interface conditions given by (2.5) and $(2.2)_2$. The benefits of this approach are threefold:

- the implicit treatment of the solid inertial term in (2.5) guarantees (added-mass free) stability;
- the explicit treatment of the solid viscoelastic terms in (2.5) enables the full fluid-solid splitting without compromising stability;
- the resulting schemes are genuine partitioned methods with an intrinsic explicit Robin-Neumann pattern (e.g., independent of the extrapolations of the right-hand side of (2.5)).

2.3.1 Explicit coupling schemes

In what follows, $\tau > 0$ denotes the time-step length, $t^n \overset{\text{def}}{=} n\tau$, for $n \in \mathbb{N}$, and

$$\partial_\tau x^n \overset{\text{def}}{=} \frac{1}{\tau}\big(x^n - x^{n-1}\big),$$

stands for the first-order backward difference. The approximation of (2.1)-(2.2) is split into two sequential sub-steps:

1. solve for the fluid with a semi-implicit time-discretization of (2.5), that is, the solid inertia is treated implicitly whereas the viscoelastic contribution is treated explicitly via extrapolation. This yields the following explicit Robin condition for the fluid:

$$\boldsymbol{\sigma}(\boldsymbol{u}^n, p^n)\boldsymbol{n} + \frac{\rho^{\mathrm{s}}\epsilon}{\tau}\boldsymbol{u}^n = \frac{\rho^{\mathrm{s}}\epsilon}{\tau}\dot{\boldsymbol{d}}^{n-1} - \boldsymbol{L}^{\mathrm{e}}\boldsymbol{d}^\star - \boldsymbol{L}^{\mathrm{v}}\dot{\boldsymbol{d}}^\star \quad \text{on} \quad \Sigma, \tag{2.6}$$

   with

$$(\boldsymbol{d}^\star, \dot{\boldsymbol{d}}^\star) = \begin{cases} \boldsymbol{0} & \text{if} \quad r = 0, \\ (\boldsymbol{d}^{n-1}, \dot{\boldsymbol{d}}^{n-1}) & \text{if} \quad r = 1, \\ (2\boldsymbol{d}^{n-1} - \boldsymbol{d}^{n-2}, 2\dot{\boldsymbol{d}}^{n-1} - \dot{\boldsymbol{d}}^{n-2}) & \text{if} \quad r = 2 \end{cases} \tag{2.7}$$

   and where r denotes the displacement-velocity extrapolation order;

2. solve for the solid "Neumann problem" (i.e., fluid stresses are transferred to the solid):

$$\rho^{\mathrm{s}}\epsilon\partial_\tau\dot{\boldsymbol{d}}^n + \boldsymbol{L}^{\mathrm{e}}\boldsymbol{d}^n + \boldsymbol{L}^{\mathrm{v}}\dot{\boldsymbol{d}}^n = -\boldsymbol{\sigma}(\boldsymbol{u}^n, p^n)\boldsymbol{n} \quad \text{on} \quad \Sigma. \tag{2.8}$$

The resulting schemes enable the uncoupled sequential time-marching of the fluid and the solid (explicit coupling scheme).

Remark 2.3.1. *The implicit treatment of the solid-damping, as advocated in [67, 88, 15], yields the following non-standard boundary condition for the fluid (see [44]):*

$$\boldsymbol{\sigma}(\boldsymbol{u}^n, p^n)\boldsymbol{n} + \frac{\rho^{\mathrm{s}}\epsilon}{\tau}\boldsymbol{u}^n + \boldsymbol{L}^{\mathrm{v}}\boldsymbol{u}^n = \frac{\rho^{\mathrm{s}}\epsilon}{\tau}\dot{\boldsymbol{d}}^{n-1} - \boldsymbol{L}^{\mathrm{e}}\boldsymbol{d}^{\star} \quad on \quad \Sigma. \tag{2.9}$$

It should be noted that, in contrast to (2.6)*, the relation* (2.9) *leads to a coupling scheme which is not explicit (it is semi-implicit). Moreover, the resulting solution procedure is not partitioned, since it integrates the solid viscous behavior within the fluid solver. For a simple Kelvin-Voigt modeling of the damping (e.g., with* $\alpha_0 = 0$ *and* $\alpha_1 > 0$*, see Remark 2.2.1), solving the fluid with the interface condition* (2.9) *has a computational complexity similar to the monolithic solution of a fully implicit scheme. Indeed, with* (2.9) *the fluid system must include the interface term* $\alpha_1\boldsymbol{L}^{\mathrm{e}}$*, which is practically the same as the term* $(\alpha_1 + \tau)\boldsymbol{L}^{\mathrm{e}}$ *involved in the monolithic solver. The relation* (2.9) *becomes particularly cumbersome in the case of the coupling with the general shell model* (2.4)*, since the viscous term* $\boldsymbol{L}^{\mathrm{v}}_{\boldsymbol{d}}(\dot{\boldsymbol{d}}, \dot{\boldsymbol{\theta}})$ *includes interface rotation unknowns which are not present in the fluid solver. The situation can be even more critical in the case of more realistic viscoelastic laws (see, e.g., [86, 74]), which involve time derivatives and not only a simple proportionality between stress and strain.* ◇

Remark 2.3.2. *The interface relation* (2.9) *has clear connections with the time-stepping procedures traditionally used in the Immersed Boundary Method (see, e.g., [102, 11]), which only treat explicitly the solid elastic contributions. Another key difference with respect to* (2.6)-(2.8) *concerns the solid sub-step* (2.8)*, which in the Immersed Boundary Method simply reduces to the displacement-velocity relation*

$$\boldsymbol{d}^n = \boldsymbol{d}^{n-1} + \tau\boldsymbol{u}^n|_{\Sigma}.$$

In other words, the structure solver is never called. The price to pay for stability is a restrictive CFL-like condition, which demands very small time-steps in practice (see, e.g., [11, Lemma 7.3] and [113]). We shall see in Section 2.4.4 that the combination of (2.6) *and* (2.8) *fixes this issue.* ◇

In order to avoid the extrapolations, $-\boldsymbol{L}^{\mathrm{e}}\boldsymbol{d}^{\star} - \boldsymbol{L}^{\mathrm{v}}\dot{\boldsymbol{d}}^{\star}$, of the solid viscoelastic contributions in the fluid Robin-step (2.6), we observe that, from (2.8), we have

$$\boldsymbol{L}^{\mathrm{e}}\boldsymbol{d}^{\star} + \boldsymbol{L}^{\mathrm{v}}\dot{\boldsymbol{d}}^{\star} = -\rho^{\mathrm{s}}\epsilon\partial_\tau\dot{\boldsymbol{d}}^{\star} - \boldsymbol{\sigma}(\boldsymbol{u}^{\star}, p^{\star})\boldsymbol{n} \quad \text{on} \quad \Sigma, \tag{2.10}$$

for $n > r$ ($r = 1, 2$) and with obvious notation for $\boldsymbol{u}^{\star}$ and $p^{\star}$. Hence, by inserting (2.10) into (2.6) we get the alternative explicit Robin interface condition

$$\boldsymbol{\sigma}(\boldsymbol{u}^n, p^n)\boldsymbol{n} + \frac{\rho^{\mathrm{s}}\epsilon}{\tau}\boldsymbol{u}^n = \frac{\rho^{\mathrm{s}}\epsilon}{\tau}\left(\dot{\boldsymbol{d}}^{n-1} + \tau\partial_\tau\dot{\boldsymbol{d}}^{\star}\right) + \boldsymbol{\sigma}(\boldsymbol{u}^{\star}, p^{\star})\boldsymbol{n} \quad \text{on} \quad \Sigma. \tag{2.11}$$

In fact, this relation holds for $n > r$ and for all the extrapolations $r = 0$, 1 and 2. A salient feature of this new formulation is its intrinsic character: it does not depend

on the structure of the solid operator. In fact, (2.11) can be seen as an explicit time discretization of the following Robin condition:

$$\boldsymbol{\sigma}(\boldsymbol{u},p)\boldsymbol{n}+\frac{\rho^{\mathrm{s}}\epsilon}{\tau}\boldsymbol{u}=\frac{\rho^{\mathrm{s}}\epsilon}{\tau}\dot{\boldsymbol{d}}+\boldsymbol{\sigma}(\boldsymbol{u},p)\boldsymbol{n}\quad\text{on}\quad\Sigma, \tag{2.12}$$

in the sense that the right-hand side of (2.11) is an explicit approximation of the right-hand side of (2.12). As shown in Table 2.1, the extrapolation of the solid velocity has one order of accuracy higher than the resulting extrapolation of the fluid stress. This compensates the $\mathcal{O}(\tau^{-1})$ scaling of the Robin coefficient in (2.12).

r	$\dot{\boldsymbol{d}}^{n-1}+\tau\partial_\tau\dot{\boldsymbol{d}}^{\star}$	$\boldsymbol{\sigma}(\boldsymbol{u}^{\star},p^{\star})\boldsymbol{n}$
0	$\dot{\boldsymbol{d}}^{n-1}$	$\boldsymbol{0}$
1	$2\dot{\boldsymbol{d}}^{n-1}-\dot{\boldsymbol{d}}^{n-2}$	$\boldsymbol{\sigma}(\boldsymbol{u}^{n-1},p^{n-1})\boldsymbol{n}$
2	$3\dot{\boldsymbol{d}}^{n-1}-3\dot{\boldsymbol{d}}^{n-2}+\dot{\boldsymbol{d}}^{n-3}$	$2\boldsymbol{\sigma}(\boldsymbol{u}^{n-1},p^{n-1})\boldsymbol{n}-\boldsymbol{\sigma}(\boldsymbol{u}^{n-2},p^{n-2})\boldsymbol{n}$

Table 2.1: Correspondence between the solid displacement/velocity extrapolations (2.7) and the resulting extrapolations of the solid velocity and the fluid stress in (2.11).

Algorithm 2.1 Explicit Robin-Neumann schemes

For $n>r$:

1. Fluid step: find $\boldsymbol{u}^n:\Omega\times\mathbb{R}^+\to\mathbb{R}^d$ and $p^n:\Omega\times\mathbb{R}^+\to\mathbb{R}$ such that

$$\begin{cases}\rho^{\mathrm{f}}\partial_\tau\boldsymbol{u}^n-\mathbf{div}\boldsymbol{\sigma}(\boldsymbol{u}^n,p^n)=\boldsymbol{0} & \text{in}\quad\Omega,\\ \mathrm{div}\boldsymbol{u}^n=0 & \text{in}\quad\Omega,\\ \boldsymbol{u}^n=\boldsymbol{0} & \text{on}\quad\Gamma^{\mathrm{d}},\\ \boldsymbol{\sigma}(\boldsymbol{u}^n,p^n)\boldsymbol{n}=\boldsymbol{h} & \text{on}\quad\Gamma^{\mathrm{n}},\\ \boldsymbol{\sigma}(\boldsymbol{u}^n,p^n)\boldsymbol{n}+\dfrac{\rho^{\mathrm{s}}\epsilon}{\tau}\boldsymbol{u}^n=\dfrac{\rho^{\mathrm{s}}\epsilon}{\tau}\left(\dot{\boldsymbol{d}}^{n-1}+\tau\partial_\tau\dot{\boldsymbol{d}}^{\star}\right)+\boldsymbol{\sigma}(\boldsymbol{u}^{\star},p^{\star})\boldsymbol{n} & \text{on}\quad\Sigma.\end{cases} \tag{2.13}$$

2. Solid step: find $\boldsymbol{d}^n:\Sigma\times\mathbb{R}^+\to\mathbb{R}^d$ and $\dot{\boldsymbol{d}}^n:\Sigma\times\mathbb{R}^+\to\mathbb{R}^d$ such that

$$\begin{cases}\rho^{\mathrm{s}}\epsilon\partial_\tau\dot{\boldsymbol{d}}^n+\boldsymbol{L}^{\mathrm{e}}\boldsymbol{d}^n+\boldsymbol{L}^{\mathrm{v}}\dot{\boldsymbol{d}}^n=-\boldsymbol{\sigma}(\boldsymbol{u}^n,p^n)\boldsymbol{n} & \text{on}\quad\Sigma,\\ \dot{\boldsymbol{d}}^n=\partial_\tau\boldsymbol{d}^n & \text{on}\quad\Sigma,\\ \boldsymbol{d}^n=\boldsymbol{0} & \text{on}\quad\partial\Sigma.\end{cases} \tag{2.14}$$

To sum up, the proposed explicit Robin-Neumann schemes are detailed in Algorithm 2.1, with the different extrapolations listed in Table 2.1.

Remark 2.3.3. *It should be noted that, according to Table 2.1, the schemes with the first- and the second-order extrapolations ($r=1$ or 2) are multi-step methods on the interface ($n\geq 2$ and $n\geq 3$, respectively). Hence, additional data is needed to start*

the time-marching. In practice, this data can be obtained by performing one step of the scheme with $r = 0$, this yields $(\boldsymbol{u}^1, p^1, \dot{\boldsymbol{d}}^1)$, and then one step of the scheme with $r = 1$, which gives $(\boldsymbol{u}^2, p^2, \dot{\boldsymbol{d}}^2)$. As we shall see in Section 2.6, these initializations guarantee the optimal first-order accuracy of Algorithm 2.1 with $r = 1$, 2. $\diamond$

Remark 2.3.4. *For $r = 0$, the relations* (2.6) *and* (2.11) *coincide and, thus, the interface splittings* (2.6)-(2.8) *and* (2.11)-(2.8) *yield the same time-marching scheme for $n \geq 1$. For $r = 1$ or $r = 2$, the equivalence of the interface splittings* (2.6)-(2.8) *and* (2.11)-(2.8) *holds for $n > r$. Hence, resulting schemes are equivalent only if they are initialized using the same procedure.* $\diamond$

Remark 2.3.5. *In the case of the coupling with an undamped thin-solid model (i.e., with $\boldsymbol{L}^{\mathrm{v}} = \boldsymbol{0}$ in $(2.2)_2$), Algorithm 2.1 yields the explicit coupling schemes introduced in [45], provided that the same initialization procedure is used.* $\diamond$

Remark 2.3.6. *Explicit coupling schemes have been traditionally referred to in the literature as weakly or loosely coupled (see, e.g., [42] and the references therein). Nevertheless, we prefer to avoid this appellation since, as highlighted thereafter, it can lead to misinterpretation. Even though Algorithm 2.1 has a computational complexity similar to a standard Dirichlet-Neumann weakly coupled scheme, in essence, it is a strongly-weakly coupled scheme (or semi-implicit coupling scheme), in the spirit of [47, 48]. Indeed, the strong (or implicit) part of the coupling involves the solid inertia contribution, appearing in the left-hand side of* (2.11)*, whereas the weak (or explicit) coupling is given by the extrapolation of the solid visco-elastic contributions. The crucial point is that, since we consider a thin-solid model for the structure, the strongly coupled part of the scheme is fully embedded into the fluid sub-step, through the explicit Robin condition* (2.11) *which, in fine, makes the coupling scheme explicit.* $\diamond$

Remark 2.3.7. *In the case of the coupling with the general shell model* (2.4)*, the interface Robin consistency* (2.5) *becomes*

$$\boldsymbol{\sigma}(\boldsymbol{u}, p)\boldsymbol{n} + \rho^{\mathrm{s}}\epsilon\,\partial_t \boldsymbol{u} = -\boldsymbol{L}^{\mathrm{e}}_{\boldsymbol{d}}(\boldsymbol{d}, \boldsymbol{\theta}) - \boldsymbol{L}^{\mathrm{v}}_{\boldsymbol{d}}(\dot{\boldsymbol{d}}, \dot{\boldsymbol{\theta}}) \quad \text{on} \quad \Sigma. \tag{2.15}$$

Hence, in the first step of Algorithm 2.1, the explicit interface condition (2.6) *has to be replaced by*

$$\boldsymbol{\sigma}(\boldsymbol{u}^n, p^n)\boldsymbol{n} + \frac{\rho^{\mathrm{s}}\epsilon}{\tau}\boldsymbol{u}^n = \frac{\rho^{\mathrm{s}}\epsilon}{\tau}\dot{\boldsymbol{d}}^{n-1} - \boldsymbol{L}^{\mathrm{e}}_{\boldsymbol{d}}(\boldsymbol{d}^\star, \boldsymbol{\theta}^\star) - \boldsymbol{L}^{\mathrm{v}}_{\boldsymbol{d}}(\dot{\boldsymbol{d}}^\star, \dot{\boldsymbol{\theta}}^\star) \quad \text{on} \quad \Sigma,$$

with obvious notation for the extrapolations $\boldsymbol{\theta}^\star$ and $\dot{\boldsymbol{\theta}}^\star$. By applying the same argument as above, we can eliminate the extrapolations of the right-hand side in a intrinsic fashion, yielding an unchanged interface condition (2.11) *for the fluid. As a result, we only need to replace the second step by In Algorithm 2.1 we simply need to replace the*

second step (2.14) *by*

$$\left\{\begin{array}{rll} \rho^{\mathrm{s}}\epsilon\partial_\tau\dot{\boldsymbol{d}}^n + \boldsymbol{L}^{\mathrm{e}}_{\boldsymbol{d}}(\boldsymbol{d}^n,\boldsymbol{\theta}^n) + \boldsymbol{L}^{\mathrm{v}}_{\boldsymbol{d}}(\dot{\boldsymbol{d}}^n,\dot{\boldsymbol{\theta}}^n) = -\,\boldsymbol{\sigma}(\boldsymbol{u}^n,p^n)\boldsymbol{n} & on & \Sigma, \\ \boldsymbol{L}^{\mathrm{e}}_{\boldsymbol{\theta}}(\boldsymbol{d}^n,\boldsymbol{\theta}^n) + \boldsymbol{L}^{\mathrm{v}}_{\boldsymbol{\theta}}(\dot{\boldsymbol{d}}^n,\dot{\boldsymbol{\theta}}^n) = \boldsymbol{0} & on & \Sigma, \\ \dot{\boldsymbol{d}}^n = \partial_\tau\boldsymbol{d}^n, \quad \dot{\boldsymbol{\theta}}^n = \partial_\tau\boldsymbol{\theta}^n & on & \Sigma, \\ \boldsymbol{d}^n = \boldsymbol{\theta}^n = \boldsymbol{0} & on & \partial\Sigma, \end{array}\right. \tag{2.16}$$

which corresponds to the implicit first-order time-discretization of the shell model $(2.4)_{2-5}$*. This clearly demonstrates the intrinsic nature of the explicit Robin interface condition* (2.11) *and, in return, the partitioned features of Algorithm 2.1.* $\diamond$

2.4 Stability analysis

This section is devoted to the stability and convergence analysis of the explicit Robin-Neumann schemes introduced in the previous section (after finite element discretization in space). In what follows, the symbols $\lesssim$ and $\gtrsim$ will indicate inequalities up to a multiplicative constant (independent of the physical and discretization parameters).

2.4.1 Notation and weak formulation

In the subsequent text, we will consider the usual Sobolev spaces $H^m(\Omega)$ $(m \geq 0)$, with norm $\|\cdot\|_{m,\Omega}$. The closed subspaces $H^1_0(\Omega)$, of functions in $H^1(\Omega)$ with zero trace on $\partial\Omega$, and $L^2_0(\Omega)$, of functions in $L^2(\Omega)$ with zero mean in Ω, will also be used. The scalar product in $L^2(\Omega)$ is denoted by $(\cdot,\cdot)_\Omega$ and its norm by $\|\cdot\|_{0,\Omega}$. In order to ease the notation, we set $(\cdot,\cdot) \stackrel{\text{def}}{=} (\cdot,\cdot)_\Omega$. We consider the fluid velocity and pressure functional spaces

$$\boldsymbol{V} \stackrel{\text{def}}{=} \left\{\boldsymbol{v} \in [H^1(\Omega)]^3 \,/\, \boldsymbol{v}|_{\Gamma^{\mathrm{d}}} = \boldsymbol{0}\right\}, \quad \boldsymbol{V}_\Sigma \stackrel{\text{def}}{=} \left\{\boldsymbol{v} \in \boldsymbol{V} \,/\, \boldsymbol{v}|_\Sigma = \boldsymbol{0}\right\}, \quad Q \stackrel{\text{def}}{=} L^2(\Omega),$$

equipped with the norms

$$\|\boldsymbol{v}\|_{\boldsymbol{V}} \stackrel{\text{def}}{=} \|\mu^{\frac{1}{2}}\boldsymbol{\nabla}\boldsymbol{v}\|_{0,\Omega} \quad \text{and} \quad \|q\|_Q = \|\mu^{-\frac{1}{2}}q\|_{0,\Omega}.$$

The space $\boldsymbol{W} \subset [H^1_0(\Sigma)]^3$ stands for the space of admissible displacements. At last, the following bi-linear and linear forms $a : \boldsymbol{V}\times\boldsymbol{V} \to \mathbb{R}$, $b : Q\times\boldsymbol{V} \to \mathbb{R}$ and $l : \boldsymbol{V} \to \mathbb{R}$, given by

$$a(\boldsymbol{u},\boldsymbol{v}) \stackrel{\text{def}}{=} 2\mu\big(\boldsymbol{\epsilon}(\boldsymbol{u}),\boldsymbol{\epsilon}(\boldsymbol{v})\big), \quad b(q,\boldsymbol{v}) \stackrel{\text{def}}{=} -(q,\mathrm{div}\boldsymbol{v}), \quad l(v) \stackrel{\text{def}}{=} (\boldsymbol{h},\boldsymbol{v})_{\Gamma^{\mathrm{n}}},$$

will be used.

The strong formulation of the thin-solid viscoelastic contributions is supposed to be given in terms of densely defined, self-adjoint and unbounded linear operators

$$\boldsymbol{L}^{\mathrm{e}} : \boldsymbol{D}^{\mathrm{e}} \subset [L^2(\Sigma)]^3 \to [L^2(\Sigma)]^3, \quad \boldsymbol{L}^{\mathrm{v}} : \boldsymbol{D}^{\mathrm{v}} \subset [L^2(\Sigma)]^3 \to [L^2(\Sigma)]^3,$$

and we define two bilinear forms a^{e} and a^{v} by

$$a^{\mathrm{e}}(\boldsymbol{d},\boldsymbol{w}) = \left(\boldsymbol{L}^{\mathrm{e}}\boldsymbol{d},\boldsymbol{w}\right)_{\Sigma}, \quad a^{\mathrm{v}}(\dot{\boldsymbol{d}},\boldsymbol{w}) = \left(\boldsymbol{L}^{\mathrm{v}}\dot{\boldsymbol{d}},\boldsymbol{w}\right)_{\Sigma}, \tag{2.17}$$

for all $\boldsymbol{d} \in \boldsymbol{D}^{\mathrm{e}}$, $\dot{\boldsymbol{d}} \in \boldsymbol{D}^{\mathrm{v}}$ and $\boldsymbol{w} \in \boldsymbol{W}$. We further assume that a^{e} and a^{v} are inner-products into $\boldsymbol{W}$ and that, endowed with the inner-product a^{e}, $\boldsymbol{W}$ is a Hilbert space. We set

$$\|\boldsymbol{w}\|_{\mathrm{e}} \stackrel{\mathrm{def}}{=} \left(a^{\mathrm{e}}(\boldsymbol{w},\boldsymbol{w})\right)^{\frac{1}{2}}, \quad \|\boldsymbol{w}\|_{\mathrm{v}} \stackrel{\mathrm{def}}{=} \left(a^{\mathrm{v}}(\boldsymbol{w},\boldsymbol{w})\right)^{\frac{1}{2}},$$

and we assume that the following continuity estimate holds

$$\|\boldsymbol{w}\|_{\mathrm{e}}^2 \leq \beta_{\mathrm{e}} \|\boldsymbol{w}\|_{1,\Sigma}^2, \tag{2.18}$$

for all $\boldsymbol{w} \in \boldsymbol{W}$, and with β_{e} a positive constant.

The weak form of the linear coupled problem (2.1)-(2.2) reads as follows: find $(\boldsymbol{u}(t), p(t), \boldsymbol{d}(t), \dot{\boldsymbol{d}}(t)) \in \boldsymbol{V} \times Q \times \boldsymbol{W} \times \boldsymbol{W}$ such that

$$\begin{cases} \boldsymbol{u}|_{\Sigma} = \dot{\boldsymbol{d}}, \\ \rho^{\mathrm{f}}\left(\partial_t \boldsymbol{u}, \boldsymbol{v}\right) + a(\boldsymbol{u},\boldsymbol{v}) + b(p,\boldsymbol{v}) - b(q,\boldsymbol{u}) \\ \qquad + \rho^{\mathrm{s}}\epsilon\left(\partial_t \dot{\boldsymbol{d}}, \boldsymbol{w}\right)_{\Sigma} + a^{\mathrm{e}}(\boldsymbol{d},\boldsymbol{w}) + a^{\mathrm{v}}\left(\dot{\boldsymbol{d}},\boldsymbol{w}\right) = l(\boldsymbol{v}), \\ \dot{\boldsymbol{d}} = \partial_t \boldsymbol{d} \end{cases} \tag{2.19}$$

for all $(\boldsymbol{v}, q, \boldsymbol{w}) \in \boldsymbol{V} \times Q \times \boldsymbol{W}$ with $\boldsymbol{v}|_{\Sigma} = \boldsymbol{w}$.

2.4.2 Space discretization: fully discrete schemes

Let $\{\mathcal{T}_h\}_{0<h\leq 1}$ be a family of quasi-uniform triangulations of Ω. The subscript $h \in (0,1]$ refers to the level of refinement of the triangulation. In what follows, we let X_h and M_h denote, respectively, the standard spaces of continuous and (possibly) discontinuous piece-wise polynomial functions of degree $k \geq 1$ and $l \geq 0$ ($k-1 \leq l \leq k$):

$$X_h \stackrel{\mathrm{def}}{=} \left\{ v_h \in C^0(\overline{\Omega}) \,/\, v_{h|K} \in \mathbb{P}_k(K) \quad \forall K \in \mathcal{T}_h \right\},$$
$$M_h \stackrel{\mathrm{def}}{=} \left\{ q_h \in Q \,/\, q_{h|K} \in \mathbb{P}_l(K) \quad \forall K \in \mathcal{T}_h \right\}.$$

For the approximation of the fluid velocity we will consider the space $\boldsymbol{V}_h \stackrel{\mathrm{def}}{=} [X_h]^d \cap \boldsymbol{V}$ and for the pressure we will use either $Q_h \stackrel{\mathrm{def}}{=} M_h$ or $Q_h \stackrel{\mathrm{def}}{=} M_h \cap C^0(\overline{\Omega})$. Whenever the considered velocity/pressure pair fails to satisfy the standard inf-sup condition, we consider a symmetric pressure stabilization method (see [17, 45]), given in terms of a positive and symmetric bi-linear form $s_h : Q_h \times Q_h \to \mathbb{R}$.

The discrete space for the solid displacement and velocity is chosen as the trace space $\boldsymbol{W}_h \stackrel{\mathrm{def}}{=} \left\{ \boldsymbol{v}_h|_{\Sigma} \,/\, \boldsymbol{v}_h \in \boldsymbol{V}_h \right\} \cap \boldsymbol{W}$. Hence, the fluid and solid space discretizations match at the interface. At last, we introduce the standard fluid-sided discrete lifting operator $\boldsymbol{\mathcal{L}}_h : \boldsymbol{W}_h \to \boldsymbol{V}_h$, such that, for all $\boldsymbol{w}_h \in \boldsymbol{W}_h$, $(\boldsymbol{\mathcal{L}}_h \boldsymbol{w}_h)|_{\Sigma} = \boldsymbol{w}_h$ and $\boldsymbol{\mathcal{L}}_h \boldsymbol{w}_h$ vanishes in all nodal values whose support is out of the interface.

After finite element discretization in space, the fully discrete version of Algorithm 2.1 is detailed in Algorithm 2.2. In particular, it is worth noting that fluid stresses on the interface are evaluated in a variationnaly consistent fashion, in terms of the discrete lifting operator $\boldsymbol{\mathcal{L}}_h$.

Algorithm 2.2 Explicit Robin-Neumann schemes (fully discrete)

For $n > r$:

1. Fluid step: Find $(\boldsymbol{u}_h^n, p_h^n) \in \boldsymbol{V}_h \times Q_h$ such that

$$\left\{\begin{array}{l} \rho^{\mathrm{f}}\big(\partial_\tau \boldsymbol{u}_h^n, \boldsymbol{v}_h\big) + a(\boldsymbol{u}_h^n, \boldsymbol{v}_h) + b(p_h^n, \boldsymbol{v}_h) - b(q_h, \boldsymbol{u}_h^n) + s_h(p_h, q_h) \\ \quad + \dfrac{\rho^{\mathrm{s}}\epsilon}{\tau}\big(\boldsymbol{u}_h^n, \boldsymbol{v}_h\big)_\Sigma = \dfrac{\rho^{\mathrm{s}}\epsilon}{\tau}\big(\dot{\boldsymbol{d}}_h^{n-1} + \tau\partial_\tau \dot{\boldsymbol{d}}_h^\star, \boldsymbol{v}_h\big)_\Sigma \\ \quad + \rho^{\mathrm{f}}\big(\partial_\tau \boldsymbol{u}_h^\star, \boldsymbol{\mathcal{L}}_h \boldsymbol{v}_h\big)_\Omega + a(\boldsymbol{u}_h^\star, \boldsymbol{\mathcal{L}}_h \boldsymbol{v}_h) + b(p_h^\star, \boldsymbol{\mathcal{L}}_h \boldsymbol{v}_h) + l(\boldsymbol{v}_h) \end{array}\right. \tag{2.20}$$

   for all $(\boldsymbol{v}_h, q_h) \in \boldsymbol{V}_h \times Q_h$ with $\boldsymbol{v}_h|_\Sigma \in \boldsymbol{W}_h$.

2. Solid step: Find $\big(\dot{\boldsymbol{d}}_h^n, \boldsymbol{d}_h^n\big) \in \boldsymbol{W}_h \times \boldsymbol{W}_h$, such that

$$\left\{\begin{array}{l} \dot{\boldsymbol{d}}_h^n = \partial_\tau \boldsymbol{d}_h^n, \\ \rho^{\mathrm{s}}\epsilon\big(\partial_\tau \dot{\boldsymbol{d}}_h^n, \boldsymbol{w}_h\big)_\Sigma + a^{\mathrm{e}}(\boldsymbol{d}_h^n, \boldsymbol{w}_h) + a^{\mathrm{v}}(\dot{\boldsymbol{d}}_h^n, \boldsymbol{w}_h) \\ \quad = -\rho^{\mathrm{f}}\big(\partial_\tau \boldsymbol{u}_h^n, \boldsymbol{\mathcal{L}}_h \boldsymbol{w}_h\big) - a(\boldsymbol{u}_h^n, \boldsymbol{\mathcal{L}}_h \boldsymbol{w}_h) - b(p_h^n, \boldsymbol{\mathcal{L}}_h \boldsymbol{w}_h) \end{array}\right. \tag{2.21}$$

   for all $\boldsymbol{w}_h \in \boldsymbol{W}_h$.

2.4.3 Kinematic perturbation of implicit coupling

In what follows, we shall make use of discrete reconstructions, $\boldsymbol{L}_h^{\mathrm{e}} : \boldsymbol{W} \to \boldsymbol{W}_h$ and $\boldsymbol{L}_h^{\mathrm{v}} : \boldsymbol{W} \to \boldsymbol{W}_h$, of the elastic and viscous solid operators, defined by the relations

$$(\boldsymbol{L}_h^{\mathrm{e}} \boldsymbol{w}, \boldsymbol{w}_h)_\Sigma = a^{\mathrm{e}}(\boldsymbol{w}, \boldsymbol{w}_h), \quad (\boldsymbol{L}_h^{\mathrm{v}} \boldsymbol{w}, \boldsymbol{w}_h)_\Sigma = a^{\mathrm{v}}(\boldsymbol{w}, \boldsymbol{w}_h), \tag{2.22}$$

for all $(\boldsymbol{w}, \boldsymbol{w}_h) \in \boldsymbol{W} \times \boldsymbol{W}_h$.

An important feature of Algorithm 2.2 is that it can be interpreted as kinematic perturbations of an underlying implicit coupling scheme. Indeed, replacing n by $\star$ in $(2.21)_2$ with $\boldsymbol{w}_h = \boldsymbol{v}_h|_\Sigma$ and adding the resulting expression to (2.20) yields

$$\begin{aligned} &\rho^{\mathrm{f}}\big(\partial_\tau \boldsymbol{u}_h^n, \boldsymbol{v}_h\big) + a(\boldsymbol{u}_h^n, \boldsymbol{v}_h) + b(p_h^n, \boldsymbol{v}_h) - b(q_h, \boldsymbol{u}_h^n) + s_h(p_h, q_h) \\ &\qquad + \frac{\rho^{\mathrm{s}}\epsilon}{\tau}\big(\boldsymbol{u}_h^n, \boldsymbol{v}_h\big)_\Sigma = \frac{\rho^{\mathrm{s}}\epsilon}{\tau}\big(\dot{\boldsymbol{d}}_h^{n-1}, \boldsymbol{v}_h\big)_\Sigma - a^{\mathrm{e}}(\boldsymbol{d}_h^\star, \boldsymbol{v}_h) - a^{\mathrm{v}}(\dot{\boldsymbol{d}}_h^\star, \boldsymbol{v}_h) + l(\boldsymbol{v}_h) \end{aligned} \tag{2.23}$$

for all $(\boldsymbol{v}_h, q_h) \in \boldsymbol{V}_h \times Q_h$ with $\boldsymbol{v}_h|_\Sigma \in \boldsymbol{W}_h$ and $n > r$.

Hence, by taking $(\boldsymbol{v}_h, q_h) = (\boldsymbol{\mathcal{L}}_h \boldsymbol{w}_h, 0)$ in (2.23), subtracting the resulting expression from $(2.21)_2$ and since $l(\boldsymbol{\mathcal{L}}_h \boldsymbol{w}_h) = 0$, we obtain

$$\frac{\rho^{\mathrm{s}}\epsilon}{\tau}\big(\dot{\boldsymbol{d}}_h^n - \boldsymbol{u}_h^n, \boldsymbol{w}_h\big)_\Sigma + a^{\mathrm{e}}(\boldsymbol{d}_h^n - \boldsymbol{d}_h^\star, \boldsymbol{w}_h) + a^{\mathrm{v}}(\dot{\boldsymbol{d}}_h^n - \dot{\boldsymbol{d}}_h^\star, \boldsymbol{w}_h) = 0, \tag{2.24}$$

for all $\boldsymbol{w}_h \in \boldsymbol{W}_h$ and $n > r$. Thus, owing to (2.22), we get

$$\boldsymbol{u}_h^n|_\Sigma = \dot{\boldsymbol{d}}_h^n + \frac{\tau}{\rho^{\mathrm{s}}\epsilon}\left(\boldsymbol{L}_h^{\mathrm{e}}(\boldsymbol{d}_h^n - \boldsymbol{d}_h^\star) + \boldsymbol{L}_h^{\mathrm{v}}(\dot{\boldsymbol{d}}_h^n - \dot{\boldsymbol{d}}_h^\star)\right), \tag{2.25}$$

for $n > r$. Moreover, owing to the initialization of the schemes considered in Section 2.3.1, for the first- and the second-order extrapolation we have

$$\begin{aligned}\boldsymbol{u}_h^2|_\Sigma =& \dot{\boldsymbol{d}}_h^2 + \frac{\tau}{\rho^{\mathrm{s}}\epsilon}\left(\boldsymbol{L}_h^{\mathrm{e}}(\boldsymbol{d}_h^2 - \boldsymbol{d}_h^1) + \boldsymbol{L}_h^{\mathrm{v}}(\dot{\boldsymbol{d}}_h^2 - \dot{\boldsymbol{d}}_h^1)\right),\\ \boldsymbol{u}_h^1|_\Sigma =& \dot{\boldsymbol{d}}_h^1 + \frac{\tau}{\rho^{\mathrm{s}}\epsilon}\left(\boldsymbol{L}_h^{\mathrm{e}}\boldsymbol{d}_h^1 + \boldsymbol{L}_h^{\mathrm{v}}\dot{\boldsymbol{d}}_h^1\right).\end{aligned}$$

In addition, taking $\boldsymbol{v}_h|_\Sigma = \boldsymbol{w}_h$ in (2.23) and adding the resulting expression to (2.24) yields

$$\begin{aligned}&\rho^{\mathrm{f}}\big(\partial_\tau \boldsymbol{u}_h^n, \boldsymbol{v}_h\big) + a(\boldsymbol{u}_h^n, \boldsymbol{v}_h) + b(p_h^n, \boldsymbol{v}_h) - b(q_h, \boldsymbol{u}_h^n) + s_h(p_h^n, q_h)\\ &\quad + \rho^{\mathrm{s}}\epsilon\big(\partial_\tau \dot{\boldsymbol{d}}_h^n, \boldsymbol{w}_h\big)_\Sigma + a^{\mathrm{e}}(\boldsymbol{d}_h^n, \boldsymbol{w}_h) + a^{\mathrm{v}}\big(\dot{\boldsymbol{d}}_h^n, \boldsymbol{w}_h\big) = l(\boldsymbol{v}_h).\end{aligned} \tag{2.26}$$

for all $(\boldsymbol{v}_h, q_h, \boldsymbol{w}_h) \in \boldsymbol{V}_h \times Q_h \times \boldsymbol{W}_h$ with $\boldsymbol{v}_h|_\Sigma = \boldsymbol{w}_h$ and $n > r$. Once more, using the initialization of the schemes, this relation holds true also for $n \geq 1$ irrespectively of the considered extrapolations.

In summary, the relations (2.25) and (2.26) are nothing but an implicit time-discretization of (2.19) with the perturbed kinematic constraint (2.25). Therefore, in order to asses the stability and accuracy of Algorithm 2.2, we only need to investigate how this kinematic perturbation affects the stability and accuracy of the underlying implicit coupling scheme. This will be the topic of Sections 2.4.4 and 2.6 below.

2.4.4 A priori energy estimates

We define the total discrete energy, E_h^n, and dissipation, D_h^n, at time-step t_n by

$$\begin{aligned}E_h^n \stackrel{\mathrm{def}}{=}& \rho^{\mathrm{f}}\|\boldsymbol{u}_h^n\|_0^2 + \rho^{\mathrm{s}}\epsilon\|\dot{\boldsymbol{d}}_h^n\|_{0,\Sigma}^2 + \|\boldsymbol{d}_h^n\|_{\mathrm{e}}^2,\\ D_h^n \stackrel{\mathrm{def}}{=}& \frac{\rho^{\mathrm{f}}}{\tau}\|\boldsymbol{u}_h^n - \boldsymbol{u}_h^{n-1}\|_0^2 + \|\boldsymbol{u}_h^n\|_{\boldsymbol{V}}^2 + |p_h^n|_{s_h}^2\\ &+ \frac{\rho^{\mathrm{s}}\epsilon}{\tau}\|\dot{\boldsymbol{d}}_h^n - \dot{\boldsymbol{d}}_h^{n-1}\|_{0,\Sigma}^2 + \frac{1}{\tau}\|\boldsymbol{d}_h^n - \boldsymbol{d}_h^{n-1}\|_{\mathrm{e}}^2 + \|\dot{\boldsymbol{d}}_h^n\|_{\mathrm{v}}^2,\end{aligned}$$

where $|p_h^n|_{s_h} \stackrel{\mathrm{def}}{=} \big(s_h(p_h^n, p_h^n)\big)^{\frac{1}{2}}$. The following result states the energy stability of the explicit Robin-Neumann schemes given by Algorithm 2.2.

For the sake of clearness, we recall here without proof the discrete version of the Gronwall lemma which will be necessary for proving stability and also convergence of the schemes.

Lemma 2.4.1 (from [73, Lemma 5.1]). *Let τ, B and a_m, b_m, c_m, γ_m (for integers $m \geq 1$) be nonnegative numbers such that*

$$a_n + \tau\sum_{m=1}^{n} b_m \leq \tau\sum_{m=1}^{n}\gamma_m a_m + \tau\sum_{m=1}^{n} c_m + B,$$

for all $n \geq 1$. Suppose that $\tau\gamma_m < 1$ for all $m \geq 1$. Then, there holds

$$a_n + \tau \sum_{m=1}^{n} b_m \leq \exp\left(\tau \sum_{m=1}^{n} \frac{\gamma_m}{1-\tau\gamma_m}\right)\left(\tau \sum_{m=1}^{n} c_m + B\right),$$

for all $n \geq 1$.

We also need the following estimates:

Lemma 2.4.2. *Let $\beta_{\mathrm{e}} > 0$ be the constant from the estimate* (2.18)*. There holds*

$$\begin{aligned}
\|\boldsymbol{w}_h\|_{\mathrm{e}}^2 &\leq \frac{\beta_{\mathrm{e}} C_{\mathrm{inv}}^2}{h^2} \|\boldsymbol{w}_h\|_{0,\Sigma}^2, \\
\|\boldsymbol{L}_h^{\mathrm{e}} \boldsymbol{w}_h\|_{\mathrm{e}} &\leq \frac{\beta_{\mathrm{e}} C_{\mathrm{inv}}^2}{h^2} \|\boldsymbol{w}_h\|_{\mathrm{e}}, \\
\|\boldsymbol{L}_h^{\mathrm{e}} \boldsymbol{w}_h\|_{0,\Sigma} &\leq \frac{\beta_{\mathrm{e}}^{\frac{1}{2}} C_{\mathrm{inv}}}{h} \|\boldsymbol{w}_h\|_{\mathrm{e}}, \\
\|\boldsymbol{L}_h^{\mathrm{v}} \boldsymbol{w}_h\|_{\mathrm{v}} &\leq \left(\alpha_0 \rho^{\mathrm{s}} \epsilon + \alpha_1 \frac{\beta_{\mathrm{e}} C_{\mathrm{inv}}^2}{h^2}\right) \|\boldsymbol{w}_h\|_{\mathrm{v}}.
\end{aligned} \tag{2.27}$$

for all $\boldsymbol{w}_h \in \boldsymbol{W}_h$ and with $C_{\mathrm{inv}} > 0$ the constant of an inverse estimate.

Proof. The first estimate is obtained thanks to (2.18) and an inverse estimate:

$$\|\boldsymbol{w}_h\|_{\mathrm{e}}^2 \leq \beta_{\mathrm{e}} \|\boldsymbol{w}_h\|_{1,\Sigma}^2 \leq \frac{\beta_{\mathrm{e}} C_{\mathrm{inv}}^2}{h^2} \|\boldsymbol{w}_h\|_{0,\Sigma}^2.$$

Then, for the next estimate, we write:

$$\|\boldsymbol{L}_h^{\mathrm{e}} \boldsymbol{w}_h\|_{\mathrm{e}}^2 \leq \frac{\beta_{\mathrm{e}} C_{\mathrm{inv}}^2}{h^2} \|\boldsymbol{L}_h^{\mathrm{e}} \boldsymbol{w}_h\|_{0,\Sigma}^2 = \frac{\beta_{\mathrm{e}} C_{\mathrm{inv}}^2}{h^2} a^{\mathrm{e}}\left(\boldsymbol{w}_h, \boldsymbol{L}_h^{\mathrm{e}} \boldsymbol{w}_h\right) \leq \frac{\beta_{\mathrm{e}} C_{\mathrm{inv}}^2}{h^2} \|\boldsymbol{L}_h^{\mathrm{e}} \boldsymbol{w}_h\|_{\mathrm{e}} \|\boldsymbol{w}_h\|_{\mathrm{e}}.$$

The same argument is used for the third estimate:

$$\|\boldsymbol{L}_h^{\mathrm{e}} \boldsymbol{w}_h\|_{0,\Sigma}^2 = a^{\mathrm{e}}\left(\boldsymbol{w}_h, \boldsymbol{L}_h^{\mathrm{e}} \boldsymbol{w}_h\right) \leq \|\boldsymbol{L}_h^{\mathrm{e}} \boldsymbol{w}_h\|_{\mathrm{e}} \|\boldsymbol{w}_h\|_{\mathrm{e}} \leq \frac{\beta_{\mathrm{e}} C_{\mathrm{inv}}^2}{h^2} \|\boldsymbol{L}_h^{\mathrm{e}} \boldsymbol{w}_h\|_{0,\Sigma} \|\boldsymbol{w}_h\|_{\mathrm{e}}.$$

At last, for estimate $(2.27)_4$, we have:

$$\begin{aligned}
\|\boldsymbol{L}_h^{\mathrm{v}} \boldsymbol{w}_h\|_{\mathrm{v}}^2 &= \alpha \rho^{\mathrm{s}} \epsilon \|\boldsymbol{L}_h^{\mathrm{v}} \boldsymbol{w}_h\|_{0,\Sigma}^2 + \beta \|\boldsymbol{L}_h^{\mathrm{v}} \boldsymbol{w}_h\|_{\mathrm{e}}^2 \\
&\leq \left(\alpha_0 \rho^{\mathrm{s}} \epsilon + \alpha_1 \frac{\beta_{\mathrm{e}} C_{\mathrm{inv}}^2}{h^2}\right) \|\boldsymbol{L}_h^{\mathrm{v}} \boldsymbol{w}_h\|_{0,\Sigma}^2 \\
&\leq \left(\alpha_0 \rho^{\mathrm{s}} \epsilon + \alpha_1 \frac{\beta_{\mathrm{e}} C_{\mathrm{inv}}^2}{h^2}\right) a^{\mathrm{v}}\left(\boldsymbol{w}_h, \boldsymbol{L}_h^{\mathrm{v}} \boldsymbol{w}_h\right) \\
&\leq \left(\alpha_0 \rho^{\mathrm{s}} \epsilon + \alpha_1 \frac{\beta_{\mathrm{e}} C_{\mathrm{inv}}^2}{h^2}\right) \|\boldsymbol{L}_h^{\mathrm{v}} \boldsymbol{w}_h\|_{\mathrm{v}} \|\boldsymbol{w}_h\|_{\mathrm{v}}.
\end{aligned}$$

Hence the proof is complete. □

We now state the main result of this section.

Theorem 2.4.1. *Assume that* $\boldsymbol{h} = \boldsymbol{0}$ *(free system) and let* $\{(\boldsymbol{u}_h^n, p_h^n, \boldsymbol{d}_h^n, \dot{\boldsymbol{d}}_h^n)\}_{n>r}$ *be the sequence given by Algorithm 2.2. The initialization procedure of Remark 2.3.3 is considered for the schemes with extrapolation* ($r \geq 1$)*. The following a priori energy estimates hold:*

- *Without extrapolation* ($r = 0$) *or with first-order extrapolation* ($r = 1$)*:*

$$E_h^n + \tau \sum_{m=r+1}^{n} D_h^m \lesssim E_h^0, \tag{2.28}$$

  for $n > r$*.*

- *Second-order extrapolation* ($r = 2$)*:*

$$E_h^n + \tau \sum_{m=3}^{n} D_h^m \lesssim \exp\left(\frac{t_n \gamma}{1 - \tau\gamma}\right) E_h^0, \tag{2.29}$$

  for $n \geq 3$*, provided that* (2.3) *and the following conditions hold*

$$\begin{cases} \tau\left(\alpha_0 + \alpha_1 \left(\dfrac{\omega_{\mathrm{e}}}{h}\right)^2\right) \leq \delta, \\ \tau^5 \left(\dfrac{\omega_{\mathrm{e}}}{h}\right)^6 + \tau^2 \left(\dfrac{\omega_{\mathrm{e}}}{h}\right)^2 \left(\alpha_0 + \alpha_1 \left(\dfrac{\omega_{\mathrm{e}}}{h}\right)^2\right) \leq \gamma, \\ \tau\gamma < 1, \end{cases} \tag{2.30}$$

  where $\omega_{\mathrm{e}} \overset{\mathrm{def}}{=} C_{\mathrm{inv}} \sqrt{\beta_{\mathrm{e}}/(\rho^{\mathrm{s}} \epsilon)}$*,* C_{inv} *denotes the constant of an inverse estimate,* $0 \leq \delta \leq 1$ *and* $\gamma > 0$*.*

Proof. See Section 2.4.5. □

Theorem 2.4.1 yields the unconditionally energy stability of the proposed explicit Robin-Neumann schemes without extrapolations and with the first-order extrapolations, provided that the initial discrete energy is bounded. Moreover, the energy estimates (2.28) are derived without any major assumption on the solid damping operator $\boldsymbol{L}^{\mathrm{v}}$, only symmetric and positiveness are required for the corresponding bi-linear form (2.17). In the case of a Rayleigh modeling of the solid damping (2.3), the variant with second-order extrapolations is energy stable, provided that the CFL-like conditions (2.30) are satisfied.

It is worth noting that all these variants are energy stable, irrespectively of the amount of added-mass effect in the system. This demonstrates that the implicit treatment of the solid inertial term in (2.5) is enough to guarantee added-mass free stability.

Remark 2.4.1. *From the result of Theorem 2.4.1 with $r = 0$, we deduce that the implicit treatment of the solid viscosity in the fluid, as advocated in [67, 88, 15], is not necessary for stability in the kinematically coupled scheme. Similar conclusions can be inferred by adapting the arguments of [67, Section 6]. This important feature, which yields an explicit coupling scheme and hence a partitioned solution procedure, has been disregarded in [67, 88, 15]. It should be noted that the energy arguments of [67, Section 6] do not apply to the schemes with extrapolation ($r = 1$ and $r = 2$) considered in Theorem 2.4.1. As shown in Section 2.6 below, these schemes deliver optimal first-order accuracy.*

Remark 2.4.2. *Theorem 2.4.1 generalizes the stability results reported in [45, Theorem 1] to the case $\boldsymbol{L}^{\mathrm{v}} \neq 0$. In particular, for $r = 2$ and in the case of the coupling with an undamped thin-solid model (i.e., $\boldsymbol{L}^{\mathrm{v}} = \boldsymbol{0}$) the relations* (2.30) *reduce to the 6/5-CFL condition $\tau\omega_{\mathrm{e}}^{\frac{6}{5}} \lesssim \gamma h^{\frac{6}{5}}$ derived in [45].* $\diamond$

Remark 2.4.3. *For the scheme with $r = 2$, the nature of the stability condition* (2.30) *depends on the Rayleigh coefficient α_1 involved in* (2.3)*. For $\alpha_1 = 0$, the relations* (2.30) *are fulfilled under a 6/5-CFL condition $\tau = \mathcal{O}(h^{\frac{6}{5}})$, while a parabolic-CFL constraint $\tau = \mathcal{O}(h^2)$ is required for $\alpha_1 > 0$. As stated in [44], this parabolic-CFL condition can be circumvented by integrating the solid damping within the fluid solver (as advocated in [67, 88, 15]), but the price to pay is a coupling scheme which is no longer explicit (see Remark 2.3.1).* $\diamond$

Remark 2.4.4. *By considering appropriate discrete Ritz-projections of the initial data (see Section 2.6), it is possible to ensure that the right-hand side of* (2.28) *and* (2.29) *is bounded uniformly with respect to h, that is,*

$$E_h^0 \lesssim \rho^{\mathrm{f}} \|\boldsymbol{u}^0\|_{0,\Omega^{\mathrm{s}}}^2 + \rho^{\mathrm{s}}\epsilon \|\dot{\boldsymbol{d}}^0\|_{0,\Sigma}^2 + \|\boldsymbol{d}_h^0\|_{\mathrm{e}}^2,$$

which yields the unconditional stability of the scheme. $\diamond$

2.4.5 Proof of Theorem 2.4.1

We proceed by extending the arguments reported in [45, Section 4]. Using (2.25), we take

$$(\boldsymbol{v}_h, q_h) = \tau(\boldsymbol{u}_h^n, p_h^n), \quad \boldsymbol{w}_h = \tau\dot{\boldsymbol{d}}_h^n + \frac{\tau^2}{\rho^{\mathrm{s}}\epsilon}\left(\boldsymbol{L}_h^{\mathrm{e}}(\boldsymbol{d}_h^n - \boldsymbol{d}_h^\star) + \boldsymbol{L}_h^{\mathrm{v}}(\dot{\boldsymbol{d}}_h^n - \dot{\boldsymbol{d}}_h^\star)\right),$$

as test functions in (2.26) for $n > r$. Thus, since $\boldsymbol{f}^{\Gamma} = \mathbf{0}$, we get the following discrete energy equation

$$\begin{aligned}
&\frac{\rho^{\mathrm{f}}}{2}\left(\tau\partial_\tau\|\boldsymbol{u}_h^n\|_{0,\Omega}^2 + \|\boldsymbol{u}_h^n - \boldsymbol{u}_h^{n-1}\|_{0,\Omega}^2\right) + 2\mu\tau\|\boldsymbol{\epsilon}(\boldsymbol{u}_h^n)\|_{0,\Omega}^2 + \tau|p_h^n|_{s_h}^2 \\
&\quad + \frac{\rho^{\mathrm{s}}\epsilon}{2}\left(\tau\partial_\tau\|\dot{\boldsymbol{d}}_h^n\|_{0,\Sigma}^2 + \|\dot{\boldsymbol{d}}_h^n - \dot{\boldsymbol{d}}_h^{n-1}\|_{0,\Sigma}^2\right) + \frac{1}{2}\left(\tau\partial_\tau\|\boldsymbol{d}_h^n\|_{\mathrm{e}}^2 + \|\boldsymbol{d}_h^n - \boldsymbol{d}_h^{n-1}\|_{\mathrm{e}}^2\right) \\
&\quad + \tau\|\dot{\boldsymbol{d}}_h^n\|_{\mathrm{v}}^2 + \underbrace{\tau^2\left(\partial_\tau\dot{\boldsymbol{d}}_h^n, \boldsymbol{L}_h^{\mathrm{e}}(\boldsymbol{d}_h^n - \boldsymbol{d}_h^\star) + \boldsymbol{L}_h^{\mathrm{v}}(\dot{\boldsymbol{d}}_h^n - \dot{\boldsymbol{d}}_h^\star)\right)_\Sigma}_{T_1} \\
&\quad + \underbrace{\frac{\tau^2}{\rho^{\mathrm{s}}\epsilon}\left(\boldsymbol{L}_h^{\mathrm{e}}\boldsymbol{d}_h^n + \boldsymbol{L}_h^{\mathrm{v}}\dot{\boldsymbol{d}}_h^n, \boldsymbol{L}_h^{\mathrm{e}}(\boldsymbol{d}_h^n - \boldsymbol{d}_h^\star) + \boldsymbol{L}_h^{\mathrm{v}}(\dot{\boldsymbol{d}}_h^n - \dot{\boldsymbol{d}}_h^\star)\right)_\Sigma}_{T_2} = 0, \quad (2.31)
\end{aligned}$$

for $n > r$. To complete the proof, we only need to control the terms T_1 and T_2. We proceed by treating each case separately, depending on the extrapolation order r.
(i) Without extrapolation ($r = 0$). In this case, using Young's inequality, we have

$$T_1 + T_2 \geq -\frac{\rho^{\mathrm{s}}\epsilon}{2}\|\dot{\boldsymbol{d}}_h^n - \dot{\boldsymbol{d}}_h^{n-1}\|_{0,\Sigma}^2 + \frac{\tau^2}{2\rho^{\mathrm{s}}\epsilon}\|\boldsymbol{L}_h^{\mathrm{e}}\boldsymbol{d}_h^n + \boldsymbol{L}_h^{\mathrm{v}}\dot{\boldsymbol{d}}_h^n\|_{0,\Sigma}^2, \quad (2.32)$$

for $n \geq 1$. Hence, the estimate (2.28) follows by inserting this expression into (2.31), applying Korn's inequality to the fluid viscous dissipation and summing over $m = 1, \ldots, n$.
(ii) First-order extrapolation ($r = 1$). In this case we have

$$T_1 = \frac{\tau^2}{2}\left(\tau\partial_\tau\left\|\dot{\boldsymbol{d}}_h^n\right\|_{\mathrm{e}}^2 + \left\|\dot{\boldsymbol{d}}_h^n - \dot{\boldsymbol{d}}_h^{n-1}\right\|_{\mathrm{e}}^2\right) + \tau\left\|\dot{\boldsymbol{d}}_h^n - \dot{\boldsymbol{d}}_h^{n-1}\right\|_{\mathrm{v}}^2, \quad (2.33)$$

and

$$T_2 = \frac{\tau^2}{2\rho^{\mathrm{s}}\epsilon}\left(\tau\partial_\tau\left\|\boldsymbol{L}_h^{\mathrm{e}}\boldsymbol{d}_h^n + \boldsymbol{L}_h^{\mathrm{v}}\dot{\boldsymbol{d}}_h^n\right\|_{0,\Sigma}^2 + \left\|\boldsymbol{L}_h^{\mathrm{e}}(\boldsymbol{d}_h^n - \boldsymbol{d}_h^{n-1}) + \boldsymbol{L}_h^{\mathrm{v}}(\dot{\boldsymbol{d}}_h^n - \dot{\boldsymbol{d}}_h^{n-1})\right\|_{0,\Sigma}^2\right), \quad (2.34)$$

for $n \geq 2$. Hence, by inserting this expression into (2.31), use Korn's inequality and summing over $m = 2, \ldots, n$ we get the estimate

$$E_h^n + \tau\sum_{m=2}^{n} D_h^m \lesssim E_h^1 + \frac{\tau^2}{2}\|\dot{\boldsymbol{d}}_h^1\|_{\mathrm{e}}^2 + \frac{\tau^2}{2\rho^{\mathrm{s}}\epsilon}\left\|\boldsymbol{L}_h^{\mathrm{e}}\boldsymbol{d}_h^1 + \boldsymbol{L}_h^{\mathrm{v}}\dot{\boldsymbol{d}}_h^1\right\|_{0,\Sigma}^2.$$

The last two terms, related to the initialization of the scheme (see Remark 2.3.3), can be bounded using (2.28) with $r = 0$, $n = 1$ and the additional control given by (2.32). This yields the estimate (2.28) for $n \geq 2$.
(iii) Second-order extrapolation ($r = 2$). For term T_1 in (2.31) we simply have

$$T_1 = \tau^2\left\|\dot{\boldsymbol{d}}_h^n - \dot{\boldsymbol{d}}_h^{n-1}\right\|_{\mathrm{e}}^2 + \frac{\tau}{2}\left(\tau\partial_\tau\left\|\dot{\boldsymbol{d}}_h^n - \dot{\boldsymbol{d}}_h^{n-1}\right\|_{\mathrm{v}}^2 + \left\|\dot{\boldsymbol{d}}_h^n - 2\dot{\boldsymbol{d}}_h^{n-1} + \dot{\boldsymbol{d}}_h^{n-2}\right\|_{\mathrm{v}}^2\right). \quad (2.35)$$

Term T_2 is split as follows

$$\begin{aligned} T_2 =& \underbrace{\frac{\tau^2}{\rho^{\mathrm{s}}\epsilon}\left(\boldsymbol{L}_h^{\mathrm{v}}\dot{\boldsymbol{d}}_h^n, \boldsymbol{L}_h^{\mathrm{e}}(\boldsymbol{d}_h^n - 2\boldsymbol{d}_h^{n-1} + \boldsymbol{d}_h^{n-2})\right)_\Sigma}_{T_{2,1}} \\ &+ \underbrace{\frac{\tau^2}{\rho^{\mathrm{s}}\epsilon}\left(\boldsymbol{L}_h^{\mathrm{e}}\boldsymbol{d}_h^n, \boldsymbol{L}_h^{\mathrm{e}}(\boldsymbol{d}_h^n - 2\boldsymbol{d}_h^{n-1} + \boldsymbol{d}_h^{n-2})\right)_\Sigma}_{T_{2,2}} \\ &+ \underbrace{\frac{\tau^2}{\rho^{\mathrm{s}}\epsilon}\left(\boldsymbol{L}_h^{\mathrm{e}}\boldsymbol{d}_h^n + \boldsymbol{L}_h^{\mathrm{v}}\dot{\boldsymbol{d}}_h^n, \boldsymbol{L}_h^{\mathrm{v}}(\dot{\boldsymbol{d}}_h^n - 2\dot{\boldsymbol{d}}_h^{n-1} + \dot{\boldsymbol{d}}_h^{n-2})\right)_\Sigma}_{T_{2,3}}, \end{aligned} \tag{2.36}$$

and we estimate each term separately. Using (2.3), for the first term we have

$$\begin{aligned} T_{2,1} =& \alpha_0\tau^3\big(\dot{\boldsymbol{d}}_h^n, \boldsymbol{L}_h^{\mathrm{e}}(\dot{\boldsymbol{d}}_h^n - \dot{\boldsymbol{d}}_h^{n-1})\big)_\Sigma + \frac{\alpha_1\tau^3}{\rho^{\mathrm{s}}\epsilon}\big(\boldsymbol{L}_h^{\mathrm{e}}\dot{\boldsymbol{d}}_h^n, \boldsymbol{L}_h^{\mathrm{e}}(\dot{\boldsymbol{d}}_h^n - \dot{\boldsymbol{d}}_h^{n-1})\big)_\Sigma \\ =& \frac{\alpha_0\tau^3}{2}\left(\tau\partial_\tau\|\dot{\boldsymbol{d}}_h^n\|_{\mathrm{e}}^2 + \|\dot{\boldsymbol{d}}_h^n - \dot{\boldsymbol{d}}_h^{n-1}\|_{\mathrm{e}}^2\right) \\ &+ \frac{\alpha_1\tau^3}{2\rho^{\mathrm{s}}\epsilon}\left(\tau\partial_\tau\|\boldsymbol{L}_h^{\mathrm{e}}\dot{\boldsymbol{d}}_h^n\|_{0,\Sigma}^2 + \|\boldsymbol{L}_h^{\mathrm{e}}(\dot{\boldsymbol{d}}_h^n - \dot{\boldsymbol{d}}_h^{n-1})\|_{0,\Sigma}^2\right). \end{aligned} \tag{2.37}$$

The second term is treated as in [45, Page 38] using (2.27), which yields

$$T_{2,2} \geq -\tau^6\frac{\omega_{\mathrm{e}}^6}{h^6}\|\boldsymbol{d}_h^n\|_{\mathrm{e}}^2 - \frac{\rho^{\mathrm{s}}\epsilon}{4}\|\dot{\boldsymbol{d}}_h^n - \dot{\boldsymbol{d}}_h^{n-1}\|_{0,\Sigma}^2, \tag{2.38}$$

where we have used the notation $\omega_{\mathrm{e}} \overset{\text{def}}{=} C_{\mathrm{inv}}\sqrt{\beta_{\mathrm{e}}/(\rho^{\mathrm{s}}\epsilon)}$. Alternatively, we could have used the positive term $\tau^2\big\|\dot{\boldsymbol{d}}_h^n - \dot{\boldsymbol{d}}_h^{n-1}\big\|_{\mathrm{e}}^2$ in T_1 and write

$$\begin{aligned} |T_{2,2}| &= \frac{\tau^2}{\rho^{\mathrm{s}}\epsilon}\left|a^{\mathrm{e}}\left(\boldsymbol{L}_h^{\mathrm{e}}\boldsymbol{d}_h^n, \dot{\boldsymbol{d}}_h^n - \dot{\boldsymbol{d}}_h^{n-1}\right)\right| \\ &\leq \frac{\tau^2}{\rho^{\mathrm{s}}\epsilon}\|\boldsymbol{L}_h^{\mathrm{e}}\boldsymbol{d}_h^n\|_{\mathrm{e}}\|\dot{\boldsymbol{d}}_h^n - \dot{\boldsymbol{d}}_h^{n-1}\|_{\mathrm{e}} \\ &\leq \frac{\tau^2}{\rho^{\mathrm{s}}\epsilon}\frac{\beta_{\mathrm{e}}C_{\mathrm{inv}}^2}{h^2}\|\boldsymbol{d}_h^n\|_{\mathrm{e}}\|\dot{\boldsymbol{d}}_h^n - \dot{\boldsymbol{d}}_h^{n-1}\|_{\mathrm{e}} \\ &\leq \frac{\tau^3\omega_{\mathrm{e}}^4}{h^4}\|\boldsymbol{d}_h^n\|_{\mathrm{e}}^2 + \frac{\tau}{4}\|\dot{\boldsymbol{d}}_h^n - \dot{\boldsymbol{d}}_h^{n-1}\|_{\mathrm{e}}^2. \end{aligned}$$

In both variants, the coefficient that appears before $\|\boldsymbol{d}_h^n\|_{\mathrm{e}}^2$ has to be bounded to apply the Gronwall lemma after summation over n. For the last term, we first use relation (2.3) to obtain

$$\begin{aligned} T_{2,3} &\geq -\frac{\tau^2}{\rho^{\mathrm{s}}\epsilon}\|\boldsymbol{L}_h^{\mathrm{e}}\boldsymbol{d}_h^n + \boldsymbol{L}_h^{\mathrm{v}}\dot{\boldsymbol{d}}_h^n\|_{\mathrm{v}}\|\dot{\boldsymbol{d}}_h^n - 2\dot{\boldsymbol{d}}_h^{n-1} + \dot{\boldsymbol{d}}_h^{n-2}\|_{\mathrm{v}} \\ &\geq -\frac{\tau^3}{(\rho^{\mathrm{s}}\epsilon)^2}\|\boldsymbol{L}_h^{\mathrm{e}}\boldsymbol{d}_h^n\|_{\mathrm{v}}^2 - \frac{\tau^3}{(\rho^{\mathrm{s}}\epsilon)^2}\|\boldsymbol{L}_h^{\mathrm{v}}\dot{\boldsymbol{d}}_h^n\|_{\mathrm{v}}^2 - \frac{\tau}{2}\|\dot{\boldsymbol{d}}_h^n - 2\dot{\boldsymbol{d}}_h^{n-1} + \dot{\boldsymbol{d}}_h^{n-2}\|_{\mathrm{v}}^2. \end{aligned}$$

Then, using (2.27), we get

$$T_{2,3} \geq -\frac{\tau^3\omega_{\mathrm{e}}^2}{h^2}\left(\alpha_0+\alpha_1\frac{\omega_{\mathrm{e}}^2}{h^2}\right)\|\boldsymbol{d}_h^n\|_{\mathrm{e}}^2-\tau^3\left(\alpha_0+\alpha_1\frac{\omega_{\mathrm{e}}^2}{h^2}\right)^2\|\dot{\boldsymbol{d}}_h^n\|_{\mathrm{v}}^2 - \frac{\tau}{2}\|\dot{\boldsymbol{d}}_h^n-2\dot{\boldsymbol{d}}_h^{n-1}+\dot{\boldsymbol{d}}_h^{n-2}\|_{\mathrm{v}}^2. \tag{2.39}$$

Finally, by collecting the estimates (2.38)-(2.39) and using the conditions $(2.30)_{1,2}$, we obtain

$$T_{2,2}+T_{2,3} \geq -\gamma\tau\|\boldsymbol{d}_h^n\|_{\mathrm{e}}^2-\delta^2\tau\|\dot{\boldsymbol{d}}_h^n\|_{\mathrm{v}}^2-\frac{\rho^{\mathrm{s}}\epsilon}{4}\|\dot{\boldsymbol{d}}_h^n-\dot{\boldsymbol{d}}_h^{n-1}\|_{0,\Sigma}^2 - \frac{\tau}{2}\|\dot{\boldsymbol{d}}_h^n-2\dot{\boldsymbol{d}}_h^{n-1}+\dot{\boldsymbol{d}}_h^{n-2}\|_{\mathrm{v}}^2. \tag{2.40}$$

We now proceed by inserting (2.35), (2.37) and (2.40) into (2.31), using Korn's inequality and summing over $m=3,\dots,n$. The last three negative terms of (2.40) are controlled by the physical and numerical dissipation provided by (2.31) and (2.35), while the first is handled via Lemma 2.4.1 (discrete Gronwall) with

$$\begin{cases} a_n = E_h^n + E_{\mathrm{cpl}}^n, \\ b_n = D_h^n + D_{\mathrm{cpl}}^n, \\ c_n = 0, \\ \gamma_n = \gamma, \\ B = a_2, \end{cases}$$

under the condition $(2.30)_3$ and with

$$\begin{cases} E_{\mathrm{cpl}}^n \overset{\mathrm{def}}{=} \dfrac{\tau}{2}\|\dot{\boldsymbol{d}}_h^n-\dot{\boldsymbol{d}}_h^{n-1}\|_{\mathrm{v}}^2+\dfrac{\alpha_0\tau^3}{2}\|\dot{\boldsymbol{d}}_h^n\|_{\mathrm{e}}^2+\dfrac{\alpha_1\tau^3}{2\rho^{\mathrm{s}}\epsilon}\|\boldsymbol{L}_h^{\mathrm{e}}\dot{\boldsymbol{d}}_h^n\|_{0,\Sigma}^2, \\ D_{\mathrm{cpl}}^n \overset{\mathrm{def}}{=} \tau\|\dot{\boldsymbol{d}}_h^n-\dot{\boldsymbol{d}}_h^{n-1}\|_{\mathrm{e}}^2+\dfrac{\alpha_0\tau^2}{2}\|\dot{\boldsymbol{d}}_h^n-\dot{\boldsymbol{d}}_h^{n-1}\|_{\mathrm{e}}^2+\dfrac{\alpha_1\tau^2}{2\rho^{\mathrm{s}}\epsilon}\|\boldsymbol{L}_h^{\mathrm{e}}(\dot{\boldsymbol{d}}_h^n-\dot{\boldsymbol{d}}_h^{n-1})\|_{0,\Sigma}^2. \end{cases}$$

This yields the bound

$$E_h^n+\tau\sum_{m=3}^{n}D_h^m \lesssim \exp\left(\frac{t_n\gamma}{1-\tau\gamma}\right)\left(E_h^2+\tau\|\dot{\boldsymbol{d}}_h^2-\dot{\boldsymbol{d}}_h^1\|_{\mathrm{v}}^2+\alpha_0\tau^3\|\dot{\boldsymbol{d}}_h^2\|_{\mathrm{e}}^2 + \frac{\alpha_1\tau^3}{\rho^{\mathrm{s}}\epsilon}\|\boldsymbol{L}_h^{\mathrm{e}}\dot{\boldsymbol{d}}_h^2\|_{0,\Sigma}^2\right).$$

The estimate (2.29) then follows by using the energy estimate (2.28) with $r=1$ and $n=2$, the additional control provided by (2.33) and (2.34), and the stability condition (2.30).

2.5 Iterative partitioned solution of implicit coupling

Algorithm 2.1 can also be interpreted as a single iteration (with appropriate initializations) of a Robin-Neumann method for the partitioned solution of the following implicit coupling scheme:

$$\begin{cases} \rho^{\mathrm{f}}\partial_\tau \boldsymbol{u}^n - \mathbf{div}\boldsymbol{\sigma}(\boldsymbol{u}^n, p^n) = \mathbf{0} & \text{in} \quad \Omega, \\ \mathrm{div}\boldsymbol{u}^n = 0 & \text{in} \quad \Omega, \\ \boldsymbol{u}^n = \mathbf{0} & \text{on} \quad \Gamma^{\mathrm{d}}, \\ \boldsymbol{\sigma}(\boldsymbol{u}^n, p^n)\boldsymbol{n} = \boldsymbol{h} & \text{on} \quad \Gamma^{\mathrm{n}}, \\ \boldsymbol{u}^n = \dot{\boldsymbol{d}}^n & \text{on} \quad \Sigma. \end{cases} \tag{2.41}$$

$$\begin{cases} \rho^{\mathrm{s}}\epsilon\partial_\tau \dot{\boldsymbol{d}}^n + \boldsymbol{L}^{\mathrm{e}}\boldsymbol{d}^n + \boldsymbol{L}^{\mathrm{v}}\dot{\boldsymbol{d}}^n = -\boldsymbol{\sigma}(\boldsymbol{u}^n, p^n)\boldsymbol{n} & \text{on} \quad \Sigma, \\ \dot{\boldsymbol{d}}^n = \partial_\tau \boldsymbol{d}^n & \text{on} \quad \Sigma, \\ \boldsymbol{d}^n = \mathbf{0} & \text{on} \quad \partial\Sigma. \end{cases} \tag{2.42}$$

The corresponding Robin-Neumann iterations are detailed in Algorithm 2.3, where $\dot{\boldsymbol{d}}_0$ and $\boldsymbol{\sigma}(\boldsymbol{u}_0, p_0)\boldsymbol{n}$ are initialized, respectively, with $\dot{\boldsymbol{d}}^{n-1} + \tau\partial_\tau \dot{\boldsymbol{d}}^\star$ and $\boldsymbol{\sigma}(\boldsymbol{u}^\star, p^\star)\boldsymbol{n}$ for $n > r$ (see Table 2.1).

Algorithm 2.3 Partitioned Robin-Neumann iterations

1. Initialize $\dot{\boldsymbol{d}}_0$ and $\boldsymbol{\sigma}(\boldsymbol{u}_0, p_0)\boldsymbol{n}$.
2. For $k = 1, \ldots$ until convergence:
   - Fluid step:

$$\begin{cases} \dfrac{\rho^{\mathrm{f}}}{\tau}\big(\boldsymbol{u}_k - \boldsymbol{u}^{n-1}\big) - \mathbf{div}\boldsymbol{\sigma}(\boldsymbol{u}_k, p_k) = \mathbf{0} & \text{in} \quad \Omega, \\ \mathrm{div}\,\boldsymbol{u}_k = 0 & \text{in} \quad \Omega, \\ \boldsymbol{u}_k = \mathbf{0} & \text{on} \quad \Gamma^{\mathrm{d}}, \\ \boldsymbol{\sigma}(\boldsymbol{u}_k, p_k)\boldsymbol{n} = \boldsymbol{h} & \text{on} \quad \Gamma^{\mathrm{n}}, \\ \boldsymbol{\sigma}(\boldsymbol{u}_k, p_k)\boldsymbol{n} + \dfrac{\rho^{\mathrm{s}}\epsilon}{\tau}\boldsymbol{u}_k = \dfrac{\rho^{\mathrm{s}}\epsilon}{\tau}\dot{\boldsymbol{d}}_{k-1} + \boldsymbol{\sigma}(\boldsymbol{u}_{k-1}, p_{k-1})\boldsymbol{n} & \text{on} \quad \Sigma. \end{cases} \tag{2.43}$$

   - Solid step:

$$\begin{cases} \dfrac{\rho^{\mathrm{s}}\epsilon}{\tau}\big(\dot{\boldsymbol{d}}_k - \dot{\boldsymbol{d}}^{n-1}\big) + \boldsymbol{L}^{\mathrm{e}}\boldsymbol{d}_k + \boldsymbol{L}^{\mathrm{v}}\dot{\boldsymbol{d}}_k = -\boldsymbol{\sigma}(\boldsymbol{u}_k, p_k)\boldsymbol{n} & \text{on} \quad \Sigma, \\ \dot{\boldsymbol{d}}_k = \dfrac{1}{\tau}\big(\boldsymbol{d}_k - \boldsymbol{d}^{n-1}\big). \end{cases} \tag{2.44}$$

This kind of iterative solution procedures has been introduced in [3], as added-mass free alternatives to the standard Dirichlet-Neumann iterations. It should be noted that

the Robin coefficient $\rho^{\mathrm{s}}\epsilon/\tau$ involved in (2.43), has no free parameter and differs from the one originally proposed in [3]. In fact, only inertial effects are included since Algorithm 2.1 explicitly treats the whole viscoelastic contribution of the structure, as usual in explicit coupling schemes.

As we shall see in Section 2.5.1, the energy stability analysis of Algorithm 2.1 yields a new result on the convergence properties of Algorithm 2.3.

2.5.1 Convergence of the iterative solution procedure

A salient feature the arguments involved in the energy based stability analysis of Section 2.4.4 is that they can be reshaped to prove the convergence of Algorithm 2.3 towards the implicit coupling solution (2.41)-(2.42). This result is stated in the next theorem where, for the sake of simplicity, we have considered only the time semi-discrete version of the methods.

Theorem 2.5.1. *For $n \geq 1$, let $(\boldsymbol{u}^n, p^n, \dot{\boldsymbol{d}}^n, \boldsymbol{d}^n)$ be given by the implicit scheme (2.41)-(2.42) and $\{(\boldsymbol{u}_k, p_k, \dot{\boldsymbol{d}}_k, \boldsymbol{d}_k)\}_{k\geq 1}$ be the sequence of approximations given by Algorithm 2.3. Then, the following estimate holds*

$$\sum_{k=1}^{\infty}\Big(\rho^{\mathrm{f}}\|\boldsymbol{u}_k-\boldsymbol{u}^n\|_{0,\Omega}^2+\rho^{\mathrm{s}}\epsilon\|\dot{\boldsymbol{d}}_k-\dot{\boldsymbol{d}}^n\|_{0,\Sigma}^2+\|\boldsymbol{d}_k-\boldsymbol{d}^n\|_{\mathrm{e}}^2\Big)$$
$$\lesssim \|\boldsymbol{d}_0-\boldsymbol{d}^n\|_{\mathrm{e}}^2+\tau\|\dot{\boldsymbol{d}}_0-\dot{\boldsymbol{d}}^n\|_{\mathrm{v}}^2+\frac{\tau^2}{\rho^{\mathrm{s}}\epsilon}\|\boldsymbol{L}^{\mathrm{e}}(\boldsymbol{d}_0-\boldsymbol{d}^n)+\boldsymbol{L}^{\mathrm{v}}(\dot{\boldsymbol{d}}_0-\dot{\boldsymbol{d}}^n)\|_{0,\Sigma}^2. \quad (2.45)$$

In particular, we have

$$\lim_{k\to\infty}\Big(\big(\rho^{\mathrm{f}}\big)^{\frac{1}{2}}\|\boldsymbol{u}_k-\boldsymbol{u}^n\|_{0,\Omega}+(\rho^{\mathrm{s}}\epsilon)^{\frac{1}{2}}\|\dot{\boldsymbol{d}}_k-\dot{\boldsymbol{d}}^n\|_{0,\Sigma}+\|\boldsymbol{d}_k-\boldsymbol{d}^n\|_{\mathrm{e}}\Big)=0.$$

Proof. For $k\geq 1$, we consider $(2.44)_1$ at the $(k-1)$-th iteration and add the resulting expression to $(2.43)_5$. This yields

$$\frac{\rho^{\mathrm{s}}\epsilon}{\tau}\big(\boldsymbol{u}_k-\dot{\boldsymbol{d}}^{n-1}\big)+\boldsymbol{L}^{\mathrm{e}}\boldsymbol{d}_{k-1}+\boldsymbol{L}^{\mathrm{v}}\dot{\boldsymbol{d}}_{k-1}=-\boldsymbol{\sigma}(\boldsymbol{u}_k,p_k)\boldsymbol{n}\quad\text{on}\quad\Sigma.$$

Hence, by combining this relation with $(2.44)_1$ we get

$$\boldsymbol{u}_k=\dot{\boldsymbol{d}}_k+\frac{\tau}{\rho^{\mathrm{s}}\epsilon}\Big(\boldsymbol{L}^{\mathrm{e}}(\boldsymbol{d}_k-\boldsymbol{d}_{k-1})+\boldsymbol{L}^{\mathrm{v}}(\dot{\boldsymbol{d}}_k-\dot{\boldsymbol{d}}_{k-1})\Big)\quad\text{on}\quad\Sigma. \quad (2.46)$$

It should be noted that $\boldsymbol{d}_0$ is defined through $(2.44)_1$, with $k=0$, in terms of $\dot{\boldsymbol{d}}_0$ and $\boldsymbol{\sigma}(\boldsymbol{u}_0,p_0)\boldsymbol{n}$. We now introduce the following errors between the k-th iteration of Algorithm 2.3 and the n-th step of (2.41)-(2.42):

$$\boldsymbol{e}_k^{\boldsymbol{u}}\overset{\text{def}}{=}\boldsymbol{u}_k-\boldsymbol{u}^n,\quad e_k^{p}\overset{\text{def}}{=}p_k-p^n,\quad \boldsymbol{e}_k^{\dot{\boldsymbol{d}}}\overset{\text{def}}{=}\dot{\boldsymbol{d}}_k-\dot{\boldsymbol{d}}^n,\quad \boldsymbol{e}_k^{\boldsymbol{d}}\overset{\text{def}}{=}\boldsymbol{d}_k-\boldsymbol{d}^n. \quad (2.47)$$

By subtracting (2.41)-(2.42) from $(2.43)_{1-4}$, (2.44) and (2.46), we get the following system of equations for the errors:

$$\begin{cases} \dfrac{\rho^{\mathrm{f}}}{\tau}\boldsymbol{e}_k^{\boldsymbol{u}} - \mathbf{div}\boldsymbol{\sigma}(\boldsymbol{e}_k^{\boldsymbol{u}}, e_k^p) = \mathbf{0} \quad \text{in} \quad \Omega, \\ \mathrm{div}\boldsymbol{e}_k^{\boldsymbol{u}} = 0 \quad \text{in} \quad \Omega, \\ \boldsymbol{e}_k^{\boldsymbol{u}} = \mathbf{0} \quad \text{on} \quad \Gamma^{\mathrm{d}}, \\ \boldsymbol{\sigma}(\boldsymbol{e}_k^{\boldsymbol{u}}, e_k^p)\boldsymbol{n} = \mathbf{0} \quad \text{on} \quad \Gamma^{\mathrm{n}}, \\ \boldsymbol{e}_k^{\boldsymbol{u}} = \boldsymbol{e}_k^{\dot{\boldsymbol{d}}} + \dfrac{\tau}{\rho^{\mathrm{s}}\epsilon}\left(\boldsymbol{L}^{\mathrm{e}}(\boldsymbol{e}_k^{\boldsymbol{d}} - \boldsymbol{e}_{k-1}^{\boldsymbol{d}}) + \boldsymbol{L}^{\mathrm{v}}(\boldsymbol{e}_k^{\dot{\boldsymbol{d}}} - \boldsymbol{e}_{k-1}^{\dot{\boldsymbol{d}}})\right) \quad \text{on} \quad \Sigma, \end{cases} \tag{2.48}$$

$$\begin{cases} \dfrac{\rho^{\mathrm{s}}\epsilon}{\tau}\boldsymbol{e}_k^{\dot{\boldsymbol{d}}} + \boldsymbol{L}^{\mathrm{e}}\boldsymbol{e}_k^{\boldsymbol{d}} + \boldsymbol{L}^{\mathrm{v}}\boldsymbol{e}_k^{\dot{\boldsymbol{d}}} = -\boldsymbol{\sigma}(\boldsymbol{e}_k^{\boldsymbol{u}}, e_k^p)\boldsymbol{n} \quad \text{on} \quad \Sigma, \\ \boldsymbol{e}_k^{\dot{\boldsymbol{d}}} = \dfrac{1}{\tau}\boldsymbol{e}_k^{\boldsymbol{d}}. \end{cases} \tag{2.49}$$

We now proceed similarly to the proof of Theorem 2.4.1 with the first-order extrapolation. We first multiply $(2.48)_1$ by $\tau\boldsymbol{e}_k^{\boldsymbol{u}}$ and integrate by parts in Ω. Then we multiply $(2.49)_2$ by $\tau\boldsymbol{e}_k^{\boldsymbol{u}}|_\Sigma$ and integrate the resulting expression over Σ. By adding these two expressions and using $(2.49)_{1,3}$ we get

$$\begin{aligned} \rho^{\mathrm{f}}\|\boldsymbol{e}_k^{\boldsymbol{u}}\|_{0,\Omega}^2 + 2\mu\tau\|\boldsymbol{\epsilon}(\boldsymbol{e}_k^{\boldsymbol{u}})\|_{0,\Omega}^2 + \rho^{\mathrm{s}}\epsilon\|\boldsymbol{e}^{\dot{\boldsymbol{d}}_k}\|_{0,\Sigma}^2 + \|\boldsymbol{e}^{\boldsymbol{d}_k}\|_{\mathrm{e}}^2 + \tau\|\boldsymbol{e}^{\dot{\boldsymbol{d}}_k}\|_{\mathrm{v}}^2 \\ \underbrace{+ \tau\left(\boldsymbol{e}_k^{\dot{\boldsymbol{d}}}, \boldsymbol{L}^{\mathrm{e}}(\boldsymbol{e}_k^{\boldsymbol{d}} - \boldsymbol{e}_{k-1}^{\boldsymbol{d}}) + \boldsymbol{L}^{\mathrm{v}}(\boldsymbol{e}_k^{\dot{\boldsymbol{d}}} - \boldsymbol{e}_{k-1}^{\dot{\boldsymbol{d}}})\right)_\Sigma}_{T_1} \\ \underbrace{+ \frac{\tau^2}{\rho^{\mathrm{s}}\epsilon}\left(\boldsymbol{L}^{\mathrm{e}}\boldsymbol{e}_k^{\boldsymbol{d}} + \boldsymbol{L}^{\mathrm{v}}\boldsymbol{e}_k^{\dot{\boldsymbol{d}}}, \boldsymbol{L}^{\mathrm{e}}(\boldsymbol{e}_k^{\boldsymbol{d}} - \boldsymbol{e}_{k-1}^{\boldsymbol{d}}) + \boldsymbol{L}^{\mathrm{v}}(\boldsymbol{e}_k^{\dot{\boldsymbol{d}}} - \boldsymbol{e}_{k-1}^{\dot{\boldsymbol{d}}})\right)_\Sigma}_{T_2} = 0, \end{aligned} \tag{2.50}$$

where it only remains to estimate the terms T_1 and T_2. For the first term, using $(2.49)_3$, we have

$$T_1 = \frac{1}{2}\left(\|\boldsymbol{e}_k^{\boldsymbol{d}}\|_{\mathrm{e}}^2 - \|\boldsymbol{e}_{k-1}^{\boldsymbol{d}}\|_{\mathrm{e}}^2 + \|\boldsymbol{e}_k^{\boldsymbol{d}} - \boldsymbol{e}_{k-1}^{\boldsymbol{d}}\|_{\mathrm{e}}^2\right) + \frac{\tau}{2}\left(\|\boldsymbol{e}_k^{\dot{\boldsymbol{d}}}\|_{\mathrm{v}}^2 - \|\boldsymbol{e}_{k-1}^{\dot{\boldsymbol{d}}}\|_{\mathrm{v}}^2 + \|\boldsymbol{e}_k^{\dot{\boldsymbol{d}}} - \boldsymbol{e}_{k-1}^{\dot{\boldsymbol{d}}}\|_{\mathrm{v}}^2\right),$$

while, for the second, we get

$$\begin{aligned} T_2 = &\frac{\tau^2}{2\rho^{\mathrm{s}}\epsilon}\left(\|\boldsymbol{L}^{\mathrm{e}}\boldsymbol{e}_k^{\boldsymbol{d}} + \boldsymbol{L}^{\mathrm{v}}\boldsymbol{e}_k^{\dot{\boldsymbol{d}}}\|_{0,\Sigma}^2 - \|\boldsymbol{L}^{\mathrm{e}}\boldsymbol{e}_{k-1}^{\boldsymbol{d}} + \boldsymbol{L}^{\mathrm{v}}\boldsymbol{e}_{k-1}^{\dot{\boldsymbol{d}}}\|_{0,\Sigma}^2\right) \\ &+ \frac{\tau^2}{2\rho^{\mathrm{s}}\epsilon}\|\boldsymbol{L}^{\mathrm{e}}(\boldsymbol{e}_k^{\boldsymbol{d}} - \boldsymbol{e}_{k-1}^{\boldsymbol{d}}) + \boldsymbol{L}^{\mathrm{v}}(\boldsymbol{e}_k^{\dot{\boldsymbol{d}}} - \boldsymbol{e}_{k-1}^{\dot{\boldsymbol{d}}})\|_{0,\Sigma}^2 \end{aligned}$$

The estimate (2.45) follows by inserting these last two identities into (2.50) and after summation over $k = 1, \ldots, \infty$. □

To the best of our knowledge, the result stated in Theorem 2.5.1 is the first which guarantees the convergence of a Robin-Neumann iterative procedure towards the implicit coupling solution (2.41)-(2.42). In fact, so far the convergence of these methods has been addressed in further simplified models using modal analysis (see, e.g., [3]). A second valuable consequence of Theorem 2.5.1 is that the pure inertial character of the Robin coefficient $\rho^{\mathrm{s}}\epsilon/\tau$ is enough to guarantee the convergence of the iterations.

2.6 A priori error estimates

This section is devoted to the convergence analysis of Algorithm 2.2 in a linear framework.

2.6.1 Preliminaries and main result

In what follows, we shall make use of the Ritz-projector

$$\boldsymbol{\pi}_h^{\mathrm{e}} : \boldsymbol{W} \to \boldsymbol{W}_h,$$

associated to the inner-product a^{e} given by (2.17). Thus, for all $\boldsymbol{w} \in \boldsymbol{W}$, $\boldsymbol{\pi}_h^{\mathrm{e}}\boldsymbol{w} \in \boldsymbol{W}_h$ is defined by the relation

$$a^{\mathrm{e}}(\boldsymbol{w} - \boldsymbol{\pi}_h^{\mathrm{e}}\boldsymbol{w}, \boldsymbol{w}_h) = 0 \tag{2.51}$$

for all $\boldsymbol{w}_h \in \boldsymbol{W}_h$. We assume that the following error estimate holds

$$\|\boldsymbol{w} - \boldsymbol{\pi}_h^{\mathrm{e}}\boldsymbol{w}\|_{0,\Sigma} + h\|\boldsymbol{w} - \boldsymbol{\pi}_h^{\mathrm{e}}\boldsymbol{w}\|_{1,\Sigma} \lesssim h^{k+1}\|\boldsymbol{w}\|_{k+1,\Sigma} \tag{2.52}$$

for all $\boldsymbol{w} \in \left[H^{k+1}(\Sigma)\right]^d \cap \boldsymbol{W}$. For the fluid velocity, we consider the Stokes-like operator $(\boldsymbol{P}_h, R_h) : \boldsymbol{V} \to \boldsymbol{V}_h \times Q_h$ defined, for all $\boldsymbol{v} \in \boldsymbol{V}$, by

$$\begin{cases} \boldsymbol{P}_h\boldsymbol{v}|_\Sigma = \boldsymbol{\pi}_h^{\mathrm{e}}\left(\boldsymbol{v}|_\Sigma\right), \\ a(\boldsymbol{P}_h\boldsymbol{v}, \boldsymbol{v}_h) + b(R_h\boldsymbol{v}, \boldsymbol{v}_h) = a(\boldsymbol{v}, \boldsymbol{v}_h) \quad \forall \boldsymbol{v}_h \in \boldsymbol{V}_{\Sigma,h}, \\ b(q_h, \boldsymbol{P}_h\boldsymbol{v}) = s_h(q_h, R_h\boldsymbol{v}) \quad \forall q_h \in Q_h. \end{cases} \tag{2.53}$$

Remark 2.6.1. *Note that the fluid and solid velocity projectors match at the interface. This point is fundamental for the convergence analysis below since it guarantees that* (2.68)*, that is, the discrete error counterpart of* (2.25) *holds. The choice of a Ritz-projector $\boldsymbol{\pi}_h^{\mathrm{e}}$ for the solid velocity is also a critical point. It is motivated by the relation* (2.67) *which avoids the need of a control on $\|\boldsymbol{u}_h^n\|_{\mathrm{v}}$. In fact, since the solid damping is explicitly coupled with the fluid, we have control only on $\|\dot{\boldsymbol{d}}_h^n\|_{\mathrm{v}}$.*

We assume that the following approximation properties hold for $\boldsymbol{P}_h$:

$$\begin{aligned} &\|\boldsymbol{v} - \boldsymbol{P}_h\boldsymbol{v}\|_{\boldsymbol{V}} + |R_h\boldsymbol{v}|_{s_h} \lesssim h^k\mu^{\frac{1}{2}}\left(\|\boldsymbol{v}\|_{k+1,\Omega} + h^{\frac{1}{2}}\|\boldsymbol{v}\|_{k+1,\Sigma}\right), \\ &\|\boldsymbol{v} - \boldsymbol{P}_h\boldsymbol{v}\|_{0,\Omega} \le c_\mu h^{k+1}\left(\|\boldsymbol{v}\|_{k+1,\Omega} + h^{\frac{1}{2}}\|\boldsymbol{v}\|_{k+1,\Sigma}\right), \end{aligned} \tag{2.54}$$

for all $\boldsymbol{v} \in [H^{k+1}(\Omega)]^d$ with $\boldsymbol{v}|_\Sigma \in [H^{k+1}(\Sigma)]^d$ and $\operatorname{div}\boldsymbol{v} = 0$.

Remark 2.6.2. *A similar estimate to* (2.54) *was proved in [45, Lemma 3] with the Lagrange interpolant* $\boldsymbol{I}_h(\boldsymbol{v}|_\Sigma)$ *playing the role of the Ritz-projection* $\boldsymbol{\pi}_h^{\mathrm{e}}(\boldsymbol{v}|_\Sigma)$ *in* (2.53). *Note that a purely elastic structure is considered in [45]. In the present setting, the estimate* (2.54) *follows from the general approximation result of [45, Lemma 5] which yields*

$$\|\boldsymbol{v}-\boldsymbol{P}_h\boldsymbol{v}\|_{\boldsymbol{V}}+|R_h\boldsymbol{v}|_{s_h}\lesssim\mu^{\frac{1}{2}}h^k\|\boldsymbol{v}\|_{k+1,\Omega}+\mu^{\frac{1}{2}}h^{\frac{d-2}{2}}\|(\boldsymbol{I}_h-\boldsymbol{\pi}_h^{\mathrm{e}})\boldsymbol{v}\|_{\infty,\Sigma}.$$

Hence, using an inverse inequality (see, e.g., [12, Theorem 4.5.11]), we have

$$\begin{aligned}\|\boldsymbol{v}-\boldsymbol{P}_h\boldsymbol{v}\|_{\boldsymbol{V}}+|R_h\boldsymbol{v}|_{s_h}&\lesssim\mu^{\frac{1}{2}}h^k\|\boldsymbol{v}\|_{k+1,\Omega}+\mu^{\frac{1}{2}}h^{\frac{1}{2}}\|(\boldsymbol{I}_h-\boldsymbol{\pi}_h^{\mathrm{e}})\boldsymbol{v}\|_{1,\Sigma}\\&\lesssim\mu^{\frac{1}{2}}h^k\|\boldsymbol{v}\|_{k+1,\Omega}+\mu^{\frac{1}{2}}h^{\frac{1}{2}}\|\boldsymbol{I}_h\boldsymbol{v}-\boldsymbol{v}\|_{1,\Sigma}+\mu^{\frac{1}{2}}h^{\frac{1}{2}}\|\boldsymbol{v}-\boldsymbol{\pi}_h^{\mathrm{e}}\boldsymbol{v}\|_{1,\Sigma}.\end{aligned}$$

We can then retrieve $(2.54)_1$ *from standard approximation theory and* (2.52). *At last, estimate follows* $(2.54)_2$ *by an Aubin-Nitsche argument (see, e.g., [45, Lemma 6]).*

Remark 2.6.3. *The estimates* (2.54) *hold for inf-sup compatible velocity/pressure approximations (with* $s_h=0$*) or under suitable assumptions on the symmetric stabilization operator* s_h *(see [45, Section 3.1.1]). In particular, the consistency of* s_h *is said to be of order* $\tilde{l}\in\{l,l+1\}$ *if there exits a projection operator* $\Pi_h:Q\to Q_h$ *such that*

$$\begin{aligned}|\Pi_h q|_{s_h}\lesssim&\mu^{-\frac{1}{2}}h^{\tilde{l}}\|q\|_{\tilde{l},\Omega}\quad\forall q\in H^{\tilde{l}}(\Omega),\\\|q-\Pi_h q\|_Q\lesssim&\mu^{-\frac{1}{2}}h^{l+1}\|q\|_{l+1,\Omega}\quad\forall q\in H^{l+1}(\Omega).\end{aligned}\tag{2.55}$$

Examples of such stabilization operators are discussed in [17]. We can mention, for instance, the methods reported in [29, 8, 23] which are optimal for arbitrary polynomial order, or the method introduced in [13] which is optimal for piece-wise affine approximations. ◇

We assume that the exact solution of problem (2.19) has the following regularity, for a given final time $T\geq\tau$:

$$\begin{aligned}\boldsymbol{u}&\in\big[H^1\big(0,T;H^{k+1}(\Omega)\big)\big]^d,\quad\boldsymbol{u}|_\Sigma\in\big[H^1\big(0,T;H^{k+1}(\Sigma)\big)\big]^d,\\\partial_{tt}\boldsymbol{u}&\in\big[L^2\big(0,T;L^2(\Omega)\big)\big]^d,\qquad\partial_{tt}\boldsymbol{u}|_\Sigma\in\big[L^2\big(0,T;L^2(\Sigma)\big)\big]^d,\\p&\in C^0\big([0,T];H^{\tilde{l}}(\Omega)\big),\end{aligned}\tag{2.56}$$

and

$$\boldsymbol{L}^{\mathrm{e}}\boldsymbol{d}+\boldsymbol{L}^{\mathrm{v}}\dot{\boldsymbol{d}}\in\begin{cases}\big[C^0\big([0,T];L^2(\Sigma)\big)\big]^d&\text{if}\quad r=0,\\\big[H^1\big(0,T;L^2(\Sigma)\big)\big]^d&\text{if}\quad r=1,\\\big[H^2\big(0,T;L^2(\Sigma)\big)\big]^d&\text{if}\quad r=2.\end{cases}\tag{2.57}$$

In (2.56), the symbol $\tilde{l}\in\{l,l+1\}$ denotes the consistency order of s_h (see Remark 2.6.3). We take $\tilde{l}=l$ in the case of inf-sup compatible velocity/pressure approximations.

At last, we define the energy-norm of the error, at the time step t^n, as

$$\mathcal{E}_h^n \stackrel{\text{def}}{=} (\rho^{\text{f}})^{\frac{1}{2}} \|\boldsymbol{u}(t_n) - \boldsymbol{u}_h^n\|_{0,\Omega} + \left(\tau \sum_{m=r+1}^{n} \|\boldsymbol{u}(t^m) - \boldsymbol{u}_h^m\|_{\boldsymbol{V}}^2 \right)^{\frac{1}{2}} + \left(\tau \sum_{m=r+1}^{n} |p_h^m|_{s_h}^2 \right)^{\frac{1}{2}}$$
$$+ (\rho^{\text{s}}\epsilon)^{\frac{1}{2}} \|\dot{\boldsymbol{d}}(t_n) - \dot{\boldsymbol{d}}_h^n\|_{0,\Sigma} + \|\boldsymbol{d}(t_n) - \boldsymbol{d}_h^n\|_{\text{e}} + \left(\tau \sum_{m=r+1}^{n} \|\dot{\boldsymbol{d}}(t^m) - \dot{\boldsymbol{d}}_h^m\|_{\text{v}}^2 \right)^{\frac{1}{2}},$$

for $n > r$. The following result states an priori error estimate for the fully discrete explicit Robin-Neumann schemes introduced in Section 2.4.2.

Theorem 2.6.1. *Let $(\boldsymbol{u}, p, \boldsymbol{d}, \dot{\boldsymbol{d}})$ be the solution of the coupled problem (2.19) and $\{(\boldsymbol{u}_h^n, p_h^n, \boldsymbol{d}_h^n, \dot{\boldsymbol{d}}_h^n)\}_{n>r}$ be the discrete solution given by Algorithm 2.2 with initial data $\left(\boldsymbol{u}_h^0, \boldsymbol{d}_h^0, \dot{\boldsymbol{d}}_h^0\right) = \left(\boldsymbol{P}_h \boldsymbol{u}^0, \boldsymbol{\pi}_h^{\text{e}} \boldsymbol{d}^0, \boldsymbol{\pi}_h^{\text{v}} \dot{\boldsymbol{d}}^0\right)$. The initialization procedure of Remark 2.3.3 is considered for the schemes with with extrapolation ($r \geq 1$). Suppose that (2.52)-(2.55) hold and that the exact solution has the regularity (2.56)-(2.57). For the scheme with $r = 2$ we assume, in addition, that (2.3) and the stability condition (2.30) hold. Then, we have the following error estimates, for $n > r$ such that $n\tau < T$:*

$$\mathcal{E}_h^n \lesssim c_1^\star h^k + c_2^\star h^{\tilde{l}} + c_3^\star \tau + c_4^\star \begin{cases} \tau^{\frac{1}{2}} & \text{if} \quad r = 0, \\ \tau & \text{if} \quad r = 1, \\ \tau^2 & \text{if} \quad r = 2. \end{cases} \tag{2.58}$$

Here, the symbols $\{c_i^\star\}_{i=1}^4$ denote positive constants independent of h and τ, but which depend on the physical parameters and on the regularity of $(\boldsymbol{u}, p, \boldsymbol{d}, \dot{\boldsymbol{d}})$.

Proof. See Section 2.6.2. □

Theorem 2.6.1 shows that, for regular enough solutions, the proposed explicit Robin-Neumann schemes converge to the solution of (2.1)-(2.2). The last term of (2.58) represents the truncation error introduced by the Robin-Neumann splitting, that is, the time-consistency of the kinematic perturbation in (2.25). For the variant without extrapolation, the error estimate (2.58) predicts a sub-optimal $\mathcal{O}(\tau^{\frac{1}{2}})$ time-convergence rate in the energy-norm. This is due to the low-order consistency of the perturbation in the case $r = 0$. On the contrary, for the variants with extrapolation, the consistency of the perturbations scale as $\mathcal{O}(\tau)$ and $\mathcal{O}(\tau^2)$, respectively. An overall optimal convergence-rate $\mathcal{O}(h^k + h^{\tilde{l}} + \tau)$ is hence recovered.

In view of Theorems 2.4.1 and 2.6.1, the explicit Robin-Neumann scheme with $r = 1$ simultaneously yields stability and optimal accuracy with no restrictions on the discretization parameters nor on the polynomial order.

Remark 2.6.4. *Theorem 4.3.3 generalizes the error estimates reported in [45, Section 5] to the case $\boldsymbol{L}^{\text{v}} \neq 0$.* ◇

2.6.2 Proof of Theorem 4.3.3

We proceed by extending the arguments reported in [45, Section 5]. The error estimate (2.58) is based on the following decomposition of the error

$$\begin{aligned}
\boldsymbol{u}(t_n) - \boldsymbol{u}_h^n &= \underbrace{\boldsymbol{u}(t_n) - \boldsymbol{P}_h\boldsymbol{u}(t_n)}_{\boldsymbol{\theta}_\pi^n} + \underbrace{\boldsymbol{P}_h\boldsymbol{u}(t_n) - \boldsymbol{u}_h^n}_{\boldsymbol{\theta}_h^n}, \\
p(t_n) - p_h^n &= \underbrace{p(t_n) - \Pi_h p(t_n)}_{y_\pi^n} + \underbrace{\Pi_h p(t_n) - p_h^n}_{y_h^n}, \\
\boldsymbol{d}(t_n) - \boldsymbol{d}_h^n &= \underbrace{\boldsymbol{d}(t_n) - \boldsymbol{\pi}_h^{\mathrm{e}}\boldsymbol{d}(t_n)}_{\boldsymbol{\xi}_\pi^n} + \underbrace{\boldsymbol{\pi}_h^{\mathrm{e}}\boldsymbol{d}(t_n) - \boldsymbol{d}_h^n}_{\boldsymbol{\xi}_h^n}, \\
\dot{\boldsymbol{d}}(t_n) - \dot{\boldsymbol{d}}_h^n &= \underbrace{\dot{\boldsymbol{d}}(t_n) - \boldsymbol{\pi}_h^{\mathrm{e}}\dot{\boldsymbol{d}}(t_n)}_{\dot{\boldsymbol{\xi}}_\pi^n} + \underbrace{\boldsymbol{\pi}_h^{\mathrm{e}}\dot{\boldsymbol{d}}(t_n) - \dot{\boldsymbol{d}}_h^n}_{\dot{\boldsymbol{\xi}}_h^n},
\end{aligned} \tag{2.59}$$

where the projection operators $\boldsymbol{P}_h$, Π_h and $\boldsymbol{\pi}_h^{\mathrm{e}}$ are defined in Section 2.6.1. Hence, owing to (2.52)-(2.55), it only remains to estimate the discrete contributions $\boldsymbol{\theta}_h^n$, y_h^n, $\boldsymbol{\xi}_h^n$ and $\dot{\boldsymbol{\xi}}_h^n$. An a priori bound for these terms is stated in Lemma 2.6.1 below, with the energy-norm of the discrete error being defined by

$$\begin{aligned}
\mathcal{Z}_h^n \overset{\text{def}}{=} &(\rho^{\mathrm{f}})^{\frac{1}{2}}\|\boldsymbol{\theta}_h^n\|_{0,\Omega} + \left(\tau\sum_{m=r+1}^{n}\|\boldsymbol{\theta}_h^m\|_{\boldsymbol{V}}^2\right)^{\frac{1}{2}} + \left(\tau\sum_{m=r+1}^{n}|y_h^m|_{s_h}^2\right)^{\frac{1}{2}} \\
&+ (\rho^{\mathrm{s}}\epsilon)^{\frac{1}{2}}\|\dot{\boldsymbol{\xi}}_h^n\|_{0,\Sigma} + \|\boldsymbol{\xi}_h^n\|_{\mathrm{e}} + \left(\tau\sum_{m=r+1}^{n}\|\dot{\boldsymbol{\xi}}_h^m\|_{\mathrm{v}}^2\right)^{\frac{1}{2}},
\end{aligned}$$

for $n > r$.

Lemma 2.6.1. *Under the assumptions of Theorem 2.6.1, the following error estimates hold:*

- *Without extrapolation ($r = 0$):*

$$\mathcal{Z}_h^n \lesssim c_1 h^k + c_2 h^{\tilde{l}} + c_3\tau + c_4\tau^{\frac{1}{2}}\left(\frac{T}{\rho^{\mathrm{s}}\epsilon}\right)^{\frac{1}{2}}\|\boldsymbol{L}^{\mathrm{e}}\boldsymbol{d} + \boldsymbol{L}^{\mathrm{v}}\dot{\boldsymbol{d}}\|_{L^\infty(0,T;L^2(\Sigma))}, \tag{2.60}$$

  for $n \geq 1$.

- *First-order extrapolation ($r = 1$):*

$$\mathcal{Z}_h^n \lesssim c_1 h^k + c_2 h^{\tilde{l}} + c_3\tau + c_4\tau\left(\frac{T}{\rho^{\mathrm{s}}\epsilon}\right)^{\frac{1}{2}}\|\partial_t(\boldsymbol{L}^{\mathrm{e}}\boldsymbol{d} + \boldsymbol{L}^{\mathrm{v}}\dot{\boldsymbol{d}})\|_{L^2(0,T;L^2(\Sigma))}, \tag{2.61}$$

  for $n \geq 2$.

- *Second-order extrapolation ($r = 2$):*

$$\mathcal{Z}_h^n \lesssim c_5 h^k + c_6 h^{\tilde{l}} + c_7 \tau + c_8 \tau^2 \left(\frac{T}{\rho^{\mathrm{s}}\epsilon}\right)^{\frac{1}{2}} \|\partial_{tt}(\boldsymbol{L}^{\mathrm{e}}\boldsymbol{d} + \boldsymbol{L}^{\mathrm{v}}\dot{\boldsymbol{d}})\|_{L^2(0,T;L^2(\Sigma))}, \qquad (2.62)$$

  for $n \geq 3$.

Here, the symbols $\{c_i\}_{i=1}^8$ denote positive constants independent of h and τ, but which depend on the physical parameters and on the regularity of $(\boldsymbol{u}, p, \boldsymbol{d}, \dot{\boldsymbol{d}})$.

Proof. We first recall the following properties of the discrete solid operators $\boldsymbol{L}_h^{\mathrm{e}}$ and $\boldsymbol{L}_h^{\mathrm{v}}$ (see, e.g., [45, Lemma 1]), which will be used below:

$$\boldsymbol{L}_h^{\mathrm{e}}\boldsymbol{\pi}_h^{\mathrm{e}} = \boldsymbol{L}_h^{\mathrm{e}}, \quad \boldsymbol{L}_h^{\mathrm{v}}\boldsymbol{\pi}_h^{\mathrm{v}} = \boldsymbol{L}_h^{\mathrm{v}}, \qquad (2.63)$$

and

$$\|\boldsymbol{L}_h^{\mathrm{e}}\boldsymbol{w}\|_{0,\Sigma} \leq \|\boldsymbol{L}^{\mathrm{e}}\boldsymbol{w}\|_{0,\Sigma}, \quad \|\boldsymbol{L}_h^{\mathrm{v}}\dot{\boldsymbol{w}}\|_{0,\Sigma} \leq \|\boldsymbol{L}^{\mathrm{v}}\dot{\boldsymbol{w}}\|_{0,\Sigma}, \qquad (2.64)$$

for all $\boldsymbol{w} \in \boldsymbol{D}^{\mathrm{e}}$ and $\dot{\boldsymbol{w}} \in \boldsymbol{D}^{\mathrm{v}}$.

We consider the continuous problem (2.19) at time $t = t_n$ with $(\boldsymbol{v}, q, \boldsymbol{w}) = (\boldsymbol{v}_h, q_h, \boldsymbol{w}_h) \in \boldsymbol{V}_h \times Q_h \times \boldsymbol{W}_h$, and subtract (2.26) from the resulting expression. This yields the following modified Galerkin orthogonality:

$$\begin{aligned}
&\rho^{\mathrm{f}}\left(\partial_\tau(\boldsymbol{u}(t_n) - \boldsymbol{u}_h^n), \boldsymbol{v}_h\right) + a(\boldsymbol{u}(t_n) - \boldsymbol{u}_h^n, \boldsymbol{v}_h) + b(p(t_n) - p_h^n, \boldsymbol{v}_h) - b(q_h, \boldsymbol{u}(t_n) - \boldsymbol{u}_h^n) \\
&\quad + \rho^{\mathrm{s}}\epsilon\big(\partial_\tau(\dot{\boldsymbol{d}}(t_n) - \dot{\boldsymbol{d}}_h^n), \boldsymbol{w}_h\big)_\Sigma + a^{\mathrm{e}}\big(\boldsymbol{d}(t_n) - \boldsymbol{d}_h^n, \boldsymbol{w}_h\big) + a^{\mathrm{v}}\big(\dot{\boldsymbol{d}}(t_n) - \dot{\boldsymbol{d}}_h^n, \boldsymbol{w}_h\big) \\
&\quad = -\rho^{\mathrm{f}}\big((\partial_t - \partial_\tau)\boldsymbol{u}(t_n), \boldsymbol{v}_h\big) - \rho^{\mathrm{s}}\epsilon\big((\partial_t - \partial_\tau)\dot{\boldsymbol{d}}(t_n), \boldsymbol{w}_h\big)_\Sigma + s_h(p_h^n, q_h), \qquad (2.65)
\end{aligned}$$

for all $(\boldsymbol{v}_h, q_h, \boldsymbol{w}_h) \in \boldsymbol{V}_h \times Q_h \times \boldsymbol{W}_h$ with $\boldsymbol{v}_h|_\Sigma = \boldsymbol{w}_h$. Hence, using (2.59), we infer the following equation for the discrete errors $\boldsymbol{\theta}_h^n$, y_h^n, $\boldsymbol{\xi}_h^n$ and $\dot{\boldsymbol{\xi}}_h^n$:

$$\begin{aligned}
&\rho^{\mathrm{f}}\big(\partial_\tau\boldsymbol{\theta}_h^n, \boldsymbol{v}_h\big) + a\big(\boldsymbol{\theta}_h^n, \boldsymbol{v}_h\big) + b\big(y_h^n, \boldsymbol{v}_h\big) - b\big(q_h, \boldsymbol{\theta}_h^n\big) + s_h\big(y_h^n, q_h\big) \\
&\quad + \rho^{\mathrm{s}}\epsilon\big(\partial_\tau\dot{\boldsymbol{\xi}}_h^n, \boldsymbol{v}_h\big)_\Sigma + a^{\mathrm{e}}\big(\boldsymbol{\xi}_h^n, \boldsymbol{v}_h\big) + a^{\mathrm{v}}\big(\dot{\boldsymbol{\xi}}_h^n, \boldsymbol{v}_h\big) \\
&= \underbrace{-\rho^{\mathrm{f}}\big((\partial_t - \partial_\tau)\boldsymbol{u}(t_n), \boldsymbol{v}_h\big) - \rho^{\mathrm{f}}\left(\partial_\tau\boldsymbol{\theta}_\pi^n, \boldsymbol{v}_h\right)}_{T_1(\boldsymbol{v}_h)} \\
&\quad \underbrace{- \rho^{\mathrm{s}}\epsilon\big((\partial_t - \partial_\tau)\dot{\boldsymbol{d}}(t_n), \boldsymbol{v}_h\big)_\Sigma - \rho^{\mathrm{s}}\epsilon\big(\partial_\tau\dot{\boldsymbol{\xi}}_\pi^n, \boldsymbol{v}_h\big)_\Sigma}_{T_2(\boldsymbol{v}_h)} \\
&\quad \underbrace{+ s_h\big(\Pi_h p^n, q_h\big) - a\big(\boldsymbol{\theta}_\pi^n, \boldsymbol{v}_h\big) - b\big(y_\pi^n, \boldsymbol{v}_h\big) + b\big(q_h, \boldsymbol{\theta}_\pi^n\big)}_{T_3(\boldsymbol{v}_h, q_h)} \\
&\quad \underbrace{- a^{\mathrm{e}}\big(\boldsymbol{\xi}_\pi^n, \boldsymbol{v}_h\big)}_{=0} \underbrace{- a^{\mathrm{v}}\big(\dot{\boldsymbol{\xi}}_\pi^n, \boldsymbol{v}_h\big)}_{T_4(\boldsymbol{v}_{h|\Sigma})}, \qquad (2.66)
\end{aligned}$$

for all $(\boldsymbol{v}_h, q_h) \in \boldsymbol{V}_h \times Q_h$ with $\boldsymbol{v}_h|_\Sigma \in \boldsymbol{W}_h$ and $n > r$. It should be noted that the term $a^{\mathrm{e}}\big(\boldsymbol{\xi}_\pi^n, \boldsymbol{v}_h\big)$ vanishes due to definition (2.51) of the solid projection operator. In additon, thanks to (2.3), (2.17) and (2.51), the term T_4 reduces to

$$T_4(\boldsymbol{v}_{h|\Sigma}) = \alpha_0 \rho^{\mathrm{s}} \epsilon \, (\boldsymbol{\xi}_\pi^n, \boldsymbol{v}_h)_\Sigma \, . \tag{2.67}$$

Moreover, by combining (2.25) and (2.63) with (2.59), we have

$$\begin{aligned} \boldsymbol{\theta}_h^n|_\Sigma = \dot{\boldsymbol{\xi}}_h^n &+ \frac{\tau}{\rho^{\mathrm{s}}\epsilon} \Big(\boldsymbol{L}_h^{\mathrm{e}}(\boldsymbol{\xi}_h^n - \boldsymbol{\xi}_h^\star) + \boldsymbol{L}_h^{\mathrm{v}}(\dot{\boldsymbol{\xi}}_h^n - \dot{\boldsymbol{\xi}}_h^\star) \Big) \\ &- \frac{\tau}{\rho^{\mathrm{s}}\epsilon} \Big(\boldsymbol{L}_h^{\mathrm{e}}(\boldsymbol{d}(t_n) - \boldsymbol{d}^\star) + \boldsymbol{L}_h^{\mathrm{v}}(\dot{\boldsymbol{d}}(t_n) - \dot{\boldsymbol{d}}^\star) \Big) \, , \end{aligned} \tag{2.68}$$

for $n > r$, with the natural notations $\boldsymbol{\xi}_h^\star \overset{\text{def}}{=} \boldsymbol{\pi}_h^{\mathrm{e}} \boldsymbol{d}^\star - \boldsymbol{d}_h^\star$, $\dot{\boldsymbol{\xi}}_h^\star \overset{\text{def}}{=} \boldsymbol{\pi}_h^{\mathrm{e}} \dot{\boldsymbol{d}}^\star - \dot{\boldsymbol{d}}_h^\star$ and

$$\big(\boldsymbol{d}^\star, \dot{\boldsymbol{d}}^\star\big) = \begin{cases} \boldsymbol{0} & \text{if} \quad r = 0, \\ \big(\boldsymbol{d}(t_{n-1}), \dot{\boldsymbol{d}}(t_{n-1})\big) & \text{if} \quad r = 1, \\ \big(2\boldsymbol{d}(t_{n-1}) - \boldsymbol{d}(t_{n-2}), 2\dot{\boldsymbol{d}}(t_{n-1}) - \dot{\boldsymbol{d}}(t_{n-2})\big) & \text{if} \quad r = 2. \end{cases}$$

Similarly, from $(2.21)_1$ and (2.59), it follows that

$$\dot{\boldsymbol{\xi}}_h^n = \partial_\tau \boldsymbol{\xi}_h^n + \underbrace{\boldsymbol{\pi}_h^{\mathrm{e}}\big(\dot{\boldsymbol{d}}(t_n) - \partial_\tau \boldsymbol{d}(t_n)\big)}_{\boldsymbol{z}_h^n} . \tag{2.69}$$

The control of the perturbations $\boldsymbol{z}_h^n$ in (2.69) is given by the following estimate:

$$\begin{aligned} \|\boldsymbol{z}_h^n\|_{\mathrm{e}} &= \|\boldsymbol{\pi}_h^{\mathrm{e}}\big(\partial_t - \partial_\tau\big)\boldsymbol{d}(t_n)\|_{\mathrm{e}} \\ &\leq \|\big(\partial_t - \partial_\tau\big)\boldsymbol{d}(t_n)\|_{\mathrm{e}} \\ &\leq (\tau\beta_{\mathrm{e}})^{\frac{1}{2}} \, \| \, \partial_t \boldsymbol{u}\|_{L^2(t_{n-1},t_n;H^1(\Sigma))} \end{aligned} \tag{2.70}$$

Taking $(\boldsymbol{v}_h, q_h) = \tau(\boldsymbol{\theta}_h^n, y_h^n)$ in (2.66), and using (2.68) yields the following energy

equation for the discrete errors:

$$
\begin{aligned}
&\frac{\rho^{\mathrm{f}}}{2}\left(\tau\partial_\tau\|\boldsymbol{\theta}_h^n\|_{0,\Omega}^2+\tau^2\|\partial_\tau\boldsymbol{\theta}_h^n\|_{0,\Omega}^2\right)+2\mu\tau\|\boldsymbol{\epsilon}(\boldsymbol{\theta}_h^n)\|_{0,\Omega}^2+\tau|y_h^n|_{s_h}^2\\
&\quad+\frac{\rho^{\mathrm{s}}\epsilon}{2}\left(\tau\partial_\tau\|\dot{\boldsymbol{\xi}}_h^n\|_{0,\Sigma}^2+\tau^2\|\partial_\tau\dot{\boldsymbol{\xi}}_h^n\|_{0,\Sigma}^2\right)+\frac{1}{2}\left(\tau\partial_\tau\|\boldsymbol{\xi}_h^n\|_{\mathrm{e}}^2+\tau^2\|\partial_\tau\boldsymbol{\xi}_h^n\|_{\mathrm{e}}^2\right)\\
&\quad+\tau\|\dot{\boldsymbol{\xi}}_h^n\|_{\mathrm{v}}^2+\underbrace{\tau^2\left(\partial_\tau\dot{\boldsymbol{\xi}}_h^n,\boldsymbol{L}_h^{\mathrm{e}}(\boldsymbol{\xi}_h^n-\boldsymbol{\xi}_h^\star)+\boldsymbol{L}_h^{\mathrm{v}}\big(\dot{\boldsymbol{\xi}}_h^n-\dot{\boldsymbol{\xi}}_h^\star\big)\right)_\Sigma}_{T_6}\\
&\quad+\underbrace{\frac{\tau^2}{\rho^{\mathrm{s}}\epsilon}\left(\boldsymbol{L}_h^{\mathrm{e}}\boldsymbol{\xi}_h^n+\boldsymbol{L}_h^{\mathrm{v}}\dot{\boldsymbol{\xi}}_h^n,\boldsymbol{L}_h^{\mathrm{e}}(\boldsymbol{\xi}_h^n-\boldsymbol{\xi}_h^\star)+\boldsymbol{L}_h^{\mathrm{v}}\big(\dot{\boldsymbol{\xi}}_h^n-\dot{\boldsymbol{\xi}}_h^\star\big)\right)_\Sigma}_{T_7}\\
&=T_1(\tau\boldsymbol{\theta}_h^n)+T_2(\tau\boldsymbol{\theta}_h^n)+T_3(\tau\boldsymbol{\theta}_h^n,\tau y_h^n)+T_4(\tau\boldsymbol{\theta}_h^n)-\underbrace{\tau a^{\mathrm{e}}(\boldsymbol{\xi}_h^n,\boldsymbol{z}_h^n)}_{T_5}\\
&\quad+\underbrace{\tau^2\left(\partial_\tau\dot{\boldsymbol{\xi}}_h^n,\boldsymbol{L}_h^{\mathrm{e}}(\boldsymbol{d}(t_n)-\boldsymbol{d}^\star)+\boldsymbol{L}_h^{\mathrm{v}}\big(\dot{\boldsymbol{d}}(t_n)-\dot{\boldsymbol{d}}^\star\big)\right)_\Sigma}_{T_8}\\
&\quad+\underbrace{\frac{\tau^2}{\rho^{\mathrm{s}}\epsilon}\left(\boldsymbol{L}_h^{\mathrm{e}}\boldsymbol{\xi}_h^n+\boldsymbol{L}_h^{\mathrm{v}}\dot{\boldsymbol{\xi}}_h^n,\boldsymbol{L}_h^{\mathrm{e}}(\boldsymbol{d}(t_n)-\boldsymbol{d}^\star)+\boldsymbol{L}_h^{\mathrm{v}}\big(\dot{\boldsymbol{d}}(t_n)-\dot{\boldsymbol{d}}^\star\big)\right)_\Sigma}_{T_9},
\end{aligned}
\tag{2.71}
$$

for $n>r$. In this equation, the terms $(T_i)_{i\in[[1,3]]}$ are standard terms and do not come from our specific treatment of the interface transmission condition. The terms T_6 and T_7 are specific to our corrected scheme and have already been treated in the proof of the stability. At last, the terms T_8 and T_9 have to be controlled by the previous stability terms to get the convergence of the scheme.

The terms $T_1,\ldots,T_3$ and T_5 are estimated as in [45, Section 5], using (2.52)-(2.55) and Taylor expansions. We simply recall the corresponding bound

$$
\begin{aligned}
\sum_{i=1}^{3}T_i\lesssim&\frac{(\rho^{\mathrm{f}}C_{\mathrm{P}}\tau)^2}{\varepsilon_1\mu}\|\partial_{tt}\boldsymbol{u}\|_{L^2(t^{n-1},t^n;L^2(\Omega))}^2+\frac{(\rho^{\mathrm{s}}\epsilon C_{\mathrm{T}}\tau)^2}{\varepsilon_2\mu}\|\partial_{tt}\boldsymbol{u}\|_{L^2(t^{n-1},t^n;L^2(\Sigma))}^2\\
&+\frac{(\rho^{\mathrm{f}}C_{\mathrm{P}}c_\mu)^2}{\varepsilon_1\mu}h^{2k+2}\|\partial_t\boldsymbol{u}\|_{L^2(t_{n-1},t_n;H^{k+1}(\Omega))}^2\\
&+\left(\frac{(\rho^{\mathrm{f}}C_{\mathrm{P}}c_\mu)^2h}{\varepsilon_1\mu}+\frac{(\rho^{\mathrm{s}}\epsilon C_{\mathrm{T}})^2}{\varepsilon_2\mu}\right)h^{2k+2}\|\partial_t\boldsymbol{u}\|_{L^2(t^{n-1},t^n;H^{k+1}(\Sigma))}^2\\
&+\frac{\mu\tau h^{2k}}{\varepsilon_3}\left(\|\boldsymbol{u}(t_n)\|_{k+1,\Omega}^2+h\|\boldsymbol{u}(t_n)\|_{k+1,\Sigma}^2\right)\\
&+\frac{\tau}{\varepsilon_3\mu}\left(h^{2\tilde{l}}\|p(t_n)\|_{\tilde{l},\Omega}^2+h^{2l+1}\|p(t_n)\|_{l+1,\Omega}^2\right)\\
&+\tau(\varepsilon_1+\varepsilon_2+\varepsilon_3)\|\boldsymbol{\theta}_h^n\|_{\boldsymbol{V}}^2+\tau\varepsilon_3|y_h^n|_{s_h}^2
\end{aligned}
\tag{2.72}
$$

where ε_i, $i = 1, \dots, 3$, are free positive parameters and C_{P},C_{T} are the constant of the Poincaré and trace inequality respectively. In (2.72), the terms involving $\|\boldsymbol{\theta}_h^n\|_{\boldsymbol{V}}^2$ and $|y_h^n|_{s_h}^2$ can be absorbed by the left-hand side of (2.71), by choosing ε_i sufficiently small. As regards the term T_5, thanks to (2.70), we have that

$$|T_5| \leq \frac{\tau}{T}\|\boldsymbol{\xi}_h^n\|_{\mathrm{e}}^2 + \tau^2 T\beta_{\mathrm{e}}\|\partial_t \boldsymbol{u}\|_{L^2(t^{n-1},t^n;H^1(\Sigma))}^2$$

and the first term is controlled via Gronwall's Lemma. As regards the term T_4, estimate (2.52) and a trace inequality gives

$$\begin{aligned} T_4(\tau\boldsymbol{\theta}_h^n) &\leq \alpha_0\rho^{\mathrm{s}}\epsilon\tau\|\boldsymbol{\xi}_\pi^n\|_{0,\Sigma}\|\boldsymbol{\theta}_h^n\|_{0,\Sigma} \\ &\leq \alpha_0\rho^{\mathrm{s}}\epsilon\tau h^{k+1}\beta_{\mathrm{e}}^{\frac{1}{2}}\|\boldsymbol{u}(t_n)\|_{k+1,\Sigma}C_{\mathrm{P}}h^{-\frac{1}{2}}\|\boldsymbol{\theta}_h^n\|_{1,\Omega} \\ &\leq \tau h^{2k+1}\frac{(\alpha_0\rho^{\mathrm{s}}\epsilon C_{\mathrm{P}})^2\beta_{\mathrm{e}}}{4\mu\varepsilon_4}\|\boldsymbol{u}(t_n)\|_{k+1,\Sigma}^2 + \tau\varepsilon_4\|\boldsymbol{\theta}_h^n\|_{\boldsymbol{V}}^2, \end{aligned} \tag{2.73}$$

for $\varepsilon_4 > 0$. The last term can be absorbed by the left-hand side of (2.71) for ε_4 sufficiently small.

As regards the remaining terms $T_6, \dots, T_9$ in (2.71), we proceed by treating each extrapolation separately.

(i) Without extrapolation ($r = 0$). Terms T_6 and T_7 are bounded as terms T_1 and T_2 in section 2.4.5, which yields

$$T_6 + T_7 \geq -\frac{\rho^{\mathrm{s}}\epsilon}{3}\|\dot{\boldsymbol{\xi}}_h^n - \dot{\boldsymbol{\xi}}_h^{n-1}\|_{0,\Sigma}^2 + \frac{\tau^2}{4\rho^{\mathrm{s}}\epsilon}\|\boldsymbol{L}_h^{\mathrm{e}}\boldsymbol{\xi}_h^n + \boldsymbol{L}_h^{\mathrm{v}}\dot{\boldsymbol{\xi}}_h^n\|_{0,\Sigma}^2. \tag{2.74}$$

For the remaining terms, using Young's inequality and (2.64), we have

$$\begin{aligned} T_8 + T_9 \leq &\frac{\rho^{\mathrm{s}}\epsilon}{8}\|\dot{\boldsymbol{\xi}}_h^n - \dot{\boldsymbol{\xi}}_h^{n-1}\|_{0,\Sigma}^2 + \frac{\tau^2}{8\rho^{\mathrm{s}}\epsilon}\|\boldsymbol{L}_h^{\mathrm{e}}\boldsymbol{\xi}_h^n + \boldsymbol{L}_h^{\mathrm{v}}\dot{\boldsymbol{\xi}}_h^n\|_{0,\Sigma}^2 \\ &+ \frac{4\tau^2}{\rho^{\mathrm{s}}\epsilon}\|\boldsymbol{L}^{\mathrm{e}}\boldsymbol{d}(t_n) + \boldsymbol{L}^{\mathrm{v}}\dot{\boldsymbol{d}}(t_n)\|_{0,\Sigma}^2. \end{aligned} \tag{2.75}$$

The estimate (2.60) then follows by inserting (2.72), (2.73) (2.74) and (2.75) into (2.71), using Korn's inequality, summing over $m = 1, \dots, n$, and applying Gronwall's lemma.

(ii) First-order extrapolation ($r = 1$). Terms T_7 is treated as term T_2 in section 2.4.5, yielding

$$T_7 = \frac{\tau^2}{2\rho^{\mathrm{s}}\epsilon}\left(\tau\partial_\tau\left\|\boldsymbol{L}_h^{\mathrm{e}}\boldsymbol{\xi}_h^n + \boldsymbol{L}_h^{\mathrm{v}}\dot{\boldsymbol{\xi}}_h^n\right\|_{0,\Sigma}^2 + \tau^2\left\|\partial_\tau(\boldsymbol{L}_h^{\mathrm{e}}\boldsymbol{\xi}_h^n + \boldsymbol{L}_h^{\mathrm{v}}\dot{\boldsymbol{\xi}}_h^n)\right\|_{0,\Sigma}^2\right). \tag{2.76}$$

For term T_6, we have

$$T_6 = \frac{\tau^2}{2}\left(\tau\partial_\tau\left\|\dot{\boldsymbol{\xi}}_h^n\right\|_{\mathrm{e}}^2 + \left\|\dot{\boldsymbol{\xi}}_h^n - \dot{\boldsymbol{\xi}}_h^{n-1}\right\|_{\mathrm{e}}^2\right) + \tau\left\|\dot{\boldsymbol{\xi}}_h^n - \dot{\boldsymbol{\xi}}_h^{n-1}\right\|_{\mathrm{v}}^2 + \tau^2 a^{\mathrm{e}}(\dot{\boldsymbol{\xi}}_h^n - \dot{\boldsymbol{\xi}}_h^{n-1}, \boldsymbol{z}_h^n),$$

where the last contribution is due to the modified displacement-velocity relation (2.69). Thus, using (2.70), we get

$$T_6 \gtrsim \frac{\tau^2}{2}\big(\|\dot{\boldsymbol{\xi}}_h^n\|_{\mathrm{e}}^2 - \|\dot{\boldsymbol{\xi}}_h^{n-1}\|_{\mathrm{e}}^2\big) + \tau\big\|\dot{\boldsymbol{\xi}}_h^n - \dot{\boldsymbol{\xi}}_h^{n-1}\big\|_{\mathrm{v}}^2 - \beta_{\mathrm{e}}\tau^3\|\partial_t \boldsymbol{u}\|^2_{L^2(t_{n-1},t_n;H^1(\Sigma))}.$$

For the terms T_8 and T_9, using Taylor expansions and (2.64), we have

$$\begin{aligned} T_8 + T_9 \leq & \frac{\rho^{\mathrm{s}}\epsilon}{2T}\left(\|\dot{\boldsymbol{\xi}}_h^n\|_{0,\Sigma}^2 + \|\dot{\boldsymbol{\xi}}_h^{n-1}\|_{0,\Sigma}^2\right) + \frac{3T\tau^2}{2\rho^{\mathrm{s}}\epsilon}\|\boldsymbol{L}^{\mathrm{e}}\partial_t \boldsymbol{d} + \boldsymbol{L}^{\mathrm{v}}\partial_t \dot{\boldsymbol{d}}\|^2_{L^2(t^{n-1},t^n;L^2(\Sigma))} \\ & + \frac{\tau^3}{2\rho^{\mathrm{s}}\epsilon T}\|\boldsymbol{L}_h^{\mathrm{e}}\boldsymbol{\xi}_h^n + \boldsymbol{L}_h^{\mathrm{v}}\dot{\boldsymbol{\xi}}_h^n\|_{0,\Sigma}^2, \end{aligned}$$

where last term can be treated via Gronwall's Lemma, using the control provided by (2.76).

In summary, the estimate (2.61) follows by inserting the above bounds into (2.71), using Korn's inequality, summing over $m = 2, \ldots, n$, and applying Gronwall's Lemma. The part of the discrete error corresponding to the initialization step is bounded from (2.60) with $n = 1$ and $T = \tau$.

(iii) Second-order extrapolation ($r = 2$). Terms T_6 and T_7 are treated as terms T_1 and T_2 in section 2.4.5. We have

$$\begin{aligned} T_6 = & \tau^2\big\|\dot{\boldsymbol{\xi}}_h^n - \dot{\boldsymbol{\xi}}_h^{n-1}\big\|_{\mathrm{e}}^2 + \frac{\tau}{2}\left(\tau\partial_\tau\big\|\dot{\boldsymbol{\xi}}_h^n - \dot{\boldsymbol{\xi}}_h^{n-1}\big\|_{\mathrm{v}}^2 + \big\|\dot{\boldsymbol{\xi}}_h^n - 2\dot{\boldsymbol{\xi}}_h^{n-1} + \dot{\boldsymbol{\xi}}_h^{n-2}\big\|_{\mathrm{v}}^2\right) \\ & + \underbrace{\tau^2 a^{\mathrm{e}}\big(\dot{\boldsymbol{\xi}}_h^n - \dot{\boldsymbol{\xi}}_h^{n-1}, \boldsymbol{z}_h^n - \boldsymbol{z}_h^{n-1}\big)}_{T_{6,1}}, \end{aligned}$$

where the last term is bounded, using (2.70), as follows

$$T_{6,1} \gtrsim -\frac{\tau^2}{2}\|\dot{\boldsymbol{\xi}}_h^n - \dot{\boldsymbol{\xi}}_h^{n-1}\|_{\mathrm{e}}^2 - \beta_{\mathrm{e}}\tau^3\|\partial_t \boldsymbol{u}\|^2_{L^2(t^{n-2},t^n;H^1(\Sigma))}.$$

For T_7, we have

$$\begin{aligned} T_7 \geq & \frac{\alpha_0\tau^3}{2\rho^{\mathrm{s}}\epsilon}\left(\tau\partial_\tau\|\dot{\boldsymbol{\xi}}_h^n\|_{\mathrm{e}}^2 + \|\dot{\boldsymbol{\xi}}_h^n - \dot{\boldsymbol{\xi}}_h^{n-1}\|_{\mathrm{e}}^2\right) \\ & + \frac{\alpha_1\tau^3}{2\rho^{\mathrm{s}}\epsilon}\left(\tau\partial_\tau\|\boldsymbol{L}_h^{\mathrm{e}}\dot{\boldsymbol{\xi}}_h^n\|_{0,\Sigma}^2 + \|\boldsymbol{L}_h^{\mathrm{e}}(\dot{\boldsymbol{\xi}}_h^n - \dot{\boldsymbol{\xi}}_h^{n-1})\|_{0,\Sigma}^2\right) \\ & - \tau\frac{\gamma}{2}\|\boldsymbol{\xi}_h^n\|_{\mathrm{e}}^2 - \tau\delta\|\dot{\boldsymbol{\xi}}_h^n\|_{\mathrm{v}}^2 - \frac{\rho^{\mathrm{s}}\epsilon}{4}\|\dot{\boldsymbol{\xi}}_h^n - \dot{\boldsymbol{\xi}}_h^{n-1}\|_{0,\Sigma}^2 \\ & - \frac{\tau}{4}\|\dot{\boldsymbol{\xi}}_h^n - 2\dot{\boldsymbol{\xi}}_h^{n-1} + \dot{\boldsymbol{\xi}}_h^{n-2}\|_{\mathrm{v}}^2 \underbrace{- \frac{\tau^3}{\rho^{\mathrm{s}}\epsilon}a^{\mathrm{e}}\big(\boldsymbol{L}_h^{\mathrm{e}}\boldsymbol{\xi}_h^n + \boldsymbol{L}_h^{\mathrm{v}}\dot{\boldsymbol{\xi}}_h^n, \boldsymbol{z}_h^n - \boldsymbol{z}_h^{n-1}\big)}_{T_{7,1}}. \end{aligned}$$

The last term in this bounded through (2.3), (2.27) as follows

$$\begin{aligned}
T_{7,1} \geq & -\frac{\tau^5}{2T(\rho^{\mathrm{s}}\epsilon)^2}\|\boldsymbol{L}_h^{\mathrm{e}}\boldsymbol{\xi}_h^n + \boldsymbol{L}_h^{\mathrm{v}}\dot{\boldsymbol{\xi}}_h^n\|_{\mathrm{e}}^2 - \frac{\tau T}{2}\|\boldsymbol{z}_h^n - \boldsymbol{z}_h^{n-1}\|_{\mathrm{e}}^2 \\
\geq & -\frac{\beta_{\mathrm{e}}C_{\mathrm{inv}}^2\tau^5}{T(\rho^{\mathrm{s}}\epsilon)^2h^2}\left(\|\boldsymbol{L}_h^{\mathrm{e}}\boldsymbol{\xi}_h^n\|_{0,\Sigma}^2 + \|\boldsymbol{L}_h^{\mathrm{v}}\dot{\boldsymbol{\xi}}_h^n\|_{0,\Sigma}^2\right) - \frac{\tau T}{2}\|\boldsymbol{z}_h^n - \boldsymbol{z}_h^{n-1}\|_{\mathrm{e}}^2 \\
\geq & -\frac{\beta_{\mathrm{e}}C_{\mathrm{inv}}^2\tau^5}{T(\rho^{\mathrm{s}}\epsilon)^2h^2}\left[\frac{\beta_{\mathrm{e}}C_{\mathrm{inv}}^2}{h^2}\|\boldsymbol{\xi}_h^n\|_{\mathrm{e}}^2 + \left(\alpha_0\rho^{\mathrm{s}}\epsilon + \alpha_1\frac{\beta_{\mathrm{e}}C_{\mathrm{inv}}^2}{h^2}\right)\|\dot{\boldsymbol{\xi}}_h^n\|_{\mathrm{v}}^2\right] \\
& - \frac{\tau T}{2}\|\boldsymbol{z}_h^n - \boldsymbol{z}_h^{n-1}\|_{\mathrm{e}}^2 \\
\geq & -\frac{\tau^5\omega_{\mathrm{e}}^4}{Th^4}\|\boldsymbol{\xi}_h^n\|_{\mathrm{e}}^2 - \frac{\tau^5\omega_{\mathrm{e}}^2}{Th^2}\left(\alpha_0 + \alpha_1\frac{\omega_{\mathrm{e}}^2}{h^2}\right)\|\dot{\boldsymbol{\xi}}_h^n\|_{\mathrm{v}}^2 - \frac{\tau T}{2}\|\boldsymbol{z}_h^n - \boldsymbol{z}_h^{n-1}\|_{\mathrm{e}}^2,
\end{aligned} \tag{2.77}$$

where we have used the notation $\omega_{\mathrm{e}} \stackrel{\mathrm{def}}{=} C_{\mathrm{inv}}\sqrt{\beta_{\mathrm{e}}/(\rho^{\mathrm{s}}\epsilon)}$. Hence, using (2.30) and (2.70), we finally infer that

$$T_{7,1} \gtrsim -\tau^2\beta_{\mathrm{e}}T\|\partial_t\boldsymbol{u}\|_{L^2(t_{n-2},t_n;H^1(\Sigma))}^2 - \frac{\tau}{T}\left(\frac{\gamma\tau}{2}\right)^{\frac{2}{3}}\|\boldsymbol{\xi}_h^n\|_{\mathrm{e}}^2 - \frac{\tau^3\gamma}{4T}\|\dot{\boldsymbol{\xi}}_h^n\|_{\mathrm{v}}^2. \tag{2.78}$$

The second terms is controlled via Gronwall's Lemma, while the last can be absorbed by the left-hand side of (2.71).

We conclude the proof with the estimation of the remaining terms in the right-hand side of (2.71). For T_8, using a Taylor expansion, we simply have

$$T_8 \leq \tau\frac{\rho^{\mathrm{s}}\epsilon}{2T}\left(\|\dot{\boldsymbol{\xi}}_h^n\|_{0,\Sigma}^2 + \|\dot{\boldsymbol{\xi}}_h^{n-1}\|_{0,\Sigma}^2\right) + \frac{T\tau^4}{2\rho^{\mathrm{s}}\epsilon}\|\boldsymbol{L}^{\mathrm{e}}\partial_{tt}\boldsymbol{d} + \boldsymbol{L}^{\mathrm{v}}\partial_{tt}\dot{\boldsymbol{d}}\|_{L^2(t^{n-1},t^n;L^2(\Sigma))}^2,$$

where the first term can be controlled via Gronwall's Lemma. At last, for T_9, we have that

$$\begin{aligned}
T_9 \leq & \frac{\tau^3}{\rho^{\mathrm{s}}\epsilon T}\left(\|\boldsymbol{L}_h^{\mathrm{e}}\boldsymbol{\xi}_h^n\|_{0,\Sigma}^2 + \|\boldsymbol{L}_h^{\mathrm{v}}\dot{\boldsymbol{\xi}}_h^n\|_{0,\Sigma}^2\right) + \frac{T\tau^4}{2\rho^{\mathrm{s}}\epsilon}\|\boldsymbol{L}^{\mathrm{e}}\partial_{tt}\boldsymbol{d} + \boldsymbol{L}^{\mathrm{v}}\partial_{tt}\dot{\boldsymbol{d}}\|_{L^2(t^{n-1},t^n;L^2(\Sigma))}^2 \\
\leq & \frac{\tau^3\omega_{\mathrm{e}}^2}{Th^2}\|\boldsymbol{\xi}_h^n\|_{\mathrm{e}}^2 + \frac{\tau^3}{T}\left(\alpha_0 + \alpha_1\frac{\omega_{\mathrm{e}}^2}{h^2}\right)\|\dot{\boldsymbol{\xi}}_h^n\|_{\mathrm{v}}^2 \\
& + \frac{T\tau^4}{2\rho^{\mathrm{s}}\epsilon}\|\boldsymbol{L}^{\mathrm{e}}\partial_{tt}\boldsymbol{d} + \boldsymbol{L}^{\mathrm{v}}\partial_{tt}\dot{\boldsymbol{d}}\|_{L^2(t^{n-1},t^n;L^2(\Sigma))}^2.
\end{aligned}$$

Hence, from (2.30), we infer that

$$T_9 \leq \frac{\tau}{T}\left(\frac{\tau\gamma}{2}\right)^{\frac{1}{3}}\|\boldsymbol{\xi}_h^n\|_{\mathrm{e}}^2 + \frac{\tau^2\delta^{\frac{1}{2}}}{T}\|\dot{\boldsymbol{\xi}}_h^n\|_{\mathrm{v}}^2 + \frac{T\tau^4}{2\rho^{\mathrm{s}}\epsilon}\|\boldsymbol{L}^{\mathrm{e}}\partial_{tt}\boldsymbol{d} + \boldsymbol{L}^{\mathrm{v}}\partial_{tt}\dot{\boldsymbol{d}}\|_{L^2(t^{n-1},t^n;L^2(\Sigma))}^2,$$

where the first two terms are controlled via Gronwall's Lemma and the left-hand side of (2.71), respectively.

In summary, the estimate (2.62) follows by inserting the above bounds into (2.71), using Korn's inequality, summing over $m = 3, \ldots, n$, and applying Gronwall's Lemma. The remaining terms, corresponding to the initialization step, are bounded via (2.61) with $n = 2$ and $T = 2\tau$. □

2.7 Formulation in the non-linear case

In this section we extend the explicit Robin-Neumann paradigm of Section 2.3.1 to the case of a non-linear fluid-structure problem, involving a viscous incompressible fluid and thin-walled structure. The fluid is described by the incompressible Navier-Stokes equations in ALE formalism (see, e.g., [60, Chapter 3]) and the structure by a non-linear *Reissner-Mindlin* shell model (see, e.g., [26, 10]).

2.7.1 The non-linear coupled problem

Let $\Omega \cup \Sigma$ be a reference configuration of the system. The current configurationof the fluid domain, $\Omega(t)$, is parametrized by the ALE map $\boldsymbol{\mathcal{A}} \stackrel{\text{def}}{=} \boldsymbol{I}_\Omega + \boldsymbol{d}^{\text{f}}$ as $\Omega(t) = \boldsymbol{\mathcal{A}}(\Omega, t)$, where $\boldsymbol{d}^{\text{f}} : \Omega \times \mathbb{R}^+ \to \mathbb{R}^d$ stands for the displacement of the fluid domain. In practice, $\boldsymbol{d}^{\text{f}} = \text{Ext}(\boldsymbol{d}|_\Sigma)$, where $\text{Ext}(\cdot)$ denotes any reasonable lifting operator from the (reference) interface Σ into the (reference) fluid domain Ω. For instance, an harmonic lifting operator is used in the numerical experiments reported in Section 4.4.

The non-linear fluid-structure problem under consideration reads as follows: Find the fluid domain displacement $\boldsymbol{d}^{\text{f}} : \Omega \times \mathbb{R}^+ \to \mathbb{R}^d$, the fluid velocity $\boldsymbol{u} : \Omega \times \mathbb{R}^+ \to \mathbb{R}^d$, the fluid pressure $p : \Omega \times \mathbb{R}^+ \to \mathbb{R}^d$ the solid displacement $\boldsymbol{d} : \Sigma \times \mathbb{R}^+ \to \mathbb{R}^d$ and the surface vector field $\boldsymbol{\theta} : \Sigma \times \mathbb{R}^+ \to \mathbb{R}^3$ such that

$$\boldsymbol{d}^{\text{f}} = \text{Ext}(\boldsymbol{d}|_\Sigma), \quad \boldsymbol{w} = \partial_t \boldsymbol{d}^{\text{f}}, \quad \boldsymbol{\mathcal{A}} \stackrel{\text{def}}{=} \boldsymbol{I}_\Omega + \boldsymbol{d}^{\text{f}}, \quad \Omega(t) = \boldsymbol{\mathcal{A}}(\Omega, t),$$

$$\begin{cases} \rho^{\text{f}} \partial_t|_{\boldsymbol{\mathcal{A}}} \boldsymbol{u} + \rho^{\text{f}} (\boldsymbol{u} - \boldsymbol{w}) \cdot \boldsymbol{\nabla} \boldsymbol{u} - \boldsymbol{\nabla} \cdot \boldsymbol{\sigma}(\boldsymbol{u}, p) = \boldsymbol{0} & \text{in} \quad \Omega(t), \\ \boldsymbol{\nabla} \cdot \boldsymbol{u} = 0 & \text{in} \quad \Omega(t), \\ \boldsymbol{u} = \boldsymbol{0} & \text{on} \quad \Gamma^{\text{d}}, \\ \boldsymbol{\sigma}(\boldsymbol{u}, p)\boldsymbol{n} = \boldsymbol{h} & \text{on} \quad \Gamma^{\text{n}}, \end{cases} \tag{2.79}$$

$$\begin{cases} \boldsymbol{u} = \dot{\boldsymbol{d}} & \text{on} \quad \Sigma, \\ \rho^{\text{s}} \epsilon \partial_t \dot{\boldsymbol{d}} + \boldsymbol{L}^{\text{e}}_{\boldsymbol{d}}(\boldsymbol{d}, \boldsymbol{\theta}) + \boldsymbol{L}^{\text{v}}_{\boldsymbol{d}}(\dot{\boldsymbol{d}}, \dot{\boldsymbol{\theta}}) = - J \boldsymbol{\sigma}(\boldsymbol{u}, p) \boldsymbol{F}^{-\text{T}} \boldsymbol{n} & \text{on} \quad \Sigma, \\ \boldsymbol{L}^{\text{e}}_{\boldsymbol{\theta}}(\boldsymbol{d}, \boldsymbol{\theta}) + \boldsymbol{L}^{\text{v}}_{\boldsymbol{\theta}}(\dot{\boldsymbol{d}}, \dot{\boldsymbol{\theta}}) = \boldsymbol{0} & \text{on} \quad \Sigma, \\ \dot{\boldsymbol{d}} = \partial_t \boldsymbol{d}, \quad \dot{\boldsymbol{\theta}} = \partial_t \boldsymbol{\theta} & \text{on} \quad \Sigma, \\ \boldsymbol{d} = \boldsymbol{\theta} = \boldsymbol{0} & \text{on} \quad \partial\Sigma, \end{cases} \tag{2.80}$$

where $\partial_t|_{\boldsymbol{\mathcal{A}}}$ represents the ALE time derivative, $\boldsymbol{F} \stackrel{\text{def}}{=} \boldsymbol{\nabla} \boldsymbol{\mathcal{A}}$ the fluid domain gradient of deformation and $J \stackrel{\text{def}}{=} \det \boldsymbol{F}$ the Jacobian. The surface elastic and viscous operators, $(\boldsymbol{L}^{\text{e}}_{\boldsymbol{d}}, \boldsymbol{L}^{\text{e}}_{\boldsymbol{\theta}})$ and $(\boldsymbol{L}^{\text{v}}_{\boldsymbol{d}}, \boldsymbol{L}^{\text{v}}_{\boldsymbol{\theta}})$, can be non-linear. As usual, a field defined in the reference fluid domain, Ω, is evaluated in the current fluid domain, $\Omega(t)$, by composition with $\boldsymbol{\mathcal{A}}^{-1}(\cdot, t)$.

2.7.2 Explicit Robin-Neumann schemes

The proposed fully explicit coupling schemes combine an explicit treatment of the interface geometrical compatibility $(2.79)_1$ with an explicit Robin-Neumann treatment of the interface kinematic and kinetic coupling $(2.80)_{1,2}$. Following the initial argument of Section 2.3, the interface Robin consistency of the coupled problem (2.79)-(2.80) is given by the relation

$$J\boldsymbol{\sigma}(\boldsymbol{u},p)\boldsymbol{F}^{-\mathrm{T}}\boldsymbol{n}+\rho^{\mathrm{s}}\epsilon\partial_t\boldsymbol{u}=-\boldsymbol{L}^{\mathrm{e}}_{\boldsymbol{d}}(\boldsymbol{d},\boldsymbol{\theta})-\boldsymbol{L}^{\mathrm{v}}_{\boldsymbol{d}}(\dot{\boldsymbol{d}},\dot{\boldsymbol{\theta}})\quad\text{on}\quad\Sigma.$$

Nevertheless, in order to avoid the extrapolation of the viscoelastic non-linear terms in

Algorithm 2.4 Explicit Robin-Neumann schemes (non-linear problems)

For $n>r$:

1. Fluid domain update:

$$\boldsymbol{d}^{\mathrm{f,n}}=\mathrm{Ext}(\boldsymbol{d}^{n-1}|_{\Sigma}),\quad \boldsymbol{w}^n=\partial_\tau\boldsymbol{d}^{\mathrm{f,n}},\quad \boldsymbol{\mathcal{A}}^n\overset{\mathrm{def}}{=}\boldsymbol{I}_\Omega+\boldsymbol{d}^{\mathrm{f,n}},\quad \Omega^n\overset{\mathrm{def}}{=}\boldsymbol{\mathcal{A}}^n\big(\Omega\big)$$

   and we set $\boldsymbol{F}^n=\boldsymbol{\nabla}\boldsymbol{\mathcal{A}}^n$ and $J^n=\det\boldsymbol{F}^n$.

2. Fluid step: find $\boldsymbol{u}^n:\Omega\times\mathbb{R}^+\to\mathbb{R}^3$ and $p^n:\Omega\times\mathbb{R}^+\to\mathbb{R}$ such that

$$\begin{cases}\rho^{\mathrm{f}}\partial_\tau|_{\boldsymbol{\mathcal{A}}}\boldsymbol{u}^n+\rho^{\mathrm{f}}(\boldsymbol{u}^{n-1}-\boldsymbol{w}^n)\cdot\boldsymbol{\nabla}\boldsymbol{u}^n-\boldsymbol{\nabla}\cdot\boldsymbol{\sigma}(\boldsymbol{u}^n,p^n)=\boldsymbol{0}, & \text{in}\quad\Omega^n,\\ \mathrm{div}\boldsymbol{u}^n=0 & \text{in}\quad\Omega^n,\\ \boldsymbol{u}^n=\boldsymbol{0} & \text{on}\quad\Gamma^{\mathrm{d}},\\ \boldsymbol{\sigma}(\boldsymbol{u}^n,p^n)\boldsymbol{n}=\boldsymbol{h} & \text{on}\quad\Gamma^{\mathrm{n}},\\ J^n\boldsymbol{\sigma}(\boldsymbol{u}^n,p^n)(\boldsymbol{F}^n)^{-\mathrm{T}}\boldsymbol{n}+\dfrac{\rho^{\mathrm{s}}\epsilon}{\tau}\boldsymbol{u}^n=\dfrac{\rho^{\mathrm{s}}\epsilon}{\tau}\big(\dot{\boldsymbol{d}}^{n-1}+\tau\partial_\tau\dot{\boldsymbol{d}}^{\star}\big)+\boldsymbol{t}^* & \text{on}\quad\Sigma,\end{cases}$$

   with the fluid stress extrapolations $\boldsymbol{t}^\star$ given by (2.83).

3. Solid step: find $\boldsymbol{d}^n:\Sigma\times\mathbb{R}^+\to\mathbb{R}^3$ and $\boldsymbol{\theta}^n:\Sigma\times\mathbb{R}^+\to\mathbb{R}^3$ such that

$$\begin{cases}\rho^{\mathrm{s}}\epsilon\partial_\tau\dot{\boldsymbol{d}}^n+\boldsymbol{L}^{\mathrm{e}}_{\boldsymbol{d}}(\boldsymbol{d}^n,\boldsymbol{\theta}^n)+\boldsymbol{L}^{\mathrm{v}}_{\boldsymbol{d}}(\dot{\boldsymbol{d}}^n,\dot{\boldsymbol{\theta}}^n)=-J^n\boldsymbol{\sigma}(\boldsymbol{u}^n,p^n)(\boldsymbol{F}^n)^{-\mathrm{T}}\boldsymbol{n} & \text{on}\quad\Sigma,\\ \boldsymbol{L}^{\mathrm{e}}_{\boldsymbol{\theta}}(\boldsymbol{d}^n,\boldsymbol{\theta}^n)+\boldsymbol{L}^{\mathrm{v}}_{\boldsymbol{\theta}}(\dot{\boldsymbol{d}}^n,\dot{\boldsymbol{\theta}}^n)=\boldsymbol{0} & \text{on}\quad\Sigma,\\ \dot{\boldsymbol{d}}=\partial_\tau\boldsymbol{d}^n,\quad\dot{\boldsymbol{\theta}}^n=\partial_\tau\boldsymbol{\theta}^n & \text{on}\quad\Sigma,\\ \boldsymbol{d}^n=\boldsymbol{\theta}^n=\boldsymbol{0} & \text{on}\quad\partial\Sigma.\end{cases}$$

the right-hand side, we instead consider the non-linear counterpart of the alternative condition given by (2.12), that is,

$$J\boldsymbol{\sigma}(\boldsymbol{u},p)\boldsymbol{F}^{-\mathrm{T}}\boldsymbol{n}+\frac{\rho^{\mathrm{s}}\epsilon}{\tau}\boldsymbol{u}=\frac{\rho^{\mathrm{s}}\epsilon}{\tau}\dot{\boldsymbol{d}}+J\boldsymbol{\sigma}(\boldsymbol{u},p)\boldsymbol{F}^{-\mathrm{T}}\boldsymbol{n}\quad\text{on}\quad\Sigma,\tag{2.81}$$

which motivates the following intrinsic explicit Robin condition for the fluid

$$J^n\boldsymbol{\sigma}(\boldsymbol{u}^n,p^n)(\boldsymbol{F}^n)^{-\mathrm{T}}\boldsymbol{n}+\frac{\rho^{\mathrm{S}}\epsilon}{\tau}\boldsymbol{u}^n=\frac{\rho^{\mathrm{S}}\epsilon}{\tau}\left(\dot{\boldsymbol{d}}^{n-1}+\tau\partial_\tau\dot{\boldsymbol{d}}^\star\right)+\boldsymbol{t}^\star\quad\text{on}\quad\Sigma, \tag{2.82}$$

where $\dot{\boldsymbol{d}}^\star=\boldsymbol{0}$, $\dot{\boldsymbol{d}}^{n-1}$, $2\dot{\boldsymbol{d}}^{n-1}+\dot{\boldsymbol{d}}^{n-2}$ and

$$\boldsymbol{t}^\star=\begin{cases}\boldsymbol{0},\\ J^{n-1}\boldsymbol{\sigma}(\boldsymbol{u}^{n-1},p^{n-1})(\boldsymbol{F}^{n-1})^{-\mathrm{T}}\boldsymbol{n},\\ 2J^{n-1}\boldsymbol{\sigma}(\boldsymbol{u}^{n-1},p^{n-1})(\boldsymbol{F}^{n-1})^{-\mathrm{T}}\boldsymbol{n}-J^{n-2}\boldsymbol{\sigma}(\boldsymbol{u}^{n-2},p^{n-2})(\boldsymbol{F}^{n-2})^{-\mathrm{T}}\boldsymbol{n},\end{cases} \tag{2.83}$$

stands, respectively, for the zeroth- ($r=0$), first- ($r=1$) and second-order ($r=2$) extrapolations of the solid velocity, $\dot{\boldsymbol{d}}$, and of the interface fluid stress in the reference configuration, $J\boldsymbol{\sigma}(\boldsymbol{u},p)\boldsymbol{F}^{-\mathrm{T}}\boldsymbol{n}$. The explicit Robin condition (2.82) corresponds to the non-linear counterpart of (2.11). The resulting explicit coupling schemes are detailed in Algorithm 2.4.

It should be noted that the geometrical quantities involved in (2.82) and (2.83) do not need any specific treatment and appear because the interface relation (2.81) is formulated in the reference configuration. In practice, the interface fluid stresses are consistently evaluated as variationnal residuals in the deformed configurations, while the solid inertial contributions are integrated in the reference configuration. These hybrid characteristics of the explicit Robin condition (2.82) are handled in a natural manner by the ALE formalism.

Remark 2.7.1. *Though non trivial, the separate solution of the structure and fluid sub-problems of Alogirhtm 2.4 is not a contribution of the present work. In fact, all the numerical experiments involving non-linear models have been performed with pre-existing separate fluid and solid solvers by exploiting the partitioned nature of the Robin-Neumann schemes proposed in this PhD thesis. Hence only minimal information on this aspect is given (e.g., type of finite element approximation, stabilization method for the fluid, etc.). The structure problem involved in sub-step 3 of Algorithm 2.4 is nonlinear. In the numerical experiments reported in the next section, this non-linearity is solved using Newton's method (see, e.g., [84]). These observations also apply to Chapter 3.*

2.8 Numerical experiments

In order to assess the behavior and robustness of the explicit Robin-Neumann schemes, we have considered a number of fluid-structure interaction examples from the literature. Section 2.8.1 presents a convergence study in 2D, using the linear model problem (2.1)-(2.2). Numerical results with 3D geometries and non-linear models (2.79)-(2.80) are reported in the subsequent Sections 2.8.2-2.8.5.

2.8.1 Convergence study in a two-dimensional test-case

The first example simulates a pressure wave propagation within a compliant channel in 2D (see, e.g., [67, 45]). We couple the Stokes equations with a damped generalized string model. More precisely, in (2.2) we take

$$\boldsymbol{d} = \begin{pmatrix} 0 \\ \boldsymbol{d}_y \end{pmatrix}, \quad \boldsymbol{L}^{\mathrm{e}}\boldsymbol{d} = \begin{pmatrix} 0 \\ -\lambda_1 \partial_{xx}\boldsymbol{d}_y + \lambda_0 \boldsymbol{d}_y \end{pmatrix}, \quad \boldsymbol{L}^{\mathrm{v}}\dot{\boldsymbol{d}} = \begin{pmatrix} 0 \\ \alpha\rho^{\mathrm{s}}\epsilon\dot{\boldsymbol{d}}_y - \beta\lambda_1\partial_{xx}\dot{\boldsymbol{d}}_y \end{pmatrix},$$

with $\lambda_1 \overset{\text{def}}{=} E\epsilon/(2(1+\nu))$ and $\lambda_0 \overset{\text{def}}{=} E\epsilon/(R^2(1-\nu^2))$. As usual, here E denotes the Young modulus and ν the Poisson ratio of the solid. All the quantities will be given in the CGS system. The fluid domain and the fluid-solid interface are, respectively, $\Omega = [0, L] \times [0, R]$, $\quad \Sigma = [0, L] \times \{R\}$, with $L = 6$ and $R = 0.5$. At $x = 0$ we impose

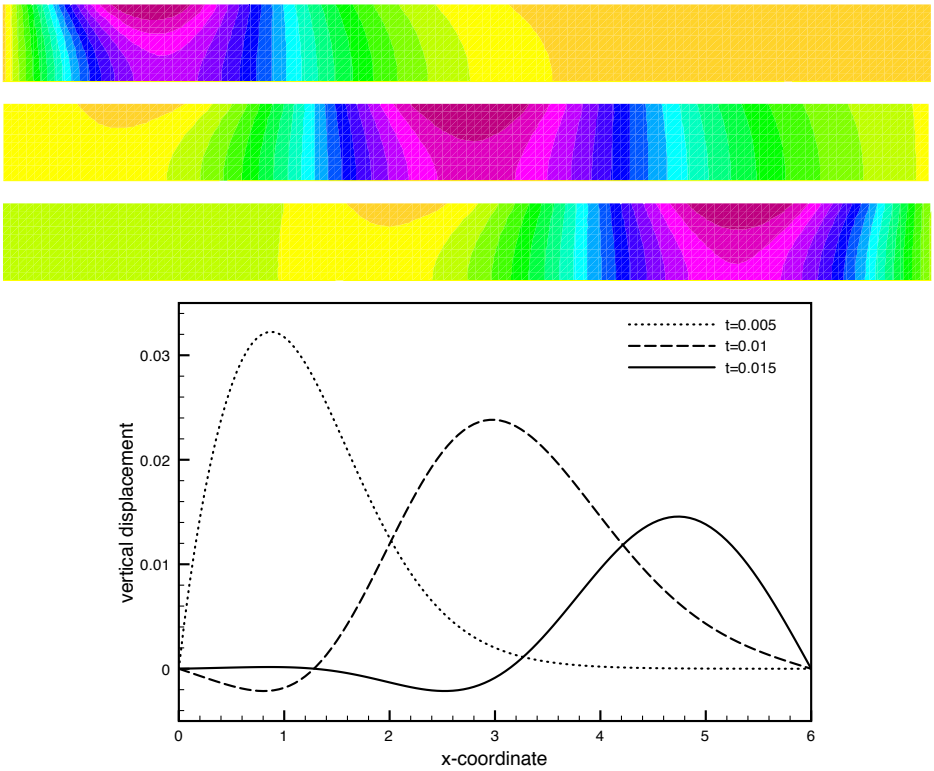

Figure 2.1: Snapshots of the fluid pressure and solid displacement at $t = 0.005, 0.01, 0.015$ (from top to bottom). Algorithm 2.2 with first-order extrapolation, $\tau = 10^{-4}$ and $h = 0.05$.

a sinusoidal normal traction of maximal amplitude $2 \cdot 10^4$ during $5 \cdot 10^{-3}$ seconds, corresponding to half a period. Zero traction is enforced at $x = 6$ and a symmetry condition is applied on the lower wall $y = 0$. The solid is clamped at its extremities, $x = 0, L$. The fluid physical parameters are given by $\rho^{\mathrm{f}} = 1.0$ and $\mu = 0.035$, while for the solid we have $\rho^{\mathrm{s}} = 1.1$, $\epsilon = 0.1$, $E = 0.75 \times 10^6$, $\nu = 0.5$, $\alpha = 1$ and $\beta = 10^{-3}$.

Continuous piece-wise affine approximations are considered for both the fluid and the structure, with the symmetric pressure stabilization method introduced in [13].

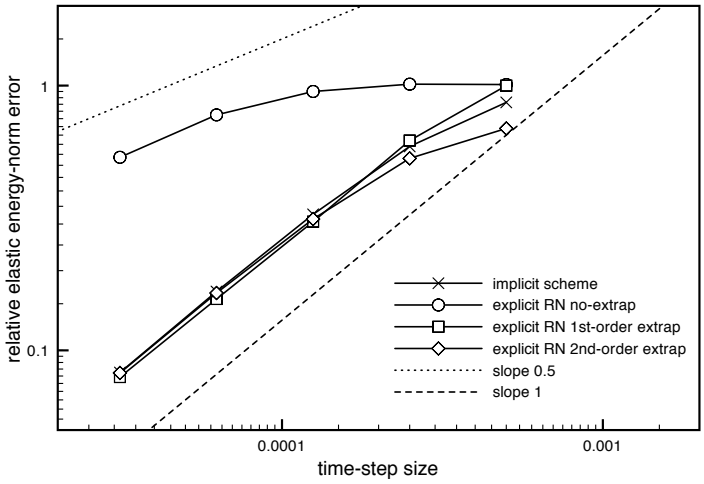

Figure 2.2: Time-convergence history of the displacement at $t = 0.015$, with $h = \mathcal{O}(\tau)$.

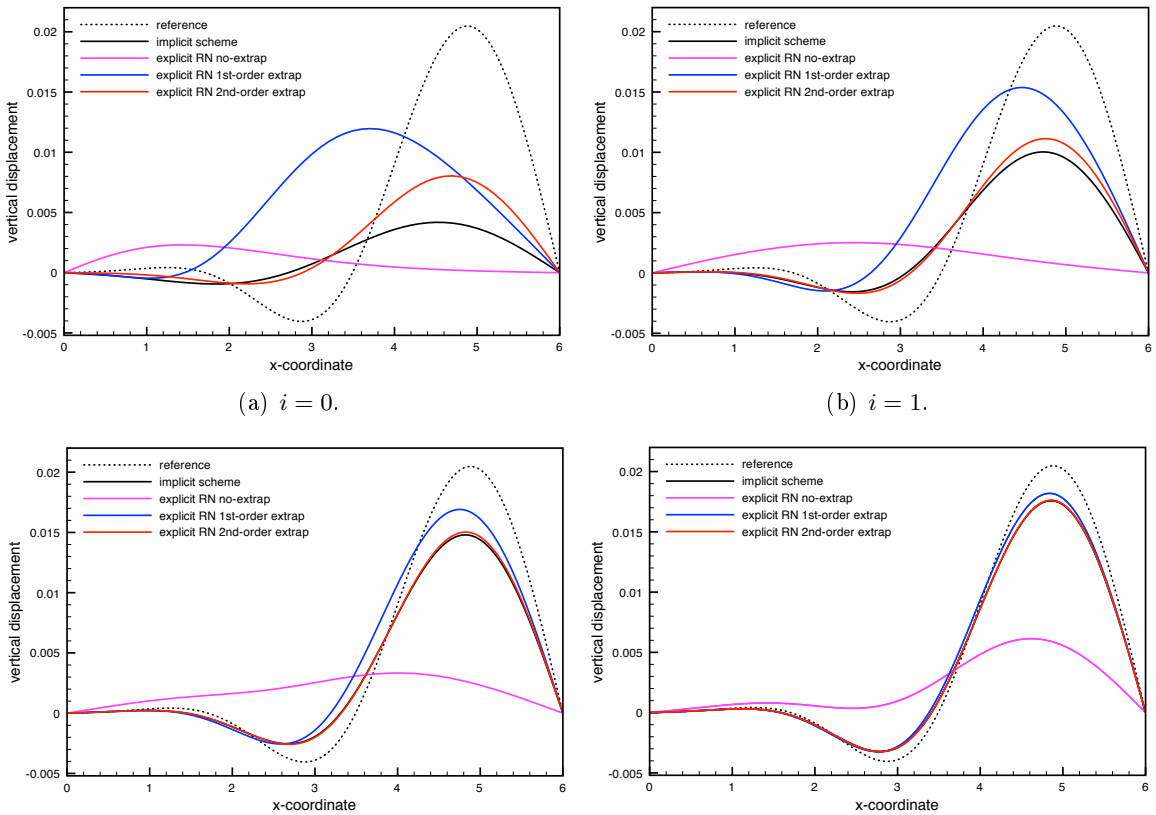

(a) $i = 0$. (b) $i = 1$.

(c) $i = 2$. (d) $i = 3$.

Figure 2.3: Comparison of the solid displacements at $t = 0.015$ for different levels of (τ, h)-refinement, given by (2.84) with $i = 0, \ldots, 3$.

We have reported in Figure 2.1 a few snapshots of the pressure and displacement fields obtained using Algorithm 2.2 with the first-order extrapolation, $\tau = 10^{-4}$ and $h = 0.05$. All the computations have been performed with FreeFem++ [70]. The numerical solution remains stable, as predicted by Theorem 2.4.1, and a propagating pressure-wave is observed.

In order to highlight the h-uniformity of the convergence in time, we have refined both in time and in space at the same rate, with the following set of discrete parameters:

$$(\tau, h) \in \left\{2^{-i}\left(5 \cdot 10^{-4}, 0.1\right)\right\}_{i=0}^{4}. \tag{2.84}$$

A reference solution has been generated using a fully implicit scheme with a high space-time grid resolution ($h = 3.125 \times 10^{-3}$, $\tau = 10^{-6}$). Figure 2.2 reports the corresponding time-convergence history of the solid displacement at time $t = 0.015$, in the relative elastic energy-norm, for the proposed explicit Robin-Neumann schemes (with and without extrapolation) and the implicit scheme. The explicit Robin-Neumann schemes with first- and second-order extrapolation yield an overall $\mathcal{O}(\tau)$ optimal accuracy, while a sub-optimal $\mathcal{O}(\tau^{\frac{1}{2}})$ rate is observed without extrapolation. Thus, in agreement with the error estimates provided by Theorem 2.6.1. The impact of the sub-optimal rate is clearly visible in Figure 2.3, where we have displayed the interface displacements associated to Figure 2.2 (first four points of each curve). For comparison purposes, the reference displacement is also shown. Observe that, even with the smallest time-steps sizes (e.g., Figure 2.3(d)), the Robin-Neumann scheme without extrapolation provides a rather poor approximation. On the contrary, the extrapolated variants are able to retrieve the accuracy of the implicit coupling scheme. In the case of the coupling with an undamped structure (i.e., with $\alpha_0 = \alpha_1 = 0$), a similar behavior was observed in [45].

2.8.2 Pressure wave propagation in a straight tube

The second example is the three-dimensional test-case proposed in [59] (see also [60, Chapter 12]). The fluid domain is a straight tube of radius $R = 0.5$ and of length $L = 5$. All the units are given in the CGS system. The fluid is governed by the incompressible Navier-Stokes equations in ALE formism, discretized in space with $\mathbb{Q}_1/\mathbb{Q}_1$ finite elements and a SUPG/PSPG stabilized formulation. The vessel wall is described by the linear shell model (2.4) (we refer to [26, Section 4.2.1] for the details), discretized in space by quadrilateral MITC4 shell elements (see [26, Section 8.2.1]). The fluid physical parameters are given by $\rho^{\mathrm{f}} = 1.0$ and $\mu = 0.035$, while for the solid we have $\rho^{\mathrm{s}} = 1.2$, $\epsilon = 0.1$, $E = 3 \times 10^6$ and $\nu = 0.5$. We will consider the case of both a Rayleigh solid damping, viz.,

$$\boldsymbol{L}^{\mathrm{v}}_{\boldsymbol{d}}(\dot{\boldsymbol{d}}, \dot{\boldsymbol{\theta}}) = \alpha_0 \rho^{\mathrm{s}} \epsilon \dot{\boldsymbol{d}} + \alpha_1 \boldsymbol{L}^{\mathrm{e}}_{\boldsymbol{d}}(\dot{\boldsymbol{d}}, \dot{\boldsymbol{\theta}}), \quad \text{and} \quad \boldsymbol{L}^{\mathrm{v}}_{\boldsymbol{\theta}}(\dot{\boldsymbol{d}}, \dot{\boldsymbol{\theta}}) = \alpha_1 \boldsymbol{L}^{\mathrm{e}}_{\boldsymbol{\theta}}(\dot{\boldsymbol{d}}, \dot{\boldsymbol{\theta}}),$$

with $\alpha_0 = 1$, $\alpha_1 = 10^{-3}$, and an undamped solid ($\alpha_0 = \alpha_1 = 0$).

The overall system is initially at rest. During the time-interval $[0, 5 \cdot 10^{-3}]$, an over pressure of 1.3332×10^4 is imposed on the inlet boundary. The simulations are carried

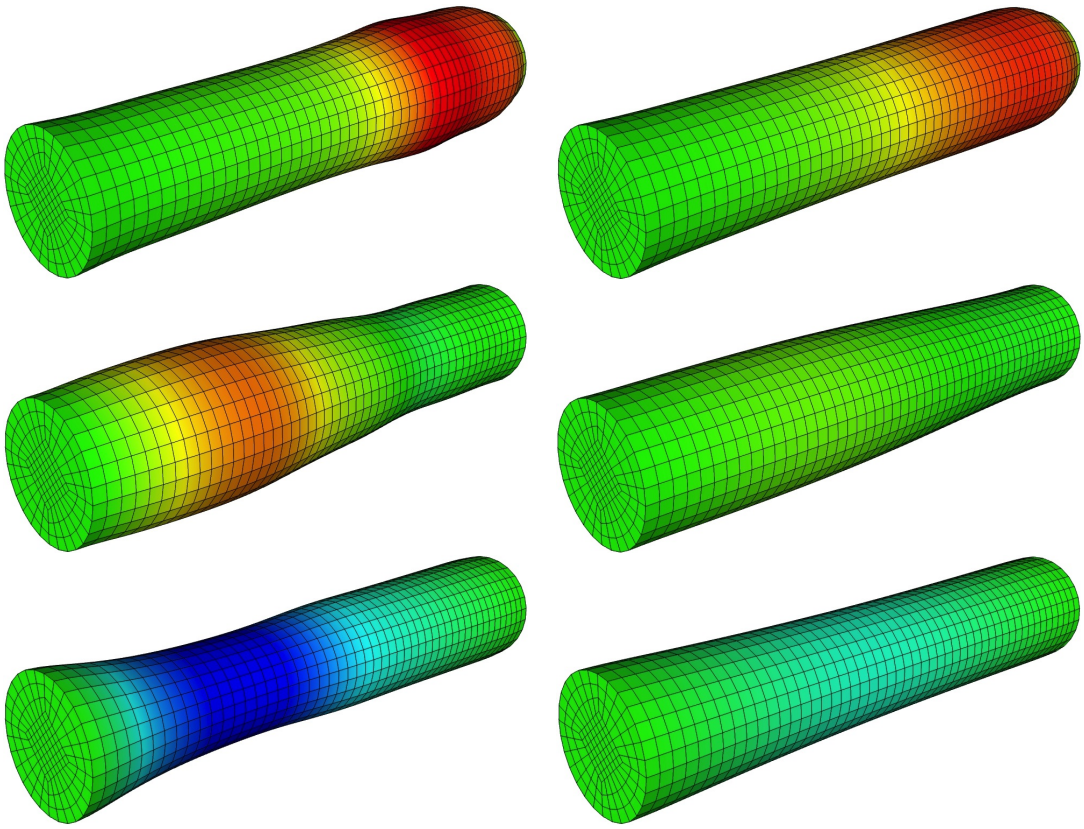

Figure 2.4: Snapshots of the fluid pressure at $t = 0.005, 0.01, 0.015$ (from top to bottom). Algorithm 2.4 with first-order extrapolation, $\tau = 10^{-4}$. Left: Shell model without damping ($\alpha_0 = \alpha_1 = 0$). Right: Shell model with damping ($\alpha_0 = 1$, $\alpha_1 = 10^{-3}$).

out over 150 time-steps of length $\tau = 10^{-4}$. Figure 2.4 shows the fluid pressure and the solid deformation (amplified by a factor 10) at different time instants obtained with Algorithm 2.4 and the first-order extrapolation, $\tau = 10^{-4}$. A stable pressure wave propagation is observed. The impact of the solid damping is also clearly visible.

For comparison purposes, Figure 2.5 reports the interface mid-point displacement magnitudes obtained with Algorithm 2.4 and the implicit coupling scheme. Once more, the Robin-Neumann scheme without extrapolation provides a very poor approximation, while the extrapolated variants are able to retrieve the accuracy of the implicit coupling scheme. It is worth noting that the solid damping has a rather limited impact on the numerical solution without extrapolation. This suggests that the artificial dissipation of the scheme (due to its $\mathcal{O}(\tau^{\frac{1}{2}})$ loss in accuracy) is at least of the same order as the physical dissipation considered in the solid. Similar conclusions can be inferred from Figure 2.6, which reports the out-flows obtained with the different schemes.

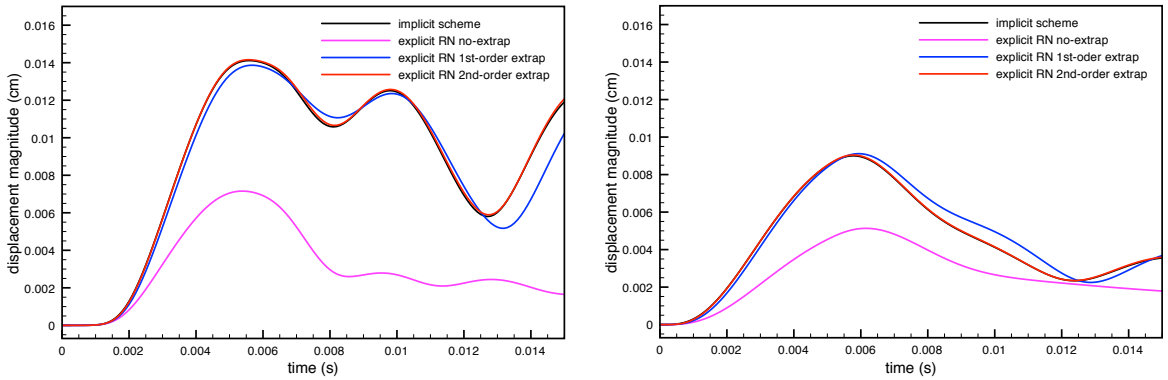

Figure 2.5: Comparison of the implicit and Robin-Neuman explicit coupling schemes: interface mid-point displacement magnitude *vs.* time. Left: Shell model without damping ($\alpha_0 = \alpha_1 = 0$). Right: Shell model with damping ($\alpha_0 = 1$, $\alpha_1 = 10^{-3}$).

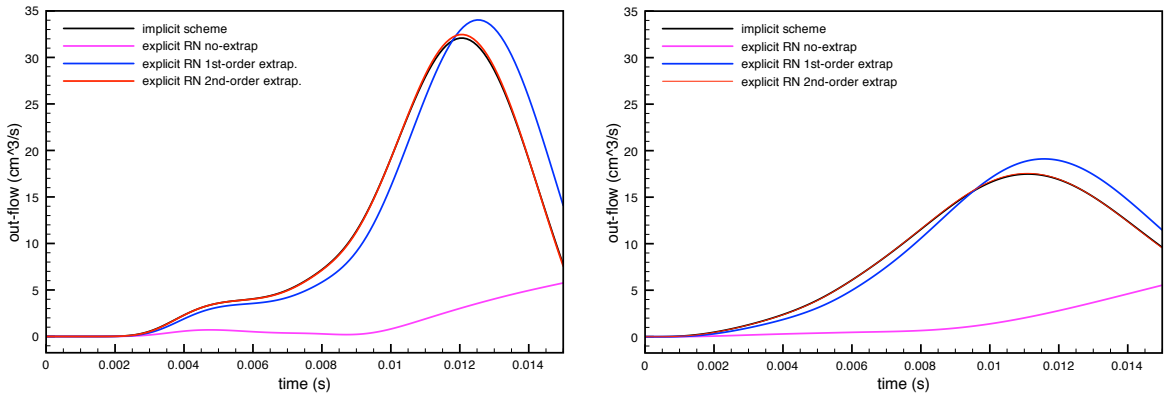

Figure 2.6: Comparison of the implicit and Robin-Neuman explicit coupling schemes: out-flow *vs.* time. Left: Shell model without damping ($\alpha_0 = \alpha_1 = 0$). Right: Shell model with damping ($\alpha_0 = 1$, $\alpha_1 = 10^{-3}$).

2.8.3 Blood flow in an abdominal aortic aneurysm

We consider the numerical example presented in [1] using an *in vitro* aneurysm geometry. The fluid computational domain is the idealized abdominal aortic aneurysm given in Figure 2.7 (left). We refer to [105] for the details. The whole compliant wall has a uniform thickness of 0.17 and length of 22.95. All the units are given in the CGS system. The fluid is governed by the incompressible Navier-Stokes equations in ALE formalism, discretized in space with $\mathbb{Q}_1/\mathbb{Q}_1$ finite elements and a SUPG/PSPG stabilized formulation. The vessel wall is described by the linear shell model (2.4), discretized in space by quadrilateral MITC4 shell elements. The fluid physical parameters are given by $\rho^{\mathrm{f}} = 1.0$ and $\mu = 0.035$, while for the solid we have $\rho^{\mathrm{s}} = 1.2$, $\epsilon = 0.1$, $E = 3 \times 10^6$, $\nu = 0.5$, $\alpha_0 = 1$ and $\alpha_1 = 10^{-3}$. The overall system is initially at rest. An in-flow rate corresponding to a cardiac cycle, see Figure 2.7(right), is imposed on the inlet boundary. A resistive-like boundary condition is prescribed on the outlet

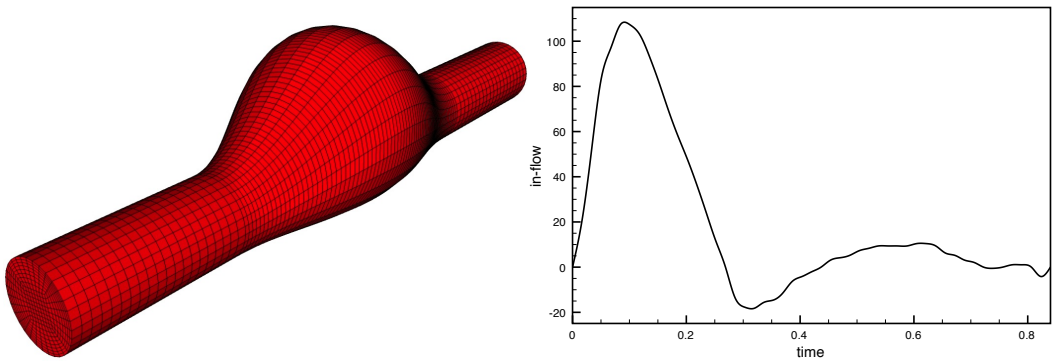

Figure 2.7: Aneurysm geometry (left) and in-flow rate data (right)

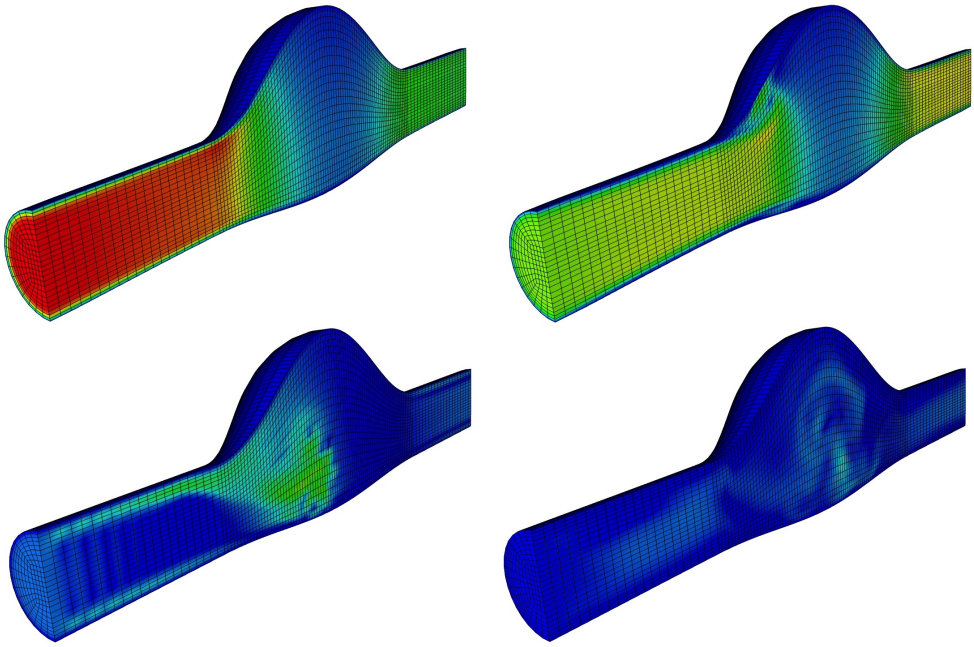

Figure 2.8: Snapshots of the fluid velocity $t = 0.084, 0.168, 0.336, 0.672$ (from left to right and top to bottom). Algorithm 2.4 with first-order extrapolation, $\tau = 4.2 \cdot 10^{-4}$.

boundary, the value of the resistance being $R_{\text{out}} = 6 \times 10^2$.

We have simulated 2000 time-steps of size $\tau = 4.2 \times 10^{-4}$ s, which corresponds to a full cardiac cycle. Figure 2.8 shows the fluid velocity and the solid deformation at different time instants obtained with Algorithm 2.4 and the first-order extrapolation. For comparison purposes, Figure 2.9 reports the interface mid-point displacement magnitudes and out-flow obtained with Algorithm 2.4 and the implicit coupling scheme. The Robin-Neumann schemes with first- and second-order extrapolation provide numerical solutions close to the implicit coupling scheme. The superior accuracy of the higher order kinematic perturbation introduced by the second-order extrapolation is clearly visible. At last, the Robin-Neumann scheme without extrapolation yields an extremely

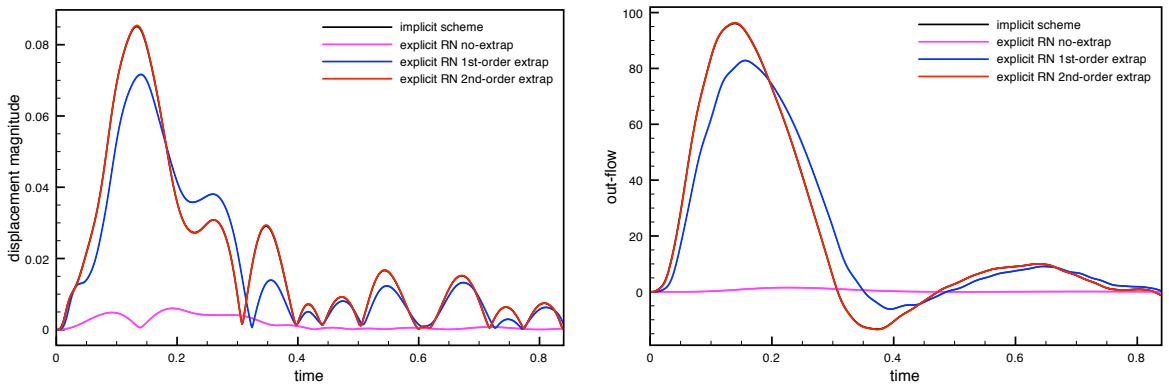

Figure 2.9: Comparison of the implicit and Robin-Neuman explicit coupling schemes: Left: Interface displacement. Right: Out-flow.

poor approximation. Once more, this illustrates the striking impact of the $\mathcal{O}(\tau^{\frac{1}{2}})$-loss on the accuracy of the scheme without extrapolation.

2.8.4 Lid-driven cavity with flexible bottom

We consider the classical shear-driven cavity problem with a flexible bottom (see, e.g., [61]). The fluid domain is the unit square $\Omega = [0,1]\times[0,1]$ with the fluid-solid interface on the lower boundary $\Sigma = [0,1] \times \{0\}$. All the units are given in the SI system. The overall system is initially at rest and an oscillating shear velocity profile is imposed on the upper boundary $\boldsymbol{u}(t) = (1 - \cos(0.4\pi t), 0)^{\mathrm{T}}$ on $[0,1] \times \{1\}$. A non-slip condition is enforced on the portions $\{0,1\} \times [0,0.9]$ of the lateral cavity walls. The system is described by the non-linear coupled problem (2.79)-(2.80), with a non-linear shell model and a Saint Venant-Kirchhoff constitutive law (see [26]). The fluid equations are discretized in space with $\mathbb{Q}_1/\mathbb{Q}_1$ finite elements and a SUPG/PSPG stabilized formulation. Quadrilateral MITC4 shell elements are considered for the structure. The fluid physical parameters are given by $\rho^{\mathrm{f}} = 1.0$ and $\mu = 0.01$, while for the solid (undamped) we have $\rho^{\mathrm{s}} = 250$, $\epsilon = 0.002$, $E = 250$, and $\nu = 0$.

The simulations are performed in three-dimensions, by imposing symmetry conditions along the extrusion direction, and carried out over 800 time-steps of size $\tau = 0.1$. Figure 2.10 shows the fluid velocity and the solid deformation at different time instants obtained with Algorithm 2.4 and the first-order extrapolation.

For comparison purposes, Figure 2.11 reports the interface mid-point displacement magnitudes obtained with Algorithm 2.4 and the implicit coupling scheme. Once again, the superior accuracy of the Robin-Neumann schemes with first- and second-order extrapolation is noticeable.

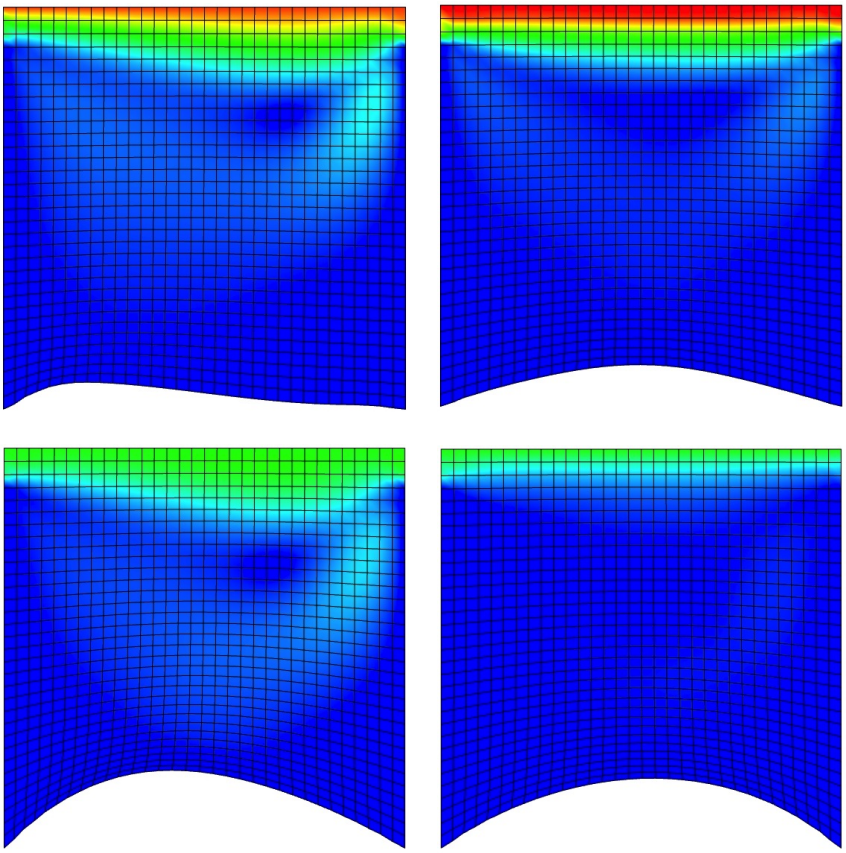

Figure 2.10: Snapshots of the fluid velocity magnitude at $t = 3.5$, 8, 14, 21 (from left to right and top to bottom). Algorithm 2.4 with first-order extrapolation, $\tau = 0.1$.

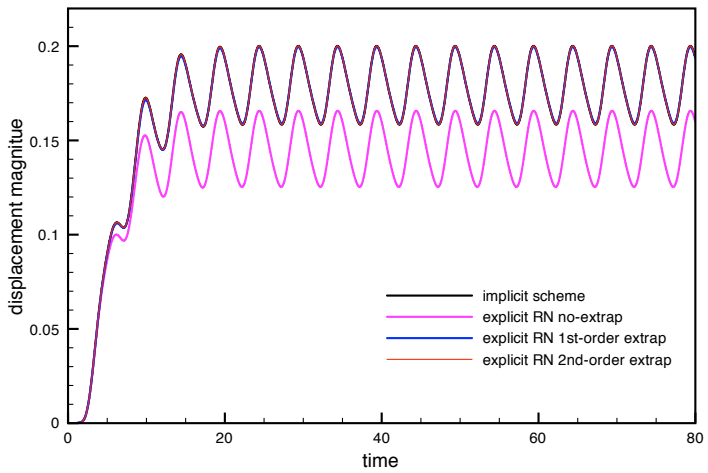

Figure 2.11: Comparison of the implicit and Robin-Neuman explicit coupling schemes: interface mid-point displacement magnitude *vs.* time.

2.8.5 Damped structural instability

The last example considers a curved fluid domain surrounded by two thin structures with different stiffness, as proposed in [80]. Both structures are fixed on their extremities. A constant parabolic velocity profile is prescribed on the left and right inflow

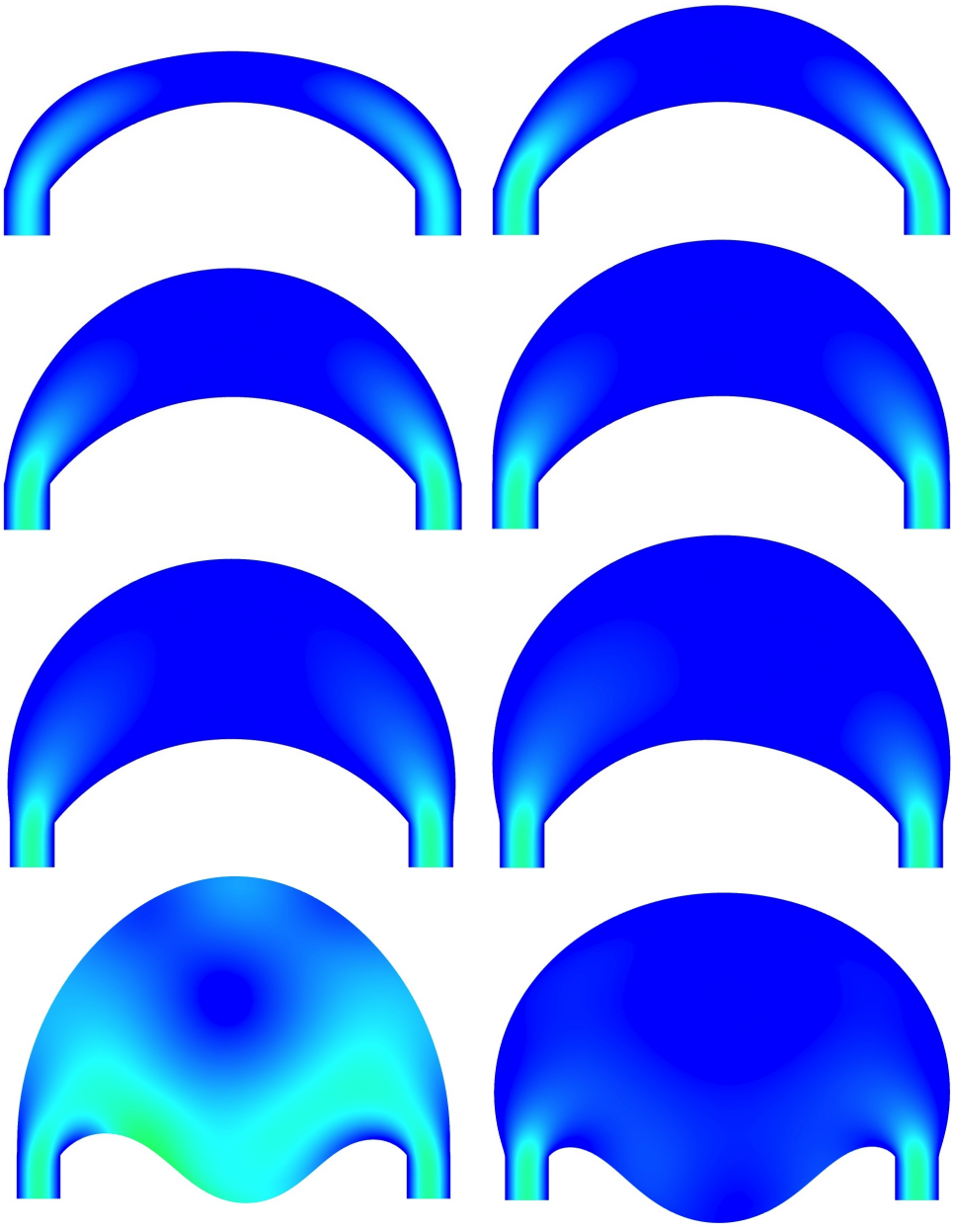

Figure 2.12: Snapshots of the fluid velocity $t = 0.5$, 1, 1.5, 2, 2.5, 3, 3.5, 4 (from left to right and top to bottom). Algorithm 2.4 with first-order extrapolation.

boundaries, with maximal magnitudes 10 and 10.1, respectively (to avoid perfect sym-

metry). All the units are given in the SI system. Zero velocity is enforced on the remaining fluid boundaries. The fluid is loaded with the volume force $\boldsymbol{f} = (0, -1)^{\mathrm{T}}$. As in the previous example, the system is described by the non-linear coupled problem (2.79)-(2.80), with a non-linear shell model and a Saint Venant-Kirchhoff constitutive law. We consider also the same spatial discretization. The fluid physical parameters are given by $\rho^{\mathrm{f}} = 1.0$ and $\mu = 9$, while for the top and bottom (undamped) structures we have $\rho^{\mathrm{s}} = 500$, $\epsilon = 0.1$, $E_{\mathrm{top}} = 9 \cdot 10^5$, $E_{\mathrm{bottom}} = 9 \cdot 10^8$ and $\nu = 0.3$. The simulations are performed in three-dimensions by imposing symmetry conditions along the extrusion direction.

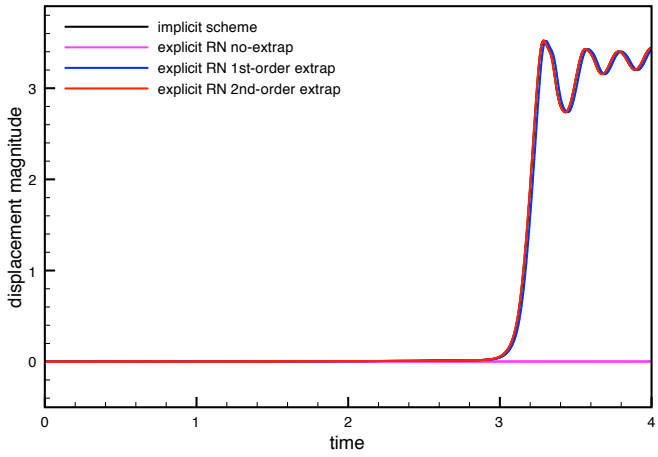

Figure 2.13: Comparison of the of the implicit and Robin-Neuman explicit coupling schemes: interface mid-point displacement magnitude of the bottom structure *vs.* time.

A salient difficulty of this *ballon-type* problem is that it cannot be solved via standard Dirichlet-Neumann procedures, since the interface solid velocity does not necessarily satisfy the compatibility condition enforced by the incompressibility of the fluid (unless directly prescribed in the structure [80]). The explicit Robin-Neumann coupling schemes given by Algorithm 2.4 get rid of this issue without any extra adjustment. Indeed, the consistent perturbation of the kinematic coupling induced by the Robin-Neumann interface conditions removes the constraint on the interface solid velocity.

In Figure 2.12 we have reported the fluid velocity magnitude snapshots and the solid deformations at different time instants, obtained with Algorithm 2.4 (first-order extrapolation) and time-step length of $\tau = 0.005$. As in [80], the deformation is first mainly visible in the upper (more flexible) structure and then, when the fluid pressure reaches a critical value, the lower structure buckles.

Figure 2.13 reports the interface mid-point displacement magnitude of the bottom structure obtained with Algorithm 2.4 and the implicit coupling scheme. The poor accuracy of the Robin-Neumann scheme without extrapolation is striking: the lower order perturbation of the kinematic coupling yields an excess of mass-loss across the

interface which prevents the buckling. On the contrary, the variants with the first- and second-order extrapolations give practically the same result as the implicit scheme and predict the collapse of the bottom structure.

2.9 Conclusion

In this chapter, we have introduced and analyzed a class of explicit Robin-Neumann schemes for the coupling of a viscous incompressible fluid and a general thin-walled structure (including damping and non-linear behavior). The basis of these methods is the underlying Robin consistency of the interface coupling. This has motivated an explicit Robin interface condition for the fluid, which combines extrapolations of the solid viscoelastic contributions with an implicit treatment of the solid inertia. The former enables full fluid-solid splitting (i.e., explicit coupling), while the latter guarantees added-mass free stability (Theorem 2.4.1).

The schemes admit an intrinsic explicit Robin-Neumann formulation which makes them genuinely partitioned: only extrapolations of the solid velocity and interface fluid stress are necessary. The methods have been interpreted as single iterations, with appropriate initializations, of a (parameter free) Robin-Neumann iterative solution procedure of implicit coupling. New insights on the convergence of these procedures (Theorem 2.5.1) have been derived from this connection.

The error analysis (Theorem 2.6.1) has shown that the variants with extrapolation yield an optimal first time-accuracy in the energy-norm, while a sub-optimal convergence rate is expected without extrapolation. In summary, the key result is that the explicit Robin-Neumann scheme with first-order extrapolation simultaneously yields added-mass free unconditional stability and optimal (first-order) time accuracy.

A comprehensive list of numerical tests from the literature confirmed these findings, and indicate that the proposed methods provide a simple and robust approach to the explicit coupling of fluid-structure interaction problems, involving an incompressible fluid and a thin-walled structure.

The next chapter is devoted to the generalization of this approach to the case of the coupling with thick-walled structures.

Chapter 3

Generalized Robin-Neumann explicit coupling schemes for the coupling with general thick-walled structures

The results presented in this chapter lead to the paper [57]: M.A. Fernández, J. Mullaert, M. Vidrascu. **Generalized Robin-Neumann explicit coupling schemes for incompressible fluid-structure interaction: stability analysis and numerics**. *Internat. J. Numer. Methods Engrg.*, 2014, DOI: 10.1002/nme.4785.

Some preliminary results of this chapter have been announced, without proof, in [54]: M.A. Fernández, J. Mullaert. **Displacement-velocity correction schemes for incompressible fluid-structure interaction.** *C. R. Math. Acad. Sci. Paris*, 349(17-18):1011–1015, 2011.

Contents

3.1 Introduction . . . 82
3.2 Problem setting . . . 83
3.3 Generalized Robin-Neumann methods . . . 84
3.3.1 Space semi-discretization . . . 84
3.3.2 Generalized interface Robin consistency . . . 86
3.3.3 Time discretization: explicit coupling schemes . . . 88
3.3.4 Partitioned solution of implicit coupling . . . 93
3.4 Numerical analysis . . . 94
3.4.1 Preliminaries . . . 95
3.4.2 Stability analysis of the explicit coupling schemes . . . 97
3.4.3 Convergence of the iterative solution procedure . . . 101
3.5 The non-linear case . . . 103
3.5.1 The non-linear coupled problem . . . 103
3.5.2 Explicit coupling schemes . . . 104
3.6 Numerical experiments . . . 105
3.6.1 Numerical study in a two-dimensional test-case . . . 105
3.6.2 Pressure wave propagation in a straight tube . . . 111
3.6.3 Cantilever test problem . . . 112
3.6.4 Damped structural instability . . . 115
3.7 Conclusion . . . 116

3.1 Introduction

The design of explicit coupling schemes requires a careful treatment of the interface condition, to avoid added-mass issues that can compromise stability and convergence. In the case of the coupling with a thin-walled structure, both added-mass free stability and optimal (first-order) time accuracy are obtained with the explicit Robin-Neumann schemes proposed in Chapter 2. The fundamental ingredient in the derivation of these schemes is the interface Robin consistency of the continuous problem, which is intimately related to thin-walled character of the solid model.

In this chapter, we propose an extension (the first, to the best of our knowledge) of the explicit coupling schemes reported in Chapter 2 to the case of the coupling with thick-walled structures: linear and non-linear (possibly damped) elasticity. We show that an intrinsic (parameter free) interface Robin consistency can be recovered at the space semi-discrete level, using a lumped-mass approximation in the structure. Instead of the usual identity operator, the generalized Robin condition involves a new interface operator which consistently accounts for the solid inertial effects within the fluid. The fluid-solid splitting is hence performed through appropriate extrapolations of the solid velocity and stress on the interface. A priori energy estimates, guaranteeing (added-mass) free stability, are derived for all the extrapolations considered within a representative linear framework.

The second contribution of this work deals with the partitioned solution of implicit coupling. In fact, the proposed explicit coupling schemes can be interpreted as a single iteration (with appropriate initializations) of a new Robin-Neumann iterative method. Unlike traditional Robin based procedures (see, e.g., [3]), these iterations are parameter free. Using energy arguments within a representative linear setting, we demonstrate the (added-mass free) convergence of this iterative procedure towards the implicit coupling solution. To the best of our knowledge, the error estimate proposed is the first which yields convergence of a Robin-Neumann procedure in the framework of the coupling with a thick-walled structure (linear viscoelasticity).

Several numerical experiments, based on different linear and non-linear fluid-structure interaction examples from the literature, illustrate the accuracy and performance of the methods proposed.

This chapter is organized as follows. In Section 3.2, we present the linear continuous setting which serves as model coupled problem. In Section 3.3, we introduce the generalized Robin-Neumann explicit coupling schemes. The iterative procedure for the partitioned solution of implicit coupling is also presented. Section 3.4 is devoted to the numerical analysis of the methods. In Section 3.5, the coupling schemes are formulated in a fully non-linear framework. The numerical experiments are reported in Section 3.6. Finally, Section 3.7 summarizes the conclusions.

3.2 Problem setting

In this part, we consider a linear modelization of a fluid-structure system described by the Stokes equations in a domain $\Omega^{\rm f} \subset \mathbb{R}^d$ and by the linear visco-elasticity equations in an adjacent domain $\Omega^{\rm s} \subset \mathbb{R}^d$ ($d = 2$ or 3). We denote by $\Sigma \stackrel{\rm def}{=} \partial\Omega^{\rm s} \cap \partial\Omega^{\rm f}$ the fluid-structure interface. We assume that $\partial\Omega^{\rm f} = \Gamma^{\rm f,d} \cup \Gamma^{\rm f,n} \cup \Sigma$ and $\partial\Omega^{\rm s} = \Gamma^{\rm s,d} \cup \Gamma^{\rm s,n} \cup \Sigma$ are given partitions of the fluid and solid boundaries, respectively.

The considered linear coupled problem reads therefore as follows: find the fluid velocity $\boldsymbol{u} : \Omega^{\rm f} \times \mathbb{R}^+ \to \mathbb{R}^d$, the fluid pressure $p : \Omega^{\rm f} \times \mathbb{R}^+ \to \mathbb{R}$, the structure displacement $\boldsymbol{d} : \Omega^{\rm s} \times \mathbb{R}^+ \to \mathbb{R}^d$ and the structure velocity $\dot{\boldsymbol{d}} : \Omega^{\rm s} \times \mathbb{R}^+ \to \mathbb{R}^d$ such that

$$\text{(Fluid)} \quad \left\{ \begin{array}{rl} \rho^{\rm f}\partial_t \boldsymbol{u} - \mathbf{div}\,\boldsymbol{\sigma}^{\rm f}(\boldsymbol{u},p) = \boldsymbol{0} & \text{in} \quad \Omega^{\rm f}, \\ {\rm div}\boldsymbol{u} = 0 & \text{in} \quad \Omega^{\rm f}, \\ \boldsymbol{u} = \boldsymbol{0} & \text{on} \quad \Gamma^{\rm f,d}, \\ \boldsymbol{\sigma}^{\rm f}(\boldsymbol{u},p)\boldsymbol{n}^{\rm f} = \boldsymbol{h} & \text{on} \quad \Gamma^{\rm f,n}, \end{array} \right. \tag{3.1}$$

$$\text{(Solid)} \quad \left\{ \begin{array}{rl} \rho^{\rm s}\partial_t \dot{\boldsymbol{d}} - \mathbf{div}\boldsymbol{\sigma}^{\rm s}(\boldsymbol{d},\dot{\boldsymbol{d}}) + \alpha_0\rho^{\rm s}\dot{\boldsymbol{d}} = \boldsymbol{0} & \text{in} \quad \Omega^{\rm s}, \\ \dot{\boldsymbol{d}} = \partial_t \boldsymbol{d} & \text{in} \quad \Omega^{\rm s}, \\ \boldsymbol{d} = \boldsymbol{0}, \quad \alpha_1\dot{\boldsymbol{d}} = \boldsymbol{0} & \text{on} \quad \Gamma^{\rm s,d}, \\ \boldsymbol{\sigma}^{\rm s}(\boldsymbol{d},\dot{\boldsymbol{d}})\boldsymbol{n}^{\rm s} = \boldsymbol{0} & \text{on} \quad \Gamma^{\rm s,n}, \end{array} \right. \tag{3.2}$$

$$\text{(Coupling)} \quad \left\{ \begin{array}{rl} \boldsymbol{u} = \dot{\boldsymbol{d}} & \text{on} \quad \Sigma, \\ \boldsymbol{\sigma}^{\rm s}(\boldsymbol{d},\dot{\boldsymbol{d}})\boldsymbol{n}^{\rm s} = -\boldsymbol{\sigma}^{\rm f}(\boldsymbol{u},p)\boldsymbol{n}^{\rm f} & \text{on} \quad \Sigma \end{array} \right. \tag{3.3}$$

and satisfying the initial conditions $\boldsymbol{u}(0) = \boldsymbol{u}_0$, $\boldsymbol{d}(0) = \boldsymbol{d}_0$ and $\dot{\boldsymbol{d}}(0) = \boldsymbol{v}_0$. Here, $\rho^{\rm f}, \rho^{\rm s} > 0$ stand for the fluid and solid densities, $\boldsymbol{h}$ for a given surface traction on $\Gamma^{\rm f,n}$ and $\boldsymbol{n}^{\rm f}, \boldsymbol{n}^{\rm s}$ for the exterior unit normal vectors to the boundaries of $\Omega^{\rm f}$ and $\Omega^{\rm s}$, respectively. The fluid stress tensor $\boldsymbol{\sigma}^{\rm f}(\boldsymbol{u},p)$ is given by

$$\boldsymbol{\sigma}^{\rm f}(\boldsymbol{u},p) \stackrel{\rm def}{=} -p\boldsymbol{I} + 2\mu\boldsymbol{\epsilon}(\boldsymbol{u}), \quad \boldsymbol{\epsilon}(\boldsymbol{u}) \stackrel{\rm def}{=} \frac{1}{2}(\boldsymbol{\nabla}\boldsymbol{u} + \boldsymbol{\nabla}\boldsymbol{u}^{\rm T}),$$

where $\mu > 0$ denotes the fluid dynamic viscosity. For the solid, the stress tensor is defined by the relations

$$\boldsymbol{\sigma}^{\rm s}(\boldsymbol{d},\dot{\boldsymbol{d}}) \stackrel{\rm def}{=} \boldsymbol{\sigma}(\boldsymbol{d}) + \alpha_1\boldsymbol{\sigma}(\dot{\boldsymbol{d}}), \quad \boldsymbol{\sigma}(\boldsymbol{d}) \stackrel{\rm def}{=} 2L_1\boldsymbol{\epsilon}(\boldsymbol{d}) + L_2({\rm div}\boldsymbol{d})\boldsymbol{I},$$

where $L_1, L_2 > 0$ stand for the Lamé coefficients. Well-posedness results for this type of linear fluid-structure interaction problem can be found in [39].

In what follows, we will make use of the functional spaces

$$\begin{aligned} \boldsymbol{V}^{\rm f} &\stackrel{\rm def}{=} \left\{ \boldsymbol{v}^{\rm s} \in [H^1(\Omega^{\rm f})]^d \,/\, \boldsymbol{v}^{\rm f}|_{\Gamma^{\rm f,d}} = \boldsymbol{0} \right\}, \\ Q &\stackrel{\rm def}{=} L^2(\Omega^{\rm f}), \\ \boldsymbol{V}^{\rm s} &\stackrel{\rm def}{=} \left\{ \boldsymbol{v}^{\rm s} \in [H^1(\Omega^{\rm s})]^d \,/\, \boldsymbol{v}^{\rm s}|_{\Gamma^{\rm s,d}} = \boldsymbol{0} \right\}, \\ \boldsymbol{W} &\stackrel{\rm def}{=} \left\{ (\boldsymbol{v}^{\rm f}, \boldsymbol{v}^{\rm s}) \in \boldsymbol{V}^{\rm f} \times \boldsymbol{V}^{\rm s} \,/\, \boldsymbol{v}^{\rm f}|_{\Sigma} = \boldsymbol{v}^{\rm s}|_{\Sigma} \right\} \end{aligned}$$

and the following bi-linear and linear forms:

$$a(\boldsymbol{u},\boldsymbol{v}^{\rm f}) \stackrel{\rm def}{=} 2\mu\big(\boldsymbol{\epsilon}(\boldsymbol{u}),\boldsymbol{\epsilon}(\boldsymbol{v}^{\rm f})\big)_{\Omega^{\rm f}},\quad b(p,\boldsymbol{v}^{\rm f}) \stackrel{\rm def}{=} -(p,{\rm div}\boldsymbol{v}^{\rm f})_{\Omega^{\rm f}},\quad l(\boldsymbol{v}^{\rm f}) \stackrel{\rm def}{=} (\boldsymbol{h},\boldsymbol{v}^{\rm f})_{\Gamma},$$
$$a^{\rm e}(\boldsymbol{d},\boldsymbol{v}^{\rm s}) \stackrel{\rm def}{=} \big(\boldsymbol{\sigma}(\boldsymbol{d}),\boldsymbol{\epsilon}(\boldsymbol{v}^{\rm s})\big)_{\Omega^{\rm s}},\quad a^{\rm v}(\dot{\boldsymbol{d}},\boldsymbol{v}^{\rm s}) \stackrel{\rm def}{=} \alpha_0\rho^{\rm s}(\dot{\boldsymbol{d}},\boldsymbol{v}^{\rm s})_{\Omega^{\rm s}} + \alpha_1\big(\boldsymbol{\sigma}(\dot{\boldsymbol{d}}),\boldsymbol{\epsilon}(\boldsymbol{v}^{\rm s})\big)_{\Omega^{\rm s}}.$$

Here, the symbol $(\cdot,\cdot)_\omega$ stands for the standard inner-product of $L^2(\omega)$, for a given domain ω of $\mathbb{R}^d$ or $\mathbb{R}^{d-1}$. We denote by $\|\cdot\|_{\rm e}$ and $\|\cdot\|_{\rm v}$ the norms associated to the inner-products $a^{\rm e}$ and $a^{\rm v}$, in particular, we have:

$$\|\dot{\boldsymbol{d}}\|_{\rm v}^2 \stackrel{\rm def}{=} \alpha_0\rho^{\rm s}\|\dot{\boldsymbol{d}}\|_{0,\Omega^{\rm s}}^2 + \alpha_1\|\dot{\boldsymbol{d}}\|_{\rm e}^2.$$

We also set

$$\|\boldsymbol{v}\|_{\boldsymbol{V}} \stackrel{\rm def}{=} \mu^{\frac{1}{2}}\|\boldsymbol{\nabla}\boldsymbol{v}\|_{0,\Omega^{\rm f}},\quad \|q\|_Q \stackrel{\rm def}{=} \mu^{-\frac{1}{2}}\|q\|_{0,\Omega^{\rm f}}.$$

The coupled problem (3.1)-(3.3) admits the following variationnal formulation: for $t>0$, find $(\boldsymbol{u}(t),\dot{\boldsymbol{d}}(t)) \in \boldsymbol{W}$, $p(t)\in Q$ and $\boldsymbol{d}(t)\in \boldsymbol{V}^{\rm s}$ such that

$$\left\{\begin{array}{l} \dot{\boldsymbol{d}} = \partial_t\boldsymbol{d}, \\ \rho^{\rm f}\big(\partial_t\boldsymbol{u},\boldsymbol{v}^{\rm f}\big)_{\Omega^{\rm f}} + a(\boldsymbol{u},\boldsymbol{v}^{\rm f}) + b(p,\boldsymbol{v}^{\rm f}) - b(q,\boldsymbol{u}) \\ \qquad\qquad + \rho^{\rm s}\big(\partial_t\dot{\boldsymbol{d}},\boldsymbol{v}^{\rm s}\big)_{\Omega^{\rm s}} + a^{\rm e}(\boldsymbol{d},\boldsymbol{v}^{\rm s}) + a^{\rm v}(\dot{\boldsymbol{d}},\boldsymbol{v}^{\rm s}) = l(\boldsymbol{v}^{\rm f}), \end{array}\right. \tag{3.4}$$

for all $(\boldsymbol{v}^{\rm f},\boldsymbol{v}^{\rm s})\in\boldsymbol{W}$ and $q\in Q$.

3.3 Generalized Robin-Neumann methods

This section is devoted to the numerical approximation of the coupled problem (3.4). The time-marching procedures proposed (Section 3.3.3 below) allow an uncoupled sequential computation of the fluid and solid discrete approximations (explicit coupling scheme). These methods can be viewed as a generalization to the coupling with thick-walled structures of the Robin-Neumann explicit schemes introduced in Chapter 2.

A fundamental ingredient in the derivation of the schemes reported in Chapter 2 is the interface Robin consistency of the continuous problem. Clearly, this property is not shared by the coupled problem (3.1)-(3.3), since it is intimately related to the thin-walled character of the structure. In Section 3.3.2, we show that an underlying interface Robin consistency can be recovered after discretization in space, using a lumped-mass approximation in the structure. This generalized notion of interface Robin consistency is the basis of the new explicit coupling schemes introduced in Section 3.3.3 and of the new iterative procedure proposed in Section 3.3.4.

3.3.1 Space semi-discretization

In this part, we consider a finite element approximations in space based on continuous piecewise affine functions. The corresponding finite element spaces are denoted by

$$\boldsymbol{V}_h^{\rm f}\subset\boldsymbol{V}^{\rm f},\quad Q_h\subset Q\quad\text{and}\quad \boldsymbol{V}_h^{\rm s}\subset\boldsymbol{V}^{\rm s},$$

where the subscript $h > 0$ indicates the level of spatial refinement. Since the fluid velocity/pressure pair $\boldsymbol{V}_h^{\mathrm{f}}/Q_h$ fails to satisfy the inf-sup condition (see, e.g. [65]), we consider, without loss of generality, a symmetric pressure stabilization method defined by a non-negative bilinear form, $s_h : Q_h \times Q_h \to \mathbb{R}$, entering the abstract framework introduced in [17]. Furthermore, we assume that the fluid and solid discretizations match at the interface, that is,

$$\boldsymbol{\Lambda}_{\Sigma,h} \stackrel{\text{def}}{=} \left\{ \boldsymbol{v}_h^{\mathrm{f}}|_\Sigma \,/\, \boldsymbol{v}_h^{\mathrm{f}} \in \boldsymbol{V}_h^{\mathrm{f}} \right\} = \left\{ \boldsymbol{v}_h^{\mathrm{s}}|_\Sigma \,/\, \boldsymbol{v}_h^{\mathrm{s}} \in \boldsymbol{V}_h^{\mathrm{s}} \right\},$$

and we set

$$\boldsymbol{W}_h \stackrel{\text{def}}{=} \left\{ (\boldsymbol{v}_h^{\mathrm{f}}, \boldsymbol{v}_h^{\mathrm{s}}) \in \boldsymbol{V}_h^{\mathrm{f}} \times \boldsymbol{V}_h^{\mathrm{s}} \,/\, \boldsymbol{v}_h^{\mathrm{f}}|_\Sigma = \boldsymbol{v}_h^{\mathrm{s}}|_\Sigma \right\} \subset \boldsymbol{W},$$

$$\boldsymbol{V}_{\Sigma,h}^{\mathrm{f}} \stackrel{\text{def}}{=} \left\{ \boldsymbol{v}_h^{\mathrm{f}} \in \boldsymbol{V}_h^{\mathrm{f}} \,/\, \boldsymbol{v}_h^{\mathrm{f}}|_\Sigma = \boldsymbol{0} \right\},$$

and

$$\boldsymbol{V}_{\Sigma,h}^{\mathrm{s}} \stackrel{\text{def}}{=} \left\{ \boldsymbol{v}_h^{\mathrm{s}} \in \boldsymbol{V}_h^{\mathrm{s}} \,/\, \boldsymbol{v}_h^{\mathrm{s}}|_\Sigma = \boldsymbol{0} \right\}.$$

We denote by $(\cdot,\cdot)_{\Omega^{\mathrm{s}},h}$ the lumped-mass approximation of the inner-product $(\cdot,\cdot)_{\Omega^{\mathrm{s}}}$ (see, e.g., [78, Section 2.3] and [112, Chapter 15]). We then set

$$\begin{aligned} a^{\mathrm{e}}(\boldsymbol{d}_h, \boldsymbol{v}_h^{\mathrm{s}}) &\stackrel{\text{def}}{=} \left(\boldsymbol{\sigma}(\boldsymbol{d}_h), \boldsymbol{\epsilon}(\boldsymbol{v}_h^{\mathrm{s}})\right)_{\Omega^{\mathrm{s}}}, \\ a_h^{\mathrm{v}}(\dot{\boldsymbol{d}}_h, \boldsymbol{v}_h^{\mathrm{s}}) &\stackrel{\text{def}}{=} \alpha_0 \rho^{\mathrm{s}} (\dot{\boldsymbol{d}}_h, \boldsymbol{v}_h^{\mathrm{s}})_{\Omega^{\mathrm{s}},h} + \alpha_1 a^{\mathrm{e}}(\dot{\boldsymbol{d}}_h, \boldsymbol{v}_h^{\mathrm{s}})_{\Omega^{\mathrm{s}}} \end{aligned} \tag{3.5}$$

for all $\boldsymbol{d}_h, \dot{\boldsymbol{d}}_h, \boldsymbol{v}_h^{\mathrm{s}} \in \boldsymbol{V}_h^{\mathrm{s}}$.

The space semi-discrete formulation of problem (3.4), including a mass-lumping approximation in the structure, reads therefore as follows: for all $t > 0$, find $(\boldsymbol{u}_h(t), \dot{\boldsymbol{d}}_h(t)) \in \boldsymbol{W}_h$, $p_h(t) \in Q_h$ and $\boldsymbol{d}_h(t) \in \boldsymbol{V}_h^{\mathrm{s}}$ such that $\dot{\boldsymbol{d}}_h = \partial_t \boldsymbol{d}_h$ and

$$\begin{aligned} \rho^{\mathrm{f}} \left(\partial_t \boldsymbol{u}_h, \boldsymbol{v}_h^{\mathrm{f}}\right)_{\Omega^{\mathrm{f}}} + a(\boldsymbol{u}_h, \boldsymbol{v}_h^{\mathrm{f}}) + b(p_h, \boldsymbol{v}_h^{\mathrm{f}}) - b(q_h, \boldsymbol{u}_h) + s_h(p_h, q_h) \\ + \rho^{\mathrm{s}} \left(\partial_t \dot{\boldsymbol{d}}_h, \boldsymbol{v}_h^{\mathrm{s}}\right)_{\Omega^{\mathrm{s}},h} + a^{\mathrm{e}}(\boldsymbol{d}_h, \boldsymbol{v}_h^{\mathrm{s}}) + a_h^{\mathrm{v}}(\dot{\boldsymbol{d}}_h, \boldsymbol{v}_h^{\mathrm{s}}) = l(\boldsymbol{v}_h^{\mathrm{f}}), \end{aligned} \tag{3.6}$$

for all $(\boldsymbol{v}_h^{\mathrm{f}}, \boldsymbol{v}_h^{\mathrm{s}}) \in \boldsymbol{W}_h$ and $q_h \in Q_h$.

In what follows, we will consider the standard solid-sided and fluid-sided discrete lifting operators, $\boldsymbol{\mathcal{L}}_h^{\mathrm{s}} : \boldsymbol{\Lambda}_{\Sigma,h} \to \boldsymbol{V}_h^{\mathrm{s}}$ and $\boldsymbol{\mathcal{L}}_h^{\mathrm{f}} : \boldsymbol{\Lambda}_{\Sigma,h} \to \boldsymbol{V}_h^{\mathrm{f}}$, defined for all $\boldsymbol{\xi}_h \in \boldsymbol{\Lambda}_{\Sigma,h}$, such that the nodal values of $\boldsymbol{\mathcal{L}}_h^{\mathrm{s}}\boldsymbol{\xi}_h, \boldsymbol{\mathcal{L}}_h^{\mathrm{f}}\boldsymbol{\xi}_h$ vanish out of Σ and that

$$(\boldsymbol{\mathcal{L}}_h^{\mathrm{s}}\boldsymbol{\xi}_h)|_\Sigma = (\boldsymbol{\mathcal{L}}_h^{\mathrm{f}}\boldsymbol{\xi}_h)|_\Sigma = \boldsymbol{\xi}_h.$$

Note that, for all $\boldsymbol{v}_h^{\mathrm{s}} \in \boldsymbol{V}_h^{\mathrm{s}}$, we have the standard decomposition

$$\boldsymbol{v}_h^{\mathrm{s}} = \boldsymbol{\mathcal{L}}_h^{\mathrm{s}}\boldsymbol{v}_h^{\mathrm{s}} + \boldsymbol{v}_h^{\mathrm{s}} - \boldsymbol{\mathcal{L}}_h^{\mathrm{s}}\boldsymbol{v}_h^{\mathrm{s}} = \boldsymbol{\mathcal{L}}_h^{\mathrm{s}}\boldsymbol{v}_h^{\mathrm{s}} + \widetilde{\boldsymbol{v}_h^{\mathrm{s}}}, \tag{3.7}$$

with $\widetilde{\boldsymbol{v}_h^{\mathrm{s}}} \stackrel{\text{def}}{=} \boldsymbol{v}_h^{\mathrm{s}} - \boldsymbol{\mathcal{L}}_h^{\mathrm{s}}\boldsymbol{v}_h^{\mathrm{s}} \in \boldsymbol{V}_{\Sigma,h}^{\mathrm{s}}$.

We introduce also the interface operator $\boldsymbol{B}_h : \boldsymbol{\Lambda}_{\Sigma,h} \to \boldsymbol{\Lambda}_{\Sigma,h}$, defined by

$$\boldsymbol{B}_h \stackrel{\text{def}}{=} \left(\boldsymbol{\mathcal{L}}_h^{\mathrm{s}}\right)^\star \boldsymbol{\mathcal{L}}_h^{\mathrm{s}},$$

where $\left(\boldsymbol{\mathcal{L}}_h^{\mathrm{s}}\right)^\star$ stands for the adjoint operator of $\boldsymbol{\mathcal{L}}_h^{\mathrm{s}}$ with respect to the lumped-mass inner product in $\boldsymbol{V}_h^{\mathrm{s}}$. Hence, we have

$$\left(\boldsymbol{B}_h\boldsymbol{\xi}_h,\boldsymbol{\lambda}_h\right)_\Sigma=\left(\boldsymbol{\mathcal{L}}_h^{\mathrm{s}}\boldsymbol{\xi}_h,\boldsymbol{\mathcal{L}}_h^{\mathrm{s}}\boldsymbol{\lambda}_h\right)_{\Omega^{\mathrm{s}},h} \tag{3.8}$$

for all $(\boldsymbol{\xi}_h,\boldsymbol{\lambda}_h)\in\boldsymbol{\Lambda}_{\Sigma,h}\times\boldsymbol{\Lambda}_{\Sigma,h}$. A straightforward argument shows that the interface operator $\boldsymbol{B}_h$ is self-adjoint, positive definite and diagonal with respect to the finite element basis of $\boldsymbol{\Lambda}_{\Sigma,h}$.

Remark 3.3.1. *In order to simplify the presentation, for $\boldsymbol{v}_h^{\mathrm{s}}\in\boldsymbol{V}_h^{\mathrm{s}}$, we will use the notation $\boldsymbol{\mathcal{L}}_h^{\mathrm{s}}\boldsymbol{v}_h^{\mathrm{s}}$ instead of $\boldsymbol{\mathcal{L}}_h^{\mathrm{s}}(\boldsymbol{v}_h^{\mathrm{s}}|_\Sigma)$. The same applies to $\boldsymbol{\mathcal{L}}_h^{\mathrm{f}}$ and $\boldsymbol{B}_h$.*

In the next section, we will make extensive use of the following result:

Lemma 3.3.1. *For all $(\boldsymbol{v}_h^{\mathrm{s}},\boldsymbol{\xi}_h)\in\boldsymbol{V}_h^{\mathrm{s}}\times\boldsymbol{\Lambda}_{\Sigma,h}$, we have*

$$\left(\boldsymbol{v}_h^{\mathrm{s}},\boldsymbol{\mathcal{L}}_h^{\mathrm{s}}\boldsymbol{\xi}_h\right)_{\Omega^{\mathrm{s}},h}=\left(\boldsymbol{B}_h\boldsymbol{v}_h^{\mathrm{s}},\boldsymbol{\xi}_h\right)_\Sigma. \tag{3.9}$$

Proof. For all $\boldsymbol{v}_h^{\mathrm{s}}\in\boldsymbol{V}_h^{\mathrm{s}}$, we consider the decomposition $\boldsymbol{v}_h^{\mathrm{s}}=\widetilde{\boldsymbol{v}}_h^{\mathrm{s}}+\boldsymbol{\mathcal{L}}_h^{\mathrm{s}}\boldsymbol{v}_h^{\mathrm{s}}$, with $\widetilde{\boldsymbol{v}}_h^{\mathrm{s}}\in\boldsymbol{V}_{\Sigma,h}^{\mathrm{s}}$. We then observe that $\left(\widetilde{\boldsymbol{v}}_h^{\mathrm{s}},\boldsymbol{\mathcal{L}}_h^{\mathrm{s}}\boldsymbol{\xi}_h\right)_{\Omega^{\mathrm{s}},h}=0$ for all $\boldsymbol{\xi}_h\in\boldsymbol{\Lambda}_{\Sigma,h}$, by the construction of the lumped-mass approximation. Hence, owing to (3.8), we have

$$\left(\boldsymbol{v}_h^{\mathrm{s}},\boldsymbol{\mathcal{L}}_h^{\mathrm{s}}\boldsymbol{\xi}_h\right)_{\Omega^{\mathrm{s}},h}=\left(\boldsymbol{\mathcal{L}}_h^{\mathrm{s}}\boldsymbol{v}_h^{\mathrm{s}},\boldsymbol{\mathcal{L}}_h^{\mathrm{s}}\boldsymbol{\xi}_h\right)_{\Omega^{\mathrm{s}},h}+\left(\widetilde{\boldsymbol{v}}_h^{\mathrm{s}},\boldsymbol{\mathcal{L}}_h^{\mathrm{s}}\boldsymbol{\xi}_h\right)_{\Omega^{\mathrm{s}},h}=\left(\boldsymbol{B}_h\boldsymbol{v}_h^{\mathrm{s}},\boldsymbol{\xi}_h\right)_\Sigma,$$

which completes the proof. □

Remark 3.3.2. *Since, by construction, the matrix associated to the lumped-mass inner product is diagonal, from* (3.8) *we infer that the algebraic counterpart of $\boldsymbol{B}_h$ is also a diagonal matrix. In particular, the diagonal entries of this matrix are the diagonal entries of the solid lumped-mass matrix on the interface Σ (see Section 3.3.3.1).*

Remark 3.3.3. *Lemma 3.3.1 and the results of Section 3.4 below do not require any specific condition on the mass-lumping approximation, only nodal quadrature and matrix invertibility are assumed. Thus, even though* (3.6) *is based on low-order $\mathbb{P}_1$ (we could also use $\mathbb{Q}_1$) Lagrange finite elements (for which a simple vertex-ruled quadrature yields a diagonal and invertible lumped-mass matrix without any loss of accuracy), the methods and results of this chapter can be extended to the case of higher-order spatial approximations ($\mathbb{P}_k$ or $\mathbb{Q}_k$, $k>1$) for which mass-lumping is still feasible but more delicate (see, e.g., [78, Section 2.3]).*

3.3.2 Generalized interface Robin consistency

The most basic partitioned procedures for the numerical solution of (3.1)-(3.3) are generally based on the following Dirichlet-Neumann formulation of problem (3.6): for $t>0$,

- Fluid (Dirichlet): find $(\boldsymbol{u}_h(t), p_h(t)) \in \boldsymbol{V}_h^{\mathrm{f}} \times Q_h$ such that

$$\begin{cases} \boldsymbol{u}_h|_\Sigma = \dot{\boldsymbol{d}}_h|_\Sigma, \\ \rho^{\mathrm{f}}\big(\partial_t \boldsymbol{u}_h, \widetilde{\boldsymbol{v}}_h^{\mathrm{f}}\big)_{\Omega^{\mathrm{f}}} + a(\boldsymbol{u}_h, \widetilde{\boldsymbol{v}}_h^{\mathrm{f}}) + b(p_h, \widetilde{\boldsymbol{v}}_h^{\mathrm{f}}) - b(q_h, \boldsymbol{u}_h) + s_h(p_h, q_h) \\ \quad = l(\widetilde{\boldsymbol{v}}_h^{\mathrm{f}}) \end{cases} \tag{3.10}$$

  for all $(\widetilde{\boldsymbol{v}}_h^{\mathrm{f}}, q_h) \in \boldsymbol{V}_{\Sigma,h}^{\mathrm{f}} \times Q_h$.

- Solid (Neumann): find $(\dot{\boldsymbol{d}}_h(t), \boldsymbol{d}_h(t)) \in \boldsymbol{V}_h^{\mathrm{s}} \times \boldsymbol{V}_h^{\mathrm{s}}$ such that

$$\begin{cases} \dot{\boldsymbol{d}}_h = \partial_t \boldsymbol{d}_h, \\ \rho^{\mathrm{s}}\big(\partial_t \dot{\boldsymbol{d}}_h, \boldsymbol{v}_h^{\mathrm{s}}\big)_{\Omega^{\mathrm{s}},h} + a^{\mathrm{e}}(\boldsymbol{d}_h, \boldsymbol{v}_h^{\mathrm{s}}) + a_h^{\mathrm{v}}(\dot{\boldsymbol{d}}_h, \boldsymbol{v}_h^{\mathrm{s}}) \\ \quad = -\rho^{\mathrm{f}}\big(\partial_t \boldsymbol{u}_h, \boldsymbol{\mathcal{L}}_h^{\mathrm{f}} \boldsymbol{v}_h^{\mathrm{s}}\big)_{\Omega^{\mathrm{f}}} - a(\boldsymbol{u}_h, \boldsymbol{\mathcal{L}}_h^{\mathrm{f}} \boldsymbol{v}_h^{\mathrm{s}}) - b(p_h, \boldsymbol{\mathcal{L}}_h^{\mathrm{f}} \boldsymbol{v}_h^{\mathrm{s}}) \end{cases} \tag{3.11}$$

  for all $\boldsymbol{v}_h^{\mathrm{s}} \in \boldsymbol{V}_h^{\mathrm{s}}$.

Unfortunately, explicit coupling schemes based on this fluid-solid splitting are known to yield severe added-mass stability issues (see, e.g., [25, 61]). In the next paragraphs, we shall show that the monolithic problem (3.6) admits an alternative partitioned formulation based on (consistent) interface Robin conditions.

For this purpose, we test (3.11) with $\boldsymbol{v}_h^{\mathrm{s}} = \boldsymbol{\mathcal{L}}_h^{\mathrm{s}} \boldsymbol{\xi}_h$ for all $\boldsymbol{\xi}_h \in \boldsymbol{\Lambda}_{\Sigma,h}$, to get

$$\begin{aligned} &\rho^{\mathrm{f}}\big(\partial_t \boldsymbol{u}_h, \boldsymbol{\mathcal{L}}_h^{\mathrm{f}} \boldsymbol{\xi}_h\big)_{\Omega^{\mathrm{f}}} + a(\boldsymbol{u}_h, \boldsymbol{\mathcal{L}}_h^{\mathrm{f}} \boldsymbol{\xi}_h) + b(p_h, \boldsymbol{\mathcal{L}}_h^{\mathrm{f}} \boldsymbol{\xi}_h) \\ &\qquad + \rho^{\mathrm{s}}\big(\partial_t \dot{\boldsymbol{d}}_h, \boldsymbol{\mathcal{L}}_h^{\mathrm{s}} \boldsymbol{\xi}_h\big)_{\Omega^{\mathrm{s}},h} + a^{\mathrm{e}}(\boldsymbol{d}_h, \boldsymbol{\mathcal{L}}_h^{\mathrm{s}} \boldsymbol{\xi}_h) + a_h^{\mathrm{v}}(\dot{\boldsymbol{d}}_h, \boldsymbol{\mathcal{L}}_h^{\mathrm{s}} \boldsymbol{\xi}_h) = 0. \end{aligned} \tag{3.12}$$

It should be noted that this relation is nothing but the spatial discrete counterpart of the interface kinetic condition $(3.3)_2$. Furthermore, since $\boldsymbol{u}_h|_\Sigma = \dot{\boldsymbol{d}}_h|_\Sigma$, from (3.9) we have

$$\big(\partial_t \dot{\boldsymbol{d}}_h, \boldsymbol{\mathcal{L}}_h^{\mathrm{s}} \boldsymbol{\xi}_h\big)_{\Omega^{\mathrm{s}},h} = \big(\boldsymbol{B}_h \partial_t \dot{\boldsymbol{d}}_h, \boldsymbol{\xi}_h\big)_\Sigma = \big(\boldsymbol{B}_h \partial_t \boldsymbol{u}_h, \boldsymbol{\xi}_h\big)_\Sigma. \tag{3.13}$$

The relation (3.12) can thus be rewritten as

$$\begin{aligned} &\rho^{\mathrm{f}}\big(\partial_t \boldsymbol{u}_h, \boldsymbol{\mathcal{L}}_h^{\mathrm{f}} \boldsymbol{\xi}_h\big)_{\Omega^{\mathrm{f}}} + a(\boldsymbol{u}_h, \boldsymbol{\mathcal{L}}_h^{\mathrm{f}} \boldsymbol{\xi}_h) + b(p_h, \boldsymbol{\mathcal{L}}_h^{\mathrm{f}} \boldsymbol{\xi}_h) \\ &\qquad + \rho^{\mathrm{s}}\big(\boldsymbol{B}_h \partial_t \boldsymbol{u}_h, \boldsymbol{\xi}_h\big)_\Sigma = -a^{\mathrm{e}}(\boldsymbol{d}_h, \boldsymbol{\mathcal{L}}_h^{\mathrm{s}} \boldsymbol{\xi}_h) - a_h^{\mathrm{v}}(\dot{\boldsymbol{d}}_h, \boldsymbol{\mathcal{L}}_h^{\mathrm{s}} \boldsymbol{\xi}_h) \end{aligned} \tag{3.14}$$

for all $\boldsymbol{\xi}_h \in \boldsymbol{\Lambda}_{\Sigma,h}$. Equivalently, the addition and subtraction of $\rho^{\mathrm{s}}\big(\partial_t \dot{\boldsymbol{d}}_h, \boldsymbol{\mathcal{L}}_h^{\mathrm{s}} \boldsymbol{\xi}_h\big)_{\Omega^{\mathrm{s}},h}$, in combination with (3.13), yields

$$\begin{aligned} &\rho^{\mathrm{f}}\big(\partial_t \boldsymbol{u}_h, \boldsymbol{\mathcal{L}}_h^{\mathrm{f}} \boldsymbol{\xi}_h\big)_{\Omega^{\mathrm{f}}} + a(\boldsymbol{u}_h, \boldsymbol{\mathcal{L}}_h^{\mathrm{f}} \boldsymbol{\xi}_h) + b(p_h, \boldsymbol{\mathcal{L}}_h^{\mathrm{f}} \boldsymbol{\xi}_h) \\ &\qquad + \rho^{\mathrm{s}}\big(\boldsymbol{B}_h \partial_t \boldsymbol{u}_h, \boldsymbol{\xi}_h\big)_\Sigma = \rho^{\mathrm{s}}\big(\boldsymbol{B}_h \partial_t \dot{\boldsymbol{d}}_h, \boldsymbol{\xi}_h\big)_\Sigma \\ &\qquad - \Big[\rho^{\mathrm{s}}\big(\partial_t \dot{\boldsymbol{d}}_h, \boldsymbol{\mathcal{L}}_h^{\mathrm{s}} \boldsymbol{\xi}_h\big)_{\Omega^{\mathrm{s}},h} + a^{\mathrm{e}}(\boldsymbol{d}_h, \boldsymbol{\mathcal{L}}_h^{\mathrm{s}} \boldsymbol{\xi}_h) + a_h^{\mathrm{v}}(\dot{\boldsymbol{d}}_h, \boldsymbol{\mathcal{L}}_h^{\mathrm{s}} \boldsymbol{\xi}_h)\Big] \end{aligned} \tag{3.15}$$

for all $\boldsymbol{\xi}_h \in \boldsymbol{\Lambda}_{\Sigma,h}$.

The preceding relation points out a major feature of the space semi-discrete solution given by (3.6): its intrinsic Robin consistency on the interface. Indeed, the identity (3.15) can formally be interpreted as the discrete counterpart of the generalized Robin condition

$$\boldsymbol{\sigma}^{\mathrm{f}}(\boldsymbol{u},p)\boldsymbol{n}^{\mathrm{f}}+\rho^{\mathrm{s}}\boldsymbol{B}_h\partial_t\boldsymbol{u}=\rho^{\mathrm{s}}\boldsymbol{B}_h\partial_t\dot{\boldsymbol{d}}-\boldsymbol{\sigma}^{\mathrm{s}}(\boldsymbol{d},\dot{\boldsymbol{d}})\boldsymbol{n}^{\mathrm{s}}\quad\text{on}\quad\Sigma. \tag{3.16}$$

Note that, instead of the usual identity operator, the interface condition (3.16) involves the interface operator $\boldsymbol{B}_h$ defined by (3.8), hence the terminology *generalized Robin*.

Remark 3.3.4. *It should be noted that, a posteriori, one can obtain* (3.15) *from* (3.12) *and* (3.13). *However, the key ingredient in the derivation of* (3.15) *is the relation* (3.14), *which defines the structure of the Robin operator* $\boldsymbol{B}_h$ *and of multiplying coefficient* ρ^{s}.

By adding (3.15) to (3.10) we get the following Robin sub-problem for the fluid: for $t>0$, find $(\boldsymbol{u}_h(t),p_h(t))\in\boldsymbol{V}_h^{\mathrm{f}}\times Q_h$ such that

$$\begin{aligned}&\rho^{\mathrm{f}}\big(\partial_t\boldsymbol{u}_h,\boldsymbol{v}_h^{\mathrm{f}}\big)_{\Omega^{\mathrm{f}}}+a(\boldsymbol{u}_h,\boldsymbol{v}_h^{\mathrm{f}})+b(p_h,\boldsymbol{v}_h^{\mathrm{f}})-b(q_h,\boldsymbol{u}_h)+s_h(p_h,q_h)\\&\quad+\rho^{\mathrm{s}}\big(\boldsymbol{B}_h\partial_t\boldsymbol{u}_h,\boldsymbol{v}_h^{\mathrm{f}}\big)_{\Sigma}=\rho^{\mathrm{s}}\big(\boldsymbol{B}_h\partial_t\dot{\boldsymbol{d}}_h,\boldsymbol{v}_h^{\mathrm{f}}\big)_{\Sigma}+l(\boldsymbol{v}_h^{\mathrm{f}})\\&\qquad\qquad-\Big[\rho^{\mathrm{s}}\big(\partial_t\dot{\boldsymbol{d}}_h,\boldsymbol{\mathcal{L}}_h^{\mathrm{s}}\boldsymbol{v}_h^{\mathrm{f}}\big)_{\Omega^{\mathrm{s}},h}+a^{\mathrm{e}}(\boldsymbol{d}_h,\boldsymbol{\mathcal{L}}_h^{\mathrm{s}}\boldsymbol{v}_h^{\mathrm{f}})+a_h^{\mathrm{v}}(\dot{\boldsymbol{d}}_h,\boldsymbol{\mathcal{L}}_h^{\mathrm{s}}\boldsymbol{v}_h^{\mathrm{f}})\Big],\end{aligned} \tag{3.17}$$

for all $(\boldsymbol{v}_h^{\mathrm{f}},q_h)\in\boldsymbol{V}_h^{\mathrm{f}}\times Q_h$.

Therefore, instead of formulating the fluid-solid time-splitting from the traditional Dirichlet-Neumann coupling (3.10)-(3.11), in this work we consider the Robin-Neumann formulation given by (3.17) and (3.11). As in Chapter 2, we will see that the benefits of this approach are threefold:

- the implicit treatment of the interface solid inertial term in the left-hand side of (3.16) is enough to guarantee (added-mass free) stability;
- the explicit treatment of the right-hand side of (3.16) enables the full fluid-solid splitting without compromising stability;
- the resulting schemes are genuine partitioned methods with an intrinsic (i.e., parameter free) explicit Robin-Neumann pattern.

3.3.3 Time discretization: explicit coupling schemes

In what follows, the parameter $\tau>0$ stands for the time-step length, $t_n\overset{\text{def}}{=}n\tau$, for $n\in\mathbb{N}$, and $\partial_\tau x^n\overset{\text{def}}{=}(x^n-x^{n-1})/\tau$ for the first-order backward difference. The symbol $x^\star$ denotes the r-order extrapolation of x^n, namely,

$$x^\star\overset{\text{def}}{=}\begin{cases}0 & \text{if}\quad r=0,\\ x^{n-1} & \text{if}\quad r=1,\\ 2x^{n-1}-x^{n-2} & \text{if}\quad r=2.\end{cases}$$

The fully discrete approximation of (3.1)-(3.3) is split into the following sequential sub-steps: for $n > r$,

1. Fluid step (generalized Robin): find $(\boldsymbol{u}_h^n, p_h^n) \in \boldsymbol{V}_h^{\mathrm{f}} \times Q_h$ such that

$$\left\{\begin{array}{l} \rho^{\mathrm{f}}\big(\partial_\tau \boldsymbol{u}_h^n, \boldsymbol{v}_h^{\mathrm{f}}\big)_{\Omega^{\mathrm{f}}} + a(\boldsymbol{u}_h^n, \boldsymbol{v}_h^{\mathrm{f}}) + b(p_h^n, \boldsymbol{v}_h^{\mathrm{f}}) - b(q_h, \boldsymbol{u}_h^n) + s_h(p_h^n, q_h) \\ \qquad + \dfrac{\rho^{\mathrm{s}}}{\tau}\big(\boldsymbol{B}_h \boldsymbol{u}_h^n, \boldsymbol{v}_h^{\mathrm{f}}\big)_\Sigma = \dfrac{\rho^{\mathrm{s}}}{\tau}\big(\boldsymbol{B}_h(\dot{\boldsymbol{d}}_h^{n-1} + \tau\partial_\tau \dot{\boldsymbol{d}}_h^\star), \boldsymbol{v}_h^{\mathrm{f}}\big)_\Sigma + l(\boldsymbol{v}_h^{\mathrm{f}}) \\ \qquad\qquad - \Big[\rho^{\mathrm{s}}\big(\partial_\tau \dot{\boldsymbol{d}}_h^\star, \boldsymbol{\mathcal{L}}_h^{\mathrm{s}} \boldsymbol{v}_h^{\mathrm{f}}\big)_{\Omega^{\mathrm{s}},h} + a^{\mathrm{e}}(\boldsymbol{d}_h^\star, \boldsymbol{\mathcal{L}}_h^{\mathrm{s}} \boldsymbol{v}_h^{\mathrm{f}}) + a_h^{\mathrm{v}}(\dot{\boldsymbol{d}}_h^\star, \boldsymbol{\mathcal{L}}_h^{\mathrm{s}} \boldsymbol{v}_h^{\mathrm{f}})\Big], \end{array}\right. \tag{3.18}$$

   for all $(\boldsymbol{v}_h^{\mathrm{f}}, q_h) \in \boldsymbol{V}_h^{\mathrm{f}} \times Q_h$.

2. Solid step (Neumann): find $(\dot{\boldsymbol{d}}_h^n, \boldsymbol{d}_h^n) \in \boldsymbol{V}_h^{\mathrm{s}} \times \boldsymbol{V}_h^{\mathrm{s}}$ such that

$$\left\{\begin{array}{l} \dot{\boldsymbol{d}}_h^n = \partial_\tau \boldsymbol{d}_h^n, \\ \rho^{\mathrm{s}}\big(\partial_\tau \dot{\boldsymbol{d}}_h^n, \boldsymbol{v}_h^{\mathrm{s}}\big)_{\Omega^{\mathrm{s}},h} + a^{\mathrm{e}}(\boldsymbol{d}_h^n, \boldsymbol{v}_h^{\mathrm{s}}) + a_h^{\mathrm{v}}(\dot{\boldsymbol{d}}_h^n, \boldsymbol{v}_h^{\mathrm{s}}) \\ \quad = -\rho^{\mathrm{f}}\big(\partial_\tau \boldsymbol{u}_h^n, \boldsymbol{\mathcal{L}}_h^{\mathrm{f}} \boldsymbol{v}_h^{\mathrm{s}}\big)_{\Omega^{\mathrm{f}}} - a(\boldsymbol{u}_h^n, \boldsymbol{\mathcal{L}}_h^{\mathrm{f}} \boldsymbol{v}_h^{\mathrm{s}}) - b(p_h^n, \boldsymbol{\mathcal{L}}_h^{\mathrm{f}} \boldsymbol{v}_h^{\mathrm{s}}) \end{array}\right. \tag{3.19}$$

   for all $\boldsymbol{v}_h^{\mathrm{s}} \in \boldsymbol{V}_h^{\mathrm{s}}$.

In strong form, these two steps perform respectively the following time-marching on the interface

$$\left\{\begin{array}{rl} \boldsymbol{\sigma}^{\mathrm{f}}(\boldsymbol{u}^n, p^n)\boldsymbol{n}^{\mathrm{f}} + \dfrac{\rho^{\mathrm{s}}}{\tau}\boldsymbol{B}_h \boldsymbol{u}^n = \dfrac{\rho^{\mathrm{s}}}{\tau}\boldsymbol{B}_h\big(\dot{\boldsymbol{d}}^{n-1} + \tau\partial_\tau \dot{\boldsymbol{d}}^\star\big) - \boldsymbol{\sigma}^{\mathrm{s}}(\boldsymbol{d}^\star, \dot{\boldsymbol{d}}^\star)\boldsymbol{n}^{\mathrm{s}} & \text{on } \Sigma, \\ \boldsymbol{\sigma}^{\mathrm{s}}(\boldsymbol{d}^n, \dot{\boldsymbol{d}}^n)\boldsymbol{n}^{\mathrm{s}} = -\boldsymbol{\sigma}^{\mathrm{f}}(\boldsymbol{u}^n, p^n)\boldsymbol{n}^{\mathrm{f}} & \text{on } \Sigma \end{array}\right. \tag{3.20}$$

for $n > r$. The fundamental ingredient of the splitting (3.18)-(3.19) is the generalized explicit Robin condition $(3.20)_1$, which has been derived as a specific semi-implicit time discretization of (3.16):

- the solid contributions are treated explicitly via extrapolation in the right-hand side of (3.16). This provides the uncoupling of the fluid and solid time-marching (3.18)-(3.19);
- the interface solid inertia is treated implicitly in the left-hand side of (3.16). This guarantees (added-mass free) stability.

Remark 3.3.5. *The explicit coupling scheme* (3.18)-(3.19) *was originally introduced in [54] using, instead of the notion of generalized Robin consistency, an alternative approach based on operator splitting. This derivation is considered in Section 4.2.2.1 of the next chapter. A closely related operator splitting method for the approximation of* (3.1)-(3.3) *is the semi-implicit coupling scheme recently proposed in [14]. The connections and differences between these methods are discussed in Section 4.2.2.2.*

Remark 3.3.6. *The time-splitting induced by* (3.20) *is consistent with the original interface coupling* (3.3)*, in the sense that it can be interpreted as a time discretization of the equivalent interface relations*

$$\begin{cases} \boldsymbol{\sigma}^{\mathrm{f}}(\boldsymbol{u},p)\boldsymbol{n}^{\mathrm{f}} + \boldsymbol{\alpha}_h\boldsymbol{u} = \boldsymbol{\alpha}_h\dot{\boldsymbol{d}} - \boldsymbol{\sigma}^{\mathrm{s}}(\boldsymbol{d},\dot{\boldsymbol{d}})\boldsymbol{n}^{\mathrm{s}} & \text{on} \quad \Sigma, \\ \boldsymbol{\sigma}^{\mathrm{s}}(\boldsymbol{d},\dot{\boldsymbol{d}})\boldsymbol{n}^{\mathrm{s}} = -\boldsymbol{\sigma}^{\mathrm{f}}(\boldsymbol{u},p)\boldsymbol{n}^{\mathrm{f}} & \text{on} \quad \Sigma, \end{cases} \tag{3.21}$$

with the invertible interface operator $\boldsymbol{\alpha}_h \overset{\text{def}}{=} \rho^{\mathrm{s}}\tau^{-1}\boldsymbol{B}_h$*. The right-hand side of* $(3.20)_1$ *is simply an explicit approximation of the right-hand side of* $(3.21)_1$*. Moreover, owing to* $(3.20)_2$*, the role of the generalized Robin condition* $(3.20)_1$ *is the enforcement of the kinematic continuity* $(3.3)_1$*.*

Algorithm 3.1 Generalized Robin-Neumann explicit coupling schemes.

For $n > r$,

1. Fluid step (generalized Robin): find $\boldsymbol{u}^n : \Omega^{\mathrm{f}} \times \mathbb{R}^+ \to \mathbb{R}^d$ and $p^n : \Omega^{\mathrm{f}} \times \mathbb{R}^+ \to \mathbb{R}$ such that

$$\begin{cases} \rho^{\mathrm{f}}\partial_\tau\boldsymbol{u}^n - \mathbf{div}\boldsymbol{\sigma}^{\mathrm{f}}(\boldsymbol{u}^n,p^n) = \boldsymbol{0} & \text{in} \quad \Omega^{\mathrm{f}}, \\ \mathrm{div}\boldsymbol{u}^n = 0 & \text{in} \quad \Omega^{\mathrm{f}}, \\ \boldsymbol{\sigma}^{\mathrm{f}}(\boldsymbol{u}^n,p^n)\boldsymbol{n}^{\mathrm{f}} = \boldsymbol{h}(t_n) & \text{on} \quad \Gamma, \\ \boldsymbol{\sigma}^{\mathrm{f}}(\boldsymbol{u}^n,p^n)\boldsymbol{n}^{\mathrm{f}} + \dfrac{\rho^{\mathrm{s}}}{\tau}\boldsymbol{B}_h\boldsymbol{u}^n = \dfrac{\rho^{\mathrm{s}}}{\tau}\boldsymbol{B}_h\big(\dot{\boldsymbol{d}}^{n-1} + \tau\partial_\tau\dot{\boldsymbol{d}}^{\star}\big) & \\ \qquad\qquad -\boldsymbol{\sigma}^{\mathrm{s}}(\boldsymbol{d}^{\star},\dot{\boldsymbol{d}}^{\star})\boldsymbol{n}^{\mathrm{s}} & \text{on} \quad \Sigma. \end{cases} \tag{3.22}$$

2. Solid step (Neumann): find $\boldsymbol{d}^n : \Omega^{\mathrm{s}} \times \mathbb{R}^+ \to \mathbb{R}^d$ and $\dot{\boldsymbol{d}}^n : \Omega^{\mathrm{s}} \times \mathbb{R}^+ \to \mathbb{R}^d$ such that

$$\begin{cases} \rho^{\mathrm{s}}\partial_\tau\dot{\boldsymbol{d}}^n + \alpha_0\rho^{\mathrm{s}}\dot{\boldsymbol{d}}^n - \mathbf{div}\boldsymbol{\sigma}^{\mathrm{s}}(\boldsymbol{d}^n,\dot{\boldsymbol{d}}^n)\boldsymbol{0} & \text{in} \quad \Omega^{\mathrm{s}}, \\ \boldsymbol{d}^n = \boldsymbol{0},\ \alpha_1\dot{\boldsymbol{d}}^n = \boldsymbol{0} & \text{on} \quad \Gamma^{\mathrm{d}}, \\ \boldsymbol{\sigma}^{\mathrm{s}}(\boldsymbol{d}^n,\dot{\boldsymbol{d}}^n)\boldsymbol{n}^{\mathrm{s}} = \boldsymbol{0} & \text{on} \quad \Gamma^{\mathrm{n}}, \\ \boldsymbol{\sigma}^{\mathrm{s}}(\boldsymbol{d}^n,\dot{\boldsymbol{d}}^n)\boldsymbol{n}^{\mathrm{s}} = -\boldsymbol{\sigma}^{\mathrm{f}}(\boldsymbol{u}^n,p^n)\boldsymbol{n}^{\mathrm{f}} & \text{on} \quad \Sigma. \end{cases} \tag{3.23}$$

r	$\dot{\boldsymbol{d}}^{n-1} + \tau\partial_\tau\dot{\boldsymbol{d}}^{\star}$	$\boldsymbol{\sigma}^{\mathrm{s}}(\boldsymbol{d}^{\star},\dot{\boldsymbol{d}}^{\star})\boldsymbol{n}^{\mathrm{s}}$
0	$\dot{\boldsymbol{d}}^{n-1}$	$\boldsymbol{0}$
1	$2\dot{\boldsymbol{d}}^{n-1} - \dot{\boldsymbol{d}}^{n-2}$	$\boldsymbol{\sigma}^{\mathrm{s}}(\boldsymbol{d}^{n-1},\dot{\boldsymbol{d}}^{n-1})\boldsymbol{n}^{\mathrm{s}}$
2	$3\dot{\boldsymbol{d}}^{n-1} - 3\dot{\boldsymbol{d}}^{n-2} + \dot{\boldsymbol{d}}^{n-3}$	$2\boldsymbol{\sigma}^{\mathrm{s}}(\boldsymbol{d}^{n-1},\dot{\boldsymbol{d}}^{n-1})\boldsymbol{n}^{\mathrm{s}} - \boldsymbol{\sigma}^{\mathrm{s}}(\boldsymbol{d}^{n-2},\dot{\boldsymbol{d}}^{n-2})\boldsymbol{n}^{\mathrm{s}}$

Table 3.1: Extrapolations of the interface solid velocity and stress considered in (3.22).

For the sake of clarity, the strong form of the explicit coupling schemes (3.18)-(3.19) is presented in Algorithm 3.1. The corresponding extrapolations within the fluid

step are listed in Table 3.1. Note that, for $r = 1$ and 2, the schemes are multi-steps methods. The additional data needed to start the time-marching can be generated by performing one step of the scheme with $r = 0$, which yields $(\boldsymbol{d}^1, \dot{\boldsymbol{d}}^1)$, and then one step of the scheme with $r = 1$, which gives $(\boldsymbol{d}^2, \dot{\boldsymbol{d}}^2)$.

Remark 3.3.7. *Owing to the above initialization procedure and to* $(3.23)_4$*, we have*

$$\boldsymbol{\sigma}^{\mathrm{f}}(\boldsymbol{u}^\star, p^\star)\boldsymbol{n}^{\mathrm{f}} = -\boldsymbol{\sigma}^{\mathrm{s}}(\boldsymbol{d}^\star, \dot{\boldsymbol{d}}^\star)\boldsymbol{n}^{\mathrm{s}} \quad on \quad \Sigma,$$

for $n > r$*. Therefore, the generalized interface Robin condition* $(3.22)_4$ *can be rewritten as*

$$\boldsymbol{\sigma}^{\mathrm{f}}(\boldsymbol{u}^n, p^n)\boldsymbol{n}^{\mathrm{f}} + \frac{\rho^{\mathrm{s}}}{\tau}\boldsymbol{B}_h\boldsymbol{u}^n = \frac{\rho^{\mathrm{s}}}{\tau}\boldsymbol{B}_h\big(\dot{\boldsymbol{d}}^{n-1} + \tau\partial_\tau\dot{\boldsymbol{d}}^\star\big) + \boldsymbol{\sigma}^{\mathrm{f}}(\boldsymbol{u}^\star, p^\star)\boldsymbol{n}^{\mathrm{f}} \quad on \quad \Sigma, \tag{3.24}$$

for $n > r$*. The advantage with this equivalent formulation is that only interface solid velocities have to be transferred to the fluid in Algorithm 3.1, as in standard partitioned Dirichlet-Neumann procedures.*

Remark 3.3.8. *The relation* (3.24) *points out the partitioned nature of Algorithm 3.1, in the sense that additional features in the solid equation* (3.2)*, as incompressibility and more realistic viscoelastic models (see, e.g., [86, 74]), can be incorporated without any adjustment to the coupling scheme. In fact, only the solid problem* (3.23) *has to be modified accordingly.*

Remark 3.3.9. *If, instead of the Neumann condition* $(3.23)_2$*, we solve the second step of Algorithm 3.1 with the Dirichlet condition*

$$\boldsymbol{d}^n = \boldsymbol{d}^{n-1} + \tau\boldsymbol{u}^n \quad on \quad \Sigma,$$

we obtain a Robin-Dirichlet explicit coupling scheme. Note that in this case, the kinematic continuity $(3.3)_1$ *is enforced exactly in the solid step. The price to pay is a restrictive stability condition, which can demand very small time-steps in practice. Additionally, it is worth mentioning that such a Robin-Dirichlet splitting has some interesting connections with the time-stepping procedures traditionally used in the Immersed Boundary Method (see, e.g., [102, 11]).*

3.3.3.1 Computer implementation

We conclude this section by providing a few implementation details on the explicit coupling schemes (3.18)-(3.19). For the sake of simplicity, we assume that the external applied forces $\boldsymbol{f}^\Gamma$ vanish (i.e., $l(\boldsymbol{v}_h^{\mathrm{f}}) = 0$ in (3.18)). In addition, following Remark 3.3.7, we consider (3.18) with extrapolation in the fluid stresses. We denote by u^n, p^n, d^n and $\dot{\mathrm{d}}^n$ the arrays of degrees-of-freedom associated to $\boldsymbol{u}_h^n$, p_h^n, $\boldsymbol{d}_h^n$ and $\dot{\boldsymbol{d}}_h^n$, respectively. The subscript $_\Sigma$ indicates nodal values located on the interface Σ. The remaining degrees-of-freedom, located either in Ω^{f} or Ω^{s}, will be identified with the subscript $_{\mathrm{I}}$.

To fix the ideas, we first consider the separate solution of the fluid with homogeneous Neumann boundary conditions on the interface Σ. This yields the following linear system at each time-step:

$$\begin{bmatrix} \mathrm{A}^{\mathrm{f}}_{\mathrm{II}} & \mathrm{A}^{\mathrm{f}}_{\mathrm{I}\Sigma} & \mathrm{B}^{\mathrm{T}}_{\mathrm{I}} \\ \mathrm{A}^{\mathrm{f}}_{\Sigma\mathrm{I}} & \mathrm{A}^{\mathrm{f}}_{\Sigma\Sigma} & \mathrm{B}^{\mathrm{T}}_{\Sigma} \\ -\mathrm{B}_{\mathrm{I}} & -\mathrm{B}_{\Sigma} & \mathrm{S} \end{bmatrix} \begin{bmatrix} \mathrm{u}^n_{\mathrm{I}} \\ \mathrm{u}^n_{\Sigma} \\ \mathrm{p}^n \end{bmatrix} = \begin{bmatrix} \mathrm{b}^{n-1}_{\mathrm{I}} \\ \mathrm{b}^{n-1}_{\Sigma} \\ 0 \end{bmatrix}, \tag{3.25}$$

with

$$\mathrm{A}^{\mathrm{f}} \overset{\text{def}}{=} \frac{\rho^{\mathrm{f}}}{\tau}\mathrm{M}^{\mathrm{f}} + 2\mu\mathrm{K}^{\mathrm{f}}, \quad \mathrm{b}^{n-1} \overset{\text{def}}{=} \frac{\rho^{\mathrm{f}}}{\tau}\mathrm{M}^{\mathrm{f}}\mathrm{u}^{n-1}.$$

Here, the matrices M^{f}, K^{f}, B and S denote, respectively, the algebraic counterpart of the bilinear forms $(\boldsymbol{u}_h, \boldsymbol{v}^{\mathrm{f}}_h)_{\Omega^{\mathrm{f}}}$, $a(\boldsymbol{u}_h, \boldsymbol{v}^{\mathrm{f}}_h)$, $b(q_h, \boldsymbol{u}_h)$ and $s_h(p_h, q_h)$.

Similarly, if homogeneous Neumann boundary conditions are considered for the solid on the interface Σ, we get the linear system

$$\begin{bmatrix} \mathrm{A}^{\mathrm{s}}_{\mathrm{II}} & \mathrm{A}^{\mathrm{s}}_{\mathrm{I}\Sigma} \\ \mathrm{A}^{\mathrm{s}}_{\Sigma\mathrm{I}} & \mathrm{A}^{\mathrm{s}}_{\Sigma\Sigma} \end{bmatrix} \begin{bmatrix} \mathrm{d}^n_{\mathrm{I}} \\ \mathrm{d}^n_{\Sigma} \end{bmatrix} = \begin{bmatrix} \mathrm{r}_{\mathrm{I}} \\ \mathrm{r}_{\Sigma} \end{bmatrix}, \tag{3.26}$$

with

$$\mathrm{A}^{\mathrm{s}} \overset{\text{def}}{=} \frac{\rho^{\mathrm{s}}}{\tau^2}\mathrm{M}^{\mathrm{s},h} + \mathrm{K}^{\mathrm{e}} + \frac{1}{\tau}\mathrm{K}^{\mathrm{v}}, \quad \mathrm{r} \overset{\text{def}}{=} \frac{\rho^{\mathrm{s}}}{\tau^2}\mathrm{M}^{\mathrm{s},h}\big(\mathrm{d}^{n-1} + \tau\dot{\mathrm{d}}^{n-1}\big) + \frac{1}{\tau}\mathrm{K}^{\mathrm{v}}\mathrm{d}^{n-1}, \quad \dot{\mathrm{d}}^n = \partial_\tau \mathrm{d}^n.$$

Here, the matrices $\mathrm{M}^{\mathrm{s},h}$, K^{e} and K^{v} stand for the algebraic counterpart of the bilinear forms $(\dot{\boldsymbol{d}}_h, \boldsymbol{v}^{\mathrm{s}}_h)_{\Omega^{\mathrm{s}},h}$, $a^{\mathrm{e}}(\boldsymbol{d}_h, \boldsymbol{v}^{\mathrm{s}}_h)$ and $a^{\mathrm{v}}_h(\dot{\boldsymbol{d}}_h, \boldsymbol{v}^{\mathrm{s}}_h)$, respectively. Note that, due to the lumped-mass approximation, the matrix $\mathrm{M}^{\mathrm{s},h}$ is diagonal. Moreover, from (3.8), one can straightforwardly infer that the interface diagonal block $\mathrm{M}^{\mathrm{s},h}_{\Sigma\Sigma}$ of $\mathrm{M}^{\mathrm{s},h}$ is the algebraic counterpart of the interface operator $\boldsymbol{B}_h$.

Remark 3.3.10. *For linear elements, the lumped mass matrix* $\mathrm{M}^{\mathrm{s},h}$ *can be obtained directly from the standard (not lumped) mass matrix* M^{s} *via row-sum, that is:*

$$\big(\mathrm{M}^{\mathrm{s},h}\big)_{ij} = \begin{cases} \displaystyle\sum_k \big(\mathrm{M}^{\mathrm{s}}\big)_{ik} & \text{if} \quad i = j, \\ 0 & \text{if} \quad i \neq j \end{cases}$$

and $\mathrm{M}^{\mathrm{s},h}_{\Sigma\Sigma}$ *is simply the interface diagonal block of* $\mathrm{M}^{\mathrm{s},h}$*. This is the expression considered in the numerical experiments of Section 3.6 below (and of Section 4.4 in the next chapter).*

Based on the above considerations, the fluid and solid steps (3.18)-(3.19) can be equivalently reformulated, in an algebraic fashion, as follows:

1. Fluid step (generalized Robin): solve for u^n and p^n the linear system

$$\begin{bmatrix} \mathrm{A}^{\mathrm{f}}_{\mathrm{II}} & \mathrm{A}^{\mathrm{f}}_{\mathrm{I}\Sigma} & \mathrm{B}^{\mathrm{T}}_{\mathrm{I}} \\ \mathrm{A}^{\mathrm{f}}_{\Sigma\mathrm{I}} & \mathrm{A}^{\mathrm{f}}_{\Sigma\Sigma} + \frac{\rho^{\mathrm{s}}}{\tau}\mathrm{M}^{\mathrm{s},h}_{\Sigma\Sigma} & \mathrm{B}^{\mathrm{T}}_{\Sigma} \\ -\mathrm{B}_{\mathrm{I}} & -\mathrm{B}_{\Sigma} & \mathrm{S} \end{bmatrix} \begin{bmatrix} \mathrm{u}^n_{\mathrm{I}} \\ \mathrm{u}^n_{\Sigma} \\ \mathrm{p}^n \end{bmatrix} = \begin{bmatrix} \mathrm{b}^{n-1}_{\mathrm{I}} \\ \mathrm{b}^{n-1}_{\Sigma} \\ 0 \end{bmatrix} + \begin{bmatrix} 0 \\ \frac{\rho^{\mathrm{s}}}{\tau}\mathrm{M}^{\mathrm{s},h}_{\Sigma\Sigma}\big(\dot{\mathrm{d}}^{n-1}_{\Sigma} + \tau\partial_\tau \dot{\mathrm{d}}^{\star}_{\Sigma}\big) \\ 0 \end{bmatrix} + \begin{bmatrix} 0 \\ \mathrm{A}^{\mathrm{f}}_{\Sigma\mathrm{I}}\mathrm{u}^{\star}_{\mathrm{I}} + \mathrm{A}^{\mathrm{f}}_{\Sigma\Sigma}\mathrm{u}^{\star}_{\Sigma} + \mathrm{B}^{\mathrm{T}}_{\Sigma}\mathrm{p}^{\star} - \mathrm{b}^{\star-1}_{\Sigma} \\ 0 \end{bmatrix}. \tag{3.27}$$

2. Solid step (Neumann): solve for d^n the linear system

$$\begin{bmatrix} \mathrm{A}^{\mathrm{s}}_{\mathrm{II}} & \mathrm{A}^{\mathrm{s}}_{\mathrm{I}\Sigma} \\ \mathrm{A}^{\mathrm{s}}_{\Sigma\mathrm{I}} & \mathrm{A}^{\mathrm{s}}_{\Sigma\Sigma} \end{bmatrix} \begin{bmatrix} \mathrm{d}^n_{\mathrm{I}} \\ \mathrm{d}^n_{\Sigma} \end{bmatrix} = \begin{bmatrix} \mathrm{r}_{\mathrm{I}} \\ \mathrm{r}_{\Sigma} \end{bmatrix} - \begin{bmatrix} 0 \\ \mathrm{A}^{\mathrm{f}}_{\Sigma\mathrm{I}}\mathrm{u}^n_{\mathrm{I}} + \mathrm{A}^{\mathrm{f}}_{\Sigma\Sigma}\mathrm{u}^n_{\Sigma} + \mathrm{B}^{\mathrm{T}}_{\Sigma}\mathrm{p}^n - \mathrm{b}^{n-1}_{\Sigma} \end{bmatrix}. \tag{3.28}$$

   Afterwards, set $\dot{\mathrm{d}}^n = \partial_\tau \mathrm{d}^n$.

By comparing (3.27) with (3.25), we see that the interface solid lumped-mass block $\frac{\rho^{\mathrm{s}}}{\tau}\mathrm{M}^{\mathrm{s},h}_{\Sigma\Sigma}$ is added to the fluid stiffness matrix. This corresponds to the generalized Robin term in the left-hand side of (3.18). The last two terms of (3.27) represent the interface velocity and stress extrapolations of (3.18). On the solid side, the sole new contribution with respect to (3.26) is the last term of (3.28), that is, the algebraic representation of the fluid stress on the interface appearing in the right-hand side of (3.19).

3.3.4 Partitioned solution of implicit coupling

The explicit coupling schemes (3.18)-(3.19) can be viewed as a single iteration (with appropriate initializations) of a new Robin-Neumann iterative method for the partitioned solution of the following implicit coupling scheme: for $n \geq 1$, find $(\boldsymbol{u}^n_h, \dot{\boldsymbol{d}}^n_h) \in \boldsymbol{W}_h$, $p^n_h \in Q_h$ and $\boldsymbol{d}^n_h \in \boldsymbol{V}^{\mathrm{s}}_h$ such that $\dot{\boldsymbol{d}}^n_h = \partial_\tau \boldsymbol{d}^n_h$ and

$$\begin{aligned} \rho^{\mathrm{f}}\big(\partial_\tau \boldsymbol{u}^n_h, \boldsymbol{v}^{\mathrm{f}}_h\big)_{\Omega^{\mathrm{f}}} + a(\boldsymbol{u}^n_h, \boldsymbol{v}^{\mathrm{f}}_h) + b(p^n_h, \boldsymbol{v}^{\mathrm{f}}_h) - b(q_h, \boldsymbol{u}^n_h) + s_h(p^n_h, q_h) \\ + \rho^{\mathrm{s}}\big(\partial_\tau \dot{\boldsymbol{d}}^n_h, \boldsymbol{v}^{\mathrm{s}}_h\big)_{\Omega^{\mathrm{s}},h} + a^{\mathrm{e}}(\boldsymbol{d}^n_h, \boldsymbol{v}^{\mathrm{s}}_h) + a^{\mathrm{v}}_h(\dot{\boldsymbol{d}}^n_h, \boldsymbol{v}^{\mathrm{s}}_h) = l(\boldsymbol{v}^{\mathrm{f}}_h), \end{aligned} \tag{3.29}$$

for all $(\boldsymbol{v}^{\mathrm{f}}_h, \boldsymbol{v}^{\mathrm{s}}_h) \in \boldsymbol{W}_h$ and $q_h \in Q_h$. The corresponding generalized Robin-Neumann iterations read as follows:

1. Initialize $\dot{\boldsymbol{d}}_{h,0}$ and $\boldsymbol{d}_{h,0}$.

2. For $k = 1, \ldots$ until convergence:

- Fluid (generalized Robin): find $(\boldsymbol{u}_{h,k}, p_{h,k}) \in \boldsymbol{V}_h^{\mathrm{f}} \times Q_h$ such that

$$\begin{cases} \dfrac{\rho^{\mathrm{f}}}{\tau}\big(\boldsymbol{u}_{h,k} - \boldsymbol{u}_h^{n-1}, \boldsymbol{v}_h^{\mathrm{f}}\big)_{\Omega^{\mathrm{f}}} + a(\boldsymbol{u}_{h,k}, \boldsymbol{v}_h^{\mathrm{f}}) + b(p_{h,k}, \boldsymbol{v}_h^{\mathrm{f}}) - b(q_h, \boldsymbol{u}_{h,k}) \\ + s_h(p_{h,k}, q_h) + \dfrac{\rho^{\mathrm{s}}}{\tau}\big(\boldsymbol{B}_h \boldsymbol{u}_{h,k}, \boldsymbol{v}_h^{\mathrm{f}}\big)_{\Sigma} = \dfrac{\rho^{\mathrm{s}}}{\tau}\big(\boldsymbol{B}_h \dot{\boldsymbol{d}}_{h,k-1}, \boldsymbol{v}_h^{\mathrm{f}}\big)_{\Sigma} \\ \quad - \dfrac{\rho^{\mathrm{s}}}{\tau}\big(\dot{\boldsymbol{d}}_{h,k-1} - \dot{\boldsymbol{d}}_h^{n-1}, \boldsymbol{\mathcal{L}}_h^{\mathrm{s}} \boldsymbol{v}_h^{\mathrm{f}}\big)_{\Omega^{\mathrm{s}},h} - a^{\mathrm{e}}(\boldsymbol{d}_{h,k-1}, \boldsymbol{\mathcal{L}}_h^{\mathrm{s}} \boldsymbol{v}_h^{\mathrm{f}}) \\ \quad - a_h^{\mathrm{v}}(\dot{\boldsymbol{d}}_{h,k-1}, \boldsymbol{\mathcal{L}}_h^{\mathrm{s}} \boldsymbol{v}_h^{\mathrm{f}}) + l(\boldsymbol{v}_h^{\mathrm{f}}), \end{cases} \tag{3.30}$$

  for all $(\boldsymbol{v}_h^{\mathrm{f}}, q_h) \in \boldsymbol{V}_h^{\mathrm{f}} \times Q_h$.

- Solid (Neumann): find $(\dot{\boldsymbol{d}}_{h,k}, \boldsymbol{d}_{h,k}) \in \boldsymbol{V}_h^{\mathrm{s}} \times \boldsymbol{V}_h^{\mathrm{s}}$ such that

$$\begin{cases} \dot{\boldsymbol{d}}_{h,k} = \dfrac{\boldsymbol{d}_{h,k} - \boldsymbol{d}_h^{n-1}}{\tau}, \\ \dfrac{\rho^{\mathrm{s}}}{\tau}\big(\dot{\boldsymbol{d}}_{h,k} - \dot{\boldsymbol{d}}_h^{n-1}, \boldsymbol{v}_h^{\mathrm{s}}\big)_{\Omega^{\mathrm{s}},h} + a^{\mathrm{e}}(\boldsymbol{d}_{h,k}, \boldsymbol{v}_h^{\mathrm{s}}) + a_h^{\mathrm{v}}(\dot{\boldsymbol{d}}_{h,k}, \boldsymbol{v}_h^{\mathrm{s}}) \\ = -\dfrac{\rho^{\mathrm{f}}}{\tau}\big(\boldsymbol{u}_{h,k} - \boldsymbol{u}_h^{n-1}, \boldsymbol{\mathcal{L}}_h^{\mathrm{f}} \boldsymbol{v}_h^{\mathrm{s}}\big)_{\Omega^{\mathrm{f}}} - a(\boldsymbol{u}_{h,k}, \boldsymbol{\mathcal{L}}_h^{\mathrm{f}} \boldsymbol{v}_h^{\mathrm{s}}) \\ \quad - b(p_{h,k}, \boldsymbol{\mathcal{L}}_h^{\mathrm{f}} \boldsymbol{v}_h^{\mathrm{s}}), \end{cases} \tag{3.31}$$

  for all $\boldsymbol{v}_h^{\mathrm{s}} \in \boldsymbol{V}_h^{\mathrm{s}}$.

For the sake of clarity, the strong form of the above iterative procedure is reported in Algorithm 3.2.

Remark 3.3.11. *Unlike traditional Robin based procedures (see, e.g., [3]), Algorithm 3.2 is parameter free. This is of fundamental importance in practice, since inappropriate choices of free Robin parameters are known to yield slow convergence or even divergent behavior. Another key difference has to do with the interface operator $\boldsymbol{B}_h$, which here is not proportional to the identity (as usual). In fact, the underlying structure of $\boldsymbol{B}_h$ comes from the generalized Robin consistency* (3.16) *at the space semi-discrete level. In Section 3.4.3, we will see that this guarantees the convergence of the iterations. Moreover, the generalized-Robin condition is consistent as τ tends to zero whereas the consistency of the traditional Robin-Neumann coupling is only achived with a thin solid domain.*

3.4 Numerical analysis

This section is devoted to the numerical analysis of the generalized Robin-Neumann methods introduced above in the framework of the linear coupled problem (3.1)-(3.3). The stability of the explicit coupling schemes (3.18)-(3.19) is the topic of Section 3.4.2. In Section 3.4.3 we address the convergence of the iterative procedure (3.30)-(3.31).

Algorithm 3.2 Partitioned Robin-Neumann iterations based on Algorithm 3.1

1. Initialize $\boldsymbol{d}_0|_\Sigma$ and $\boldsymbol{\sigma}^{\mathrm{s}}(\boldsymbol{d}_0, \dot{\boldsymbol{d}}_0)\boldsymbol{n}^{\mathrm{s}}|_\Sigma$.

2. For $k = 1, \ldots$ until convergence:

   - Fluid: find $\boldsymbol{u}_k : \Omega^{\mathrm{f}} \times \mathbb{R}^+ \to \mathbb{R}^d$ and $p_k : \Omega^{\mathrm{f}} \times \mathbb{R}^+ \to \mathbb{R}$ such that

$$\begin{cases} \dfrac{\rho^{\mathrm{f}}}{\tau}\big(\boldsymbol{u}_k - \boldsymbol{u}^{n-1}\big) - \mathbf{div}\boldsymbol{\sigma}^{\mathrm{f}}(\boldsymbol{u}_k, p_k) = \mathbf{0} & \text{in} \quad \Omega^{\mathrm{f}}, \\ \operatorname{div} \boldsymbol{u}_k = 0 & \text{in} \quad \Omega^{\mathrm{f}}, \\ \boldsymbol{\sigma}^{\mathrm{f}}(\boldsymbol{u}_k, p_k)\boldsymbol{n}^{\mathrm{f}} = \boldsymbol{h}(t_n) & \text{on} \quad \Gamma, \\ \boldsymbol{\sigma}^{\mathrm{f}}(\boldsymbol{u}_k, p_k)\boldsymbol{n}_{\mathrm{f}} + \dfrac{\rho^{\mathrm{s}}}{\tau}\boldsymbol{B}_h\boldsymbol{u}_k = \dfrac{\rho^{\mathrm{s}}}{\tau}\boldsymbol{B}_h\dot{\boldsymbol{d}}_{k-1} & \\ \qquad\qquad -\boldsymbol{\sigma}^{\mathrm{s}}(\boldsymbol{d}_{k-1}, \dot{\boldsymbol{d}}_{k-1})\boldsymbol{n}^{\mathrm{s}} & \text{on} \quad \Sigma. \end{cases} \tag{3.32}$$

   - Solid: find $\boldsymbol{d}_k : \Omega^{\mathrm{s}} \times \mathbb{R}^+ \to \mathbb{R}^d$ and $\dot{\boldsymbol{d}}_k : \Omega^{\mathrm{s}} \times \mathbb{R}^+ \to \mathbb{R}^d$ such that $\dot{\boldsymbol{d}}_k = (\boldsymbol{d}_k - \boldsymbol{d}^{n-1})/\tau$ and

$$\begin{cases} \dfrac{\rho^{\mathrm{s}}}{\tau}\big(\dot{\boldsymbol{d}}_k - \dot{\boldsymbol{d}}^{n-1}\big) + \alpha_0\rho^{\mathrm{s}}\dot{\boldsymbol{d}}_k - \mathbf{div}\boldsymbol{\sigma}^{\mathrm{s}}(\boldsymbol{d}_k, \dot{\boldsymbol{d}}_k) = \mathbf{0} & \text{in} \quad \Omega^{\mathrm{s}}, \\ \boldsymbol{d}_k = \mathbf{0},\ \alpha_1\dot{\boldsymbol{d}}_k = \mathbf{0} & \text{on} \quad \Gamma^{\mathrm{d}}, \\ \boldsymbol{\sigma}^{\mathrm{s}}(\boldsymbol{d}_k, \dot{\boldsymbol{d}}_k)\boldsymbol{n}^{\mathrm{s}} = \mathbf{0} & \text{on} \quad \Gamma^{\mathrm{n}}, \\ \boldsymbol{\sigma}^{\mathrm{s}}(\boldsymbol{d}_k, \dot{\boldsymbol{d}}_k)\boldsymbol{n}^{\mathrm{s}} = -\boldsymbol{\sigma}^{\mathrm{f}}(\boldsymbol{u}_k, p_k)\boldsymbol{n}^{\mathrm{f}} & \text{on} \quad \Sigma. \end{cases} \tag{3.33}$$

3.4.1 Preliminaries

In what follows, the symbols $\lesssim$ and $\gtrsim$ indicate inequalities up to a multiplicative constant (independent of the physical and discretization parameters). We denote by $\|\cdot\|_{\mathrm{e}}$, $\|\cdot\|_{\mathrm{v}}$, $\|\cdot\|_{\mathrm{v},h}$ and $\|\cdot\|_{\mathrm{s},h}$ the norms associated to the inner-products a^{e}, a^{v}, a^{v}_h and $(\cdot,\cdot)_{\Omega^{\mathrm{s}},h}$, respectively.

Remark 3.4.1. *The norms $\|\cdot\|_{0,\Omega^{\mathrm{s}}}$ and $\|\cdot\|_{\mathrm{s},h}$ are equivalent in $\boldsymbol{V}^{\mathrm{s}}_h$, uniformly in h (see, e.g., [112, Chapter 15]). As a result, the same holds for $\|\cdot\|_{\mathrm{v}}$ and $\|\cdot\|_{\mathrm{v,h}}$.*

We consider discrete reconstructions,

$$\boldsymbol{L}^{\mathrm{e}}_h : \boldsymbol{V}^{\mathrm{s}} \to \boldsymbol{V}^{\mathrm{s}}_h, \qquad \text{and} \qquad \boldsymbol{L}^{\mathrm{v}}_h : \boldsymbol{V}^{\mathrm{s}}_h \to \boldsymbol{V}^{\mathrm{s}}_h,$$

of the elastic and viscous solid operators with respect to the lumped scalar product, defined with the relations:

$$(\boldsymbol{L}^{\mathrm{e}}_h\boldsymbol{d}, \boldsymbol{v}^{\mathrm{s}}_h)_{\Omega^{\mathrm{s}},h} = a^{\mathrm{e}}\big(\boldsymbol{d}, \boldsymbol{v}^{\mathrm{s}}_h\big), \quad (\boldsymbol{L}^{\mathrm{v}}_h\dot{\boldsymbol{d}}_h, \boldsymbol{v}^{\mathrm{s}}_h)_{\Omega^{\mathrm{s}},h} = a^{\mathrm{v}}_h\big(\dot{\boldsymbol{d}}_h, \boldsymbol{v}^{\mathrm{s}}_h\big), \tag{3.34}$$

for all $(\boldsymbol{d}, \dot{\boldsymbol{d}}_h, \boldsymbol{v}^{\mathrm{s}}_h) \in \boldsymbol{V}^{\mathrm{s}} \times \boldsymbol{V}^{\mathrm{s}}_h \times \boldsymbol{V}^{\mathrm{s}}_h$. Moreover, there exists a positive constant β_{e} such that

$$a^{\mathrm{e}}(\boldsymbol{d}, \boldsymbol{d}) \leq \beta_{\mathrm{e}}\|\boldsymbol{d}\|^2_{1,\Omega^{\mathrm{s}}},$$

for all $\boldsymbol{d} \in \boldsymbol{V}_h^{\mathrm{s}}$.

Lemma 3.4.1. *If C_{inv} denotes the inverse inequality constant (see, e.g., [40, Section 1.7]), we have the following estimates, valid for all $\boldsymbol{v}_h^{\mathrm{s}} \in \boldsymbol{V}_h^{\mathrm{s}}$:*

$$\begin{aligned}
\|\boldsymbol{v}_h^{\mathrm{s}}\|_{\mathrm{e}}^2 &\leq \frac{\beta_{\mathrm{e}} C_{\mathrm{inv}}^2}{h^2} \|\boldsymbol{v}_h^{\mathrm{s}}\|_{0,\Omega^{\mathrm{s}}}^2, & \|\boldsymbol{v}_h^{\mathrm{s}}\|_{\mathrm{v}}^2 &\leq \left(\alpha_0 \rho^{\mathrm{s}} + \alpha_1 \frac{\beta_{\mathrm{e}} C_{\mathrm{inv}}^2}{h^2}\right) \|\boldsymbol{v}_h^{\mathrm{s}}\|_{0,\Omega^{\mathrm{s}}}^2, \\
\|\boldsymbol{L}_h^{\mathrm{e}} \boldsymbol{v}_h^{\mathrm{s}}\|_{\mathrm{e}} &\leq \frac{\beta_{\mathrm{e}} C_{\mathrm{inv}}^2}{h^2} \|\boldsymbol{v}_h^{\mathrm{s}}\|_{\mathrm{e}}, & \|\boldsymbol{L}_h^{\mathrm{v}} \boldsymbol{v}_h^{\mathrm{s}}\|_{\mathrm{v}} &\leq \left(\alpha_0 \rho^{\mathrm{s}} + \alpha_1 \frac{\beta_{\mathrm{e}} C_{\mathrm{inv}}^2}{h^2}\right) \|\boldsymbol{v}_h^{\mathrm{s}}\|_{\mathrm{v}}, \\
\|\boldsymbol{L}_h^{\mathrm{e}} \boldsymbol{v}_h^{\mathrm{s}}\|_{0,\Omega^{\mathrm{s}}}^2 &\leq \frac{\beta_{\mathrm{e}} C_{\mathrm{inv}}^2}{h^2} \|\boldsymbol{v}_h^{\mathrm{s}}\|_{\mathrm{e}}^2, & \|\boldsymbol{L}_h^{\mathrm{v}} \boldsymbol{v}_h^{\mathrm{s}}\|_{0,\Omega^{\mathrm{s}}}^2 &\leq \left(\alpha_0 \rho^{\mathrm{s}} + \alpha_1 \frac{\beta_{\mathrm{e}} C_{\mathrm{inv}}^2}{h^2}\right) \|\boldsymbol{v}_h^{\mathrm{s}}\|_{\mathrm{v}}^2.
\end{aligned} \tag{3.35}$$

Proof. The proof uses the same arguments as in lemma 2.4.2 □

The next result states a fundamental property of the generalized Robin-Neumann schemes that will be useful for the stability analysis of Section 3.4.2.

Lemma 3.4.2. *Let $\left\{(\boldsymbol{u}_h^n, p_h^n, \boldsymbol{d}_h^n, \dot{\boldsymbol{d}}_h^n)\right\}_{n>r}$ be the sequence given by* (3.18)-(3.19). *For $n > r$, there holds*

$$\boldsymbol{u}_h^n = \dot{\boldsymbol{d}}_h^n + \frac{\tau}{\rho^{\mathrm{s}}} \left(\boldsymbol{L}_h^{\mathrm{e}}(\boldsymbol{d}_h^n - \boldsymbol{d}_h^\star) + \boldsymbol{L}_h^{\mathrm{v}}(\dot{\boldsymbol{d}}_h^n - \dot{\boldsymbol{d}}_h^\star)\right) \quad \text{on} \quad \Sigma, \tag{3.36}$$

and

$$\begin{aligned}
\rho^{\mathrm{f}}\left(\partial_\tau \boldsymbol{u}_h^n, \boldsymbol{v}_h^{\mathrm{f}}\right)_{\Omega^{\mathrm{f}}} + a(\boldsymbol{u}_h^n, \boldsymbol{v}_h^{\mathrm{f}}) + b(p_h^n, \boldsymbol{v}_h^{\mathrm{f}}) - b(q_h, \boldsymbol{u}_h^n) + s_h(p_h^n, q_h) \\
+ \rho^{\mathrm{s}}\left(\partial_t \dot{\boldsymbol{d}}_h^n, \boldsymbol{v}_h^{\mathrm{s}}\right)_{\Omega^{\mathrm{s}},h} + a^{\mathrm{e}}(\boldsymbol{d}_h^n, \boldsymbol{v}_h^{\mathrm{s}}) + a_h^{\mathrm{v}}(\dot{\boldsymbol{d}}_h^n, \boldsymbol{v}_h^{\mathrm{s}}) = l(\boldsymbol{v}_h^{\mathrm{f}}),
\end{aligned} \tag{3.37}$$

for all $(\boldsymbol{v}_h^{\mathrm{f}}, \boldsymbol{v}_h^{\mathrm{s}}) \in \boldsymbol{W}_h$ and $q_h \in Q_h$.

Proof. Due to (3.13), the fluid step (3.18) can be reformulated as

$$\begin{aligned}
\rho^{\mathrm{f}}\left(\partial_\tau \boldsymbol{u}_h^n, \boldsymbol{v}_h^{\mathrm{f}}\right)_{\Omega^{\mathrm{f}}} + a(\boldsymbol{u}_h^n, \boldsymbol{v}_h^{\mathrm{f}}) + b(p_h^n, \boldsymbol{v}_h^{\mathrm{f}}) - b(q_h, \boldsymbol{u}_h^n) + s_h(p_h^n, q_h) + \frac{\rho^{\mathrm{s}}}{\tau}\left(\boldsymbol{B}_h \boldsymbol{u}_h^n, \boldsymbol{v}_h^{\mathrm{f}}\right)_\Sigma \\
= \frac{\rho^{\mathrm{s}}}{\tau}\left(\boldsymbol{B}_h \dot{\boldsymbol{d}}_h^{n-1}, \boldsymbol{v}_h^{\mathrm{f}}\right)_\Sigma + a^{\mathrm{e}}(\boldsymbol{d}_h^\star, \boldsymbol{\mathcal{L}}_h^{\mathrm{s}} \boldsymbol{v}_h^{\mathrm{f}}) + a_h^{\mathrm{v}}(\dot{\boldsymbol{d}}_h^\star, \boldsymbol{\mathcal{L}}_h^{\mathrm{s}} \boldsymbol{v}_h^{\mathrm{f}}) + l(\boldsymbol{v}_h^{\mathrm{f}}).
\end{aligned} \tag{3.38}$$

for all $(\boldsymbol{v}_h^{\mathrm{f}}, q_h) \in \boldsymbol{V}_h^{\mathrm{f}} \times Q_h$ and $n > r$. Furthermore, by testing $(4.10)_2$ with $\boldsymbol{v}_h^{\mathrm{s}} = \boldsymbol{\mathcal{L}}_h^{\mathrm{s}} \boldsymbol{\xi}_h$ (for $\boldsymbol{\xi}_h \in \boldsymbol{\Lambda}_{\Sigma,h}$) and using (3.9), we infer that

$$\begin{aligned}
\rho^{\mathrm{s}}\left(\boldsymbol{B}_h \partial_\tau \dot{\boldsymbol{d}}_h^n, \boldsymbol{\xi}_h\right)_\Sigma + a^{\mathrm{e}}(\boldsymbol{d}_h^n, \boldsymbol{\mathcal{L}}_h^{\mathrm{s}} \boldsymbol{\xi}_h) + a_h^{\mathrm{v}}(\dot{\boldsymbol{d}}_h^n, \boldsymbol{\mathcal{L}}_h^{\mathrm{s}} \boldsymbol{\xi}_h) \\
= -\rho^{\mathrm{f}}\left(\partial_\tau \boldsymbol{u}_h^n, \boldsymbol{\mathcal{L}}_h^{\mathrm{f}} \boldsymbol{\xi}_h\right)_{\Omega^{\mathrm{f}}} - a(\boldsymbol{u}_h^n, \boldsymbol{\mathcal{L}}_h^{\mathrm{f}} \boldsymbol{\xi}_h) - b(p_h^n, \boldsymbol{\mathcal{L}}_h^{\mathrm{f}} \boldsymbol{\xi}_h).
\end{aligned} \tag{3.39}$$

Hence, taking $(\boldsymbol{v}_h^{\mathrm{f}}, q_h) = (\boldsymbol{\mathcal{L}}_h^{\mathrm{f}} \boldsymbol{\xi}_h, 0)$ in (3.38) and subtracting the resulting expression from (3.39) and since $l(\boldsymbol{\mathcal{L}}_h^{\mathrm{f}} \boldsymbol{\xi}_h) = 0$, yields

$$\frac{\rho^{\mathrm{s}}}{\tau}\left(\boldsymbol{B}_h(\dot{\boldsymbol{d}}_h^n - \boldsymbol{u}_h^n), \boldsymbol{\xi}_h\right)_\Sigma + a^{\mathrm{e}}(\boldsymbol{d}_h^n - \boldsymbol{d}_h^\star, \boldsymbol{\mathcal{L}}_h^{\mathrm{s}} \boldsymbol{\xi}_h) + a_h^{\mathrm{v}}(\dot{\boldsymbol{d}}_h^n - \dot{\boldsymbol{d}}_h^\star, \boldsymbol{\mathcal{L}}_h^{\mathrm{s}} \boldsymbol{\xi}_h) = 0,$$

for all $\boldsymbol{\xi}_h \in \boldsymbol{\Lambda}_{\Sigma,h}$ and $n > r$. Equivalently, from (4.2) and (3.9), we have

$$\frac{\rho^{\mathrm{s}}}{\tau}\boldsymbol{B}_h(\dot{\boldsymbol{d}}_h^n - \boldsymbol{u}_h^n) + \boldsymbol{B}_h\boldsymbol{L}_h^{\mathrm{e}}(\boldsymbol{d}_h^n - \boldsymbol{d}_h^\star) + \boldsymbol{B}_h\boldsymbol{L}_h^{\mathrm{v}}(\dot{\boldsymbol{d}}_h^n - \dot{\boldsymbol{d}}_h^\star) = \boldsymbol{0} \quad \text{on} \quad \Sigma,$$

for $n > r$. The identity (3.36) then results from the invertibility of the interface operator $\boldsymbol{B}_h$. At last, the relation (3.37) follows from (3.18) with $\boldsymbol{v}^{\mathrm{f}} = \widetilde{\boldsymbol{v}}^{\mathrm{f}} \in \boldsymbol{V}_{\Sigma,h}^{\mathrm{f}}$ and adding the resulting expression to (3.19). This concludes the proof. □

Lemma 3.4.2 shows that the explicit coupling schemes (3.18)-(3.19) are kinematic perturbations of the implicit coupling scheme (3.29). Note that, owing to (3.36), we do not have $(\boldsymbol{u}_h^n, \dot{\boldsymbol{d}}_h^n) \in \boldsymbol{W}_h$ in general. Note that the size of the perturbation (and hence accuracy) depends on the time-step length, the discrete solid operators and the extrapolations of the solid displacement and velocity. In the next section, the stability of (3.18)-(3.19) is analyzed by investigating the impact of the perturbed kinematic constraint (3.36) on the stability of the underlying implicit coupling scheme.

By applying to (3.30)-(3.31) the same arguments as in the proof of Lemma 3.4.2, we can state the following result, which will be useful for the convergence analysis of Section 3.4.3.

Lemma 3.4.3. *Let* $\big\{(\boldsymbol{u}_{h,k}, p_{h,k}, \boldsymbol{d}_{h,k}, \dot{\boldsymbol{d}}_{h,k})\big\}_{k\geq 1}$ *be the sequence of approximations given by* (3.30)-(3.31). *Then, for* $k \geq 1$, *there holds*

$$\begin{cases} \boldsymbol{u}_{h,k} = \dot{\boldsymbol{d}}_{h,k} + \dfrac{\tau}{\rho^{\mathrm{s}}}\Big(\boldsymbol{L}_h^{\mathrm{e}}(\boldsymbol{d}_{h,k} - \boldsymbol{d}_{h,k-1}) + \boldsymbol{L}_h^{\mathrm{v}}(\dot{\boldsymbol{d}}_{h,k} - \dot{\boldsymbol{d}}_{h,k-1})\Big) \quad \textit{on} \quad \Sigma, \\ \dot{\boldsymbol{d}}_{h,k} = \dfrac{\boldsymbol{d}_{h,k} - \boldsymbol{d}_h^{n-1}}{\tau} \quad \textit{in} \quad \Omega^{\mathrm{s}}, \\ \dfrac{\rho^{\mathrm{f}}}{\tau}\big(\boldsymbol{u}_{h,k} - \boldsymbol{u}_h^{n-1}, \boldsymbol{v}_h^{\mathrm{f}}\big)_{\Omega^{\mathrm{f}}} + a(\boldsymbol{u}_{h,k}, \boldsymbol{v}_h^{\mathrm{f}}) + b(p_{h,k}, \boldsymbol{v}_h^{\mathrm{f}}) - b(q_h, \boldsymbol{u}_{h,k}) + s_h(p_{h,k}, q_h) \\ \qquad + \dfrac{\rho^{\mathrm{s}}}{\tau}\big(\dot{\boldsymbol{d}}_{h,k} - \dot{\boldsymbol{d}}_h^{n-1}, \boldsymbol{v}_h^{\mathrm{s}}\big)_{\Omega^{\mathrm{s}},h} + a^{\mathrm{e}}(\boldsymbol{d}_{h,k}, \boldsymbol{v}_h^{\mathrm{s}}) + a_h^{\mathrm{v}}(\dot{\boldsymbol{d}}_{h,k}, \boldsymbol{v}_h^{\mathrm{s}}) = l(\boldsymbol{v}_h^{\mathrm{f}}) \end{cases} \tag{3.40}$$

for all $(\boldsymbol{v}_h^{\mathrm{f}}, \boldsymbol{v}_h^{\mathrm{s}}) \in \boldsymbol{W}_h$ *and* $q_h \in Q_h$.

3.4.2 Stability analysis of the explicit coupling schemes

For $n \geq 0$, we define the discrete energy of the fluid-structure system, at time t_n, as

$$E_h^n \stackrel{\text{def}}{=} \frac{\rho^{\mathrm{f}}}{2}\|\boldsymbol{u}_h^n\|_{0,\Omega^{\mathrm{f}}}^2 + \frac{\rho^{\mathrm{s}}}{2}\|\dot{\boldsymbol{d}}_h^n\|_{0,\Omega^{\mathrm{s}}}^2 + \frac{1}{2}\|\boldsymbol{d}_h^n\|_{\mathrm{e}}^2,$$

and, for $n \geq 1$, the total dissipation as

$$D_h^n \stackrel{\text{def}}{=} \frac{\rho^{\mathrm{f}}}{\tau}\|\boldsymbol{u}_h^n - \boldsymbol{u}_h^{n-1}\|_{0,\Omega^{\mathrm{f}}}^2 + \frac{\rho^{\mathrm{s}}}{\tau}\|\dot{\boldsymbol{d}}_h^n - \dot{\boldsymbol{d}}_h^{n-1}\|_{0,\Omega^{\mathrm{s}}}^2 + \frac{1}{\tau}\|\boldsymbol{d}_h^n - \boldsymbol{d}_h^{n-1}\|_{\mathrm{e}}^2 + 2\mu\|\boldsymbol{\epsilon}(\boldsymbol{u}_h^n)\|_{0,\Omega^{\mathrm{f}}}^2 + |p_h^n|_{s_h}^2 + \|\dot{\boldsymbol{d}}_h^n\|_{\mathrm{v}}^2,$$

where $|p_h^n|_{s_h} \stackrel{\text{def}}{=} \big(s_h(p_h^n, p_h^n)\big)^{\frac{1}{2}}$. The following result states the energy stability of the explicit coupling schemes given by (3.18)-(3.19).

Theorem 3.4.1. *Assume that* $\boldsymbol{f}^{\Gamma} = \mathbf{0}$ *(free system) and let* $\{(\boldsymbol{u}_h^n, p_h^n, \boldsymbol{d}_h^n, \dot{\boldsymbol{d}}_h^n)\}_{n>r}$ *be the sequence given by* (3.18)-(3.19)*. The following a priori energy estimates hold:*

- *Schemes with* $r = 0$ *or* $r = 1$*:*

$$E_h^n + \tau \sum_{m=r+1}^{n} D_h^m \lesssim E_h^0, \tag{3.41}$$

  for $n > r$*.*

- *Scheme with* $r = 2$*:*

$$E_h^n + \tau \sum_{m=3}^{n} D_h^m \lesssim \exp\left(\frac{t_n \gamma}{1-\gamma\tau}\right) E_h^0, \tag{3.42}$$

  for $n \geq 3$ *and provided that the following conditions hold*

$$\begin{cases} \tau\left(\alpha_0 + \alpha_1\left(\dfrac{\omega_{\mathrm{e}}}{h}\right)^2\right) < \delta, \\ \tau^5\left(\dfrac{\omega_{\mathrm{e}}}{h}\right)^6 + \tau^2\left(\dfrac{\omega_{\mathrm{e}}}{h}\right)^2\left(\alpha_0 + \alpha_1\left(\dfrac{\omega_{\mathrm{e}}}{h}\right)^2\right) < \gamma, \\ \tau\gamma < 1, \end{cases} \tag{3.43}$$

  where $\omega_{\mathrm{e}} \overset{\text{def}}{=} C_{\mathrm{inv}}\sqrt{\beta_{\mathrm{e}}/\rho^{\mathrm{s}}}$*,* $0 \leq \delta \leq 1$ *and* $\gamma > 0$*.*

Proof. The proof is based on the generalization of the arguments used in Chapter 2. Let $\boldsymbol{w}_h^n \in \boldsymbol{V}_h^{\mathrm{s}}$ be given by

$$\boldsymbol{w}_h^n \overset{\text{def}}{=} \dot{\boldsymbol{d}}_h^n + \frac{\tau}{\rho^{\mathrm{s}}}\left(\boldsymbol{L}_h^{\mathrm{e}}(\boldsymbol{d}_h^n - \boldsymbol{d}_h^\star) + \boldsymbol{L}_h^{\mathrm{v}}(\dot{\boldsymbol{d}}_h^n - \dot{\boldsymbol{d}}_h^\star)\right). \tag{3.44}$$

Owing to (3.36), we have $\boldsymbol{w}_h^n|_\Sigma = \boldsymbol{u}_h^n|_\Sigma$. Thus, we can take $(\boldsymbol{v}_h^{\mathrm{f}}, \boldsymbol{v}_h^{\mathrm{s}}) = \tau(\boldsymbol{u}_h^n, \boldsymbol{w}_h^n)$ and $q_h = \tau p_h^n$ in (3.37), which yields

$$\frac{\rho^{\mathrm{f}}}{2}\left(\|\boldsymbol{u}_h^n\|_{0,\Omega^{\mathrm{f}}}^2 - \|\boldsymbol{u}_h^{n-1}\|_{0,\Omega^{\mathrm{f}}}^2 + \|\boldsymbol{u}_h^n - \boldsymbol{u}_h^{n-1}\|_{0,\Omega^{\mathrm{f}}}^2\right) + 2\mu\tau\|\boldsymbol{\epsilon}(\boldsymbol{u}_h^n)\|_{0,\Omega^{\mathrm{f}}}^2 + \tau|p_h^n|_{\mathrm{s},h}^2$$
$$+ \tau\rho^{\mathrm{s}}\left(\partial_\tau \dot{\boldsymbol{d}}_h^n, \boldsymbol{w}_h^n\right)_{\Omega^{\mathrm{s}},h} + \tau a^{\mathrm{e}}(\boldsymbol{d}_h^n, \boldsymbol{w}_h^n) + \tau a_h^{\mathrm{v}}(\dot{\boldsymbol{d}}_h^n, \boldsymbol{w}_h^n) = 0.$$

Furthermore, by inserting (3.44) in this equality, using (3.34) and Remark 3.4.1, we get

$$E_h^n - E_h^{n-1} + \tau D_h^n + \underbrace{\tau\left(\dot{\boldsymbol{d}}_h^n - \dot{\boldsymbol{d}}_h^{n-1}, \boldsymbol{L}_h^{\mathrm{e}}(\boldsymbol{d}_h^n - \boldsymbol{d}_h^\star) + \boldsymbol{L}_h^{\mathrm{v}}(\dot{\boldsymbol{d}}_h^n - \dot{\boldsymbol{d}}_h^\star)\right)_{\Omega^{\mathrm{s}},h}}_{I_1}$$
$$+ \underbrace{\frac{\tau^2}{\rho^{\mathrm{s}}}\left(\boldsymbol{L}_h^{\mathrm{e}}\boldsymbol{d}_h^n + \boldsymbol{L}_h^{\mathrm{v}}\dot{\boldsymbol{d}}_h^n, \boldsymbol{L}_h^{\mathrm{e}}(\boldsymbol{d}_h^n - \boldsymbol{d}_h^\star) + \boldsymbol{L}_h^{\mathrm{v}}(\dot{\boldsymbol{d}}_h^n - \dot{\boldsymbol{d}}_h^\star)\right)_{\Omega^{\mathrm{s}},h}}_{I_2} \lesssim 0. \tag{3.45}$$

Therefore, it only remains to control the terms I_1 and I_2. We proceed by treating each case separately, depending on the extrapolation order r.
(i) Scheme with $r = 0$. We have

$$I_1 \geq -\frac{3\tau^2}{4\rho^{\mathrm{s}}}\|\boldsymbol{L}_h^{\mathrm{e}}\boldsymbol{d}_h^n + \boldsymbol{L}_h^{\mathrm{v}}\dot{\boldsymbol{d}}_h^n\|_{\mathrm{s},h}^2 - \frac{\rho^{\mathrm{s}}}{3}\|\dot{\boldsymbol{d}}_h^n - \dot{\boldsymbol{d}}_h^{n-1}\|_{\mathrm{s},h}^2,$$
$$I_2 = \frac{\tau^2}{\rho^{\mathrm{s}}}\|\boldsymbol{L}_h^{\mathrm{e}}\boldsymbol{d}_h^n + \boldsymbol{L}_h^{\mathrm{v}}\dot{\boldsymbol{d}}_h^n\|_{\mathrm{s},h}^2,$$

for $n \geq 1$. Hence, by inserting these estimates into (3.45) and summing over $m = 1, \ldots, n$, we get

$$E_h^n + \tau \sum_{m=1}^{n} \left(D_h^m + D_{0,\mathrm{spl}}^m\right) \lesssim E_h^0, \tag{3.46}$$

for $n \geq 1$, and with the additional dissipation related to the splitting

$$D_{0,\mathrm{spl}}^m \stackrel{\mathrm{def}}{=} \frac{\tau}{\rho^{\mathrm{s}}}\|\boldsymbol{L}_h^{\mathrm{e}}\boldsymbol{d}_h^m + \boldsymbol{L}_h^{\mathrm{v}}\dot{\boldsymbol{d}}_h^m\|_{\mathrm{s},h}^2.$$

The estimate (3.41) with $r = 0$ follows from (3.46).
(ii) Scheme with $r = 1$. In this case, we have

$$I_1 = \frac{\tau^2}{2}\left(\|\dot{\boldsymbol{d}}_h^n\|_{\mathrm{e},h}^2 - \|\dot{\boldsymbol{d}}_h^{n-1}\|_{\mathrm{e},h}^2 + \|\dot{\boldsymbol{d}}_h^n - \dot{\boldsymbol{d}}_h^{n-1}\|_{\mathrm{e,h}}^2\right) + \tau\|\dot{\boldsymbol{d}}_h^n - \dot{\boldsymbol{d}}_h^{n-1}\|_{\mathrm{v},h}^2,$$
$$I_2 = \frac{\tau^2}{2\rho^{\mathrm{s}}}\left(\|\boldsymbol{L}_h^{\mathrm{e}}\boldsymbol{d}_h^n + \boldsymbol{L}_h^{\mathrm{v}}\dot{\boldsymbol{d}}_h^n\|_{\mathrm{s},h}^2 - \|\boldsymbol{L}_h^{\mathrm{e}}\boldsymbol{d}_h^{n-1} + \boldsymbol{L}_h^{\mathrm{v}}\dot{\boldsymbol{d}}_h^{n-1}\|_{\mathrm{s},h}^2\right).$$

Hence, from (3.45), we infer that

$$E_h^n + E_{1,\mathrm{spl}}^n + \tau \sum_{m=2}^{n} \left(D_h^m + D_{1,\mathrm{spl}}^m\right) \lesssim E_h^1 + D_h^1 + D_{0,\mathrm{spl}}^1 \tag{3.47}$$

for $n \geq 2$, and with the additional dissipation introduced by the splitting

$$\begin{aligned} E_{1,\mathrm{spl}}^n &\stackrel{\mathrm{def}}{=} \tau^2\|\dot{\boldsymbol{d}}_h^n\|_{\mathrm{e},h}^2 + \frac{\tau^2}{\rho^{\mathrm{s}}}\|\boldsymbol{L}_h^{\mathrm{e}}\boldsymbol{d}_h^n + \boldsymbol{L}_h^{\mathrm{v}}\dot{\boldsymbol{d}}_h^n\|_{\mathrm{s},h}^2, \\ D_{1,\mathrm{spl}}^n &\stackrel{\mathrm{def}}{=} \tau\|\dot{\boldsymbol{d}}_h^n - \dot{\boldsymbol{d}}_h^{n-1}\|_{\mathrm{e},h}^2 + \|\dot{\boldsymbol{d}}_h^n - \dot{\boldsymbol{d}}_h^{n-1}\|_{\mathrm{v},h}^2. \end{aligned} \tag{3.48}$$

Due to the initialization procedure, the estimate (3.41) for $r = 1$ results from (3.47) and (3.46) with $n = 1$.
(iii) Scheme with $r = 2$. For the first term, We have

$$\begin{aligned} I_1 =& \tau^2\|\dot{\boldsymbol{d}}_h^n - \dot{\boldsymbol{d}}_h^{n-1}\|_{\mathrm{e},h}^2 \\ &+ \frac{\tau}{2}\left(\|\dot{\boldsymbol{d}}_h^n - \dot{\boldsymbol{d}}_h^{n-1}\|_{\mathrm{v},h}^2 - \|\dot{\boldsymbol{d}}_h^{n-1} - \dot{\boldsymbol{d}}_h^{n-2}\|_{\mathrm{v},h}^2 + \|\dot{\boldsymbol{d}}_h^n - 2\dot{\boldsymbol{d}}_h^{n-1} + \dot{\boldsymbol{d}}_h^{n-2}\|_{\mathrm{v},h}^2\right), \end{aligned}$$

for $n \geq 3$. The term I_2 is split into three parts that we estimate separately:

$$I_2 = \underbrace{\frac{\tau^3}{\rho^{\mathrm{s}}} a^{\mathrm{e}}\big(\boldsymbol{L}_h^{\mathrm{e}}\boldsymbol{d}_h^n, \dot{\boldsymbol{d}}_h^n - \dot{\boldsymbol{d}}_h^{n-1}\big)}_{J_1} + \underbrace{\frac{\tau^3}{\rho^{\mathrm{s}}}\big(\boldsymbol{L}_h^{\mathrm{v}}\dot{\boldsymbol{d}}_h^n, \boldsymbol{L}_h^{\mathrm{e}}\big(\dot{\boldsymbol{d}}_h^n - \dot{\boldsymbol{d}}_h^{n-1}\big)\big)_{\mathrm{s},h}}_{J_2}$$
$$+ \underbrace{\frac{\tau^2}{\rho^{\mathrm{s}}} a_h^{\mathrm{v}}\big(\boldsymbol{L}_h^{\mathrm{e}}\boldsymbol{d}_h^n + \boldsymbol{L}_h^{\mathrm{v}}\dot{\boldsymbol{d}}_h^n, \dot{\boldsymbol{d}}_h^n - 2\dot{\boldsymbol{d}}_h^{n-1} + \dot{\boldsymbol{d}}_h^{n-2}\big)}_{J_3}.$$

The first term is estimated, using (3.35), as follows

$$J_1 \geq -\frac{\tau^3}{\rho^{\mathrm{s}}}\|\boldsymbol{L}_h^{\mathrm{e}}\boldsymbol{d}_h^n\|_{\mathrm{e},h}\|\dot{\boldsymbol{d}}_h^n - \dot{\boldsymbol{d}}_h^{n-1}\|_{\mathrm{e},h} \geq -\frac{\tau^3}{\rho^{\mathrm{s}}}\frac{\beta_{\mathrm{e}}^{\frac{3}{2}} C_{\mathrm{inv}}^3}{h^3}\|\boldsymbol{d}_h^n\|_{\mathrm{e},h}\|\dot{\boldsymbol{d}}_h^n - \dot{\boldsymbol{d}}_h^{n-1}\|_{\mathrm{s},h}$$
$$\geq -\frac{\tau^6\omega_{\mathrm{e}}^6}{h^6}\|\boldsymbol{d}_h^n\|_{\mathrm{e},h}^2 - \frac{\rho^{\mathrm{s}}}{4}\|\dot{\boldsymbol{d}}_h^n - \dot{\boldsymbol{d}}_h^{n-1}\|_{\mathrm{s},h}^2.$$

Owing to the particular expression of the Rayleigh damping, the second term yields the following telescoping series

$$J_2 = \frac{\alpha_0\rho^{\mathrm{s}}\tau^3}{2}\left(\|\dot{\boldsymbol{d}}_h^n\|_{\mathrm{e},h}^2 - \|\dot{\boldsymbol{d}}_h^{n-1}\|_{\mathrm{e},h}^2 + \|\dot{\boldsymbol{d}}_h^n - \dot{\boldsymbol{d}}_h^{n-1}\|_{\mathrm{e},h}^2\right)$$
$$+ \frac{\alpha_1\tau^3}{2\rho^{\mathrm{s}}}\left(\|\boldsymbol{L}_h^{\mathrm{e}}\dot{\boldsymbol{d}}_h^n\|_{\mathrm{s},h}^2 - \|\boldsymbol{L}_h^{\mathrm{e}}\dot{\boldsymbol{d}}_h^{n-1}\|_{\mathrm{s},h}^2 + \|\boldsymbol{L}_h^{\mathrm{e}}(\dot{\boldsymbol{d}}_h^n - \dot{\boldsymbol{d}}_h^{n-1})\|_{\mathrm{s},h}^2\right).$$

At last, using (3.35) once more, for the third term we get

$$J_3 \geq -\frac{\tau^3}{(\rho^{\mathrm{s}})^2}\|\boldsymbol{L}_h^{\mathrm{e}}\boldsymbol{d}_h^n\|_{\mathrm{v},h}^2 - \frac{\tau^3}{(\rho^{\mathrm{s}})^2}\|\boldsymbol{L}_h^{\mathrm{v}}\dot{\boldsymbol{d}}_h^n\|_{\mathrm{v},h}^2 - \frac{\tau}{4}\|\dot{\boldsymbol{d}}_h^n - 2\dot{\boldsymbol{d}}_h^{n-1} + \dot{\boldsymbol{d}}_h^{n-2}\|_{\mathrm{v},h}^2$$
$$\geq -\frac{\tau^3\omega_{\mathrm{e}}^2}{h^2}\left(\alpha_0 + \alpha_1\frac{\omega_{\mathrm{e}}^2}{h^2}\right)\|\boldsymbol{d}_h^n\|_{\mathrm{e},h}^2 - \tau^3\left(\alpha_0 + \alpha_1\frac{\omega_{\mathrm{e}}^2}{h^2}\right)^2\|\dot{\boldsymbol{d}}_h^n\|_{\mathrm{v},h}^2$$
$$- \frac{\tau}{2}\|\dot{\boldsymbol{d}}_h^n - 2\dot{\boldsymbol{d}}_h^{n-1} + \dot{\boldsymbol{d}}_h^{n-2}\|_{\mathrm{v},h}^2.$$

By summing over $m = 1, \ldots, n$ and by applying the discrete Gronwall lemma, under conditions (3.43), we get the following bound, for $n \geq 3$,

$$E_h^n + \tau\sum_{m=3}^{n} D_h^m \lesssim e^{\left(\frac{t_n\gamma}{1-\gamma\tau}\right)}\left(E_h^2 + \tau\|\dot{\boldsymbol{d}}_h^2 - \dot{\boldsymbol{d}}_h^1\|_{\mathrm{v},h}^2 + \alpha_0\tau^3\|\dot{\boldsymbol{d}}_h^2\|_{\mathrm{e},h}^2 + \frac{\alpha_1\tau^3}{\rho^{\mathrm{s}}}\|\boldsymbol{L}_h^{\mathrm{e}}\dot{\boldsymbol{d}}_h^2\|_{\mathrm{s},h}^2\right). \tag{3.49}$$

The estimate (3.42) follows from (3.49), whose right-hand side can be bounded using the energy estimate (3.46) of the scheme with $r = 1$ and the stability condition (3.43). Hence, the proof is complete. □

We conclude this section with a series of observations. Theorem 3.4.1 guarantees the added-mass free stability of the generalized Robin-Neumann schemes (3.18)-(3.19). Unconditional stability is obtained for $r = 0$ and $r = 1$. Note that, in these cases, the results are independent of the structure of the solid viscous bilinear-form a_h^{v}. In fact, only symmetry and positiveness are necessary. Therefore, the estimate (3.41) remains valid if, instead of a_h^{v}, we consider the original bilinear-form a^{v} in (3.18)-(3.19), without mass-lumping approximation in the zeroth-order term.

Theorem 3.4.1 shows also that the scheme with second-order extrapolation ($r = 2$) and without solid damping ($\alpha_0 = \alpha_1 = 0$) is conditionally stable under a 6/5-CFL condition $\tau = \mathcal{O}(h^{6/5})$. If solid damping effects are present, additional conditions are required. In particular, for $\beta \neq 0$, stability is guaranteed under a parabolic-CFL condition $\tau = \mathcal{O}(h^2)$, which enforces much more restrictive conditions on the discretization parameters.

If conditions (3.43) are not satisfied for the scheme with second-order extrapolation, Theorem 3.4.1 is not conclusive. We will see in the numerical experiments of Section 3.6.1 that numerical instabilities might appear in this case.

Remark 3.4.2. *Similar estimates were obtained in Chapter 2 for the original Robin-Neumann schemes, in the case of the coupling with thin-walled structures. This shows that the extension proposed in this chapter preserve their stability properties.*

3.4.3 Convergence of the iterative solution procedure

This section is devoted to the convergence analysis of the iterative solution procedure (3.30)-(3.31) towards the implicit coupling solution (3.29). The main result is stated in the next theorem.

Theorem 3.4.2. *For $n \geq 1$, let $(\boldsymbol{u}_h^n, p_h^n, \boldsymbol{d}_h^n, \dot{\boldsymbol{d}}_h^n)$ be given by the implicit scheme* (3.29) *and $\left\{(\boldsymbol{u}_{h,k}, p_{h,k}, \boldsymbol{d}_{h,k}, \dot{\boldsymbol{d}}_{h,k})\right\}_{k\geq 1}$ be the sequence of approximations given by* (3.30)-(3.31)*. Then, there holds*

$$\begin{aligned}\sum_{k=1}^{\infty} \Big(\rho^{\mathrm{f}} \|\boldsymbol{u}_h^n - \boldsymbol{u}_{h,k}\|_{0,\Omega^{\mathrm{f}}}^2 + \rho^{\mathrm{s}} \|\dot{\boldsymbol{d}}_h^n - \dot{\boldsymbol{d}}_{h,k}\|_{0,\Omega^{\mathrm{s}}}^2 + \|\boldsymbol{d}_h^n - \boldsymbol{d}_{h,k}\|_{\mathrm{e}}^2\Big) \\ \lesssim \|\boldsymbol{d}_h^n - \boldsymbol{d}_{h,0}\|_{\mathrm{e}}^2 + \tau \|\dot{\boldsymbol{d}}_{h,0} - \dot{\boldsymbol{d}}_h^n\|_{\mathrm{v}}^2 \\ + \frac{\tau^2}{\rho^{\mathrm{s}}\epsilon} \|\boldsymbol{L}_h^{\mathrm{e}}(\boldsymbol{d}_h^n - \boldsymbol{d}_{h,0}) + \boldsymbol{L}_h^{\mathrm{v}}(\dot{\boldsymbol{d}}_h^n - \dot{\boldsymbol{d}}_{h,0})\|_{0,\Omega^{\mathrm{s}}}^2. \quad (3.50)\end{aligned}$$

In particular, we have

$$\left(\rho^{\mathrm{f}}\right)^{\frac{1}{2}} \|\boldsymbol{u}_h^n - \boldsymbol{u}_{h,k}\|_{0,\Omega^{\mathrm{f}}} + \left(\rho^{\mathrm{s}}\right)^{\frac{1}{2}} \|\dot{\boldsymbol{d}}_h^n - \dot{\boldsymbol{d}}_{h,k}\|_{0,\Omega^{\mathrm{s}}} + \|\boldsymbol{d}_h^n - \boldsymbol{d}_{h,k}\|_{\mathrm{e}} \underset{k\to\infty}{\longrightarrow} 0.$$

Proof. We introduce the following errors between the k-th iteration of (3.30)-(3.31) and the n-th step of (3.29):

$$\boldsymbol{e}_{h,k}^{\boldsymbol{u}} \overset{\text{def}}{=} \boldsymbol{u}_h^n - \boldsymbol{u}_{h,k}, \quad e_{h,k}^{p} \overset{\text{def}}{=} p_h^n - p_{h,k}, \quad \boldsymbol{e}_{h,k}^{\boldsymbol{d}} \overset{\text{def}}{=} \boldsymbol{d}_h^n - \boldsymbol{d}_{h,k}, \quad \boldsymbol{e}_{h,k}^{\dot{\boldsymbol{d}}} \overset{\text{def}}{=} \dot{\boldsymbol{d}}_h^n - \dot{\boldsymbol{d}}_{h,k}.$$

Since $\boldsymbol{u}_h^n|_\Sigma = \dot{\boldsymbol{d}}_h^n|_\Sigma$, the subtraction of (3.40) from (3.29) yields the following error equation

$$\begin{cases} \boldsymbol{e}_{h,k}^{\boldsymbol{u}} = \boldsymbol{e}_{h,k}^{\dot{\boldsymbol{d}}} + \dfrac{\tau}{\rho^{\mathrm{s}}}\left(\boldsymbol{L}_h^{\mathrm{e}}(\boldsymbol{e}_{h,k}^{\boldsymbol{d}} - \boldsymbol{e}_{h,k-1}^{\boldsymbol{d}}) + \boldsymbol{L}_h^{\mathrm{v}}(\boldsymbol{e}_{h,k}^{\dot{\boldsymbol{d}}} - \boldsymbol{e}_{h,k-1}^{\dot{\boldsymbol{d}}})\right) \quad \text{on} \quad \Sigma, \\ \boldsymbol{e}_{h,k}^{\dot{\boldsymbol{d}}} = \dfrac{1}{\tau}\boldsymbol{e}_{h,k}^{\boldsymbol{d}} \quad \text{in} \quad \Omega^{\mathrm{s}}, \\ \dfrac{\rho^{\mathrm{f}}}{\tau}\big(\boldsymbol{e}_{h,k}^{\boldsymbol{u}}, \boldsymbol{v}_h^{\mathrm{f}}\big)_{\Omega^{\mathrm{f}}} + a(\boldsymbol{e}_{h,k}^{\boldsymbol{u}}, \boldsymbol{v}_h^{\mathrm{f}}) + b(e_{h,k}^p, \boldsymbol{v}_h^{\mathrm{f}}) - b(q_h, \boldsymbol{e}_{h,k}^{\boldsymbol{u}}) + s_h(e_{h,k}^p, q_h) \\ \qquad + \dfrac{\rho^{\mathrm{s}}}{\tau}\big(\boldsymbol{e}_{h,k}^{\dot{\boldsymbol{d}}}, \boldsymbol{v}_h^{\mathrm{s}}\big)_{\mathrm{s},h} + a^{\mathrm{e}}(\boldsymbol{e}_{h,k}^{\boldsymbol{d}}, \boldsymbol{v}_h^{\mathrm{s}}) + a_h^{\mathrm{v}}(\boldsymbol{e}_{h,k}^{\dot{\boldsymbol{d}}}, \boldsymbol{v}_h^{\mathrm{s}}) = 0 \end{cases} \tag{3.51}$$

for all $(\boldsymbol{v}_h^{\mathrm{f}}, \boldsymbol{v}_h^{\mathrm{s}}) \in \boldsymbol{W}_h$ and $q_h \in Q_h$.

We proceed by taking $\boldsymbol{v}_h^{\mathrm{f}} = \tau \boldsymbol{e}_{h,k}^{\boldsymbol{u}}$, $q_h = \tau e_{h,k}^p$ and

$$\boldsymbol{v}_h^{\mathrm{s}} = \tau \boldsymbol{e}_{h,k}^{\dot{\boldsymbol{d}}} + \frac{\tau^2}{\rho^{\mathrm{s}}}\left(\boldsymbol{L}_h^{\mathrm{e}}(\boldsymbol{e}_{h,k}^{\boldsymbol{d}} - \boldsymbol{e}_{h,k-1}^{\boldsymbol{d}}) + \boldsymbol{L}_h^{\mathrm{v}}(\boldsymbol{e}_{h,k}^{\dot{\boldsymbol{d}}} - \boldsymbol{e}_{h,k-1}^{\dot{\boldsymbol{d}}})\right),$$

in $(3.51)_3$. Note that we do have $(\boldsymbol{v}_h^{\mathrm{f}}, \boldsymbol{v}_h^{\mathrm{s}}) \in \boldsymbol{W}_h$, thanks to $(3.51)_1$. We then get

$$\begin{aligned} &\rho^{\mathrm{f}}\|\boldsymbol{e}_{h,k}^{\boldsymbol{u}}\|_{0,\Omega^{\mathrm{f}}}^2 + \mu\tau\|\boldsymbol{e}_{h,k}^{\boldsymbol{u}}\|_{1,\Omega^{\mathrm{f}}}^2 + \rho^{\mathrm{s}}\|\boldsymbol{e}_{h,k}^{\dot{\boldsymbol{d}}}\|_{\mathrm{s},h}^2 + \|\boldsymbol{e}_{h,k}^{\boldsymbol{d}}\|_{\mathrm{e},h}^2 \\ &\qquad + \tau\|\boldsymbol{e}_{h,k}^{\dot{\boldsymbol{d}}}\|_{\mathrm{v},h}^2 + \underbrace{\tau\big(\boldsymbol{e}_{h,k}^{\dot{\boldsymbol{d}}}, \boldsymbol{L}_h^{\mathrm{e}}(\boldsymbol{e}_{h,k}^{\boldsymbol{d}} - \boldsymbol{e}_{h,k-1}^{\boldsymbol{d}}) + \boldsymbol{L}_h^{\mathrm{v}}(\boldsymbol{e}_{h,k}^{\dot{\boldsymbol{d}}} - \boldsymbol{e}_{h,k-1}^{\dot{\boldsymbol{d}}})\big)_{\Omega^{\mathrm{s}},h}}_{I_1} \\ &\qquad + \underbrace{\frac{\tau^2}{\rho^{\mathrm{s}}}\big(\boldsymbol{L}_h^{\mathrm{e}}\boldsymbol{e}_{h,k}^{\boldsymbol{d}} + \boldsymbol{L}_h^{\mathrm{v}}\boldsymbol{e}_{h,k}^{\dot{\boldsymbol{d}}}, \boldsymbol{L}_h^{\mathrm{e}}(\boldsymbol{e}_{h,k}^{\boldsymbol{d}} - \boldsymbol{e}_{h,k-1}^{\boldsymbol{d}}) + \boldsymbol{L}_h^{\mathrm{v}}(\boldsymbol{e}_{h,k}^{\dot{\boldsymbol{d}}} - \boldsymbol{e}_{h,k-1}^{\dot{\boldsymbol{d}}})\big)_{\Omega^{\mathrm{s}},h}}_{I_2} \leq 0. \end{aligned} \tag{3.52}$$

The last terms can be controlled following the same argument as in the proof of Theorem 3.4.1 with $r = 1$. Hence, using $(3.51)_2$, we get

$$\begin{aligned} I_1 &= \frac{1}{2}\left(\|\boldsymbol{e}_k^{\boldsymbol{d}}\|_{\mathrm{e},h}^2 - \|\boldsymbol{e}_{k-1}^{\boldsymbol{d}}\|_{\mathrm{e},h}^2 + \|\boldsymbol{e}_k^{\boldsymbol{d}} - \boldsymbol{e}_{k-1}^{\boldsymbol{d}}\|_{\mathrm{e},h}^2\right) \\ &\quad + \frac{\tau}{2}\left(\|\boldsymbol{e}_k^{\dot{\boldsymbol{d}}}\|_{\mathrm{v},h}^2 - \|\boldsymbol{e}_{k-1}^{\dot{\boldsymbol{d}}}\|_{\mathrm{v},h}^2 + \|\boldsymbol{e}_k^{\dot{\boldsymbol{d}}} - \boldsymbol{e}_{k-1}^{\dot{\boldsymbol{d}}}\|_{\mathrm{v},h}^2\right), \\ I_2 &= \frac{\tau^2}{2\rho^{\mathrm{s}}}\Big(\|\boldsymbol{L}_h^{\mathrm{e}}\boldsymbol{e}_k^{\boldsymbol{d}} + \boldsymbol{L}_h^{\mathrm{v}}\boldsymbol{e}_k^{\dot{\boldsymbol{d}}}\|_{\mathrm{s},h}^2 - \|\boldsymbol{L}_h^{\mathrm{e}}\boldsymbol{e}_{k-1}^{\boldsymbol{d}} + \boldsymbol{L}_h^{\mathrm{v}}\boldsymbol{e}_{k-1}^{\dot{\boldsymbol{d}}}\|_{\mathrm{s},h}^2 \\ &\qquad + \|\boldsymbol{L}_h^{\mathrm{e}}(\boldsymbol{e}_k^{\boldsymbol{d}} - \boldsymbol{e}_{k-1}^{\boldsymbol{d}}) + \boldsymbol{L}_h^{\mathrm{v}}(\boldsymbol{e}_k^{\dot{\boldsymbol{d}}} - \boldsymbol{e}_{k-1}^{\dot{\boldsymbol{d}}})\|_{\mathrm{s},h}^2\Big). \end{aligned}$$

The estimate (3.50) then follows by inserting this expressions into (3.52), summing over $k = 1, \ldots, \infty$ and using Remark 3.4.1. This concludes the proof.

□

To the best of our knowledge, Theorem 3.4.2 is the first result which guarantees the convergence of a Robin-Neumann iterative procedure towards the implicit coupling solution (3.29). From the above proof, one can infer that the structure of the

interface Robin operator $(\rho^{\mathrm{s}}/\tau)\boldsymbol{B}_h$ is a fundamental ingredient in the convergence of the iterations. Furthermore, for the initialization $(\boldsymbol{d}_{h,0}, \dot{\boldsymbol{d}}_{h,0}) = (\boldsymbol{d}_h^{n-1}, \dot{\boldsymbol{d}}_h^{n-1})$, the estimate (3.50) shows that reducing the time-step length τ increases the convergence speed of the iterations. This will be illustrated in Section 3.6.1.2 through numerical experiments.

3.5 The non-linear case

In this section, we formulate the generalized Robin-Neumann schemes of Section 3.3.3 within a fully non-linear framework, involving a viscous incompressible fluid and a thick-walled non-linear structure. The fluid is described by the incompressible Navier-Stokes equations in ALE formalism and the structure by the non-linear (visco-)elastodynamics equations.

3.5.1 The non-linear coupled problem

Let $\Omega = \Omega^{\mathrm{f}} \cup \Omega^{\mathrm{s}}$ be a reference configuration of the system. The current configuration of the fluid domain, $\Omega^{\mathrm{f}}(t)$, is parametrized by the ALE map $\boldsymbol{\mathcal{A}} \overset{\text{def}}{=} \boldsymbol{I}_{\Omega_{\mathrm{f}}} + \boldsymbol{d}_{\mathrm{f}}$ as $\Omega^{\mathrm{f}}(t) = \boldsymbol{\mathcal{A}}(\Omega^{\mathrm{f}}, t)$, where $\boldsymbol{d}^{\mathrm{f}} : \Omega^{\mathrm{f}} \times \mathbb{R}^+ \to \mathbb{R}^d$ stands for the displacement of the fluid domain. In practice, $\boldsymbol{d}^{\mathrm{f}} = \mathrm{Ext}(\boldsymbol{d}|_\Sigma)$, where $\mathrm{Ext}(\cdot)$ denotes any reasonable lifting operator from the (reference) interface Σ into the (reference) fluid domain Ω^{f}. The strong form of the non-linear fluid-structure problem reads as follows: find the fluid velocity $\boldsymbol{u} : \Omega^{\mathrm{f}} \times \mathbb{R}^+ \to \mathbb{R}^d$, the fluid pressure $p : \Omega^{\mathrm{f}} \times \mathbb{R}^+ \to \mathbb{R}$, the structure displacement $\boldsymbol{d} : \Omega^{\mathrm{s}} \times \mathbb{R}^+ \to \mathbb{R}^d$ and the structure velocity $\dot{\boldsymbol{d}} : \Omega^{\mathrm{s}} \times \mathbb{R}^+ \to \mathbb{R}^d$ such that

$$\begin{cases} \rho^{\mathrm{f}} \partial_t|_{\mathcal{A}} \boldsymbol{u} + \rho^{\mathrm{f}}(\boldsymbol{u} - \boldsymbol{w}) \cdot \boldsymbol{\nabla} \boldsymbol{u} - \mathbf{div} \boldsymbol{\sigma}^{\mathrm{f}}(\boldsymbol{u}, p) = \boldsymbol{0} & \text{in} \quad \Omega^{\mathrm{f}}(t), \\ \mathrm{div} \boldsymbol{u} = 0 & \text{in} \quad \Omega^{\mathrm{f}}(t), \\ \boldsymbol{\sigma}^{\mathrm{f}}(\boldsymbol{u}, p) \boldsymbol{n}^{\mathrm{f}} = \boldsymbol{f}^{\Gamma} & \text{on} \quad \Gamma, \end{cases} \tag{3.53}$$

$$\begin{cases} \rho^{\mathrm{s}} \partial_t \dot{\boldsymbol{d}} + \alpha_0 \rho^{\mathrm{s}} \dot{\boldsymbol{d}} - \mathbf{div} \boldsymbol{\Pi}(\boldsymbol{d}, \dot{\boldsymbol{d}}) = \boldsymbol{0} & \text{in} \quad \Omega^{\mathrm{s}}, \\ \dot{\boldsymbol{d}} = \partial_t \boldsymbol{d} & \text{in} \quad \Omega^{\mathrm{s}}, \\ \boldsymbol{d} = \boldsymbol{0},\ \alpha_1 \dot{\boldsymbol{d}} = \boldsymbol{0} & \text{on} \quad \Gamma^{\mathrm{d}}, \\ \boldsymbol{\Pi}(\boldsymbol{d}, \dot{\boldsymbol{d}}) \boldsymbol{n}^{\mathrm{s}} = \boldsymbol{0} & \text{on} \quad \Gamma^{\mathrm{n}}, \end{cases} \tag{3.54}$$

$$\begin{cases} \boldsymbol{d}^{\mathrm{f}} = \mathrm{Ext}(\boldsymbol{d}|_\Sigma), \quad \boldsymbol{w} = \partial_{\mathrm{t}} \boldsymbol{d}^{\mathrm{f}} & \text{on} \quad \Omega^{\mathrm{f}}, \\ \boldsymbol{u} = \boldsymbol{w} & \text{on} \quad \Sigma(t), \\ \boldsymbol{\Pi}(\boldsymbol{d}, \dot{\boldsymbol{d}}) \boldsymbol{n}^{\mathrm{s}} = -J \boldsymbol{\sigma}^{\mathrm{f}}(\boldsymbol{u}, p) \boldsymbol{F}^{-\mathrm{T}} \boldsymbol{n}^{\mathrm{f}} & \text{on} \quad \Sigma, \end{cases} \tag{3.55}$$

where $\partial_t|_{\boldsymbol{\mathcal{A}}}$ represents the ALE time derivative, $\boldsymbol{F} \overset{\text{def}}{=} \boldsymbol{\nabla} \boldsymbol{\mathcal{A}}$ the fluid domain gradient of deformation and $J \overset{\text{def}}{=} \det \boldsymbol{F}$ the Jacobian. As usual, a field defined in the reference fluid domain, Ω^{f}, is evaluated in the current fluid domain, $\Omega^{\mathrm{f}}(t)$, by composition with $\boldsymbol{\mathcal{A}}^{-1}(\cdot, t)$.

In (3.54), the stress tensor $\boldsymbol{\Pi}(\boldsymbol{d},\dot{\boldsymbol{d}})$ is defined by the relation $\boldsymbol{\Pi}(\boldsymbol{d},\dot{\boldsymbol{d}}) \overset{\text{def}}{=} \boldsymbol{\pi}(\boldsymbol{d}) + \alpha_1 \boldsymbol{\pi}'_{\boldsymbol{d}}\dot{\boldsymbol{d}}$, where $\boldsymbol{\pi}(\boldsymbol{d})$ denotes the first Piola-Kirchhoff tensor of the structure (related to the displacement $\boldsymbol{d}$ through an appropriate constitutive law) and $\boldsymbol{\pi}'_{\boldsymbol{d}}$ stands for Fréchet derivative of $\boldsymbol{\pi}$ at $\boldsymbol{d}$. Physical damping in the solid is hence described through the Rayleigh-like term $\alpha_0\rho^{\mathrm{s}}\dot{\boldsymbol{d}} - \alpha_1 \mathbf{div}(\boldsymbol{\pi}'_{\boldsymbol{d}}\dot{\boldsymbol{d}})$ in $(3.54)_1$, with $\alpha_0, \alpha_1 \geq 0$. In other words, the viscous contribution is proportional to a linearization of the elastic part.

3.5.2 Explicit coupling schemes

The proposed fully explicit coupling schemes combine the explicit treatment of the interface geometrical compatibility $(3.55)_1$ with the following Robin-Neumann time-

Algorithm 3.3 Generalized Robin-Neumann schemes (non-linear version).

For $n > r$:

1. Fluid domain update:

$$\boldsymbol{d}^{\mathrm{f,n}} = \mathrm{Ext}(\boldsymbol{d}^{n-1}|_\Sigma), \quad \boldsymbol{w}^n = \partial_\tau \boldsymbol{d}^{\mathrm{f,n}}, \quad \boldsymbol{\mathcal{A}}^n \overset{\text{def}}{=} \boldsymbol{I}_\Omega + \boldsymbol{d}^{\mathrm{f,n}}, \quad \Omega^{\mathrm{f,n}} \overset{\text{def}}{=} \boldsymbol{\mathcal{A}}^n\big(\Omega\big)$$

   and we set $\boldsymbol{F}^n = \boldsymbol{\nabla}\boldsymbol{\mathcal{A}}^n$ and $J^n = \det \boldsymbol{F}^n$.

2. Fluid step: find $\boldsymbol{u}^n : \Omega \times \mathbb{R}^+ \to \mathbb{R}^d$ and $p^n : \Omega \times \mathbb{R}^+ \to \mathbb{R}$ such that

$$\left\{\begin{array}{rll} \rho^{\mathrm{f}}\partial_\tau|_{\mathcal{A}}\boldsymbol{u}^n + \rho^{\mathrm{f}}(\boldsymbol{u}^{n-1} - \boldsymbol{w}^n)\cdot\boldsymbol{\nabla}\boldsymbol{u}^n - \mathbf{div}\boldsymbol{\sigma}^{\mathrm{f}}(\boldsymbol{u}^n, p^n) = \boldsymbol{0} & \text{in} & \Omega^{\mathrm{f,n}}, \\ \mathrm{div}\,\boldsymbol{u}^n = 0 & \text{in} & \Omega^{\mathrm{f,n}}, \\ \boldsymbol{\sigma}^{\mathrm{f}}(\boldsymbol{u}^n, p^n)\boldsymbol{n}^{\mathrm{f}} = \boldsymbol{f}^\Gamma(t_n) & \text{on} & \Gamma, \\ J^n\boldsymbol{\sigma}^{\mathrm{f}}(\boldsymbol{u}^n, p^n)(\boldsymbol{F}^n)^{-\mathrm{T}}\boldsymbol{n}^{\mathrm{f}} + \dfrac{\rho^{\mathrm{s}}}{\tau}\boldsymbol{B}_h\boldsymbol{u}^n = \dfrac{\rho^{\mathrm{s}}}{\tau}\boldsymbol{B}_h\left(\dot{\boldsymbol{d}}^{n-1} + \tau\partial_\tau\dot{\boldsymbol{d}}^\star\right) & & \\ \qquad\qquad -\boldsymbol{\Pi}^\star\boldsymbol{n}^{\mathrm{s}} & \text{on} & \Sigma. \end{array}\right.$$

3. Solid step: find $\boldsymbol{d}^n : \Omega^{\mathrm{s}} \times \mathbb{R}^+ \to \mathbb{R}^d$ and $\dot{\boldsymbol{d}}^n : \Omega^{\mathrm{s}} \times \mathbb{R}^+ \to \mathbb{R}^d$ such that

$$\left\{\begin{array}{rll} \rho^{\mathrm{s}}\partial_\tau\dot{\boldsymbol{d}}^n + \alpha_0\rho^{\mathrm{s}}\dot{\boldsymbol{d}}^n - \mathbf{div}\boldsymbol{\Pi}^n = \boldsymbol{0} & \text{in} & \Omega^{\mathrm{s}}, \\ \dot{\boldsymbol{d}} = \partial_\tau\boldsymbol{d}^n, \quad \boldsymbol{\Pi}^n \overset{\text{def}}{=} \boldsymbol{\pi}(\boldsymbol{d}^n) + \alpha_1\boldsymbol{\pi}'_{\boldsymbol{d}^{n-1}}(\dot{\boldsymbol{d}}^n) & \text{in} & \Omega^{\mathrm{s}}, \\ \boldsymbol{d}^n = \boldsymbol{0},\ \alpha_1\dot{\boldsymbol{d}}^n = \boldsymbol{0} & \text{on} & \Gamma^{\mathrm{d}}, \\ \boldsymbol{\Pi}^n\boldsymbol{n}^{\mathrm{s}} = \boldsymbol{0} & \text{on} & \Gamma^{\mathrm{n}}, \\ \boldsymbol{\Pi}^n\boldsymbol{n}^{\mathrm{s}} = -J^n\boldsymbol{\sigma}^{\mathrm{f}}(\boldsymbol{u}^n, p^n)(\boldsymbol{F}^n)^{-\mathrm{T}}\boldsymbol{n}^{\mathrm{f}} & \text{on} & \Sigma. \end{array}\right.$$

stepping of the interface kinematical/kinetic coupling $(3.55)_{2,3}$ on Σ:

$$\left\{\begin{array}{r} J^n\boldsymbol{\sigma}^{\mathrm{f}}(\boldsymbol{u}^n, p^n)(\boldsymbol{F}^n)^{-\mathrm{T}}\boldsymbol{n}^{\mathrm{f}} + \dfrac{\rho^{\mathrm{s}}}{\tau}\boldsymbol{B}_h\boldsymbol{u}^n = \dfrac{\rho^{\mathrm{s}}}{\tau}\boldsymbol{B}_h\left(\dot{\boldsymbol{d}}^{n-1} + \tau\partial_\tau\dot{\boldsymbol{d}}^\star\right) - \boldsymbol{\Pi}^\star\boldsymbol{n}^{\mathrm{s}}, \\ \boldsymbol{\Pi}^n\boldsymbol{n}^{\mathrm{s}} = -J^n\boldsymbol{\sigma}^{\mathrm{f}}(\boldsymbol{u}^n, p^n)(\boldsymbol{F}^n)^{-\mathrm{T}}\boldsymbol{n}^{\mathrm{f}}, \end{array}\right.$$

derived from the arguments introduced in Section 3.3.3. The solid stress tensor is given by the expression $\boldsymbol{\Pi}^n \stackrel{\text{def}}{=} \boldsymbol{\pi}(\boldsymbol{d}^n)+\alpha_1\boldsymbol{\pi}'_{\boldsymbol{d}^{n-1}}(\dot{\boldsymbol{d}}^n)$, which involves a semi-implicit treatment of the viscous contribution.

The resulting time-marching procedures are detailed in Algorithm 3.3 and will be used in some of the numerical tests in the next section. It should be noted that the computation of the extrapolated solid strain could be replaced by a fluid residual as detailed in remark 3.3.7.

3.6 Numerical experiments

In this section, we investigate through numerical experiments the properties of the explicit coupling scheme introduced above. Several fluid-structure interaction examples from the literature have been considered. Section 2.8.1 presents a convergence study in 2D, using the linear model problem (3.1)-(3.3). Numerical results based on the non-linear model (3.53)-(3.55), with a Saint Venant-Kirchhoff constitutive law for the solid and 3D geometries, are presented in the subsequent sections.

3.6.1 Numerical study in a two-dimensional test-case

The first example is the popular two-dimensional pressure-wave propagation benchmark (see, e.g., [3]). We consider (3.1)-(3.3) with $\Omega^{\mathrm{f}} = [0, L] \times [0, R]$, $\Omega^{\mathrm{s}} = [0, L] \times [R, R+\epsilon]$, $L = 6$, $R = 0.5$ and $\epsilon = 0.1$. All the units are given in the CGS sytem. At the fluid boundary $x = 0$ we impose a sinusoidal pressure of maximal amplitude 2×10^4 during 5×10^{-3} time instants, corresponding to half a period. Zero traction is enforced at $x = 6$ and a symmetry condition is applied on the lower wall. Transverse membrane effects that appear in axisymmetric formulations are included through an additional zero-th order term $c_0\boldsymbol{d}$ in the solid equation $(3.2)_1$. The solid is clamped at its extremities and zero traction is enforced on its upper boundary. The fluid physical parameters are given by $\rho^{\mathrm{f}} = 1$ and $\mu = 0.035$. For the solid we have $\rho^{\mathrm{s}} = 1.1$, $L_1 = 1.15 \cdot 10^6$, $L_2 = 1.7 \cdot 10^6$, $c_0 = 4 \cdot 10^6$, $\alpha_0\rho^{\mathrm{s}} = 10^{-3}$, $\alpha_1 = 10^{-3}$. All the computations have been performed with FreeFem++ (see [70]).

For illustration purposes, we have reported in Figure 3.1 a few snapshots of the pressure field obtained using Algorithm 3.1 with $r = 1$, $\tau = 10^{-4}$ and $h = 0.05$. The fluid and solid domains have been displayed in deformed configuration (amplified by a factor 10). The numerical solution remains stable, as predicted by Theorem 3.4.1, and a propagating pressure-wave is observed.

3.6.1.1 Accuracy of the explicit coupled schemes

We first compare the interface vertical displacement obtained with Algorithm 3.1 ($r = 0$ and $r = 1$) and the implicit scheme for $h = 0.05$ and $\tau = 10^{-4}$, $5 \cdot 10^{-5}$, $2 \cdot 10^{-5}$. A reference solution has been generated using the implicit scheme and a high grid resolution ($\tau = 10^{-6}$, $h = 3.125 \cdot 10^{-3}$). The corresponding results are reported in

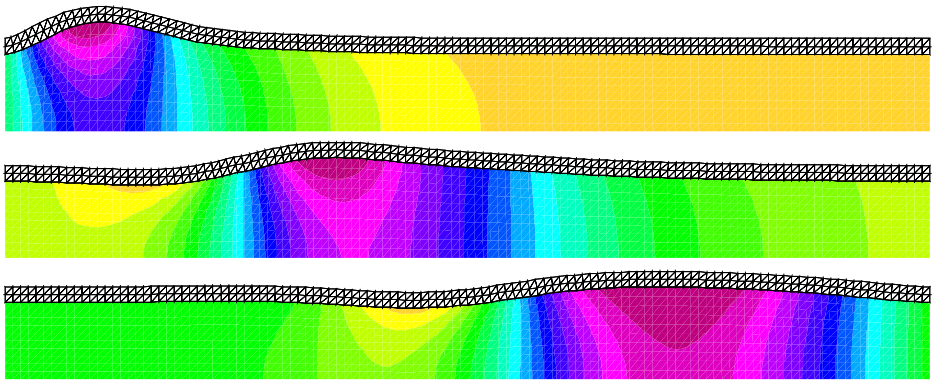

Figure 3.1: Snapshots of the fluid pressure and solid deformation at $t = 4 \cdot 10^{-3}$, $9 \cdot 10^{-3}$ and $15 \cdot 10^{-3}$ (from top to bottom). Algorithm 3.1 with $r = 1$, $\tau = 10^{-4}$ and $h = 0.05$.

Figure 3.2. We can clearly observe that the extrapolation order r has a major impact on the accuracy of Algorithm 3.1, as suggested by (3.36). The choice $r = 0$ yields a very poor accuracy, while for $r = 1$ seems to be only slightly less accurate than the implicit scheme. Accordingly with (3.36), as the time step τ tends to zero, the numerical solution obtained with $r = 1$ reaches the implicit coupling solution.

The results of Algorithm 3.1 with $r = 2$ are not reported in Figure 3.2 since the scheme is unstable for the set of physical and discretization parameters considered. The stability condition (3.43) is very restrictive in this case (parabolic-CFL condition). In order to provide a global overview of all the variants (including the case $r = 2$) we propose to switch off the solid damping (i.e., $\alpha_0 = \alpha_1 = 0$). According to Theorem 3.4.1 this yields a weakened 6/5-CFL stability condition. The results obtained with $\tau = 2 \cdot 10^{-5}$ and $h = 0.05$ are reported in Figure 3.3. Once more, for $r = 0$ we get a very poor approximation. Algorithm 3.1 with $r = 1$ and $r = 2$ yields practically the same solution as the implicit scheme. This suggests that, in this case, the magnitude of the kinematic perturbation (3.36) introduced by the splitting is lower than the remaining time and space error contributions.

We now investigate the impact of the spatial discretization on the size of the kinematic perturbation (4.11). For this purpose, we present in Figure 3.4 the results obtained with $\tau = 10^{-4}$ and $h = 0.025$. By comparing with Figure 3.2(a) we see that, for a fixed time-step length, the accuracy of Algorithm 3.1 deteriorates under spatial refinement. This behavior is even more striking in Figure 3.5 where we report the vertical displacement obtained for several values of h (and $\tau = 10^{-4}$ fixed). This clearly indicates a non-uniformity in h of the truncation error induced by the kinematic perturbation (3.36).

In order to provide a complete insight on the accuracy of the schemes, Figure 3.6(a) presents the convergence histories of the solid displacement relative energy error at time $t = 1.5 \cdot 10^{-2}$ obtained with Algorithm 3.1 and the implicit coupling scheme, by refining both in space and in time under a hyperbolic-CFL constraint ($\tau = h/200$).

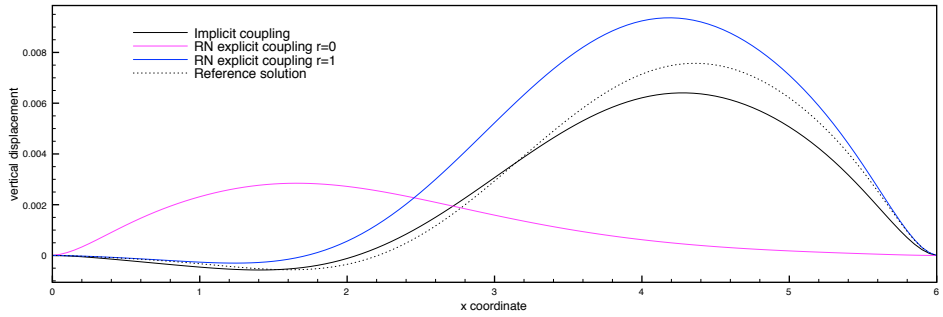

(a) $\tau = 10^{-4}$.

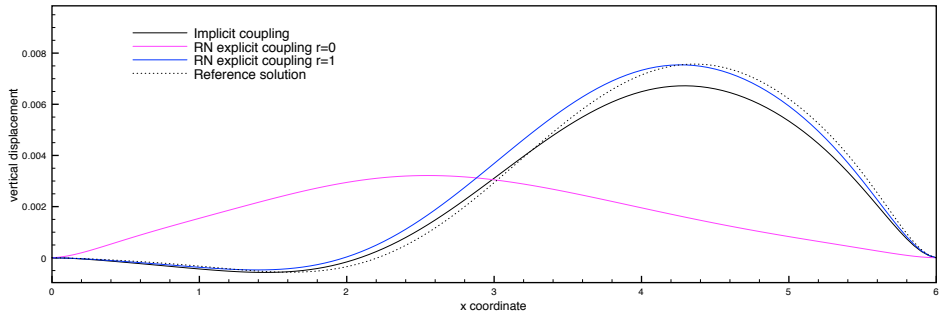

(b) $\tau = 5 \cdot 10^{-5}$.

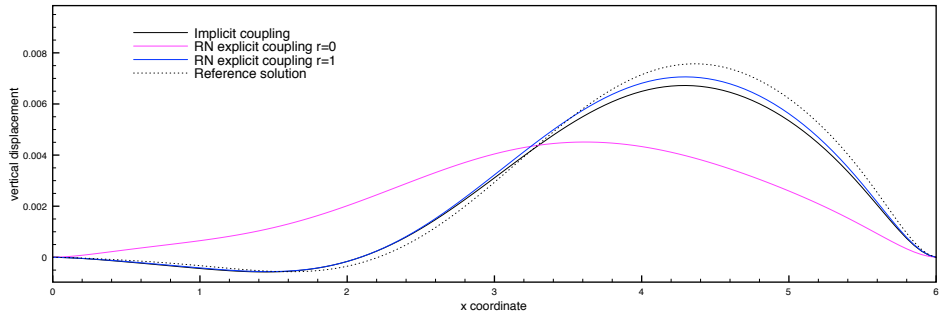

(c) $\tau = 2 \cdot 10^{-5}$.

Figure 3.2: Interface vertical displacement at time $t = 1.5 \cdot 10^{-2}$, with $h = 0.05$ (damped solid, $\beta = 10^{-3}$).

The variant with $r = 0$ is unable to show a convergent behavior towards the reference solution. On the contrary, the scheme with $r = 1$ shows a convergence rate between $\frac{1}{2}$ and 1. The superior accuracy of the the implicit scheme is clearly visible, for which we recover the expected first-order optimal rate. Note that Algorithm 3.1 with $r = 1$ yields convergence under the standard hyperbolic-CFL constraint (without the need of corrections iterations). This is a significant progress with respect to the stabilized explicit coupling scheme reported in [18], for which convergence demands strengthened CFL conditions (see [43, 21]).

In Figure 3.6(b), we report the convergence histories obtained under a parabolic-

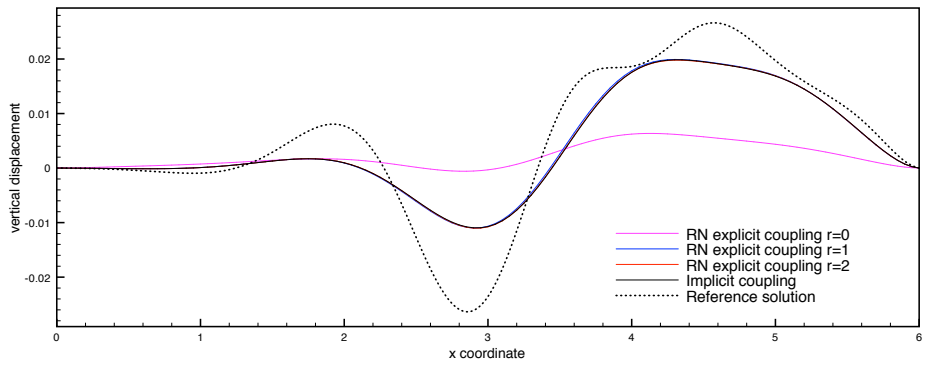

Figure 3.3: Interface vertical displacement at time $t = 1.5 \cdot 10^{-2}$, with $\tau = 2 \cdot 10^{-5}$ and $h = 0.05$, (undamped solid).

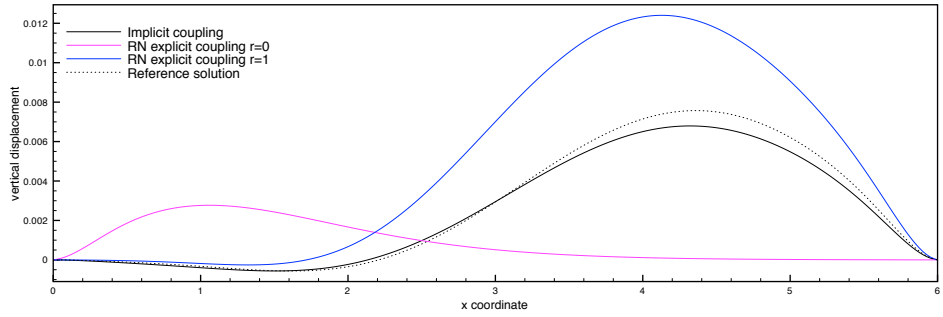

Figure 3.4: Interface vertical displacement at time $t = 1.5 \cdot 10^{-2}$ for $\tau = 10^{-4}$ and $h = 0.01$.

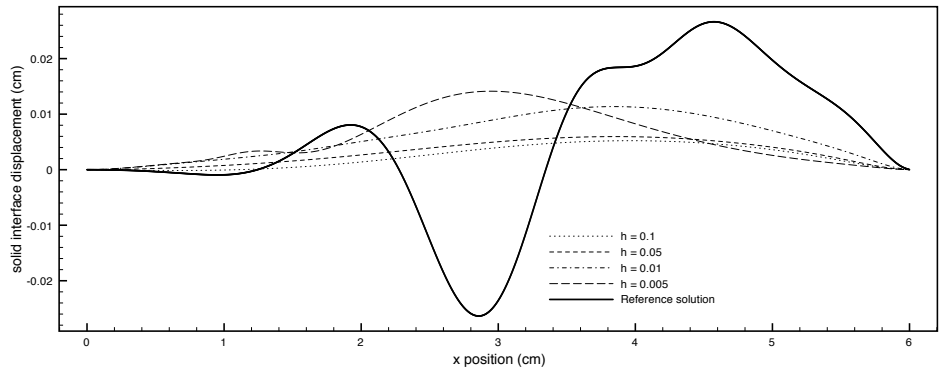

Figure 3.5: Interface vertical displacement at time $t = 1.5 \cdot 10^{-2}$. Algorithm 3.1 with $r = 1$ and $\tau = 10^{-4}$.

CFL constraint ($\tau = h^2/100$) and without damping in the solid ($\alpha_0 = \alpha_1 = 0$). In this case, the explicit variant with $r = 0$ shows a convergent behavior, with a rate between $\frac{1}{2}$ and 1. A superior convergent behavior is observed for the explicit schemes with $r = 1$ and $r = 2$ and the implicit scheme, which yield practically the same rate.

In view of the results reported in Figure 3.6, we postulate the following rates for

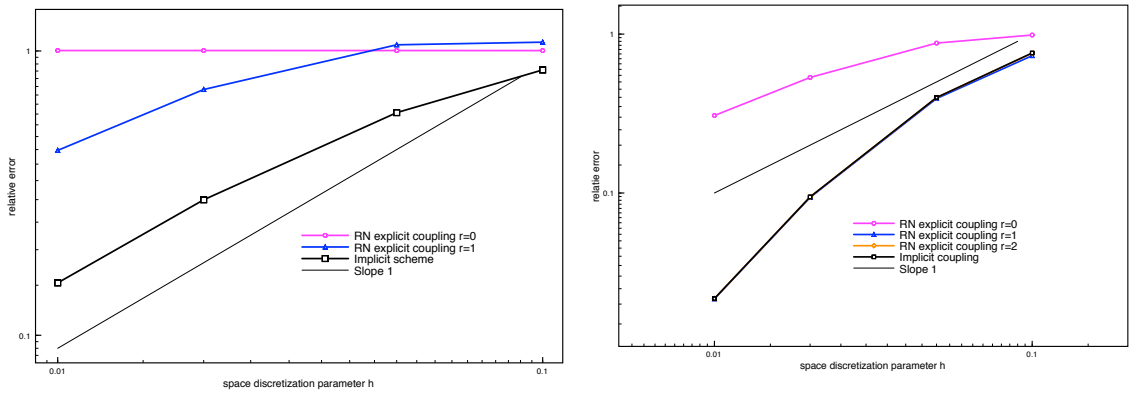

(a) $\tau = \mathcal{O}(h)$ and damped solid.

(b) $\tau = \mathcal{O}(h^2)$ and undamped solid.

Figure 3.6: Convergence history of the solid displacement relative energy error at time $t = 1.5 \cdot 10^{-2}$.

the consistency of the kinematic perturbation (3.36):

- $r = 0$: $\mathcal{O}\big((\tau/h)^{\frac{1}{2}}\big)$;
- $r = 1$: $\mathcal{O}\big(\tau/h^{\frac{1}{2}}\big)$;
- $r = 2$: $\mathcal{O}\big(\tau^2/h^{\frac{1}{2}}\big)$.

It is worth noting that the factor $h^{-\frac{1}{2}}$ is not present in the original Robin-Neumann explicit schemes of Chapter 2 (see also [45]), in the case of the coupling with a thin-walled structure.

3.6.1.2 Partitioned solution of implicit coupling

In this section we investigate numerically the convergence properties of the (parameter free) iterative procedure given by Algorithm 3.2. Figure 3.7 reports the mean number of iterations per time-step needed to simulate the wave propagation until $t = 5 \cdot 10^{-3}$, for different values of τ, h, ρ^s, Young Modulus E and domain length L. We compare the performance of Algorithm 3.2 with the standard Robin-Neumann procedure introduced in [98], using the Robin coefficient $\alpha = \rho^s \epsilon/\tau + c_0 \tau$ proposed therein. The iterations are initialized from the data of the previous time-step.

Both procedures yield a similar behavior with respect to the solid density and the domain length (see Figures 3.7(a)-(b)). Figures 3.7(c)-(d), on the contrary, show that Algorithm 3.2 is much less sensitive to τ and E than the standard Robin-Neumann procedure. In fact, as suggested by the error estimate of Theorem 3.4.2, reducing τ enhances the convergence speed of Algorithm 3.2. This can also be explained in terms of the kinematic relation $(3.40)_1$, since the size of the perturbation is proportional to $\tau E/\rho^s$. Note that the convergence of the standard Robin-Neumann method degrades as

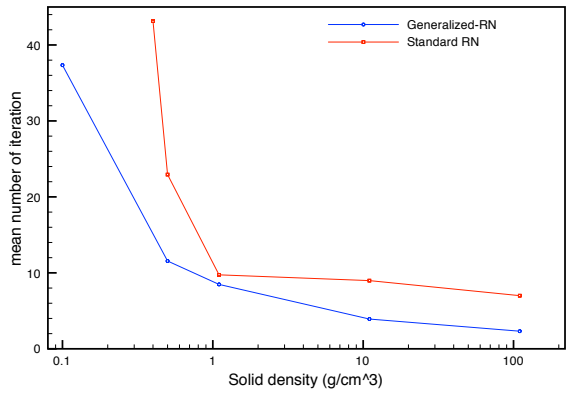

(a) Impact of ρ^s.

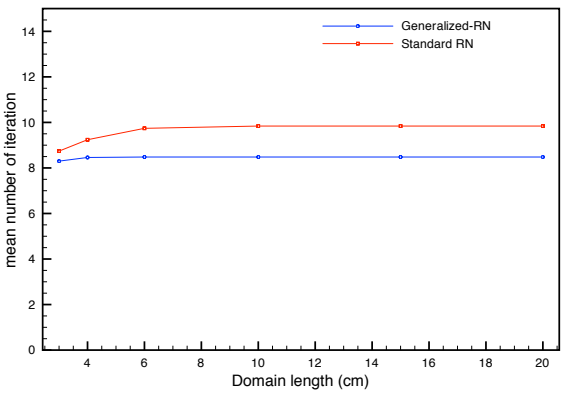

(b) Impact of L.

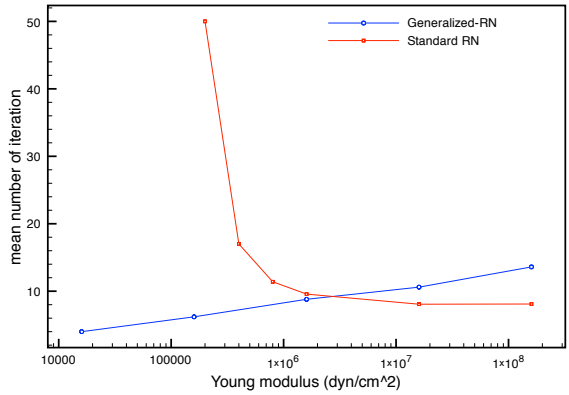

(c) Impact of E.

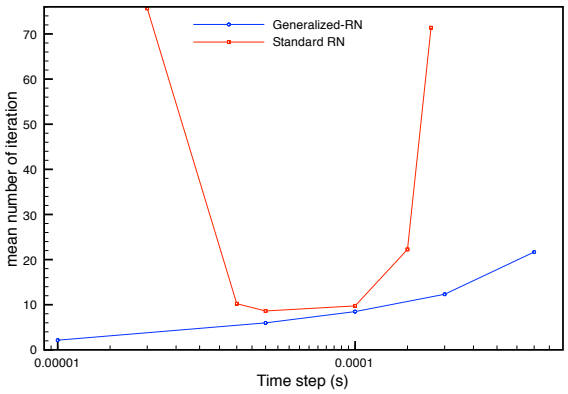

(d) Impact of τ.

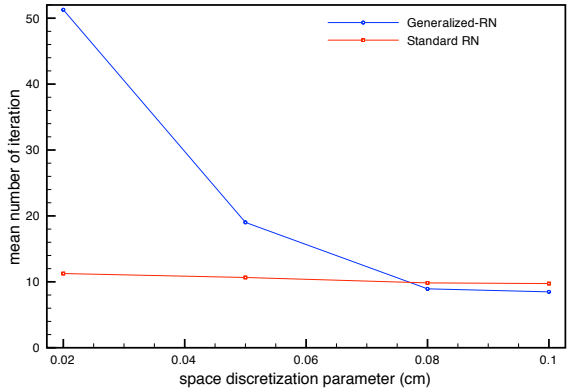

(e) Impact of h.

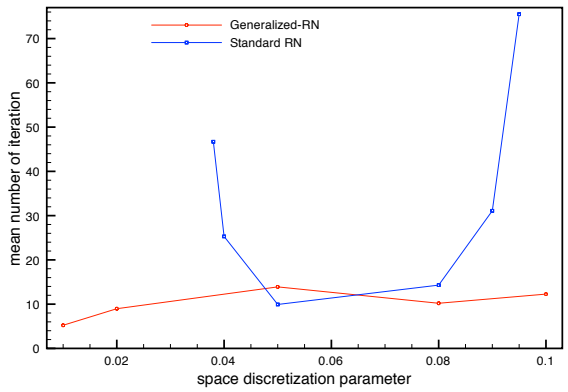

(f) Impact of h and τ, $\tau = \mathcal{O}(h^2)$.

Figure 3.7: Sensitivity of the convergence speed of the iterative procedure to the physical and discretization parameters.

τ goes to zero. This behavior is also highlighted by Figure 3.8, where we have reported the relative error per iteration for different values of τ.

In line with the non-uniformity in h observed for the accuracy of Algorithm 3.1

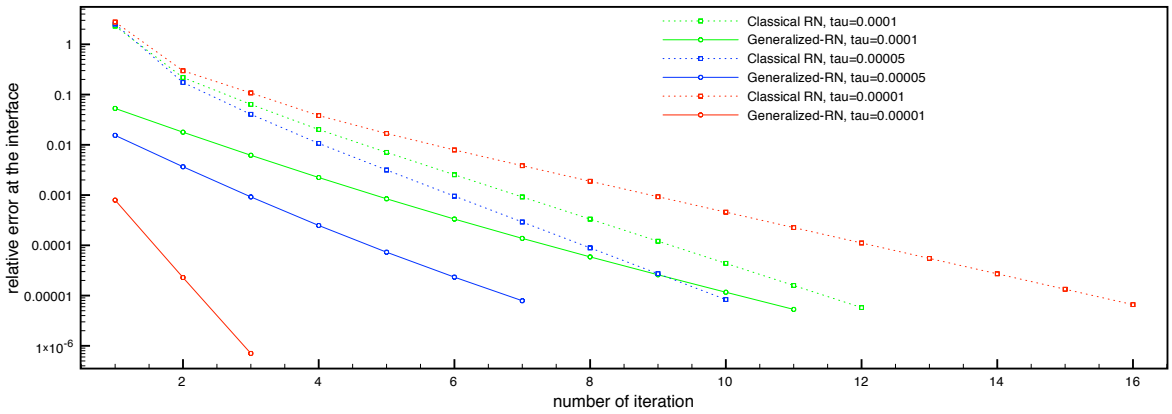

Figure 3.8: Relative error on the interface against the number of sub-iterations for the Robin-Neumann scheme and the corrected scheme with $h = 0.1$.

in Section 3.6.1.1, the convergence of Algorithm 3.2 degrades as h goes to zero (τ fixed), as shown in Figure 3.7(e). Finally, Figure 3.7(f) shows that under a parabolic-CFL condition, the standard Robin-Neumann method losses convergence, whereas the proposed Algorithm 3.2 keeps a reduced number of iterations.

3.6.2 Pressure wave propagation in a straight tube

We consider the example proposed in in [59] (see also [60, Chapter 12]). The fluid-structure system is modeled by the non-linear coupled problem (3.53)-(3.55). The fluid domain is a straight tube of radius 0.5 and length 5. All the units are given in the CGS system. The vessel wall has a thickness of 0.1 and is clamped at its extremities. The physical parameters for the fluid are $\rho^{\mathrm{f}} = 1$ and $\mu = 0.035$. For the solid we have $\rho^{\mathrm{s}} = 1.2$, Young modulus $E = 3\times10^6$ and Poisson's ratio $\nu = 0.3$. The overall system is initially at rest and an over pressure of 1.3332×10^4 is imposed on the inlet boundary during the time interval $[0, 0.005]$. The fluid and solid equations are discretized in space using continuous $\mathbb{P}_1$ finite elements (a SUPG/PSPG stabilized formulation is considered in the fluid).

In Figure 3.9 we have reported some snapshots of the fluid pressure and solid deformation (amplified by a factor 10) obtained with Algorithm 3.3 ($r = 1$) and $\tau = 10^{-4}$. A stable pressure wave propagation is observed. The impact of the solid damping ($\alpha_0 = 1$, $\alpha_1 = 10^{-3}$) is noticeable.

For comparison purposes, Figure 3.10 reports the interface mid-point displacement magnitudes obtained with Algorithm 3.3 and the implicit coupling scheme. Algorithm 3.3 with $r = 1$ yields a stable numerical solution in all the cases considered, which confirms the unconditional stability stated in Theorem 3.4.1. As regards accuracy, the scheme retrieves the overall dynamics of the solution provided implicit method, particularly, with the smallest time-step lengths. A phase mismatch is clearly visible with $\tau = 10^{-4}$.

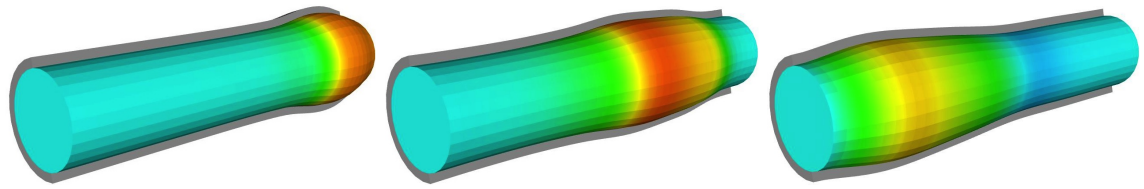

(a) Undamped solid ($\alpha_1 = \alpha_1 = 0$).

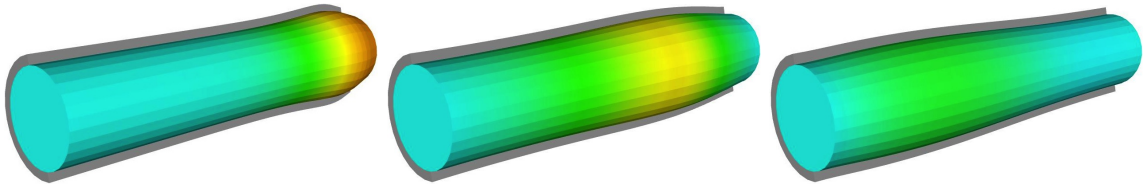

(b) Damped solid ($\alpha_0 = 1$, $\alpha_1 = 10^{-3}$).

Figure 3.9: Snapshots of the fluid pressure and solid deformation at $t = 0.003, 0.007, 0.012$ (from left to right) obtained with Algorithm 3.3 ($r = 1$) and $\tau = 10^{-4}$.

Algorithm 3.3 with $r = 0$ yields either a poor approximation or instability at the level of the inlet boundary. The accuracy issue was already observed in Section 3.6.1.1 with a linear problem. Numerical investigations (not reported here) indicate that the instabilities are the result of an intricate interaction between the low-order perturbation of the kinematic constraint, the non-linearity of the fluid equation and the natural character of the inlet boundary conditions. This explains the discrepancy with the stability result of Theorem 3.4.1 (linear case) and the fact that the spurious oscillations are not visible in Figure 3.10 (interface mid-point displacement).

Figure 3.10 points out the restrictive time-step restrictions required by Algorithm 3.3 with $r = 2$. A stable numerical approximation is observed only in the case without solid damping and for the smallest time-step length. This confirms the hybrid hyperbolic/parabolic characteristics of the stability condition (3.43) in Theorem 3.4.1. Though unstable, the high-order perturbation of the kinematic constraint introduced by the explicit scheme with $r = 2$ is clearly visible in Figure 3.10(a).

3.6.3 Cantilever test problem

In this example we consider the two-dimensional benchmark proposed in [114], describing the flow of a fluid around a cylinder with an attached elastic structure. The fluid-structure system is modeled by the non-linear coupled problem (3.53)-(3.55). The reader is referred to [114] for the complete description of the geometry. The fluid and solid are supposed to be initially at rest. A parabolic velocity profile is imposed on the inlet boundary. The mean inflow velocity is denoted by $\bar{U}$. The physical parameters for the fluid are $\rho^{\mathrm{f}} = 10^3$, $\mu = 10^{-3}$ and $\bar{U} = 2$ (i.e., Re= 200), while for the solid we have $\rho^{\mathrm{s}} = 10^3$, $E = 5.6 \cdot 10^6$, $\nu = 0.4$ and $\alpha_0 = \alpha_1 = 0$ (undamped solid). All the units are given in the SI system. Among the test-cases proposed in [114], this physical setting

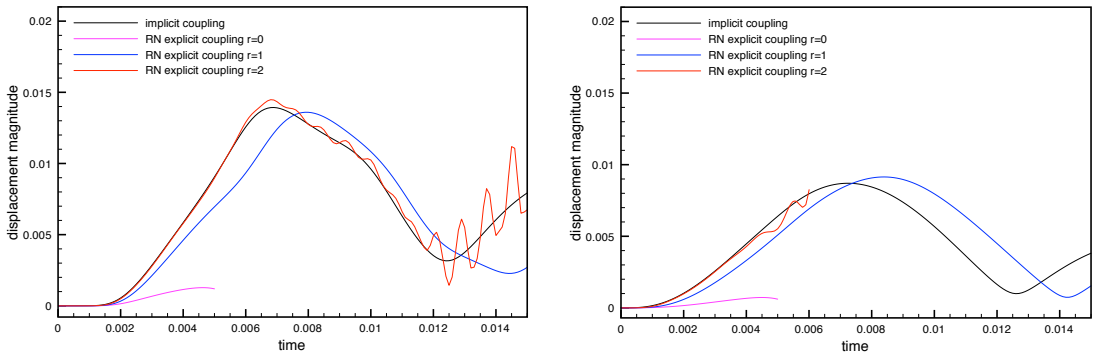

(a) $\tau = 10^{-4}$.

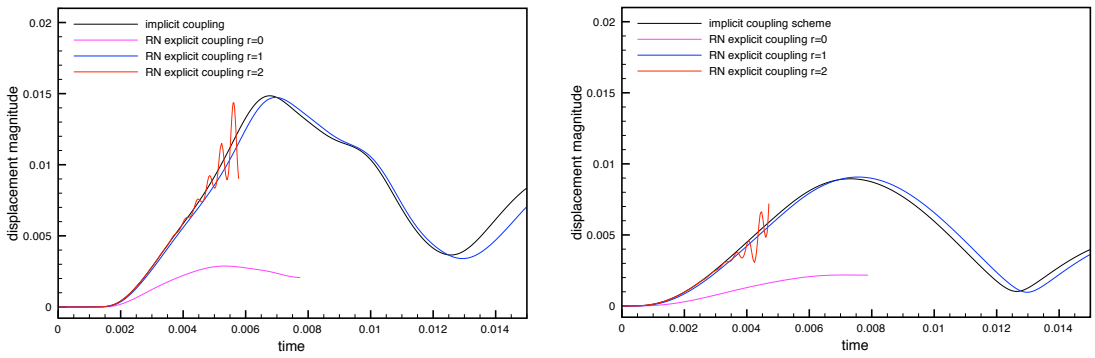

(b) $\tau = 4.4721 \cdot 10^{-5}$.

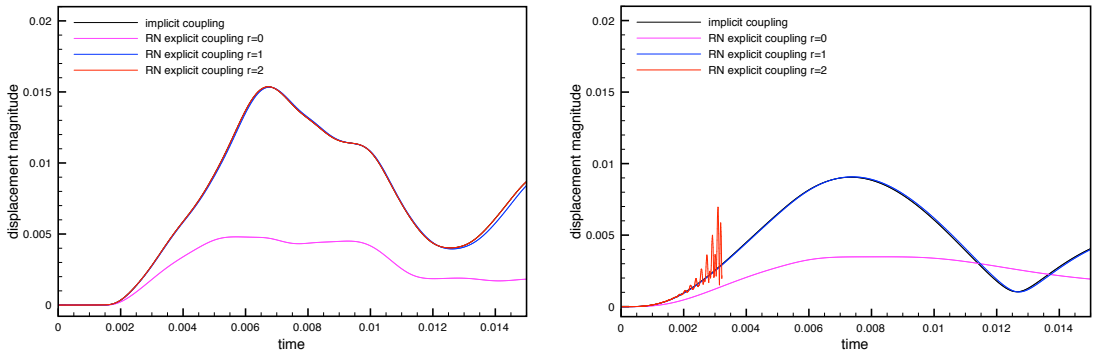

(c) $\tau = 2 \cdot 10^{-5}$.

Figure 3.10: Interface mid-point displacement magnitudes obtained with the implicit coupling scheme and Algorithm 3.3. Left: undamped solid ($\alpha_0 = \alpha_1 = 0$). Right: damped solid ($\alpha_0 = 1$, $\alpha_1 = 10^{-3}$).

(termed FSI3 in [114]) is the most difficult from the point of view of the added-mass effect issues ($\rho^s = \rho^f$).

The simulations are performed in three-dimensions, by imposing symmetry conditions along the extrusion direction. The fluid and solid equations are discretized in space using continuous $\mathbb{P}_1$ finite elements (a SUPG/PSPG stabilized formulation is considered in the fluid). The time-step length is $\tau = 10^{-3}$ and a total number of 86912

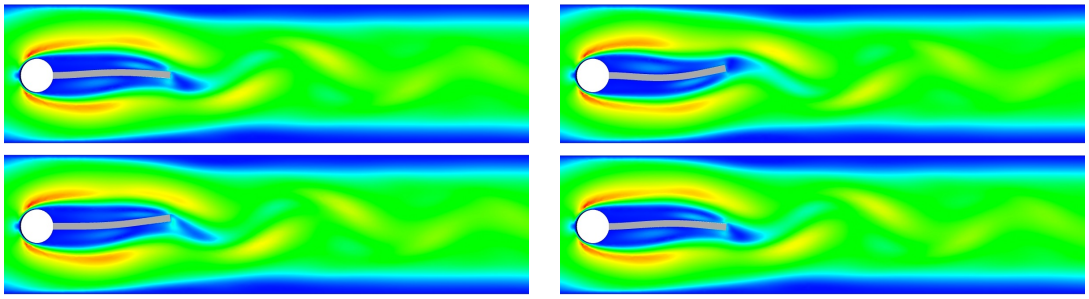

Figure 3.11: Fluid velocity magnitude and solid deformation at $t = 9.65$, 9.722, 9.848 and 10 (from left to right and top to bottom) obtained with Algorithm 3.3 ($r = 1$).

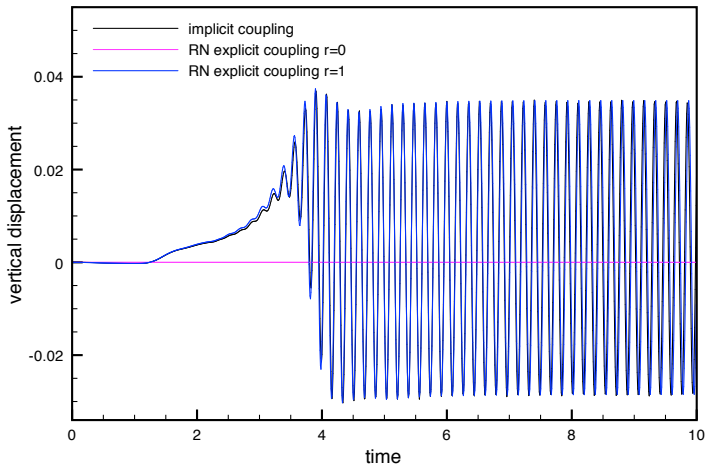

Figure 3.12: Vertical displacement at an interface node obtained with the implicit coupling scheme and Algorithm 3.3 ($\tau = 10^{-3}$).

and 1830 degrees-of-freedom is considered, respectively, for the fluid and the solid. This is among the coarsest space-time resolutions considered in [114]. For illustration purposes, some snapshots of the fluid velocity magnitude and solid deformation obtained with Algorithm 3.3 ($r = 1$) are reported in Figure 3.11. A stable solution involving periodic self-excited oscillations of large amplitude is observed. The oscillating structure generates a periodic vortex pattern that is advected along the channel.

Figure 3.12 reports the interface mid-point displacement magnitudes obtained with Algorithm 3.3 ($r = 0$ and $r = 1$) and the implicit coupling scheme. The poor accuracy of the explicit coupling scheme with $r = 0$ is striking. On the contrary, the solution obtained with $r = 1$ is practically indistinguishable from the one provided by the implicit coupling scheme. This enhanced accuracy, with respect to the results reported in Section 3.6.2, can be explained by the fact that increasing the solid density reduces the impact of the kinematic perturbation in (3.36). Numerical investigations (not reported here) showed that, for this set of discretization parameters, Algorithm 3.3 with $r = 2$ is unstable and that smaller time-steps are needed for stability.

3.6.4 Damped structural instability

We consider an adaptation of the *balloon-type* fluid-structure example proposed in [80]. A curved fluid domain is surrounded by two structures with different stiffness (see

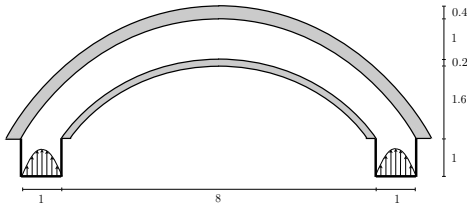

Figure 3.13: A bended fluid domain surrounded by two structures.

Figure 3.13). Both structures are fixed on their extremities. A parabolic velocity profile is prescribed on the left and right inflow boundaries, with maximal magnitudes 10 and 10.2, respectively (to avoid perfect symmetry). All the units are given in the SI system. Zero velocity is enforced on the remaining fluid boundaries. The fluid-structure system is modeled by the coupled problem (3.53)-(3.55). The fluid is loaded with the volume force $\boldsymbol{f} = (0, -1)^{\mathrm{T}}$. The fluid physical parameters are given by $\rho^{\mathrm{f}} = 1.0$ and $\mu = 9$, while for the top and bottom (undamped) structures we have $\rho^{\mathrm{s}} = 500$, $E_{\mathrm{top}} = 9 \cdot 10^5$, $E_{\mathrm{bottom}} = 9 \cdot 10^7$, $\nu = 0.3$ and $\alpha_0 = \alpha_1 = 0$. The simulations are performed in three-dimensions, by imposing symmetry conditions along the extrusion direction. The fluid and solid equations are discretized in space using continuous $\mathbb{P}_1$ finite elements (a SUPG/PSPG stabilized formulation is considered in the fluid).

It is well known that this type of problem cannot be solved via standard Dirichlet-Neumann partitioned procedures, since (at each iteration) the interface solid velocity does not necessarily satisfy the compatibility condition enforced by the incompressibility of the fluid (unless directly prescribed in the structure [80]). Algorithm 3.3 circumvents this issue in a natural fashion since the generalized Robin condition on the fluid removes the constraint on the interface solid velocity.

Figure 3.15 shows the fluid velocity magnitude snapshots and the solid deformations at different time instants, obtained with Algorithm 3.3 ($r = 1$) and a time-step of $\tau = 0.005$. As in Chapter 2 and [80, 56], the deformation is first mainly visible in the upper (more flexible) structure and then the lower structure buckles. In Figure 3.15, we have reported the interface mid-point displacement magnitude of the bottom structure obtained with Algorithm 3.3 ($r = 0$ and $r = 1$) and the implicit coupling scheme, for $\tau = 0.005$ and $\tau = 0.0025$. The results of Algorithm 3.3 with $r = 2$ are not reported in Figure 3.15 due to the lack of stability, smaller time-steps are required. The poor accuracy of the explicit coupling scheme without extrapolation $r = 0$ is, once more, striking. The excess of mass-loss across the interface induced by the low-order perturbation of the kinematic coupling prevents the buckling of the bottom structure. On the contrary, the implicit scheme and Algorithm 3.3 with $r = 1$ predict the collapse of the bottom structure for all the values of τ considered. The better accuracy of the

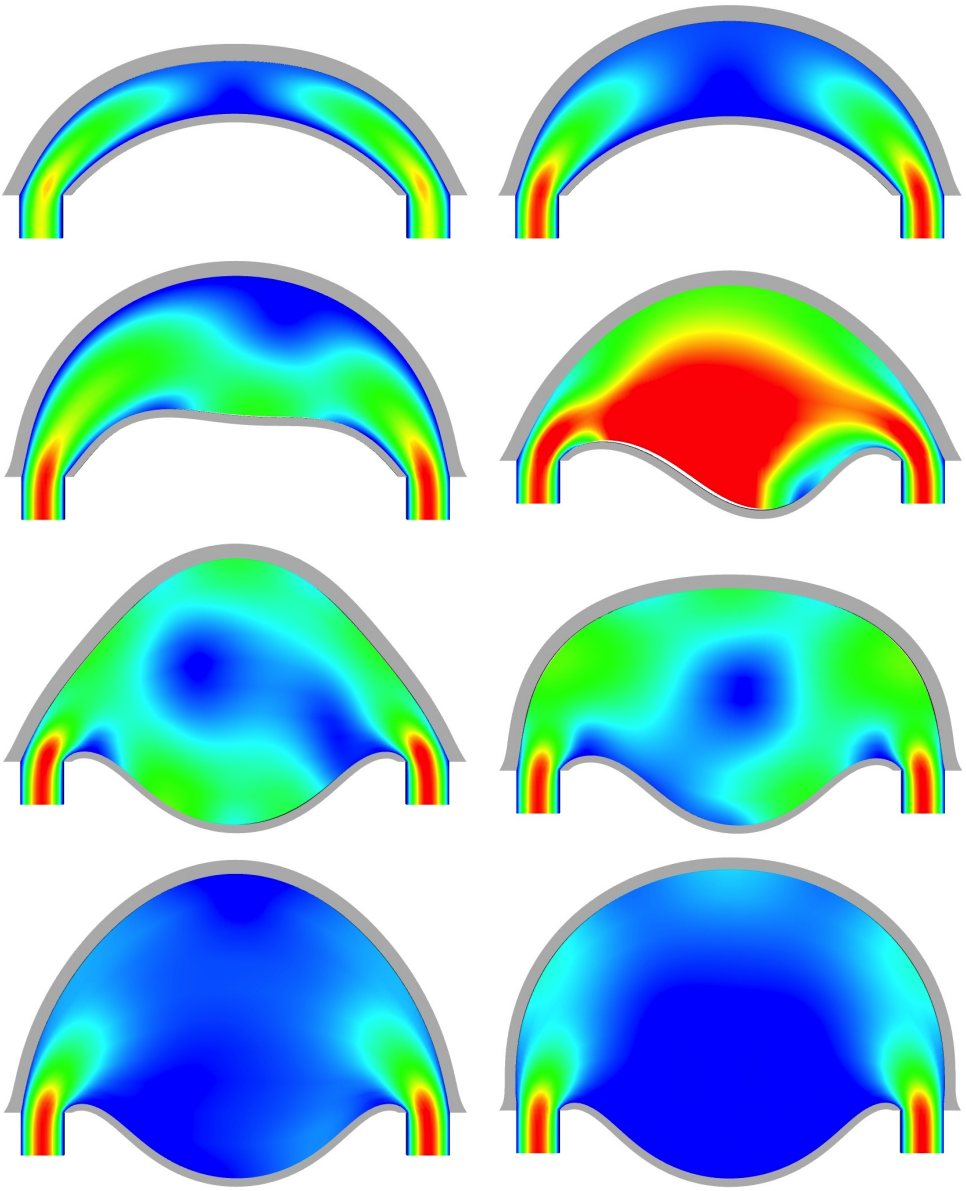

Figure 3.14: Snapshots of the fluid velocity and solid deformation at $t = 0.5, 1.15, 1.65, 1.9, 2.4, 2.5, 3.25, 3.75$ (from left to right and top to bottom). Algorithm 3.3 with $r = 1$ and $\tau = 0.005$.

implicit scheme with respect to Algorithm 3.3 with $r = 1$ is visible for the largest time-step length.

3.7 Conclusion

In this chapter, we have proposed a generalization of the explicit Robin-Neumann schemes introduced in Chapter 2 to the case of the coupling with thick-walled struc-

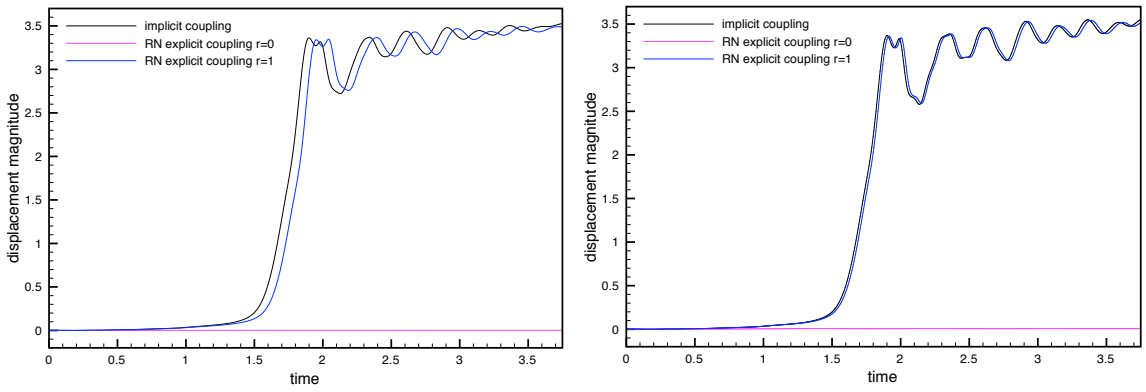

(a) $\tau = 0.005$. (b) $\tau = 0.0025$.

Figure 3.15: Interface mid-point displacement magnitudes of the bottom structure obtained with the implicit coupling scheme and Algorithm 3.3.

tures. The schemes are based on the following ingredients:

- Generalized notion of interface Robin consistency, using a mass-lumping approximation in the structure (Section 3.3.2);
- Implicit treatment of the sole interface solid inertia within the fluid;
- Appropriate extrapolations of the interface solid velocity and stress.

The second guarantees added-mass free stability (Theorem 3.4.1), while the third enables the staggered fluid-solid time-marching in a genuinely partitioned fashion.

Though the proposed extension retains the main stability properties of the original explicit Robin-Neumann schemes (proposed in [45] and Chapter 2), numerical evidence suggests that their optimal (first-order) accuracy is not necessarily preserved. Indeed, the order of the kinematic perturbation induced by the splitting is expected to be $\mathcal{O}((\tau/h)^{\frac{1}{2}})$, $\mathcal{O}(\tau/h^{\frac{1}{2}})$ or $\mathcal{O}(\tau^2/h^{\frac{1}{2}})$, depending on the order $r = 0$, 1 or 2 of the extrapolations. The factor $h^{-\frac{1}{2}}$ seems to be intrinsically related to the thick-walled character of the structure. The full convergence analysis of these methods will be the topic of the next chapter.

The comparison of the different methods has shown that the best robustness is obtained with the first-order extrapolation ($r = 1$). A salient feature of this scheme is that it simultaneously yields unconditional stability and convergence under a standard hyperbolic-CFL constraint. Furthermore, overall first-order accuracy is expected under a strengthened 3/2-CFL constraint, $\tau = \mathcal{O}(h^{\frac{3}{2}})$, without the need of correction iterations.

The schemes have been interpreted as a single iteration of a new, parameter free, Robin-Neumann iterative procedure for the partitioned solution of implicit coupling. The convergence of this iterative method has been established (Theorem 3.4.2). Numerical evidence has confirmed that, unlike standard Robin-Neumann approaches,

reducing the time-step length increases the convergence speed of the proposed iterations.

Chapter 4

Convergence analysis of the generalized Robin-Neuman explicit coupling schemes

The results presented in this chapter lead to the manuscript: M.A. Fernández, J. Mullaert. **Convergence analysis for a class of explicit coupling schemes in incompressible fluid-structure interaction**. Submitted for publication.

Contents

4.1 Introduction . . . 119
4.2 Numerical methods . . . 120
4.2.1 Spatial semi-discrete approximation . . . 120
4.2.2 Time discretization: coupling schemes . . . 122
4.3 Convergence Analysis . . . 128
4.3.1 Preliminaries . . . 128
4.3.2 Projection operators and error decomposition . . . 129
4.3.3 Discrete error estimation . . . 131
4.3.4 A priori error estimates . . . 135
4.3.5 Anlaysis of the fluid-solid hydrodynamic projector . . . 136
4.3.6 Proof of Theorem 4.3.1 . . . 140
4.3.7 Proof of Theorem 4.3.2 . . . 148
4.4 Numerical experiments . . . 149
4.5 Conclusion . . . 151

4.1 Introduction

This chapter is devoted to the a priori error analysis of the generalized Robin-Neumann methods introduced in Chapter 3. We show that these schemes can be seen as a lumped-mass approximation of a semi-implicit (fractional-step) coupling scheme with the same stability properties as the original explicit coupling.

A priori error estimates are derived for all the variants (including the case without mass-lumping in the structure) using energy arguments. The analysis proposed represents, to the best of our knowledge, the first theoretical convergence result for a explicit coupling scheme with a thick-walled structure. Though the proof of the error estimate follows the main steps of Section 2.4.4 (Chapter 2), the thick-walled nature of the solid and the mass-lumping approximation make the analysis more intricate. In

particular, a special care is needed in the design of the fluid and solid velocity projectors, depending on the presence or not of second-order terms in the solid viscous damping (i.e., $\alpha_1 > 0$ or $\alpha_1 = 0$).

The analysis predicts an $\mathcal{O}(h^{-\frac{1}{2}})$ perturbation in the splitting error, confirming the numerical results reported in Chapter 3. The analysis also shows that this perturbation is exclusively related to the thick-walled character of the structure, through the non-uniformity of the discrete viscoelastic operator, and not to the mass-lumping approximation in the solid. This point is evidenced via numerical experiments as well. We show, in addition, that splitting methods reported in the literature (e.g., [14]) suffer from this issue.

The remainder of this chapter is organized as follows. Section 4.2 presents the different coupling schemes. Section 4.3 is devoted to the error analysis of the methods. A short numerical study complementing Section 3.6 is reported in Section 4.4. Finally, a summary of the conclusions is given in Section 4.5.

4.2 Numerical methods

This section is devoted to the numerical approximation of the coupled problem (3.4), that we recall here for the sake of completeness: for $t > 0$, find $(\boldsymbol{u}(t), \dot{\boldsymbol{d}}(t)) \in \boldsymbol{W}$, $p(t) \in Q$ and $\boldsymbol{d}(t) \in \boldsymbol{V}^{\mathrm{s}}$ such that

$$\begin{cases} \dot{\boldsymbol{d}} = \partial_t \boldsymbol{d}, \\ \rho^{\mathrm{f}} \left(\partial_t \boldsymbol{u}, \boldsymbol{v}^{\mathrm{f}}\right)_{\Omega^{\mathrm{f}}} + a(\boldsymbol{u}, \boldsymbol{v}^{\mathrm{f}}) + b(p, \boldsymbol{v}^{\mathrm{f}}) - b(q, \boldsymbol{u}) \\ \qquad + \rho^{\mathrm{s}} \left(\partial_t \dot{\boldsymbol{d}}, \boldsymbol{v}^{\mathrm{s}}\right)_{\Omega^{\mathrm{s}}} + a^{\mathrm{e}}(\boldsymbol{d}, \boldsymbol{v}^{\mathrm{s}}) + a^{\mathrm{v}}(\dot{\boldsymbol{d}}, \boldsymbol{v}^{\mathrm{s}}) = l(\boldsymbol{v}^{\mathrm{f}}), \end{cases} \tag{4.1}$$

for all $(\boldsymbol{v}^{\mathrm{f}}, \boldsymbol{v}^{\mathrm{s}}) \in \boldsymbol{W}$ and $q \in Q$. The key feature of the methods analyzed is that they provide different degrees of splitting between the computation of the fluid and the solid. We recall the family of schemes introduced in Chapter 3 (Algorithm 4.2) and a variant (Algorithm 4.1) with less degree of splitting between the computation of the fluid and the solid. The error analysis of these methods (Algorithms 4.1 and 4.2) will be topic of Section 4.3. Finally, we review some alternative splitting schemes that can be found in the literature (Algorithm 4.3, see [14]).

The spatial semi-discrete finite element approximation of the coupled problem (4.1) is recalled in Section 4.2.1. Section 4.2.2 presents the time discretization and the different fluid-solid time splitting schemes.

4.2.1 Spatial semi-discrete approximation

As in Chapter 3, we consider a finite element approximation in space based on continuous piece-wise affine functions. The corresponding finite element spaces are denoted by $\boldsymbol{V}_h^{\mathrm{f}} \subset \boldsymbol{V}^{\mathrm{f}}$, $Q_h \subset Q$, $\boldsymbol{V}_h^{\mathrm{s}} \subset \boldsymbol{V}^{\mathrm{s}}$, where the subscript $h > 0$ indicates the level of spatial refinement. Since the fluid velocity/pressure pair $\boldsymbol{V}_h^{\mathrm{f}}/Q_h$ fails to satisfy the inf-sup condition (see, e.g., [40]), we consider a symmetric pressure stabilization method

defined by a non-negative bilinear form, $s_h : Q_h \times Q_h \to \mathbb{R}$ entering, for instance, the abstract framework of [17]. We define the semi-norm $|q_h|_{s_h} \stackrel{\text{def}}{=} \sqrt{s_h(q_h, q_h)}$ for all $q_h \in Q_h$.

Furthermore, we assume that the fluid and solid discretizations match at the interface, that is,

$$\boldsymbol{\Lambda}_{\Sigma,h} \stackrel{\text{def}}{=} \left\{ \boldsymbol{v}_h^{\mathrm{f}}|_\Sigma \,/\, \boldsymbol{v}_h^{\mathrm{f}} \in \boldsymbol{V}_h^{\mathrm{f}} \right\} = \left\{ \boldsymbol{v}_h^{\mathrm{s}}|_\Sigma \,/\, \boldsymbol{v}_h^{\mathrm{s}} \in \boldsymbol{V}_h^{\mathrm{s}} \right\}$$

and we set $\boldsymbol{V}_{\Sigma,h}^{\mathrm{f}} \stackrel{\text{def}}{=} \left\{ \boldsymbol{v}_h^{\mathrm{f}} \in \boldsymbol{V}_h^{\mathrm{f}} \,/\, \boldsymbol{v}_h^{\mathrm{f}}|_\Sigma = \boldsymbol{0} \right\}$, $\boldsymbol{V}_{\Sigma,h}^{\mathrm{s}} \stackrel{\text{def}}{=} \left\{ \boldsymbol{v}_h^{\mathrm{s}} \in \boldsymbol{V}_h^{\mathrm{s}} \,/\, \boldsymbol{v}_h^{\mathrm{s}}|_\Sigma = \boldsymbol{0} \right\}$ and

$$\boldsymbol{W}_h \stackrel{\text{def}}{=} \left\{ (\boldsymbol{v}_h^{\mathrm{f}}, \boldsymbol{v}_h^{\mathrm{s}}) \in \boldsymbol{V}_h^{\mathrm{f}} \times \boldsymbol{V}_h^{\mathrm{s}} \,/\, \boldsymbol{v}_h^{\mathrm{f}}|_\Sigma = \boldsymbol{v}_h^{\mathrm{s}}|_\Sigma \right\}.$$

We will consider the standard solid-sided and fluid-sided discrete lifting operators,

$$\boldsymbol{\mathcal{L}}_h^{\mathrm{s}} : \boldsymbol{\Lambda}_{\Sigma,h} \to \boldsymbol{V}_h^{\mathrm{s}}, \quad \boldsymbol{\mathcal{L}}_h^{\mathrm{f}} : \boldsymbol{\Lambda}_{\Sigma,h} \to \boldsymbol{V}_h^{\mathrm{f}},$$

defined for all $\boldsymbol{\xi}_h \in \boldsymbol{\Lambda}_{\Sigma,h}$, such that the nodal values of $\boldsymbol{\mathcal{L}}_h^{\mathrm{s}}\boldsymbol{\xi}_h, \boldsymbol{\mathcal{L}}_h^{\mathrm{f}}\boldsymbol{\xi}_h$ vanish out of Σ and that $(\boldsymbol{\mathcal{L}}_h^{\mathrm{s}}\boldsymbol{\xi}_h)|_\Sigma = (\boldsymbol{\mathcal{L}}_h^{\mathrm{f}}\boldsymbol{\xi}_h)|_\Sigma = \boldsymbol{\xi}_h$.

In what follows, the symbol $(\cdot,\cdot)_*$ designates either the standard inner-product $(\cdot,\cdot)_{\Omega^{\mathrm{s}}}$ in $L^2(\Omega^{\mathrm{s}})$, or its lumped-mass approximation $(\cdot,\cdot)_{\Omega^{\mathrm{s}},h}$ (see, e.g., [78, Section 2.3] and [112, Chapter 15]). We also set

$$a_*^{\mathrm{v}}(\dot{\boldsymbol{d}}_h, \boldsymbol{v}_h^{\mathrm{s}}) \stackrel{\text{def}}{=} \alpha_0 \rho^{\mathrm{s}} (\dot{\boldsymbol{d}}_h, \boldsymbol{v}_h^{\mathrm{s}})_* + \alpha_1 a^{\mathrm{e}}(\dot{\boldsymbol{d}}_h, \boldsymbol{v}_h^{\mathrm{s}})$$

for all $\boldsymbol{d}_h, \boldsymbol{v}_h^{\mathrm{s}} \in \boldsymbol{V}_h^{\mathrm{s}}$ and with a^{e} defined by $(3.5)_1$. We denote by $\|\cdot\|_{\mathrm{v},*}$ and $\|\cdot\|_*$ the norms associated to the inner-products a_*^{v} and $(\cdot,\cdot)_*$, respectively.

Remark 4.2.1. *We recall that the norms $\|\cdot\|_{0,\Omega^{\mathrm{s}}}$ and $\|\cdot\|_*$ are equivalent in $\boldsymbol{V}_h^{\mathrm{s}}$, uniformly in h (see, e.g., [112, Chapter 15]) and the same holds for $\|\cdot\|_{\mathrm{v}}$ and $\|\cdot\|_{\mathrm{v},*}$. We will use the symbol $\lesssim$ to indicate an inequality written up to a multiplicative constant (independent of the physical and discretization parameters). In such inequalities and for the sake of simplicity, we will only use the norms $\|\cdot\|_{0,\Omega^{\mathrm{s}}}$ and $\|\cdot\|_{\mathrm{v}}$.*

We consider the discrete reconstructions $\boldsymbol{L}_h^{\mathrm{e}} : \boldsymbol{V}^{\mathrm{s}} \to \boldsymbol{V}_h^{\mathrm{s}}$ and $\boldsymbol{L}_h^{\mathrm{v}} : \boldsymbol{V}_h^{\mathrm{s}} \to \boldsymbol{V}_h^{\mathrm{s}}$, of the elastic and viscous solid operators, defined through the relations:

$$(\boldsymbol{L}_h^{\mathrm{e}}\boldsymbol{d}, \boldsymbol{v}_h^{\mathrm{s}})_* = a^{\mathrm{e}}\big(\boldsymbol{d}, \boldsymbol{v}_h^{\mathrm{s}}\big), \quad (\boldsymbol{L}_h^{\mathrm{v}}\dot{\boldsymbol{d}}_h, \boldsymbol{v}_h^{\mathrm{s}})_* = a_*^{\mathrm{v}}\big(\dot{\boldsymbol{d}}_h, \boldsymbol{v}_h^{\mathrm{s}}\big), \tag{4.2}$$

for all $(\boldsymbol{d}, \dot{\boldsymbol{d}}_h, \boldsymbol{v}_h^{\mathrm{s}}) \in \boldsymbol{V}^{\mathrm{s}} \times \boldsymbol{V}_h^{\mathrm{s}} \times \boldsymbol{V}_h^{\mathrm{s}}$. We will also make use of the interface operator $\boldsymbol{B}_h : \boldsymbol{\Lambda}_{\Sigma,h} \to \boldsymbol{\Lambda}_{\Sigma,h}$, defined by $\boldsymbol{B}_h \stackrel{\text{def}}{=} \big(\boldsymbol{\mathcal{L}}_h^{\mathrm{s}}\big)' \boldsymbol{\mathcal{L}}_h^{\mathrm{s}}$, where $\big(\boldsymbol{\mathcal{L}}_h^{\mathrm{s}}\big)'$ stands for the adjoint operator of $\boldsymbol{\mathcal{L}}_h^{\mathrm{s}}$ with respect to the lumped-mass inner product in $\boldsymbol{V}_h^{\mathrm{s}}$. Notice that the interface operator $\boldsymbol{B}_h$ is self-adjoint, positive, definite and diagonal with respect to the finite element basis of $\boldsymbol{\Lambda}_{\Sigma,h}$. In order to simplify the presentation, we use the notation $\boldsymbol{B}_h\boldsymbol{v}_h^{\mathrm{s}}$ instead of $\boldsymbol{B}_h(\boldsymbol{v}_h^{\mathrm{s}}|_\Sigma)$ for $\boldsymbol{v}_h^{\mathrm{s}} \in \boldsymbol{V}_h^{\mathrm{s}}$.

The space semi-discrete formulation of problem (4.1), including a possible mass-lumping approximation in the structure, reads therefore as follows: for all $t > 0$, find $(\boldsymbol{u}_h(t), \dot{\boldsymbol{d}}_h(t)) \in \boldsymbol{W}_h$, $p_h(t) \in Q_h$ and $\boldsymbol{d}_h(t) \in \boldsymbol{V}_h^{\mathrm{s}}$ such that

$$\left\{\begin{array}{l} \dot{\boldsymbol{d}}_h = \partial_t \boldsymbol{d}_h, \\ \rho^{\mathrm{f}}\big(\partial_t \boldsymbol{u}_h, \boldsymbol{v}_h^{\mathrm{f}}\big)_{\Omega^{\mathrm{f}}} + a(\boldsymbol{u}_h, \boldsymbol{v}_h^{\mathrm{f}}) + b(p_h, \boldsymbol{v}_h^{\mathrm{f}}) - b(q_h, \boldsymbol{u}_h) + s_h(p_h, q_h) \\ \quad + \rho^{\mathrm{s}}\big(\partial_t \dot{\boldsymbol{d}}_h, \boldsymbol{v}_h^{\mathrm{s}}\big)_* + a^{\mathrm{e}}(\boldsymbol{d}_h, \boldsymbol{v}_h^{\mathrm{s}}) + a_*^{\mathrm{v}}(\dot{\boldsymbol{d}}_h, \boldsymbol{v}_h^{\mathrm{s}}) = l(\boldsymbol{v}_h^{\mathrm{f}}) \end{array}\right. \tag{4.3}$$

for all $(\boldsymbol{v}_h^{\mathrm{f}}, \boldsymbol{v}_h^{\mathrm{s}}) \in \boldsymbol{W}_h$ and $q_h \in Q_h$.

4.2.2 Time discretization: coupling schemes

This section is devoted to the discretization in time of (4.3). In the succeeding text, the parameter $\tau > 0$ stands for the time-step length, $t_n \overset{\text{def}}{=} n\tau$, for $n \in \mathbb{N}$, and $\partial_\tau x^n \overset{\text{def}}{=} (x^n - x^{n-1})/\tau$ for the first-order backward difference. The symbol $x^\star$ denotes the r-th order explicit extrapolation of the quantity x (that can be either $\boldsymbol{d}, \dot{\boldsymbol{d}}, \boldsymbol{u}$ or p):

$$x^\star \overset{\text{def}}{=} \left\{\begin{array}{ll} 0 & \text{if} \quad r = 0, \\ x^{n-1} & \text{if} \quad r = 1, \\ 2x^{n-1} - x^{n-2} & \text{if} \quad r = 2. \end{array}\right.$$

4.2.2.1 Generalized Robin-Neumann explicit coupling schemes

Basically, the explicit coupling schemes introduced in Chapter 3 are based on an interface Robin consistency (3.15) that can be recovered from the space semi-discrete formulation (4.3) after a mass-lumping approximation in the structure.

Here, we propose an alternative way to derive the same coupling schemes (in the spirit of [54]) based on operator splitting. The main benefit of this new approach is that the mass-lumping approximation remains optional and that it highlights the role of the mass-lumping approximation on the explicit nature of the coupling scheme. Basically, we consider the following fractional-step time-marching of (4.3): for $n \geq 1$,

1. Find $(\boldsymbol{u}_h^n, \dot{\boldsymbol{d}}_h^{n-\frac{1}{2}}) \in \boldsymbol{W}_h$ and $p_h^n \in Q_h$ such that

$$\left\{\begin{array}{l} \rho^{\mathrm{f}}\big(\partial_\tau \boldsymbol{u}_h^n, \boldsymbol{v}_h^{\mathrm{f}}\big)_{\Omega^{\mathrm{f}}} + a(\boldsymbol{u}_h^n, \boldsymbol{v}_h^{\mathrm{f}}) + b(p_h^n, \boldsymbol{v}_h^{\mathrm{f}}) - b(q_h, \boldsymbol{u}_h^n) + s_h(p_h^n, q_h) \\ \quad + \dfrac{\rho^{\mathrm{s}}}{\tau}\big(\dot{\boldsymbol{d}}_h^{n-\frac{1}{2}}, \boldsymbol{v}_h^{\mathrm{s}}\big)_* = l(\boldsymbol{v}_h^{\mathrm{f}}) + \dfrac{\rho^{\mathrm{s}}}{\tau}\big(\dot{\boldsymbol{d}}_h^{n-1}, \boldsymbol{v}_h^{\mathrm{s}}\big)_* - a^{\mathrm{e}}(\boldsymbol{d}_h^\star, \boldsymbol{v}_h^{\mathrm{s}}) - a_*^{\mathrm{v}}(\dot{\boldsymbol{d}}_h^\star, \boldsymbol{v}_h^{\mathrm{s}}) \end{array}\right. \tag{4.4}$$

   for all $(\boldsymbol{v}_h^{\mathrm{f}}, \boldsymbol{v}_h^{\mathrm{s}}) \in \boldsymbol{W}_h$ and for all $q_h \in Q_h$.

2. Find $(\boldsymbol{d}_h^n, \dot{\boldsymbol{d}}_h^n) \in \boldsymbol{V}_h^{\mathrm{s}} \times \boldsymbol{V}_h^{\mathrm{s}}$ such that

$$\left\{\begin{array}{l} \dot{\boldsymbol{d}}_h^n = \partial_\tau \boldsymbol{d}_h^n, \\ \dfrac{\rho^{\mathrm{s}}}{\tau}\big(\dot{\boldsymbol{d}}_h^n - \dot{\boldsymbol{d}}_h^{n-\frac{1}{2}}, \boldsymbol{v}_h^{\mathrm{s}}\big)_* + a^{\mathrm{e}}(\boldsymbol{d}_h^n - \boldsymbol{d}_h^\star, \boldsymbol{v}_h^{\mathrm{s}}) + a_*^{\mathrm{v}}(\dot{\boldsymbol{d}}_h^n - \dot{\boldsymbol{d}}_h^\star, \boldsymbol{v}_h^{\mathrm{s}}) = 0 \end{array}\right. \tag{4.5}$$

   for all $\boldsymbol{v}_h^{\mathrm{s}} \in \boldsymbol{V}_h^{\mathrm{s}}$.

Note that step (4.4) introduces and additional unknown, the intermediate solid velocity $\dot{\boldsymbol{d}}_h^{n-\frac{1}{2}}$, which is implicitly coupled to the fluid through the solid inertial term. Hence, step (4.4) implicitly treats the solid inertia within the fluid. The remaining solid viscoelastic contributions are treated explicitly in (4.4) via extrapolation. The end-of-step solid velocity $\dot{\boldsymbol{d}}_h^n$ is obtained by solving the solid correction step (4.5). The implicit treatment of the solid inertia in (4.4) guarantees (added-mass free) stability, while the extrapolation of the solid viscoelastic terms introduces a certain degree of splitting between the computation of the fluid and of the solid.

Algorithm 4.1 Semi-implicit coupling scheme (without solid mass-lumping).

For $n > r$,

1. Fluid with solid inertia step:

   Find $(\boldsymbol{u}_h^n, \dot{\boldsymbol{d}}_h^{n-\frac{1}{2}}) \in \boldsymbol{W}_h$ and $p_h^n \in Q_h$ such that

$$\left\{\begin{array}{l} \rho^{\mathrm{f}}\big(\partial_\tau \boldsymbol{u}_h^n, \boldsymbol{v}_h^{\mathrm{f}}\big)_{\Omega^{\mathrm{f}}} + a(\boldsymbol{u}_h^n, \boldsymbol{v}_h^{\mathrm{f}}) + b(p_h^n, \boldsymbol{v}_h^{\mathrm{f}}) - b(q_h, \boldsymbol{u}_h^n) + s_h(p_h^n, q_h) \\ \quad + \dfrac{\rho^{\mathrm{s}}}{\tau}\big(\dot{\boldsymbol{d}}_h^{n-\frac{1}{2}}, \boldsymbol{v}_h^{\mathrm{s}}\big)_{\Omega^{\mathrm{s}}} = \dfrac{\rho^{\mathrm{s}}}{\tau}\big(\dot{\boldsymbol{d}}_h^{n-1} + \tau\partial_\tau \dot{\boldsymbol{d}}_h^{\star}, \boldsymbol{v}_h^{\mathrm{s}}\big)_{\Omega^{\mathrm{s}}} \\ \quad + \rho^{\mathrm{f}}\big(\partial_\tau \boldsymbol{u}_h^{\star}, \boldsymbol{\mathcal{L}}_h^{\mathrm{f}} \boldsymbol{v}_h^{\mathrm{f}}\big)_{\Omega^{\mathrm{f}}} + a(\boldsymbol{u}_h^{\star}, \boldsymbol{\mathcal{L}}_h^{\mathrm{f}} \boldsymbol{v}_h^{\mathrm{f}}) + b(p_h^{\star}, \boldsymbol{\mathcal{L}}_h^{\mathrm{f}} \boldsymbol{v}_h^{\mathrm{f}}) + l(\boldsymbol{v}_h^{\mathrm{f}}) \end{array}\right. \tag{4.6}$$

   for all $(\boldsymbol{v}_h^{\mathrm{f}}, \boldsymbol{v}_h^{\mathrm{s}}) \in \boldsymbol{W}_h$ and $q_h \in Q_h$.

2. Solid step (Neumann):

   Find $(\dot{\boldsymbol{d}}_h^n, \boldsymbol{d}_h^n) \in \boldsymbol{V}_h^{\mathrm{s}} \times \boldsymbol{V}_h^{\mathrm{s}}$ such that

$$\left\{\begin{array}{l} \dot{\boldsymbol{d}}_h^n = \partial_\tau \boldsymbol{d}_h^n, \\ \rho^{\mathrm{s}}\big(\partial_\tau \dot{\boldsymbol{d}}_h^n, \boldsymbol{v}_h^{\mathrm{s}}\big)_{\Omega^{\mathrm{s}}} + a^{\mathrm{e}}(\boldsymbol{d}_h^n, \boldsymbol{v}_h^{\mathrm{s}}) + a^{\mathrm{v}}(\dot{\boldsymbol{d}}_h^n, \boldsymbol{v}_h^{\mathrm{s}}) \\ \quad = -\rho^{\mathrm{f}}\big(\partial_\tau \boldsymbol{u}_h^n, \boldsymbol{\mathcal{L}}_h^{\mathrm{f}} \boldsymbol{v}_h^{\mathrm{s}}\big)_{\Omega^{\mathrm{f}}} - a(\boldsymbol{u}_h^n, \boldsymbol{\mathcal{L}}_h^{\mathrm{f}} \boldsymbol{v}_h^{\mathrm{s}}) - b(p_h^n, \boldsymbol{\mathcal{L}}_h^{\mathrm{f}} \boldsymbol{v}_h^{\mathrm{s}}) \end{array}\right. \tag{4.7}$$

   for all $\boldsymbol{v}_h^{\mathrm{s}} \in \boldsymbol{V}_h^{\mathrm{s}}$.

The correction step (4.5) can be reformulated as a standard solid (Neumann) problem by eliminating the quantitites $(\dot{\boldsymbol{d}}_h^{n-\frac{1}{2}}, \boldsymbol{d}_h^{\star}, \dot{\boldsymbol{d}}_h^{\star})$. Indeed, by taking $\boldsymbol{v}_h^{\mathrm{f}} = \boldsymbol{\mathcal{L}}_h^{\mathrm{f}} \boldsymbol{v}_h^{\mathrm{s}}$ and $q_h = 0$ in (4.4) and by adding the resulting expression to $(4.5)_2$, we get

$$\begin{aligned} \rho^{\mathrm{s}}\big(\partial_\tau \dot{\boldsymbol{d}}_h^n, \boldsymbol{v}_h^{\mathrm{s}}\big)_* + a^{\mathrm{e}}(\boldsymbol{d}_h^n, \boldsymbol{v}_h^{\mathrm{s}}) + a_*^{\mathrm{v}}(\dot{\boldsymbol{d}}_h^n, \boldsymbol{v}_h^{\mathrm{s}}) = &-\rho^{\mathrm{f}}\big(\partial_\tau \boldsymbol{u}_h^n, \boldsymbol{\mathcal{L}}_h^{\mathrm{f}} \boldsymbol{v}_h^{\mathrm{s}}\big)_{\Omega^{\mathrm{f}}} \\ &- a(\boldsymbol{u}_h^n, \boldsymbol{\mathcal{L}}_h^{\mathrm{f}} \boldsymbol{v}_h^{\mathrm{s}}) - b(p_h^n, \boldsymbol{\mathcal{L}}_h^{\mathrm{f}} \boldsymbol{v}_h^{\mathrm{s}}) \end{aligned} \tag{4.8}$$

for all $\boldsymbol{v}_h^{\mathrm{s}} \in \boldsymbol{V}_h^{\mathrm{s}}$. Furthermore, for $n > r$, the extrapolated solid viscoelastic contribution in (4.4) can be eliminated thanks to (4.8) at the time levels $n-1, \ldots, n-r$, which yields

$$\begin{aligned} -a^{\mathrm{e}}(\boldsymbol{d}_h^{\star}, \boldsymbol{v}_h^{\mathrm{s}}) - a_*^{\mathrm{v}}(\dot{\boldsymbol{d}}_h^{\star}, \boldsymbol{v}_h^{\mathrm{s}}) = &\rho^{\mathrm{s}}\big(\partial_\tau \dot{\boldsymbol{d}}_h^{\star}, \boldsymbol{v}_h^{\mathrm{s}}\big)_* + \rho^{\mathrm{f}}\big(\partial_\tau \boldsymbol{u}_h^{\star}, \boldsymbol{\mathcal{L}}_h^{\mathrm{f}} \boldsymbol{v}_h^{\mathrm{f}}\big)_{\Omega^{\mathrm{f}}} \\ &+ a(\boldsymbol{u}_h^{\star}, \boldsymbol{\mathcal{L}}_h^{\mathrm{f}} \boldsymbol{v}_h^{\mathrm{f}}) + b(p_h^{\star}, \boldsymbol{\mathcal{L}}_h^{\mathrm{f}} \boldsymbol{v}_h^{\mathrm{f}}) \end{aligned}$$

for all $(\boldsymbol{v}_h^{\mathrm{f}}, \boldsymbol{v}_h^{\mathrm{s}}) \in \boldsymbol{W}_h$.

Algorithm 4.1 presents the resulting time-marching procedure without the mass-lumping approximation in the solid. It should be noted that this coupling scheme is not explicit (it is semi-implicit), since the fluid sub-problem has the same size than the original coupled problem (4.3). On the contrary, if mass-lumping is considered in the structure, the contributions of the solid intermediate velocity $\dot{\boldsymbol{d}}_h^{n-\frac{1}{2}}$ can be rewritten exclusively in terms of the interface fluid velocity $\boldsymbol{u}_h^n|_\Sigma$. Indeed, from Lemma 3.3.1 and since $\boldsymbol{u}_h^n|_\Sigma = \dot{\boldsymbol{d}}_h^{n-\frac{1}{2}}|_\Sigma$, it follows that

$$\big(\dot{\boldsymbol{d}}_h^{n-\frac{1}{2}}, \boldsymbol{\mathcal{L}}_h^{\mathrm{s}} \boldsymbol{v}_h^{\mathrm{s}}\big)_{\Omega^{\mathrm{s}},h} = \big(\boldsymbol{B}_h \dot{\boldsymbol{d}}_h^{n-\frac{1}{2}}, \boldsymbol{v}_h^{\mathrm{s}}\big)_\Sigma = \big(\boldsymbol{B}_h \boldsymbol{u}_h^n, \boldsymbol{v}_h^{\mathrm{f}}\big)_\Sigma$$

for all $(\boldsymbol{v}_h^{\mathrm{f}}, \boldsymbol{v}_h^{\mathrm{s}}) \in \boldsymbol{W}_h$. In other words, after solid mass-lumping, the intermediate solid velocity $\dot{\boldsymbol{d}}_h^{n-\frac{1}{2}}$ disappears from the computation and, therefore, the coupling scheme becomes explicit. The resulting solution procedure corresponds to (3.18)-(3.19) (with the variant of Remark 3.3.7) and it is recalled in Algorithm 4.2.

Algorithm 4.2 Generalized Robin-Neumann explicit coupling schemes (from Chapter 3).

For $n > r$,

1. Fluid step (generalized Robin): find $(\boldsymbol{u}_h^n, p_h^n) \in \boldsymbol{V}_h^{\mathrm{f}} \times Q_h$ such that

$$\left\{ \begin{array}{l} \rho^{\mathrm{f}} \big(\partial_\tau \boldsymbol{u}_h^n, \boldsymbol{v}_h^{\mathrm{f}}\big)_{\Omega^{\mathrm{f}}} + a(\boldsymbol{u}_h^n, \boldsymbol{v}_h^{\mathrm{f}}) + b(p_h^n, \boldsymbol{v}_h^{\mathrm{f}}) - b(q_h, \boldsymbol{u}_h^n) + s_h(p_h^n, q_h) \\ \quad + \dfrac{\rho^{\mathrm{s}}}{\tau} \big(\boldsymbol{B}_h \boldsymbol{u}_h^n, \boldsymbol{v}_h^{\mathrm{f}}\big)_\Sigma = \dfrac{\rho^{\mathrm{s}}}{\tau} \big(\boldsymbol{B}_h (\dot{\boldsymbol{d}}_h^{n-1} + \tau \partial_\tau \dot{\boldsymbol{d}}_h^\star), \boldsymbol{v}_h^{\mathrm{f}}\big)_\Sigma \\ \quad + \rho^{\mathrm{f}} \big(\partial_\tau \boldsymbol{u}_h^\star, \boldsymbol{\mathcal{L}}_h^{\mathrm{f}} \boldsymbol{v}_h^{\mathrm{f}}\big)_{\Omega^{\mathrm{f}}} + a(\boldsymbol{u}_h^\star, \boldsymbol{\mathcal{L}}_h^{\mathrm{f}} \boldsymbol{v}_h^{\mathrm{f}}) + b(p_h^\star, \boldsymbol{\mathcal{L}}_h^{\mathrm{f}} \boldsymbol{v}_h^{\mathrm{f}}) + l(\boldsymbol{v}_h^{\mathrm{f}}) \end{array} \right. \tag{4.9}$$

   for all $(\boldsymbol{v}_h^{\mathrm{f}}, q_h) \in \boldsymbol{V}_h^{\mathrm{f}} \times Q_h$.

2. Solid step (Neumann): find $(\dot{\boldsymbol{d}}_h^n, \boldsymbol{d}_h^n) \in \boldsymbol{V}_h^{\mathrm{s}} \times \boldsymbol{V}_h^{\mathrm{s}}$ such that

$$\left\{ \begin{array}{l} \dot{\boldsymbol{d}}_h^n = \partial_\tau \boldsymbol{d}_h^n, \\ \rho^{\mathrm{s}} \big(\partial_\tau \dot{\boldsymbol{d}}_h^n, \boldsymbol{v}_h^{\mathrm{s}}\big)_{\Omega^{\mathrm{s}},h} + a^{\mathrm{e}}(\boldsymbol{d}_h^n, \boldsymbol{v}_h^{\mathrm{s}}) + a_h^{\mathrm{v}}(\dot{\boldsymbol{d}}_h^n, \boldsymbol{v}_h^{\mathrm{s}}) \\ \quad = -\rho^{\mathrm{f}} \big(\partial_\tau \boldsymbol{u}_h^n, \boldsymbol{\mathcal{L}}_h^{\mathrm{f}} \boldsymbol{v}_h^{\mathrm{s}}\big)_{\Omega^{\mathrm{f}}} - a(\boldsymbol{u}_h^n, \boldsymbol{\mathcal{L}}_h^{\mathrm{f}} \boldsymbol{v}_h^{\mathrm{s}}) - b(p_h^n, \boldsymbol{\mathcal{L}}_h^{\mathrm{f}} \boldsymbol{v}_h^{\mathrm{s}}) \end{array} \right. \tag{4.10}$$

   for all $\boldsymbol{v}_h^{\mathrm{s}} \in \boldsymbol{V}_h^{\mathrm{s}}$.

Remark 4.2.2. *Algorithms 4.1 and 4.2 are essentially the same coupling scheme: they only differ on the discrete treatment of the inner-product* $(\cdot,\cdot)_{\Omega^{\mathrm{s}}}$.

Remark 4.2.3. *Algorithms 4.1 and 4.2 are* multi-step *methods for* $r > 0$, *meaning that an initial condition* $(\boldsymbol{u}_h^0, \boldsymbol{d}_h^0, \dot{\boldsymbol{d}}_h^0)$ *is not enough to initiate the time marching. In the case* $r = 1$, *we propose to obtain* $(\boldsymbol{u}_h^1, \boldsymbol{d}_h^1, \dot{\boldsymbol{d}}_h^1)$ *with one step of the scheme with* $r = 0$.

Similarly, the scheme with $r = 2$ is initialized by performing one step of the scheme with $r = 1$.

For further reference in the convergence analysis of Section 4.3, we now recall the energy stability result established in Chapter 3 for Algorithm 4.2. We will show that it also holds for Algorithm 4.1.

We begin with following fundamental property of Algorithms 4.1 and 4.2: they are nothing but interface kinematic perturbations of an implicit coupling scheme.

Lemma 4.2.1. *Let $\{(\boldsymbol{u}_h^n, p_h^n, \boldsymbol{d}_h^n, \dot{\boldsymbol{d}}_h^n)\}_{n>r}$ be the sequence given by Algorithm 4.1 or 4.2. For $n > r$, there holds*

$$\boldsymbol{u}_h^n = \dot{\boldsymbol{d}}_h^n + \frac{\tau}{\rho^{\mathrm{s}}}\left(\boldsymbol{L}_h^{\mathrm{e}}(\boldsymbol{d}_h^n - \boldsymbol{d}_h^\star) + \boldsymbol{L}_h^{\mathrm{v}}(\dot{\boldsymbol{d}}_h^n - \dot{\boldsymbol{d}}_h^\star)\right) \quad \text{on} \quad \Sigma \tag{4.11}$$

and

$$\begin{cases} \dot{\boldsymbol{d}}_h^n = \partial_\tau \boldsymbol{d}_h^n, \\ \rho^{\mathrm{f}}\big(\partial_\tau \boldsymbol{u}_h^n, \boldsymbol{v}_h^{\mathrm{f}}\big)_{\Omega^{\mathrm{f}}} + a(\boldsymbol{u}_h^n, \boldsymbol{v}_h^{\mathrm{f}}) + b(p_h^n, \boldsymbol{v}_h^{\mathrm{f}}) - b(q_h, \boldsymbol{u}_h^n) + s_h(p_h^n, q_h) \\ \quad + \rho^{\mathrm{s}}\big(\partial_\tau \dot{\boldsymbol{d}}_h^n, \boldsymbol{v}_h^{\mathrm{s}}\big)_* + a^{\mathrm{e}}(\boldsymbol{d}_h^n, \boldsymbol{v}_h^{\mathrm{s}}) + a_*^{\mathrm{v}}(\dot{\boldsymbol{d}}_h^n, \boldsymbol{v}_h^{\mathrm{s}}) = l(\boldsymbol{v}_h^{\mathrm{f}}) \end{cases} \tag{4.12}$$

for all $(\boldsymbol{v}_h^{\mathrm{f}}, \boldsymbol{v}_h^{\mathrm{s}}) \in \boldsymbol{W}_h$ and $q_h \in Q_h$.

Proof. The result for Algorithm 4.2 has been established in Chapter 3 (Lemma 3.4.2). We now detail the proof for Algorithm 4.1. First, the substitution of n by $\star$ in (4.7), which is valid for $n > r$, gives

$$\begin{aligned} \rho^{\mathrm{s}}\big(\partial_\tau \dot{\boldsymbol{d}}_h^\star, \boldsymbol{v}_h^{\mathrm{s}}\big)_{\Omega^{\mathrm{s}}} + a^{\mathrm{e}}(\boldsymbol{d}_h^\star, \boldsymbol{v}_h^{\mathrm{s}}) + a^{\mathrm{v}}(\dot{\boldsymbol{d}}_h^\star, \boldsymbol{v}_h^{\mathrm{s}}) \\ = -\rho^{\mathrm{f}}\big(\partial_\tau \boldsymbol{u}_h^\star, \boldsymbol{\mathcal{L}}_h^{\mathrm{f}} \boldsymbol{v}_h^{\mathrm{s}}\big)_{\Omega^{\mathrm{f}}} - a(\boldsymbol{u}_h^\star, \boldsymbol{\mathcal{L}}_h^{\mathrm{f}} \boldsymbol{v}_h^{\mathrm{s}}) - b(p_h^\star, \boldsymbol{\mathcal{L}}_h^{\mathrm{f}} \boldsymbol{v}_h^{\mathrm{s}}) \end{aligned} \tag{4.13}$$

for all $\boldsymbol{v}_h^{\mathrm{s}} \in \boldsymbol{V}_h^{\mathrm{s}}$. Then, the choice $\boldsymbol{v}_h^{\mathrm{f}} = \boldsymbol{\mathcal{L}}_h^{\mathrm{f}} \boldsymbol{v}_h^{\mathrm{s}}$ and $q_h = 0$ in (4.7) yields:

$$\begin{aligned} \rho^{\mathrm{f}}\big(\partial_\tau \boldsymbol{u}_h^n, \boldsymbol{\mathcal{L}}_h^{\mathrm{f}} \boldsymbol{v}_h^{\mathrm{s}}\big)_{\Omega^{\mathrm{f}}} + a(\boldsymbol{u}_h^n, \boldsymbol{\mathcal{L}}_h^{\mathrm{f}} \boldsymbol{v}_h^{\mathrm{s}}) + b(p_h^n, \boldsymbol{\mathcal{L}}_h^{\mathrm{f}} \boldsymbol{v}_h^{\mathrm{s}}) \\ + \frac{\rho^{\mathrm{s}}}{\tau}\big(\dot{\boldsymbol{d}}_h^{n-\frac{1}{2}}, \boldsymbol{v}_h^{\mathrm{s}}\big)_{\Omega^{\mathrm{s}}} = \frac{\rho^{\mathrm{s}}}{\tau}\big(\dot{\boldsymbol{d}}_h^{n-1} + \tau \partial_\tau \dot{\boldsymbol{d}}_h^\star, \boldsymbol{v}_h^{\mathrm{s}}\big)_{\Omega^{\mathrm{s}}} + \rho^{\mathrm{f}}\big(\partial_\tau \boldsymbol{u}_h^\star, \boldsymbol{\mathcal{L}}_h^{\mathrm{f}} \boldsymbol{v}_h^{\mathrm{s}}\big)_{\Omega^{\mathrm{f}}} \\ + a(\boldsymbol{u}_h^\star, \boldsymbol{\mathcal{L}}_h^{\mathrm{f}} \boldsymbol{v}_h^{\mathrm{s}}) + b(p_h^\star, \boldsymbol{\mathcal{L}}_h^{\mathrm{f}} \boldsymbol{v}_h^{\mathrm{s}}) \end{aligned} \tag{4.14}$$

for all $\boldsymbol{v}_h^{\mathrm{s}} \in \boldsymbol{V}_h^{\mathrm{s}}$. Finally, we sum equations (4.14), (4.13) and (4.7) to get

$$\frac{\rho^{\mathrm{s}}}{\tau}\big(\dot{\boldsymbol{d}}_h^{n-\frac{1}{2}} - \dot{\boldsymbol{d}}_h^{n-1}, \boldsymbol{v}_h^{\mathrm{s}}\big)_{\Omega^{\mathrm{s}}} + a^{\mathrm{e}}(\boldsymbol{d}_h^n - \boldsymbol{d}_h^\star, \boldsymbol{v}_h^{\mathrm{s}}) + a^{\mathrm{v}}(\dot{\boldsymbol{d}}_h^n - \dot{\boldsymbol{d}}_h^\star, \boldsymbol{v}_h^{\mathrm{s}}) = 0 \tag{4.15}$$

for all $\boldsymbol{v}_h^{\mathrm{s}} \in \boldsymbol{V}_h^{\mathrm{s}}$, or thanks to (4.2),

$$\dot{\boldsymbol{d}}_h^{n-\frac{1}{2}} = \dot{\boldsymbol{d}}_h^n + \frac{\tau}{\rho^{\mathrm{s}}}\left(\boldsymbol{L}_h^{\mathrm{e}}(\boldsymbol{d}_h^n - \boldsymbol{d}_h^\star) + \boldsymbol{L}_h^{\mathrm{v}}(\dot{\boldsymbol{d}}_h^n - \dot{\boldsymbol{d}}_h^\star)\right).$$

The transmission condition (4.11) follows from (4.6), which yields $\boldsymbol{u}_h^n = \dot{\boldsymbol{d}}_h^{n-\frac{1}{2}}$ on Σ. At last, the kinetic relation $(4.12)_2$ can be recovered from the summation of (4.6), (4.13) and (4.15). □

The next theorem states the energy stability of Algorithms 4.1 and 4.2.

Theorem 4.2.1. *Assume that* $\boldsymbol{f}^{\Gamma} = \mathbf{0}$ *(free system) and let* $\left\{(\boldsymbol{u}_h^n, p_h^n, \boldsymbol{d}_h^n, \dot{\boldsymbol{d}}_h^n)\right\}_{n>r}$ *be the sequence given by Algorithm 4.1 or 4.2 with the initiation procedure detailed in Remark 4.2.3. We denote by*

$$E_h^n \stackrel{\text{def}}{=} \frac{\rho^{\mathrm{f}}}{2}\|\boldsymbol{u}_h^n\|_{0,\Omega^{\mathrm{f}}}^2 + \frac{\rho^{\mathrm{s}}}{2}\|\dot{\boldsymbol{d}}_h^n\|_{0,\Omega^{\mathrm{s}}}^2 + \frac{1}{2}\|\boldsymbol{d}_h^n\|_{\mathrm{e}}^2$$

and

$$\begin{aligned} D_h^n \stackrel{\text{def}}{=} \frac{\rho^{\mathrm{f}}}{\tau}\|\boldsymbol{u}_h^n - \boldsymbol{u}_h^{n-1}\|_{0,\Omega^{\mathrm{f}}}^2 + \frac{\rho^{\mathrm{s}}}{\tau}\|\dot{\boldsymbol{d}}_h^n - \dot{\boldsymbol{d}}_h^{n-1}\|_{0,\Omega^{\mathrm{s}}}^2 + \frac{1}{\tau}\|\boldsymbol{d}_h^n - \boldsymbol{d}_h^{n-1}\|_{\mathrm{e}}^2 \\ + 2\mu\|\boldsymbol{\epsilon}(\boldsymbol{u}_h^n)\|_{0,\Omega^{\mathrm{f}}}^2 + |p_h^n|_{s_h}^2 + \|\dot{\boldsymbol{d}}_h^n\|_{\mathrm{v}}^2, \end{aligned}$$

the total discrete energy and dissipation, respectively. The following a priori energy estimates hold:

- *Schemes with* $r = 0$ *or* $r = 1$*: for* $n > r$

$$E_h^n + \tau \sum_{m=r+1}^{n} D_h^m \lesssim E_h^0; \tag{4.16}$$

- *Scheme with* $r = 2$*: for* $n \geq 3$

$$E_h^n + \tau \sum_{m=3}^{n} D_h^m \lesssim \exp\left(\frac{t_n \gamma}{1 - \gamma\tau}\right) E_h^0, \quad n \geq 3, \tag{4.17}$$

provided that the following set of conditions holds:

$$\begin{cases} \tau\left(\alpha_0 + \alpha_1\left(\dfrac{\omega_{\mathrm{e}}}{h}\right)^2\right) < \delta, \\ \tau^5\left(\dfrac{\omega_{\mathrm{e}}}{h}\right)^6 + \tau^2\left(\dfrac{\omega_{\mathrm{e}}}{h}\right)^2\left(\alpha_0 + \alpha_1\left(\dfrac{\omega_{\mathrm{e}}}{h}\right)^2\right) < \gamma, \\ \tau\gamma < 1, \end{cases} \tag{4.18}$$

where $\omega_{\mathrm{e}} \stackrel{\text{def}}{=} C_{\mathrm{inv}}\sqrt{\beta_{\mathrm{e}}/\rho^{\mathrm{s}}}$, $0 \leq \delta \leq 1$ *and* $\gamma > 0$.

Proof. For Algorithm 4.2 this result was established in Chapter 3 (Theorem 3.4.1). The result for Algorithm 4.1 follows from Lemma 4.2.1 by using the same arguments as in Chapter 3. □

The above result shows that Algorithms 4.1 and 4.2 retain the (added-mass free) stability properties of the original explicit Robin-Neumann schemes introduced in Chapter 2 and [45], for the coupling with thin-walled structures. Extensive numerical evidence reported in Section 3.6 demonstrated, however, that their accuracy is not preserved. More precisely, the error induced by the splitting losses the uniformity

in h: the numerically observed behavior of the energy error seems to be $\mathcal{O}(\tau^{2^{r-1}}/h^{\frac{1}{2}})$ for Algorithm 4.2, whereas an $\mathcal{O}(\tau^{2^{r-1}})$ was observed, both from the numerical and theoretical standpoint, for Robin-Neumann schemes of Chapter 2 (Algorithm 2.2) .

The present chapter aims at identifying the source of this accuracy loss induced by Algorithm 4.2:

- Is solid mass-lumping the cause of the h non-uniformity?
- Do Algorithms 4.1 and 4.2 deliver the same overall convergence rate?

All these fundamental questions will be answered in Section 4.3, via an *a priori* error analysis that covers both Algorithm 4.1 and 4.2. These theoretical findings will be then supported by further numerical evidence in Section 4.4.

4.2.2.2 Alternative splitting scheme

For further reference in the discussion and the numerical experiments of Section 4.4, we now recall the splitting scheme recently introduced in [14]. Applied to the coupled problem (4.1) this method yields the solution procedure reported in Algorithm 4.3, where $0 \leq \beta \leq 1$ denotes a free parameter. Note that this splitting treats implicitly the solid damping in (4.19). For a purely elastic structure (i.e., $\alpha_0 = \alpha_1 = 0$ in (3.2)), Algorithm 4.3 with $\beta = 0$ is the same as Algorithm 4.1 with $r = 0$, since the relations (4.4)-(4.5) follow from (4.19)-(4.20). More generally, the time-splittings provided by Algorithms 4.1 and 4.3 differ in the following two ingredients:

- the treatment of the solid damping;
- the consistency of the extrapolations on the interface.

Algorithm 4.3 treats implicitly the whole solid hydrodynamic contributions (inertia and damping) in step (4.19), whereas in Algorithm 4.1 only the solid inertial effects are included in the left-hand side of (4.6). This induces two important drawbacks with respect to Algorithm 4.1. First, the solid mass-lumping approximation in Algorithm 4.3 does not make the coupling scheme explicit; and second, the solid elastic step (4.20) cannot be reformulated as the standard solid (Neumann) problem (4.10), since the intermediate velocity cannot be eliminated $\dot{\boldsymbol{d}}_h^{n-\frac{1}{2}}$. Indeed, by taking $\boldsymbol{v}_h^{\mathrm{f}} = \boldsymbol{\mathcal{L}}_h^{\mathrm{f}} \boldsymbol{v}_h^{\mathrm{s}}$ and $q_h = 0$ in (4.19) and by adding the resulting expression to $(4.20)_2$, we get

$$\begin{aligned} \rho^{\mathrm{s}}\big(\partial_\tau \dot{\boldsymbol{d}}_h^n, \boldsymbol{v}_h^{\mathrm{s}}\big)_{\Omega^{\mathrm{s}}} + a^{\mathrm{e}}(\boldsymbol{d}_h^n, \boldsymbol{v}_h^{\mathrm{s}}) = &- a^{\mathrm{v}}(\dot{\boldsymbol{d}}_h^{n-\frac{1}{2}}, \boldsymbol{v}_h^{\mathrm{s}}) - \rho^{\mathrm{f}}\big(\partial_\tau \boldsymbol{u}_h^n, \boldsymbol{\mathcal{L}}_h^{\mathrm{f}} \boldsymbol{v}_h^{\mathrm{s}}\big)_{\Omega^{\mathrm{f}}} \\ &- a(\boldsymbol{u}_h^n, \boldsymbol{\mathcal{L}}_h^{\mathrm{f}} \boldsymbol{v}_h^{\mathrm{s}}) - b(p_h^n, \boldsymbol{\mathcal{L}}_h^{\mathrm{f}} \boldsymbol{v}_h^{\mathrm{s}}) \end{aligned} \tag{4.21}$$

for all $\boldsymbol{v}_h^{\mathrm{s}} \in \boldsymbol{V}_h^{\mathrm{s}}$.

As regards consistency, the interface term $\beta\big(p_h^{n-1}, \boldsymbol{v}_h^{\mathrm{f}} \cdot \boldsymbol{n}^{\mathrm{f}}\big)_\Sigma$ in Algorithm 4.3 is introduced, in a rather *ad hoc* fashion, with the aim of improving the accuracy of the time-splitting. Mathematically sound results on the stability and the consistency of

Algorithm 4.3 Splitting scheme from [14].

1. Fluid with solid inertia and damping step: find $(\boldsymbol{u}_h^n, \dot{\boldsymbol{d}}_h^{n-\frac{1}{2}}) \in \boldsymbol{W}_h$ and $p_h^n \in Q_h$ such that

$$\begin{cases} \rho^{\mathrm{f}}\big(\partial_\tau \boldsymbol{u}_h^n, \boldsymbol{v}_h^{\mathrm{f}}\big)_{\Omega^{\mathrm{f}}} + a(\boldsymbol{u}_h^n, \boldsymbol{v}_h^{\mathrm{f}}) + b(p_h^n, \boldsymbol{v}_h^{\mathrm{f}}) - b(q_h, \boldsymbol{u}_h^n) + s_h(p_h^n, q_h) \\ \quad + \dfrac{\rho^{\mathrm{s}}}{\tau}\big(\dot{\boldsymbol{d}}_h^{n-\frac{1}{2}}, \boldsymbol{v}_h^{\mathrm{s}}\big)_{\Omega^{\mathrm{s}}} + a^{\mathrm{v}}(\dot{\boldsymbol{d}}_h^{n-\frac{1}{2}}, \boldsymbol{v}_h^{\mathrm{s}}) = \dfrac{\rho^{\mathrm{s}}}{\tau}\big(\dot{\boldsymbol{d}}_h^{n-1}, \boldsymbol{v}_h^{\mathrm{s}}\big)_{\Omega^{\mathrm{s}}} \\ \quad - \beta\big(p_h^{n-1}, \boldsymbol{v}_h^{\mathrm{f}} \cdot \boldsymbol{n}^{\mathrm{f}}\big)_\Sigma + l(\boldsymbol{v}_h^{\mathrm{f}}) \end{cases} \tag{4.19}$$

   for all $(\boldsymbol{v}_h^{\mathrm{f}}, \boldsymbol{v}_h^{\mathrm{s}}) \in \boldsymbol{W}_h$ and $q_h \in Q_h$.

2. Solid elastic step: find $(\dot{\boldsymbol{d}}_h^n, \boldsymbol{d}_h^n) \in \boldsymbol{V}_h^{\mathrm{s}} \times \boldsymbol{V}_h^{\mathrm{s}}$ such that

$$\begin{cases} \dot{\boldsymbol{d}}_h^n = \partial_\tau \boldsymbol{d}_h^n, \\ \dfrac{\rho^{\mathrm{s}}}{\tau}\big(\dot{\boldsymbol{d}}_h^n - \dot{\boldsymbol{d}}_h^{n-\frac{1}{2}}, \boldsymbol{v}_h^{\mathrm{s}}\big)_{\Omega^{\mathrm{s}}} + a^{\mathrm{e}}(\boldsymbol{d}_h^n, \boldsymbol{v}_h^{\mathrm{s}}) = \beta\big(p_h^{n-1}, \boldsymbol{v}_h^{\mathrm{s}} \cdot \boldsymbol{n}^{\mathrm{f}}\big)_\Sigma \end{cases} \tag{4.20}$$

   for all $\boldsymbol{v}_h^{\mathrm{s}} \in \boldsymbol{V}_h^{\mathrm{s}}$.

Algoritm 4.3 for $\beta > 0$ are not known. Numerical evidence suggests that the best accuracy is obtained with $\beta = 1$ (see [14]). In Section 4.4 we will show that Algorithm 4.3 also suffers from the non-uniformity convergence issues mentioned in Section 4.2.2.1.

4.3 Convergence Analysis

This section is devoted to the convergence analysis of the coupling schemes given by Algorithms 4.1 and 4.2.

4.3.1 Preliminaries

For all $\boldsymbol{d}_h, \boldsymbol{w}_h \in \boldsymbol{V}_h^{\mathrm{s}}$, the relation

$$\delta_h(\boldsymbol{d}_h, \boldsymbol{w}_h) \stackrel{\mathrm{def}}{=} (\boldsymbol{d}_h, \boldsymbol{w}_h)_{\Omega^{\mathrm{s}}} - (\boldsymbol{d}_h, \boldsymbol{w}_h)_* \tag{4.22}$$

will denote the quadrature error. Without mass-lumping approximation in the solid we have $\delta_h = 0$, otherwise there holds

$$|\delta_h(\boldsymbol{d}_h, \boldsymbol{w}_h)| \lesssim h \|\boldsymbol{d}_h\|_{1,\Omega^{\mathrm{s}}} \|\boldsymbol{w}_h\|_{0,\Omega^{\mathrm{s}}} \tag{4.23}$$

for all $\boldsymbol{d}_h, \boldsymbol{w}_h \in \boldsymbol{V}_h^{\mathrm{s}}$ (see, e.g., [112, Lemma 15.1]). Due to the particular form of the bilinear form a^{e} (given in (3.5)), two positive constants α_{e} and β_{e} exists, such that

$$\alpha_{\mathrm{e}} \|\boldsymbol{d}_h\|_{1,\Omega^{\mathrm{s}}}^2 \leq a^{\mathrm{e}}(\boldsymbol{d}_h, \boldsymbol{d}_h) \leq \beta_{\mathrm{e}} \|\boldsymbol{d}_h\|_{1,\Omega^{\mathrm{s}}}^2 \tag{4.24}$$

for all $\boldsymbol{d}_h \in \boldsymbol{V}_h^{\mathrm{s}}$. Thus, using an inverse inequality, we have the following estimates, valid for all $\boldsymbol{v}_h^{\mathrm{s}} \in \boldsymbol{V}_h^{\mathrm{s}}$:

$$\begin{aligned}
\|\boldsymbol{v}_h^{\mathrm{s}}\|_{\mathrm{e}}^2 &\leq \frac{\beta_{\mathrm{e}} C_{\mathrm{inv}}^2}{h^2} \|\boldsymbol{v}_h^{\mathrm{s}}\|_{0,\Omega^{\mathrm{s}}}^2, & \|\boldsymbol{v}_h^{\mathrm{s}}\|_{\mathrm{v}}^2 &\leq \left(\alpha_0 \rho^{\mathrm{s}} + \alpha_1 \frac{\beta_{\mathrm{e}} C_{\mathrm{inv}}^2}{h^2}\right) \|\boldsymbol{v}_h^{\mathrm{s}}\|_{0,\Omega^{\mathrm{s}}}^2, \\
\|\boldsymbol{L}_h^{\mathrm{e}} \boldsymbol{v}_h^{\mathrm{s}}\|_{\mathrm{e}} &\leq \frac{\beta_{\mathrm{e}} C_{\mathrm{inv}}^2}{h^2} \|\boldsymbol{v}_h^{\mathrm{s}}\|_{\mathrm{e}}, & \|\boldsymbol{L}_h^{\mathrm{v}} \boldsymbol{v}_h^{\mathrm{s}}\|_{\mathrm{v}} &\leq \left(\alpha_0 \rho^{\mathrm{s}} + \alpha_1 \frac{\beta_{\mathrm{e}} C_{\mathrm{inv}}^2}{h^2}\right) \|\boldsymbol{v}_h^{\mathrm{s}}\|_{\mathrm{v}}, \\
\|\boldsymbol{L}_h^{\mathrm{e}} \boldsymbol{v}_h^{\mathrm{s}}\|_{0,\Omega^{\mathrm{s}}}^2 &\leq \frac{\beta_{\mathrm{e}} C_{\mathrm{inv}}^2}{h^2} \|\boldsymbol{v}_h^{\mathrm{s}}\|_{\mathrm{e}}^2, & \|\boldsymbol{L}_h^{\mathrm{v}} \boldsymbol{v}_h^{\mathrm{s}}\|_{0,\Omega^{\mathrm{s}}}^2 &\leq \left(\alpha_0 \rho^{\mathrm{s}} + \alpha_1 \frac{\beta_{\mathrm{e}} C_{\mathrm{inv}}^2}{h^2}\right) \|\boldsymbol{v}_h^{\mathrm{s}}\|_{\mathrm{v}}^2.
\end{aligned} \tag{4.25}$$

4.3.2 Projection operators and error decomposition

We introduce the Ritz-projector $\boldsymbol{\pi}_h^{\mathrm{e}} : \boldsymbol{V}^{\mathrm{s}} \to \boldsymbol{V}_h^{\mathrm{s}}$ defined by the relation

$$a^{\mathrm{e}}(\boldsymbol{w} - \boldsymbol{\pi}_h^{\mathrm{e}} \boldsymbol{w}, \boldsymbol{w}_h) = 0$$

for all $\boldsymbol{w}_h \in \boldsymbol{V}_h^{\mathrm{s}}$. We assume that the following error estimate holds

$$\|\boldsymbol{w} - \boldsymbol{\pi}_h^{\mathrm{e}} \boldsymbol{w}\|_{\mathrm{e}} \lesssim h \beta_{\mathrm{e}}^{\frac{1}{2}} \|\boldsymbol{w}\|_{2,\Omega^{\mathrm{s}}} \tag{4.26}$$

for all $\boldsymbol{w} \in \boldsymbol{V}^{\mathrm{s}} \cap \boldsymbol{H}^2(\Omega^{\mathrm{s}})$. We then split the solid displacement error as:

$$\boldsymbol{d}(t_n) - \boldsymbol{d}_h^n = \underbrace{\boldsymbol{d}(t_n) - \boldsymbol{\pi}_h^{\mathrm{e}} \boldsymbol{d}(t_n)}_{\stackrel{\mathrm{def}}{=} \boldsymbol{\xi}_\pi^n} + \underbrace{\boldsymbol{\pi}_h^{\mathrm{e}} \boldsymbol{d}(t_n) - \boldsymbol{d}_h^n}_{\stackrel{\mathrm{def}}{=} \boldsymbol{\xi}_h^n}. \tag{4.27}$$

For the fluid and solid velocities, we consider a global fluid-solid hydrodynamic projector

$$\big((\boldsymbol{P}_h^{\mathrm{f}}, \boldsymbol{P}_h^{\mathrm{s}}), R_h\big) : \boldsymbol{W} \longrightarrow \boldsymbol{W}_h \times Q_h,$$

defined as follows. For $(\boldsymbol{u}, \dot{\boldsymbol{d}}) \in \boldsymbol{W}$ and $\alpha_1 > 0$, we consider the problem: find $\big((\boldsymbol{u}_h, \dot{\boldsymbol{d}}_h), p_h\big) \in \boldsymbol{W}_h \times Q_h$ such that

$$\begin{cases} a(\boldsymbol{u}_h, \boldsymbol{v}_h^{\mathrm{f}}) + \alpha_1 a^{\mathrm{e}}(\dot{\boldsymbol{d}}_h, \boldsymbol{v}_h^{\mathrm{s}}) + b(p_h, \boldsymbol{v}_h^{\mathrm{f}}) = a(\boldsymbol{u}, \boldsymbol{v}_h^{\mathrm{f}}) + \alpha_1 a^{\mathrm{e}}(\dot{\boldsymbol{d}}, \boldsymbol{v}_h^{\mathrm{s}}), \\ b(q_h, \boldsymbol{u}_h) - s_h(p_h, q_h) = 0 \end{cases} \tag{4.28}$$

for all $\big((\boldsymbol{v}_h^{\mathrm{f}}, \boldsymbol{v}_h^{\mathrm{s}}), q_h\big) \in \boldsymbol{W}_h \times Q_h$, and we set

$$\big(\boldsymbol{P}_h^{\mathrm{f}}(\boldsymbol{u}, \dot{\boldsymbol{d}}), \boldsymbol{P}_h^{\mathrm{s}}(\boldsymbol{u}, \dot{\boldsymbol{d}})\big) \stackrel{\mathrm{def}}{=} \big(\boldsymbol{u}_h, \dot{\boldsymbol{d}}_h\big), \quad R_h(\boldsymbol{u}, \dot{\boldsymbol{d}}) \stackrel{\mathrm{def}}{=} p_h.$$

Notice that, by construction, we have

$$\boldsymbol{P}_h^{\mathrm{f}}(\boldsymbol{u}, \dot{\boldsymbol{d}}) = \boldsymbol{P}_h^{\mathrm{s}}(\boldsymbol{u}, \dot{\boldsymbol{d}}) \quad \text{on} \quad \Sigma. \tag{4.29}$$

Remark 4.3.1. *Note that the fluid projection operator* (2.53) *of Chapter 2 (thin-walled solid) can not be considered here (thick-walled solid) since the error estimate* (2.54) *relies on approximation properties on the interface. This motivates the introduction of the new projection operator* (4.28).

The approximation properties of $\big((\boldsymbol{P}_h^{\mathrm{f}}, \boldsymbol{P}_h^{\mathrm{s}}), R_h\big)$ are given in the next lemma, whose proof is postponed to Section 4.3.5.

Lemma 4.3.1. *Let $(\boldsymbol{u}, \dot{\boldsymbol{d}}) \in \boldsymbol{W}$ be given functions with $\boldsymbol{u} \in \boldsymbol{H}^2(\Omega^{\mathrm{f}})$, $div\, \boldsymbol{u} = 0$ in Ω^{f}, and $\dot{\boldsymbol{d}} \in \boldsymbol{H}^2(\Omega^{\mathrm{s}})$. The following estimates hold:*

$$\|\boldsymbol{P}_h^{\mathrm{f}}(\boldsymbol{u}, \dot{\boldsymbol{d}})\|_{\boldsymbol{V}} + \alpha_1^{\frac{1}{2}} \|\boldsymbol{P}_h^{\mathrm{s}}(\boldsymbol{u}, \dot{\boldsymbol{d}})\|_{\mathrm{e}} + |R_h(\boldsymbol{u}, \dot{\boldsymbol{d}})|_{s_h} \lesssim \|\boldsymbol{u}\|_{\boldsymbol{V}} + \alpha_1^{\frac{1}{2}} \|\dot{\boldsymbol{d}}\|_{\mathrm{e}}, \tag{4.30}$$

$$\begin{aligned} &\|\boldsymbol{u} - \boldsymbol{P}_h^{\mathrm{f}}(\boldsymbol{u}, \dot{\boldsymbol{d}})\|_{\boldsymbol{V}} + \alpha_1^{\frac{1}{2}} \|\dot{\boldsymbol{d}} - \boldsymbol{P}_h^{\mathrm{s}}(\boldsymbol{u}, \dot{\boldsymbol{d}})\|_{\mathrm{e}} + \|R_h(\boldsymbol{u}, \dot{\boldsymbol{d}})\|_Q + |R_h(\boldsymbol{u}, \dot{\boldsymbol{d}})|_{s_h} \\ &\quad \lesssim h\mu^{\frac{1}{2}} \|\boldsymbol{u}\|_{2,\Omega^{\mathrm{f}}} + h\big(\alpha_1 \beta_{\mathrm{e}}\big)^{\frac{1}{2}} \|\dot{\boldsymbol{d}}\|_{2,\Omega^{\mathrm{s}}}. \end{aligned} \tag{4.31}$$

Proof. See Section 4.3.5. □

The fluid and solid velocity errors are hence decomposed as

$$\begin{aligned} \boldsymbol{u}(t_n) - \boldsymbol{u}_h^n &= \underbrace{\boldsymbol{u}(t_n) - \boldsymbol{P}_h^{\mathrm{f}}\big(\boldsymbol{u}(t_n), \dot{\boldsymbol{d}}(t_n)\big)}_{\stackrel{\mathrm{def}}{=} \boldsymbol{\theta}_\pi^n} + \underbrace{\boldsymbol{P}_h^{\mathrm{f}}\big(\boldsymbol{u}(t_n), \dot{\boldsymbol{d}}(t_n)\big) - \boldsymbol{u}_h^n}_{\stackrel{\mathrm{def}}{=} \boldsymbol{\theta}_h^n}, \\ \dot{\boldsymbol{d}}^n - \dot{\boldsymbol{d}}_h^n &= \underbrace{\dot{\boldsymbol{d}}(t_n) - \boldsymbol{P}_h^{\mathrm{s}}\big(\boldsymbol{u}(t_n), \dot{\boldsymbol{d}}(t_n)\big)}_{\stackrel{\mathrm{def}}{=} \dot{\boldsymbol{\xi}}_\pi^n} + \underbrace{\boldsymbol{P}_h^{\mathrm{s}}\big(\boldsymbol{u}(t_n), \dot{\boldsymbol{d}}(t_n)\big) - \dot{\boldsymbol{d}}_h^n}_{\stackrel{\mathrm{def}}{=} \dot{\boldsymbol{\xi}}_h^n}. \end{aligned} \tag{4.32}$$

At last, for the pressure we consider de decomposition

$$p(t_n) - p_h^n = \underbrace{p(t_n) - \Pi_h p(t_n)}_{\stackrel{\mathrm{def}}{=} y_\pi^n} + \underbrace{\Pi_h p(t_n) - p_h^n}_{\stackrel{\mathrm{def}}{=} y_h^n}, \tag{4.33}$$

where $\Pi_h : Q \to Q_h$ denotes de projection operator associated to the weak-consistency of the pressure stabilization operator s_h, for which we assume that

$$\begin{aligned} \|p - \Pi_h p\|_Q &\lesssim \frac{h^2}{\mu^{\frac{1}{2}}} \|p\|_{2,\Omega^{\mathrm{f}}} \quad \forall p \in Q \cap H^2(\Omega^{\mathrm{f}}), \\ |\Pi_h p|_{s_h} &\lesssim \frac{h}{\mu^{\frac{1}{2}}} \|p\|_{1,\Omega^{\mathrm{f}}} \quad \forall p \in Q \cap H^1(\Omega^{\mathrm{f}}). \end{aligned} \tag{4.34}$$

An example of a symmetric pressure stabilization operator s_h satisfying these properties is given in Section 4.4. Further examples can be found in [17, Section 3.1.1].

4.3.3 Discrete error estimation

We define the energy norm of the error (resp. the discrete) $\mathcal{E}_h^n$ (resp $\mathcal{Z}_h^n$) at time t_n and for $n > r$ as:

$$\begin{aligned}
\mathcal{E}_h^n \overset{\text{def}}{=} & (\rho^{\mathrm{f}})^{\frac{1}{2}} \|\boldsymbol{u}(t_n) - \boldsymbol{u}_h^n\|_{0,\Omega^{\mathrm{f}}} + \left(\sum_{m=r+1}^{n} \tau \|\boldsymbol{u}(t_m) - \boldsymbol{u}_h^m\|_{\boldsymbol{V}}^2 \right)^{\frac{1}{2}} + \left(\sum_{m=r+1}^{n} \tau |p_h^m|_{s_h}^2 \right)^{\frac{1}{2}} \\
& + \rho^{\mathrm{s}\frac{1}{2}} \|\dot{\boldsymbol{d}}(t_n) - \dot{\boldsymbol{d}}_h^n\|_{0,\Omega^{\mathrm{s}}} + \|\boldsymbol{d}(t_n) - \boldsymbol{d}_h^n\|_{\mathrm{e}} + \left(\sum_{m=r+1}^{n} \tau \|\dot{\boldsymbol{d}}(t_m) - \dot{\boldsymbol{d}}_h^m\|_{\mathrm{v}}^2 \right)^{\frac{1}{2}}, \\
\mathcal{Z}_h^n \overset{\text{def}}{=} & (\rho^{\mathrm{f}})^{\frac{1}{2}} \|\boldsymbol{\theta}_h^n\|_{0,\Omega^{\mathrm{f}}} + \left(\sum_{m=r+1}^{n} \tau \|\boldsymbol{\theta}_h^m\|_{\boldsymbol{V}}^2 \right)^{\frac{1}{2}} + \left(\sum_{m=r+1}^{n} \tau |y_h^m|_{s_h}^2 \right)^{\frac{1}{2}} \\
& + \rho^{\mathrm{s}\frac{1}{2}} \|\dot{\boldsymbol{\xi}}_h^n\|_{0,\Omega^{\mathrm{s}}} + \|\boldsymbol{\xi}_h^n\|_{\mathrm{e}} + \left(\sum_{m=r+1}^{n} \tau \|\dot{\boldsymbol{\xi}}_h^m\|_{\mathrm{v}}^2 \right)^{\frac{1}{2}}.
\end{aligned} \tag{4.35}$$

The aim of this section is to get an estimation of $\mathcal{E}_h^n$, but we first start to estimate $\mathcal{Z}_h^n$. We make the following assumptions on the exact solution $(\boldsymbol{u}, p, \boldsymbol{d}, \dot{\boldsymbol{d}})$ of the continuous problem (4.1):

$$\begin{aligned}
& \boldsymbol{u} \in \left[H^1(0,T;H^2(\Omega^{\mathrm{f}}))\right]^d, \\
& \partial_{tt}\boldsymbol{u} \in \left[L^2(0,T;L^2(\Omega^{\mathrm{f}}))\right]^d, \\
& p \in L^2(0,T;H^2(\Omega^{\mathrm{f}})) \\
& \dot{\boldsymbol{d}} \in \left[H^1(0,T;H^2(\Omega^{\mathrm{s}}))\right]^d, \\
& \partial_{tt}\dot{\boldsymbol{d}} \in \left[L^2(0,T;H^1(\Omega^{\mathrm{s}}))\right]^d, \\
& \boldsymbol{L}^{\mathrm{e}}\boldsymbol{d}, \boldsymbol{L}^{\mathrm{v}}\dot{\boldsymbol{d}} \in \begin{cases} \left[L^2(0,T;L^2(\Omega^{\mathrm{s}}))\right]^d & \text{if} \quad r = 0, \\ \left[H^1(0,T;L^2(\Omega^{\mathrm{s}}))\right]^d & \text{if} \quad r = 1, \\ \left[H^2(0,T;L^2(\Omega^{\mathrm{s}}))\right]^d & \text{if} \quad r = 2, \end{cases}
\end{aligned} \tag{4.36}$$

where $\boldsymbol{L}^{\mathrm{e}}\boldsymbol{d} \overset{\text{def}}{=} -\mathbf{div}\boldsymbol{\sigma}(\boldsymbol{d})$ and $\boldsymbol{L}^{\mathrm{v}}\dot{\boldsymbol{d}} \overset{\text{def}}{=} \alpha_0\rho^{\mathrm{s}}\dot{\boldsymbol{d}} - \alpha_1\mathbf{div}\boldsymbol{\sigma}(\dot{\boldsymbol{d}})$ with $\alpha_0, \alpha_1 \geq 0$. If $r = 2$ and $\alpha_1 = 0$, we further assume that

$$\dot{\boldsymbol{d}} \in \left[H^2(0,T;H^2(\Omega^{\mathrm{s}}))\right]^d$$

The next theorem states an a priori estimate for the discrete error $\mathcal{Z}_h^n$.

Theorem 4.3.1. *Let $(\boldsymbol{u}, p, \boldsymbol{d}, \dot{\boldsymbol{d}})$ be the solution of the coupled problem (4.1) with $\alpha_1 > 0$, and $\{(\boldsymbol{u}_h^n, p_h^n, \boldsymbol{d}_h^n, \dot{\boldsymbol{d}}_h^n)\}_{n>r}$ be the discrete solution given by Algorithm 4.1 or 4.2 with initial data*

$$\left(\boldsymbol{u}_h^0, \boldsymbol{d}_h^0, \dot{\boldsymbol{d}}_h^0\right) = \left(\boldsymbol{P}_h^{\mathrm{f}}(\boldsymbol{u}^0, \dot{\boldsymbol{d}}^0), \boldsymbol{\pi}_h^{\mathrm{e}}\boldsymbol{d}^0, \boldsymbol{P}_h^{\mathrm{s}}(\boldsymbol{u}^0, \dot{\boldsymbol{d}}^0)\right)$$

and, depending on the extrapolation order $r \in \{0,1,2\}$, with the initiation procedure detailed in Remark 4.2.3. We assume that the exact solution has the regularity provided by (4.36). Then, we have the following error estimate, for $n > r$ such that $n\tau < T$ and $(\alpha_0 + 1/T)\tau < 1$:

$$\mathcal{Z}_h^n \lesssim c_1 \left(1 + \frac{c_2}{\alpha_1}\right) h + c_3\tau + c_4\tau^{2^{r-1}} \left\| \boldsymbol{L}_h^{\mathrm{e}}\boldsymbol{d} + \boldsymbol{L}_h^{\mathrm{v}}\boldsymbol{P}_h^{\mathrm{s}}(\boldsymbol{u}, \dot{\boldsymbol{d}}) \right\|_{H^r(0,T;L^2(\Omega^{\mathrm{s}}))}. \tag{4.37}$$

Here, the symbols $\{c_i\}_{i=1}^4$ denote positive constants independent of h and τ, but which depend on the extrapolation order r, on the physical parameters and after all on the regularity of the exact solution $(\boldsymbol{u}, p, \boldsymbol{d}, \dot{\boldsymbol{d}})$. Moreover, the constants $\{c_i\}_{i=1}^3$ are bounded as α_1 tends to zero.

We note that Theorem 4.3.1 provides discrete error estimates which are valid only if $\alpha_1 > 0$. Indeed, in the case where there is no second-order viscosity in the solid model, the fluid-solid hydrodynamic projector (4.28) is not well defined. We propose an alternative approach in the spirit of Chapter 2 and [45], based on another choice of the fluid and solid velocity projectors. As highlighted above, the key point is that they have to match on the interface Σ. For the solid velocity, we consider the Lagrange interpolant onto $\boldsymbol{\mathcal{I}}_h^{\Omega^{\mathrm{s}}}$ on $\boldsymbol{V}_h^{\mathrm{s}}$. For the fluid velocity, we consider the Stokes-like operator $(\boldsymbol{P}_h, R_h) : \boldsymbol{V} \to \boldsymbol{V}_h \times Q_h$ defined, for all $\boldsymbol{v} \in \boldsymbol{V}$, by

$$\begin{cases} \boldsymbol{P}_h\boldsymbol{v}|_\Sigma = \boldsymbol{\mathcal{I}}_h^\Sigma(\boldsymbol{v}|_\Sigma), \\ a(\boldsymbol{P}_h\boldsymbol{v}, \boldsymbol{v}_h) + b(R_h\boldsymbol{v}, \boldsymbol{v}_h) = a(\boldsymbol{v}, \boldsymbol{v}_h) \quad \forall \boldsymbol{v}_h \in \boldsymbol{V}_{\Sigma,h}, \\ b(q_h, \boldsymbol{P}_h\boldsymbol{v}) = s_h(q_h, R_h\boldsymbol{v}) \quad \forall q_h \in Q_h. \end{cases} \tag{4.38}$$

As the interface restriction of the Lagrange interpolant $\boldsymbol{\mathcal{I}}_h^{\Omega^{\mathrm{s}}}$ is nothing but the Lagrange interpolant $\boldsymbol{\mathcal{I}}_h^\Sigma$ on Σ, we have that

$$\boldsymbol{P}_h\boldsymbol{u} = \boldsymbol{\mathcal{I}}_h^{\Omega^{\mathrm{s}}}\dot{\boldsymbol{d}} \quad \text{on} \quad \Sigma.$$

Moreover, we have the following standard estimate:

$$\|\dot{\boldsymbol{d}} - \boldsymbol{\mathcal{I}}_h^{\Omega^{\mathrm{s}}}\dot{\boldsymbol{d}}\|_{0,\Omega^{\mathrm{s}}} + h\|\dot{\boldsymbol{d}} - \boldsymbol{\mathcal{I}}_h^{\Omega^{\mathrm{s}}}\dot{\boldsymbol{d}}\|_{1,\Omega^{\mathrm{s}}} \lesssim h^{k+1}\|\dot{\boldsymbol{d}}\|_{k+1,\Omega^{\mathrm{s}}}$$

and, from [45, Lemma 3], it follows that

$$\begin{aligned} &\|\boldsymbol{v} - \boldsymbol{P}_h\boldsymbol{v}\|_{\boldsymbol{V}} + |R_h\boldsymbol{v}|_{s_h} + \|R_h\boldsymbol{v}\|_Q \lesssim h\mu^{\frac{1}{2}}\|\boldsymbol{v}\|_{2,\Omega^{\mathrm{f}}}, \\ &\|\boldsymbol{v} - \boldsymbol{P}_h\boldsymbol{v}\|_{0,\Omega^{\mathrm{f}}} \leq c_\mu\mu^{\frac{1}{2}}h^2\|\boldsymbol{v}\|_{2,\Omega^{\mathrm{f}}} + \tilde{c}_\mu h^2\|\boldsymbol{v}\|_{2,\Sigma}, \end{aligned} \tag{4.39}$$

for all $\boldsymbol{v} \in [H^2(\Omega^{\mathrm{f}})]^d$ with $\boldsymbol{v}|_\Sigma \in [H^2(\Sigma)]^d$ and $\operatorname{div}\boldsymbol{v} = 0$.

We finally have the following result:

Theorem 4.3.2. *Let $(\boldsymbol{u}, p, \boldsymbol{d}, \dot{\boldsymbol{d}})$ be the solution of the coupled problem (4.1) with $\alpha_1 = 0$, and $\{(\boldsymbol{u}_h^n, p_h^n, \boldsymbol{d}_h^n, \dot{\boldsymbol{d}}_h^n)\}_{n>r}$ be the discrete solution given by Algorithm 4.1 or 4.2 with initial data*

$$\left(\boldsymbol{u}_h^0, \boldsymbol{d}_h^0, \dot{\boldsymbol{d}}_h^0\right) = \left(\boldsymbol{P}_h\boldsymbol{u}^0, \boldsymbol{\pi}_h^{\mathrm{e}}\boldsymbol{d}^0, \boldsymbol{\mathcal{I}}_h^{\Omega^{\mathrm{s}}}\dot{\boldsymbol{d}}^0\right)$$

and, depending on the extrapolation order $r \in \{0,1,2\}$, with the initiation procedure detailed in Remark 4.2.3. We assume that the exact solution has the regularity provided by (4.36). Then, we have the following error estimate, for $n > r$ such that $n\tau < T$ and $(\alpha_0 + 1/T)\tau < 1$:

$$\begin{aligned}\mathcal{Z}_h^n \lesssim\, & c_1 h + c_2 \tau \\ & + c_3 \tau^{2^{r-1}} \left[\left\| \boldsymbol{L}_h^{\mathrm{e}} \boldsymbol{d} \right\|_{H^r(0,T;L^2(\Omega^{\mathrm{s}}))} + \alpha_0 \rho^{\mathrm{s}} \left(h^2 \left\| \dot{\boldsymbol{d}} \right\|_{H^r(0,T;H^2(\Omega^{\mathrm{s}}))} + \left\| \dot{\boldsymbol{d}} \right\|_{H^r(0,T;L^2(\Omega^{\mathrm{s}}))} \right) \right]\end{aligned} \tag{4.40}$$

Here, the symbols $\{c_i\}_{i=1}^3$ denote positive constants independent of h and τ, but which depend on the extrapolation order r, on the physical parameters and after all on the regularity of the exact solution $(\boldsymbol{u}, p, \boldsymbol{d}, \dot{\boldsymbol{d}})$.

Proof. The outline of the proof is similar to the one of Theorem 4.3.1 given in Section 4.3.6. The main steps and differences are summarized in Section 4.3.7. □

Theorems 4.3.1 and 4.3.2 provide estimates of $\mathcal{Z}_h^n$ that involve the terms

$$\left\| \boldsymbol{L}_h^{\mathrm{e}} \partial_t^r \boldsymbol{d} + \boldsymbol{L}_h^{\mathrm{v}} \boldsymbol{P}_h^{\mathrm{s}} (\partial_t^r \boldsymbol{u}, \partial_t^r \dot{\boldsymbol{d}}) \right\|_{L^2(0,T;L^2(\Omega^{\mathrm{s}}))}, \quad \left\| \boldsymbol{L}_h^{\mathrm{e}} \partial_t^r \boldsymbol{d} \right\|_{L^2(0,T;L^2(\Omega^{\mathrm{s}}))}, \tag{4.41}$$

with $r \in \{0,1,2\}$. The next lemma gives estimates for these quantities in terms of h.

Lemma 4.3.2. *Let $(\boldsymbol{u}, \dot{\boldsymbol{d}}) \in \boldsymbol{W}$ with $\boldsymbol{u} \in \boldsymbol{H}^2(\Omega^{\mathrm{f}})$ and $\dot{\boldsymbol{d}} \in \boldsymbol{H}^2(\Omega^{\mathrm{s}})$ be given. Then, there holds:*

$$\begin{aligned}\|\boldsymbol{L}_h^{\mathrm{v}} \boldsymbol{P}_h^{\mathrm{s}} (\boldsymbol{u}, \dot{\boldsymbol{d}})\|_{0,\Omega^{\mathrm{s}}} \lesssim\, & \|\boldsymbol{L}^{\mathrm{v}} \dot{\boldsymbol{d}}\|_{0,\Omega^{\mathrm{s}}} + \alpha_1 h^{-\frac{1}{2}} \|\boldsymbol{\sigma}(\dot{\boldsymbol{d}}) \boldsymbol{n}^{\mathrm{s}}\|_{0,\Sigma \cup \Gamma^{\mathrm{s,n}}} \\ & + c_1 (\alpha_1 + h c_2) \left(\alpha_1^{-\frac{1}{2}} \|\boldsymbol{u}\|_{2,\Omega^{\mathrm{f}}} + c_3 \|\dot{\boldsymbol{d}}\|_{2,\Omega^{\mathrm{s}}} \right) \\ & + c_4 \left(c_5 \alpha_1^{-\frac{1}{2}} \|\boldsymbol{u}\|_{1,\Omega^{\mathrm{f}}} + \|\dot{\boldsymbol{d}}\|_{1,\Omega^{\mathrm{s}}} \right), \\ \|\boldsymbol{L}_h^{\mathrm{e}} \boldsymbol{d}\|_{0,\Omega^{\mathrm{s}}} \lesssim\, & \|\boldsymbol{L}^{\mathrm{e}} \boldsymbol{d}\|_{0,\Omega^{\mathrm{s}}} + h^{-\frac{1}{2}} \|\boldsymbol{\sigma}(\boldsymbol{d}) \boldsymbol{n}^{\mathrm{s}}\|_{0,\Sigma \cup \Gamma^{\mathrm{s,n}}},\end{aligned} \tag{4.42}$$

where the the symbols $\{c_i\}_{i=1}^5$ denote positive constants which depend on physical quantities, but not on α_1, h and τ.

Proof. From (4.2) and (4.22), we have that

$$\begin{aligned}\left(\boldsymbol{L}_h^{\mathrm{v}} \boldsymbol{P}_h^{\mathrm{s}} (\boldsymbol{u}, \dot{\boldsymbol{d}}), \boldsymbol{v}_h^{\mathrm{s}} \right)_* =\, & \alpha_0 \rho^{\mathrm{s}} \left(\boldsymbol{P}_h^{\mathrm{s}} (\boldsymbol{u}, \dot{\boldsymbol{d}}), \boldsymbol{v}_h^{\mathrm{s}} \right)_* + \alpha_1 a^{\mathrm{e}} \left(\boldsymbol{P}_h^{\mathrm{s}} (\boldsymbol{u}, \dot{\boldsymbol{d}}), \boldsymbol{v}_h^{\mathrm{s}} \right) \\ =\, & \alpha_0 \rho^{\mathrm{s}} \left(\boldsymbol{P}_h^{\mathrm{s}} (\boldsymbol{u}, \dot{\boldsymbol{d}}), \boldsymbol{v}_h^{\mathrm{s}} \right)_{\Omega^{\mathrm{s}}} + \alpha_1 a^{\mathrm{e}} \left(\boldsymbol{P}_h^{\mathrm{s}} (\boldsymbol{u}, \dot{\boldsymbol{d}}), \boldsymbol{v}_h^{\mathrm{s}} \right) \\ & - \alpha_0 \rho^{\mathrm{s}} \delta_h (\boldsymbol{P}_h^{\mathrm{s}} (\boldsymbol{u}, \dot{\boldsymbol{d}}), \boldsymbol{v}_h^{\mathrm{s}}) \\ =\, & \alpha_0 \rho^{\mathrm{s}} \left(\boldsymbol{P}_h^{\mathrm{s}} (\boldsymbol{u}, \dot{\boldsymbol{d}}) - \dot{\boldsymbol{d}}, \boldsymbol{v}_h^{\mathrm{s}} \right)_{\Omega^{\mathrm{s}}} + \alpha_1 a^{\mathrm{e}} \left(\boldsymbol{P}_h^{\mathrm{s}} (\boldsymbol{u}, \dot{\boldsymbol{d}}) - \dot{\boldsymbol{d}}, \boldsymbol{v}_h^{\mathrm{s}} \right) \\ & - \alpha_0 \rho^{\mathrm{s}} \delta_h (\boldsymbol{P}_h^{\mathrm{s}} (\boldsymbol{u}, \dot{\boldsymbol{d}}), \boldsymbol{v}_h^{\mathrm{s}}) + a^{\mathrm{v}} (\dot{\boldsymbol{d}}, \boldsymbol{v}_h^{\mathrm{s}}).\end{aligned}$$

Thus, owing to (4.23)-(4.24) and using an inverse inequality (see, e.g., [12, Theorem 4.5.11]), we get

$$\begin{aligned}\Big(\boldsymbol{L}_h^{\mathrm{v}}\boldsymbol{P}_h^{\mathrm{s}}(\boldsymbol{u},\dot{\boldsymbol{d}}),\boldsymbol{v}_h^{\mathrm{s}}\Big)_* \lesssim\ & \alpha_0\rho^{\mathrm{s}}\|\boldsymbol{P}_h^{\mathrm{s}}(\boldsymbol{u},\dot{\boldsymbol{d}})-\dot{\boldsymbol{d}}\|_{0,\Omega^{\mathrm{s}}}\|\boldsymbol{v}_h^{\mathrm{s}}\|_{0,\Omega^{\mathrm{s}}}\\ &+\alpha_1\frac{\beta_{\mathrm{e}}^{\frac{1}{2}}}{h}\|\boldsymbol{P}_h^{\mathrm{s}}(\boldsymbol{u},\dot{\boldsymbol{d}})-\dot{\boldsymbol{d}}\|_{\mathrm{e}}\|\boldsymbol{v}_h^{\mathrm{s}}\|_{0,\Omega^{\mathrm{s}}}\\ &+\frac{\alpha_0\rho^{\mathrm{s}}}{\alpha_{\mathrm{e}}^{\frac{1}{2}}}\|\boldsymbol{P}_h^{\mathrm{s}}(\boldsymbol{u},\dot{\boldsymbol{d}})\|_{\mathrm{e}}\|\boldsymbol{v}_h^{\mathrm{s}}\|_{0,\Omega^{\mathrm{s}}}+a^{\mathrm{v}}(\dot{\boldsymbol{d}},\boldsymbol{v}_h^{\mathrm{s}}).\end{aligned}\tag{4.43}$$

Moreover, integrating by parts in the last term and using the discrete trace inequality $\|\boldsymbol{v}_h^{\mathrm{s}}\|_{0,\partial\Omega^{\mathrm{s}}}\lesssim h^{-\frac{1}{2}}\|\boldsymbol{v}_h^{\mathrm{s}}\|_{0,\Omega^{\mathrm{s}}}$ (see, e.g., [28]), we have

$$\begin{aligned}a^{\mathrm{v}}(\dot{\boldsymbol{d}},\boldsymbol{v}_h^{\mathrm{s}}) =&\alpha_0\rho^{\mathrm{s}}(\dot{\boldsymbol{d}},\boldsymbol{v}_h^{\mathrm{s}})_{\Omega^{\mathrm{s}}}+\alpha_1 a^{\mathrm{e}}(\dot{\boldsymbol{d}},\boldsymbol{v}_h^{\mathrm{s}})\\ =&\alpha_0\rho^{\mathrm{s}}(\dot{\boldsymbol{d}},\boldsymbol{v}_h^{\mathrm{s}})_{\Omega^{\mathrm{s}}}+\alpha_1\big(\boldsymbol{\sigma}(\dot{\boldsymbol{d}}),\boldsymbol{\epsilon}(\boldsymbol{v}_h^{\mathrm{s}})\big)_{\Omega^{\mathrm{s}}}\\ =&\big(\boldsymbol{L}^{\mathrm{v}}\dot{\boldsymbol{d}},\boldsymbol{v}_h^{\mathrm{s}}\big)_{\Omega^{\mathrm{s}}}+\alpha_1\int_{\Sigma\cup\Gamma^{\mathrm{s,n}}}\boldsymbol{\sigma}(\dot{\boldsymbol{d}})\boldsymbol{n}^{\mathrm{s}}\cdot\boldsymbol{v}_h^{\mathrm{s}}\\ \lesssim&\left(\|\boldsymbol{L}^{\mathrm{v}}\dot{\boldsymbol{d}}\|_{0,\Omega^{\mathrm{s}}}+\frac{\alpha_1}{h^{\frac{1}{2}}}\|\boldsymbol{\sigma}(\dot{\boldsymbol{d}})\boldsymbol{n}^{\mathrm{s}}\|_{0,\Sigma\cup\Gamma^{\mathrm{s,n}}}\right)\|\boldsymbol{v}_h^{\mathrm{s}}\|_{0,\Omega^{\mathrm{s}}}.\end{aligned}\tag{4.44}$$

As a result, by inserting this estimate in (4.43), it follows that

$$\begin{aligned}\Big(\boldsymbol{L}_h^{\mathrm{v}}\boldsymbol{P}_h^{\mathrm{s}}(\boldsymbol{u},\dot{\boldsymbol{d}}),\boldsymbol{v}_h^{\mathrm{s}}\Big)_* \lesssim\ & \left(\alpha_0\rho^{\mathrm{s}}\|\boldsymbol{P}_h^{\mathrm{s}}(\boldsymbol{u},\dot{\boldsymbol{d}})-\dot{\boldsymbol{d}}\|_{0,\Omega^{\mathrm{s}}}+\alpha_1\frac{\beta_{\mathrm{e}}^{\frac{1}{2}}}{h}\|\boldsymbol{P}_h^{\mathrm{s}}(\boldsymbol{u},\dot{\boldsymbol{d}})-\dot{\boldsymbol{d}}\|_{\mathrm{e}}\right.\\ &\left.+\frac{\alpha_0\rho^{\mathrm{s}}}{\alpha_{\mathrm{e}}^{\frac{1}{2}}}\|\boldsymbol{P}_h^{\mathrm{s}}(\boldsymbol{u},\dot{\boldsymbol{d}})\|_{\mathrm{e}}+\|\boldsymbol{L}^{\mathrm{v}}\dot{\boldsymbol{d}}\|_{0,\Omega^{\mathrm{s}}}+\frac{\alpha_1}{h^{\frac{1}{2}}}\|\boldsymbol{\sigma}(\dot{\boldsymbol{d}})\boldsymbol{n}^{\mathrm{s}}\|_{0,\Sigma\cup\Gamma^{\mathrm{s,n}}}\right)\|\boldsymbol{v}_h^{\mathrm{s}}\|_{0,\Omega^{\mathrm{s}}}.\end{aligned}\tag{4.45}$$

The estimate $(4.42)_1$ then follows from the Poincaré inequality and Lemma 4.3.1, by taking $\boldsymbol{v}_h^{\mathrm{s}}=\boldsymbol{L}_h^{\mathrm{v}}\boldsymbol{P}_h^{\mathrm{s}}(\boldsymbol{u},\dot{\boldsymbol{d}})$ in (4.45).

At last, the estimate $(4.42)_2$ follows by using the same arguments as in (4.44). □

Lemma 4.3.2 predicts an $\mathcal{O}(h^{-\frac{1}{2}})$ behavior for the quantities (4.41). This is due to the fact that the discrete operators $\boldsymbol{L}_h^{\mathrm{e}}$ and $\boldsymbol{L}_h^{\mathrm{v}}\boldsymbol{P}_h^{\mathrm{s}}$ are not uniform in h. Basically, the issue comes from the interface terms arising in the integration by parts of (4.44).

Remark 4.3.2. *It should be noted that the above issue does not appear in the case of coupling with a thin-walled structure (as shown in Chapter 2), since by construction the fluid-structure interface Σ and the solid domain Ω^{s} coincide. This explains the differences on the convergence rates observed in Sections 2.8.1 and 3.6.1.1.*

We conclude this section with the following two corollaries, which combine the results of Theorems 4.3.1 and 4.3.2 and Lemma 4.3.2.

Corollary 4.3.1. *Under the hypothesis of Theorem 4.3.1, we have the following estimation of the discrete error* $\mathcal{Z}_h^n$*:*

$$\mathcal{Z}_h^n \lesssim c_4\left(1+\frac{c_5}{\alpha_1}\right)h + c_6\tau + c_7\tau^{2^{r-1}}\left(1+c_8h+c_9\alpha_1^{-\frac{1}{2}}+c_{10}h\alpha_1^{-\frac{1}{2}}+c_{11}\alpha_1^{\frac{1}{2}}+c_{12}\alpha_1\right) + \frac{\tau^{2^{r-1}}}{\sqrt{h}}\left(\|\boldsymbol{\sigma}\left(\boldsymbol{d}\right)\boldsymbol{n}^{\mathrm{s}}\|_{H^r(0,T;L^2(\Sigma\cup\Gamma^{\mathrm{s,n}}))}+\alpha_1\|\boldsymbol{\sigma}(\dot{\boldsymbol{d}})\boldsymbol{n}^{\mathrm{s}}\|_{H^r(0,T;L^2(\Sigma\cup\Gamma^{\mathrm{s,n}}))}\right). \tag{4.46}$$

Corollary 4.3.2. *Under the hypothesis of Theorem 4.3.2, we have the following estimation of the discrete error* $\mathcal{Z}_h^n$*:*

$$\mathcal{Z}_h^n \lesssim c_{13}h + c_{14}\tau + c_{15}\tau^{2^{r-1}}\left(1+c_{16}h^2+\frac{1}{\sqrt{h}}\|\boldsymbol{\sigma}\left(\boldsymbol{d}\right)\boldsymbol{n}^{\mathrm{s}}\|_{H^r(0,T;L^2(\Sigma\cup\Gamma^{\mathrm{s,n}}))}\right). \tag{4.47}$$

4.3.4 A priori error estimates

The next two theorems state a priori error estimates for Algorithms 4.1 or 4.2, depending on the value of $\alpha_1 \geq 0$.

Theorem 4.3.3. *Let* $(\boldsymbol{u},p,\boldsymbol{d},\dot{\boldsymbol{d}})$ *be the solution of the coupled problem* (4.1) *and* $\{(\boldsymbol{u}_h^n,p_h^n,\boldsymbol{d}_h^n,\dot{\boldsymbol{d}}_h^n)\}_{n>r}$ *be the discrete solution given by Algorithm 4.1 or 4.2 with* $\alpha_1>0$ *and initial data*

$$\left(\boldsymbol{u}_h^0,\boldsymbol{d}_h^0,\dot{\boldsymbol{d}}_h^0\right)=\left(\boldsymbol{P}_h^{\mathrm{f}}(\boldsymbol{u}^0,\dot{\boldsymbol{d}}^0),\boldsymbol{\pi}_h^{\mathrm{e}}\boldsymbol{d}^0,\boldsymbol{P}_h^{\mathrm{s}}(\boldsymbol{u}^0,\dot{\boldsymbol{d}}^0)\right)$$

and, depending on the extrapolation order $r\in\{0,1,2\}$*, with the initiation procedure detailed in Remark 4.2.3. We assume that the exact solution has the regularity provided by* (4.36)*. Then, we have the following error estimates, for* $n>r$ *such that* $n\tau<T$ *and* $(\alpha_0+1/T)\tau<1$*:*

$$\mathcal{E}_h^n \lesssim c_1^\star\left(1+\frac{c_2^\star}{\alpha_1}\right)h + c_3^\star\tau + c_4^\star\tau^{2^{r-1}}\left(1+c_5^\star h+c_6^\star\alpha_1^{-\frac{1}{2}}+c_7^\star h\alpha_1^{-\frac{1}{2}}+c_8^\star\alpha_1^{\frac{1}{2}}+c_9^\star\alpha_1\right) + \frac{\tau^{2^{r-1}}}{\sqrt{h}}\left(\|\boldsymbol{\sigma}\left(\boldsymbol{d}\right)\boldsymbol{n}\|_{H^r([0,T];L^2(\Sigma\cup\Gamma^{\mathrm{s,n}}))}+\alpha_1\|\boldsymbol{\sigma}(\dot{\boldsymbol{d}})\boldsymbol{n}^{\mathrm{s}}\|_{H^r(0,T;L^2(\Sigma\cup\Gamma^{\mathrm{s,n}}))}\right). \tag{4.48}$$

Here, the symbols $\{c_i^\star\}_{i=1}^9$ *denote positive constants independent of* h*,* τ *and* α_1*, but which depend on other physical parameters and on the regularity of* $(\boldsymbol{u},p,\boldsymbol{d},\dot{\boldsymbol{d}})$*.*

Proof. This result is straightforward using the decomposition of the total error $\mathcal{E}_h^n$ given by (4.27) and (4.32). A first part is represented by $\mathcal{Z}_h^n$ and the remaining part is estimated with (4.31) and (4.26). □

In the case of a vanishing $\alpha_1=0$ then we have the following result:

Theorem 4.3.4. *Let* $(\boldsymbol{u}, p, \boldsymbol{d}, \dot{\boldsymbol{d}})$ *be the solution of the coupled problem* (4.1) *and* $\{(\boldsymbol{u}_h^n, p_h^n, \boldsymbol{d}_h^n, \dot{\boldsymbol{d}}_h^n)\}_{n>r}$ *be the discrete solution given by Algorithm 4.1 or 4.2 with* $\alpha_1 = 0$ *and initial data*

$$\left(\boldsymbol{u}_h^0, \boldsymbol{d}_h^0, \dot{\boldsymbol{d}}_h^0\right) = \left(\boldsymbol{P}_h \boldsymbol{u}^0, \boldsymbol{\pi}_h^{\mathrm{e}} \boldsymbol{d}^0, \boldsymbol{\mathcal{I}}_h^{\Omega^{\mathrm{s}}} \dot{\boldsymbol{d}}^0\right)$$

and, depending on the extrapolation order $r \in \{0, 1, 2\}$*, with the initiation procedure detailed in Remark 4.2.3. We assume that the exact solution has the regularity provided by* (4.36)*. Then, we have the following error estimates, for* $n > r$ *such that* $n\tau < T$ *and* $(\alpha_0 + 1/T)\tau < 1$*:*

$$\mathcal{E}_h^n \lesssim c_{10}^\star h + c_{11}^\star \tau + c_{12}^\star \tau^{2^{r-1}} \left(1 + c_{13}^\star h^2 + \frac{1}{\sqrt{h}} \|\boldsymbol{\sigma}(\boldsymbol{d})\, \boldsymbol{n}\|_{H^r([0,T];L^2(\Sigma \cup \Gamma^{\mathrm{s,n}}))}\right). \tag{4.49}$$

Here, the symbols $\{c_i^\star\}_{i=10}^{13}$ *denote positive constants independent of* h *and* τ*, but which depend on the physical parameters and on the regularity of* $(\boldsymbol{u}, p, \boldsymbol{d}, \dot{\boldsymbol{d}})$*.*

Proof. This result is straightforward using the decomposition of the total error $\mathcal{E}_h^n$ given by (4.27) and (4.32). A first part is represented by $\mathcal{Z}_h^n$ and the remaining part is estimated with (4.39) and (4.26). □

The results of Theorems 4.3.3 and 4.3.4 confirm the numerical evidence reported in Chapter 3. Provided that the exact solution has the appropriate regularity, the error introduced by the kinematic perturbation has an order $\mathcal{O}(\sqrt{\tau/h})$ if $r = 0$. In this case, the standard hyperbolic-CFL scaling $\tau = \mathcal{O}(h)$ is not enough to guarantee the convergence of the scheme. A sub-optimal convergence is recovered for the scheme with $r = 0$ under the restrictive parabolic-CFL condition $\tau = \mathcal{O}(h^2)$.

For the scheme with first-order extrapolation ($r = 1$), the error is of order $\mathcal{O}(\tau/\sqrt{h})$. This means that a sub-optimal convergence rate is obtained under $\tau = \mathcal{O}(h)$. In order to guarantee a first-order convergence rate, the scaling $\tau = \mathcal{O}(h^{3/2})$ is needed. We recall that the scheme is unconditionally stable in this case (as for the non incremental case $r = 0$).

At last, for the scheme with second-order extrapolation ($r = 2$), the error introduced by the kinematic perturbation is of order $\mathcal{O}(\tau^2/\sqrt{h})$, which is enough to ensure an optimal convergence rate if $\tau = \mathcal{O}(h)$. But the stability condition (3.43) enforces $\tau = \mathcal{O}(h^{6/5})$ to be fulfilled when there is no viscosity in the solid model (i.e. $\alpha_0 = \alpha_1 = 0$) and $\tau = \mathcal{O}(h^2)$ in other cases.

Another salient consequence of Theorems 4.3.3 and 4.3.4 is that the mass-lumping approximation does not perturbs the overall accuracy of the coupling scheme.

4.3.5 Anlaysis of the fluid-solid hydrodynamic projector

This section is devoted to the proof of Lemma 4.3.1. We proceed by adapting the arguments reported in [68] and [45, Appendix B].

We first prove the following generalized inf-sup condition.

Lemma 4.3.3. *There holds*

$$\|q_h\|_Q \lesssim \sup_{(\boldsymbol{v}_h^{\mathrm{f}},\boldsymbol{v}_h^{\mathrm{s}})\in \boldsymbol{W}_h\setminus\{\boldsymbol{0}\}} \frac{b(q_h,\boldsymbol{v}_h^{\mathrm{f}})}{\|\boldsymbol{v}_h^{\mathrm{f}}\|_{\boldsymbol{V}}+\alpha_1^{\frac{1}{2}}\|\boldsymbol{v}_h^{\mathrm{s}}\|_{\mathrm{e}}} + |q_h|_{s_h}$$

for all $q_h \in Q_h$.

Proof. From [45, Lemma 4] we know that

$$\|q_h\|_Q \lesssim \sup_{\boldsymbol{v}_h^{\mathrm{f}}\in \boldsymbol{V}_h^{\mathrm{f}}\setminus\{\boldsymbol{0}\}} \frac{b(q_h,\boldsymbol{v}_h^{\mathrm{f}})}{\|\boldsymbol{v}_h^{\mathrm{f}}\|_{\boldsymbol{V}}} + |q_h|_{s_h}$$

for all $q_h \in Q_h$. Therefore, it only remains to prove that

$$\sup_{\boldsymbol{v}_h^{\mathrm{f}}\in \boldsymbol{V}_h^{\mathrm{f}}\setminus\{\boldsymbol{0}\}} \frac{b(q_h,\boldsymbol{v}_h^{\mathrm{f}})}{\|\boldsymbol{v}_h^{\mathrm{f}}\|_{\boldsymbol{V}}} \lesssim \sup_{(\boldsymbol{v}_h^{\mathrm{f}},\boldsymbol{v}_h^{\mathrm{s}})\in \boldsymbol{W}_h\setminus\{\boldsymbol{0}\}} \frac{b(q_h,\boldsymbol{v}_h^{\mathrm{f}})}{\|\boldsymbol{v}_h^{\mathrm{f}}\|_{\boldsymbol{V}}+\alpha_1^{\frac{1}{2}}\|\boldsymbol{v}_h^{\mathrm{s}}\|_{\mathrm{e}}}$$

for all $q_h \in Q_h$. More precisely, let $q_h \in Q_h$ and $\boldsymbol{v}_h^{\mathrm{f}} \in \boldsymbol{V}_h^{\mathrm{f}} \setminus \{\boldsymbol{0}\}$, it is sufficient to find $\boldsymbol{v}_h^{\mathrm{s}} \in \boldsymbol{V}_h^{\mathrm{s}}$ satisfying $(\boldsymbol{v}_h^{\mathrm{f}}, \boldsymbol{v}_h^{\mathrm{s}}) \in \boldsymbol{W}_h^{\mathrm{s}}$ and

$$\frac{b(q_h,\boldsymbol{v}_h^{\mathrm{f}})}{\|\boldsymbol{v}_h^{\mathrm{f}}\|_{\boldsymbol{V}}} \lesssim \frac{b(q_h,\boldsymbol{v}_h^{\mathrm{f}})}{\|\boldsymbol{v}_h^{\mathrm{f}}\|_{\boldsymbol{V}}+\alpha_1^{\frac{1}{2}}\|\boldsymbol{v}_h^{\mathrm{s}}\|_{\mathrm{e}}}.$$

To this purpose, we set $\boldsymbol{v}_h^{\mathrm{s}} = E_h\left(\boldsymbol{v}_h^{\mathrm{f}}|_\Sigma\right)$, where $E_h : \Lambda_{\Sigma,h} \to \boldsymbol{V}_h^{\mathrm{s}}$ denotes a uniformly bounded discrete lifting operator (see, e.g., [38, Theorem 2.2]), viz.,

$$(E_h\boldsymbol{\xi}_h)|_\Sigma = \boldsymbol{\xi}_h, \quad \|E_h\boldsymbol{\xi}_h\|_{1,\Omega^{\mathrm{s}}} \lesssim \|\boldsymbol{\xi}_h\|_{\frac{1}{2},\Sigma}$$

for all $\boldsymbol{\xi}_h \in \Lambda_{\Sigma,h}$. Hence, thanks to (4.24) and to the continuity of the trace, we have that

$$\begin{aligned}
\alpha_1\|\boldsymbol{v}_h^{\mathrm{s}}\|_{\mathrm{e}}^2 &\le \alpha_1\beta_{\mathrm{e}}\|\boldsymbol{v}_h^{\mathrm{s}}\|_{1,\Omega^{\mathrm{s}}}^2 \\
&\lesssim \alpha_1\beta_{\mathrm{e}}\|\boldsymbol{v}_h^{\mathrm{f}}\|_{\frac{1}{2},\Sigma}^2 \\
&\lesssim \alpha_1\beta_{\mathrm{e}}\|\boldsymbol{v}_h^{\mathrm{f}}\|_{1,\Omega^{\mathrm{f}}}^2 \\
&\lesssim \frac{\alpha_1\beta_{\mathrm{e}}}{\mu}\|\boldsymbol{v}_h^{\mathrm{f}}\|_{\boldsymbol{V}}^2,
\end{aligned}$$

which completes the proof. □

The previous result guarantees the well-posedness of problem (4.28) (see, e.g., [22, Theorem 3.5]). The energy estimate (4.30) hence follows by taking

$$\begin{cases}
\boldsymbol{v}_h^{\mathrm{f}} = \boldsymbol{P}_h^{\mathrm{f}}(\boldsymbol{u},\dot{\boldsymbol{d}}), \\
\boldsymbol{v}_h^{\mathrm{s}} = \boldsymbol{P}_h^{\mathrm{s}}(\boldsymbol{u},\dot{\boldsymbol{d}}), \\
q_h = R_h(\boldsymbol{u},\dot{\boldsymbol{d}}),
\end{cases}$$

in (4.28) and applying standard control methods to the right-hand side.

We now focus on the *a priori* error estimate (4.31). To this purpose we first state the following approximation result.

Lemma 4.3.4. *Let* $\big((\boldsymbol{u}_h, \dot{\boldsymbol{d}}_h), p_h\big) \in \boldsymbol{W}_h \times Q_h$ *be given by* (4.28). *There holds*

$$\begin{aligned}\|\boldsymbol{u}-\boldsymbol{u}_h\|_{\boldsymbol{V}} + \alpha_1^{\frac{1}{2}}\|\dot{\boldsymbol{d}}-\dot{\boldsymbol{d}}_h\|_{\mathrm{e}} + \|p_h\|_Q + |p_h|_{s_h} \\ \lesssim \inf_{\big((\hat{\boldsymbol{v}}_h^{\mathrm{f}},\hat{\boldsymbol{v}}_h^{\mathrm{s}}),\hat{p}_h\big)\in \boldsymbol{Z}_h} \Big\{\|\boldsymbol{u}-\hat{\boldsymbol{v}}_h^{\mathrm{f}}\|_{\boldsymbol{V}} + \alpha_1^{\frac{1}{2}}\|\dot{\boldsymbol{d}}-\hat{\boldsymbol{v}}_h^{\mathrm{s}}\|_{\mathrm{e}} + \|\hat{p}_h\|_Q + |\hat{p}_h|_{s_h}\Big\}, \quad (4.50)\end{aligned}$$

where

$$\boldsymbol{Z}_h \overset{\mathrm{def}}{=} \big\{\big((\hat{\boldsymbol{v}}_h^{\mathrm{f}}, \hat{\boldsymbol{v}}_h^{\mathrm{s}}), \hat{p}_h\big) \in \boldsymbol{W}_h \times Q_h \,/\, b(q_h, \hat{\boldsymbol{v}}_h^{\mathrm{f}}) = s_h(\hat{p}_h, q_h) \quad \forall q_h \in Q_h\big\}.$$

Proof. Let $\big((\hat{\boldsymbol{v}}_h^{\mathrm{f}}, \hat{\boldsymbol{v}}_h^{\mathrm{s}}), \hat{p}_h\big)$ be given in $\boldsymbol{Z}_h$, for all $(\boldsymbol{w}_h^{\mathrm{f}}, \boldsymbol{w}_h^{\mathrm{s}}) \in \boldsymbol{W}_h$, we have

$$\begin{aligned}a(\boldsymbol{u}_h-\hat{\boldsymbol{v}}_h^{\mathrm{f}}, \boldsymbol{w}_h^{\mathrm{f}}) + \alpha_1 a^{\mathrm{e}}(\dot{\boldsymbol{d}}_h-\hat{\boldsymbol{v}}_h^{\mathrm{s}}, \boldsymbol{w}_h^{\mathrm{s}}) =& a(\boldsymbol{u}_h-\boldsymbol{u}, \boldsymbol{w}_h^{\mathrm{f}}) + \alpha_1 a^{\mathrm{e}}(\dot{\boldsymbol{d}}_h-\dot{\boldsymbol{d}}, \boldsymbol{w}_h^{\mathrm{s}}) \\ &+ a(\boldsymbol{u}-\hat{\boldsymbol{v}}_h^{\mathrm{f}}, \boldsymbol{w}_h^{\mathrm{f}}) + \alpha_1 a^{\mathrm{e}}(\dot{\boldsymbol{d}}-\hat{\boldsymbol{v}}_h^{\mathrm{s}}, \boldsymbol{w}_h^{\mathrm{s}}) \\ =& - b(p_h, \boldsymbol{w}_h^{\mathrm{f}}) + a(\boldsymbol{u}-\hat{\boldsymbol{v}}_h^{\mathrm{f}}, \boldsymbol{w}_h^{\mathrm{f}}) + \alpha_1 a^{\mathrm{e}}(\dot{\boldsymbol{d}}-\hat{\boldsymbol{v}}_h^{\mathrm{s}}, \boldsymbol{w}_h^{\mathrm{s}}) \\ =& - b(\hat{p}_h, \boldsymbol{w}_h^{\mathrm{f}}) + b(\hat{p}_h - p_h, \boldsymbol{w}_h^{\mathrm{f}}) \\ &+ a(\boldsymbol{u}-\hat{\boldsymbol{v}}_h^{\mathrm{f}}, \boldsymbol{w}_h^{\mathrm{f}}) + \alpha_1 a^{\mathrm{e}}(\dot{\boldsymbol{d}}-\hat{\boldsymbol{v}}_h^{\mathrm{s}}, \boldsymbol{w}_h^{\mathrm{s}}).\end{aligned}$$

Then, we take $\boldsymbol{w}_h^{\mathrm{f}} = \boldsymbol{u}_h - \hat{\boldsymbol{v}}_h^{\mathrm{f}}$ and $\boldsymbol{w}_h^{\mathrm{s}} = \dot{\boldsymbol{d}}_h - \hat{\boldsymbol{v}}_h^{\mathrm{s}}$ to get

$$\begin{aligned}\|\boldsymbol{u}_h-\hat{\boldsymbol{v}}_h^{\mathrm{f}}\|_{\boldsymbol{V}}^2 + \alpha_1\|\dot{\boldsymbol{d}}_h-\hat{\boldsymbol{v}}_h^{\mathrm{s}}\|_{\mathrm{e}}^2 =& - b(\hat{p}_h, \boldsymbol{u}_h-\hat{\boldsymbol{v}}_h^{\mathrm{f}}) - |p_h-\hat{p}_h|_{s_h}^2 \\ &+ a(\boldsymbol{u}-\hat{\boldsymbol{v}}_h^{\mathrm{f}}, \boldsymbol{u}_h-\hat{\boldsymbol{v}}_h^{\mathrm{f}}) + \alpha_1 a^{\mathrm{e}}(\dot{\boldsymbol{d}}-\hat{\boldsymbol{v}}_h^{\mathrm{s}}, \dot{\boldsymbol{d}}_h-\hat{\boldsymbol{v}}_h^{\mathrm{s}}).\end{aligned}$$

Therefore, by using the Korn inequality (see, e.g., [12, Chapter 11]), the continuity of the bilinear forms b, a and a^{e} and the Cauchy-Schwarz inequality, it follows that

$$\|\boldsymbol{u}_h-\hat{\boldsymbol{v}}_h^{\mathrm{f}}\|_{\boldsymbol{V}}^2 + \alpha_1\|\dot{\boldsymbol{d}}_h-\hat{\boldsymbol{v}}_h^{\mathrm{s}}\|_{\mathrm{e}}^2 + |p_h-\hat{p}_h|_{s_h}^2 \lesssim \|\boldsymbol{u}-\hat{\boldsymbol{v}}_h^{\mathrm{f}}\|_{\boldsymbol{V}}^2 + \alpha_1\|\dot{\boldsymbol{d}}-\hat{\boldsymbol{v}}_h^{\mathrm{s}}\|_{\mathrm{e}}^2 + \|\hat{p}_h\|_Q^2, \quad (4.51)$$

which, in combination with a triangle inequality, yields

$$\|\boldsymbol{u}-\boldsymbol{u}_h\|_{\boldsymbol{V}} + \alpha_1^{\frac{1}{2}}\|\dot{\boldsymbol{d}}-\dot{\boldsymbol{d}}_h\|_{\mathrm{e}} + |p_h|_{s_h} \lesssim \|\boldsymbol{u}-\hat{\boldsymbol{v}}_h^{\mathrm{f}}\|_{\boldsymbol{V}} + \alpha_1^{\frac{1}{2}}\|\dot{\boldsymbol{d}}-\hat{\boldsymbol{v}}_h^{\mathrm{s}}\|_{\mathrm{e}} + \|\hat{p}_h\|_Q + |\hat{p}_h|_{s_h}. \quad (4.52)$$

Finally, it remains to have a control on $\|p_h\|_{0,\Omega^{\mathrm{f}}}$. Thanks to the generalized inf-sup condition of Lemma 4.3.3, there exists $(\boldsymbol{z}_h^{\mathrm{f}}, \boldsymbol{z}_h^{\mathrm{s}}) \in \boldsymbol{W}_h^{\mathrm{f}} \setminus \{\boldsymbol{0}\}$ such that

$$\begin{aligned}\|p_h-\hat{p}_h\|_Q &\lesssim |p_h-\hat{p}_h|_{s_h} + \frac{b(p_h-\hat{p}_h, \boldsymbol{z}_h^{\mathrm{f}})}{\|\boldsymbol{z}_h^{\mathrm{f}}\|_{\boldsymbol{V}} + \alpha_1^{\frac{1}{2}}\|\boldsymbol{z}_h^{\mathrm{s}}\|_{\mathrm{e}}} \\ &\lesssim |p_h-\hat{p}_h|_{s_h} + \frac{a(\boldsymbol{u}-\boldsymbol{u}_h, \boldsymbol{z}_h^{\mathrm{f}}) + \alpha_1 a^{\mathrm{e}}(\dot{\boldsymbol{d}}-\dot{\boldsymbol{d}}_h, \boldsymbol{z}_h^{\mathrm{s}}) - b(\hat{p}_h, \boldsymbol{z}_h^{\mathrm{f}})}{\|\boldsymbol{z}_h^{\mathrm{f}}\|_{\boldsymbol{V}} + \alpha_1^{\frac{1}{2}}\|\boldsymbol{z}_h^{\mathrm{s}}\|_{\mathrm{e}}} \\ &\lesssim |p_h-\hat{p}_h|_{s_h} + \|\boldsymbol{u}-\boldsymbol{u}_h\|_{\boldsymbol{V}} + \alpha_1^{\frac{1}{2}}\|\dot{\boldsymbol{d}}-\dot{\boldsymbol{d}}_h\|_{\mathrm{e}} + \|\hat{p}_h\|_Q.\end{aligned}$$

Hence, owing to (4.51) and (4.52), we get

$$\|p_h - \hat{p}_h\|_Q \lesssim \|\boldsymbol{u} - \hat{\boldsymbol{v}}_h^{\mathrm{f}}\|_{\boldsymbol{V}} + \alpha_1^{\frac{1}{2}} \|\dot{\boldsymbol{d}} - \hat{\boldsymbol{v}}_h^{\mathrm{s}}\|_{\mathrm{e}} + \|\hat{p}_h\|_Q + |\hat{p}_h|_{s_h}.$$

We conclude the estimate for the pressure with the triangle inequality

$$\|p_h\|_Q \leq \|p_h - \hat{p}_h\|_Q + \|\hat{p}_h\|_Q.$$

Since the choice of $\big((\hat{\boldsymbol{v}}_h^{\mathrm{f}}, \hat{\boldsymbol{v}}_h^{\mathrm{s}}), \hat{p}_h\big) \in \boldsymbol{Z}_h$ is arbitrary, the lemma is proved. □

The next lemma shows that the constraint $\big((\hat{\boldsymbol{v}}_h^{\mathrm{f}}, \hat{\boldsymbol{v}}_h^{\mathrm{s}}), \hat{p}_h\big) \in \boldsymbol{Z}_h$ can be relaxed in (4.50).

Lemma 4.3.5. *Let $\big((\boldsymbol{u}_h, \dot{\boldsymbol{d}}_h), p_h\big) \in \boldsymbol{W}_h \times Q_h$ be given by (4.28) and assume that $div\, \boldsymbol{u} = 0$ in Ω^{f}. The following inequality holds:*

$$\begin{aligned}\|\boldsymbol{u} - \boldsymbol{u}_h\|_{\boldsymbol{V}} + \alpha_1^{\frac{1}{2}} \|\dot{\boldsymbol{d}} - \dot{\boldsymbol{d}}_h\|_{\mathrm{e}} + \|p_h\|_Q + |p_h|_{s_h} \\ \lesssim \inf_{\big((\boldsymbol{z}_h^{\mathrm{f}}, \boldsymbol{z}_h^{\mathrm{s}}), r_h\big) \in \boldsymbol{W}_h \times Q_h} \Big\{ \|\boldsymbol{u} - \boldsymbol{z}_h^{\mathrm{f}}\|_{\boldsymbol{V}} + \alpha_1^{\frac{1}{2}} \|\dot{\boldsymbol{d}} - \boldsymbol{z}_h^{\mathrm{s}}\|_{\mathrm{e}} + \|r_h\|_Q + |r_h|_{s_h} \Big\}.\end{aligned}$$

Proof. Let $\big((\boldsymbol{z}_h^{\mathrm{f}}, \boldsymbol{z}_h^{\mathrm{s}}), r_h\big)$ be given in $\boldsymbol{W}_h \times Q_h$. We denote by $\big((\boldsymbol{x}_h^{\mathrm{f}}, \boldsymbol{x}_h^{\mathrm{s}}), y_h\big) \in \boldsymbol{W}_h \times Q_h$ the solution of the following auxiliary problem:

$$\begin{cases} a(\boldsymbol{x}_h^{\mathrm{f}}, \boldsymbol{v}_h^{\mathrm{f}}) + \alpha_1 a^{\mathrm{e}}(\boldsymbol{x}_h^{\mathrm{s}}, \boldsymbol{v}_h^{\mathrm{s}}) + b(y_h, \boldsymbol{v}_h^{\mathrm{f}}) = 0, \\ \qquad\qquad b(q_h, \boldsymbol{x}_h^{\mathrm{f}}) - s_h(y_h, q_h) = b(q_h, \boldsymbol{u} - \boldsymbol{z}_h^{\mathrm{f}}) + s_h(r_h, q_h) \end{cases} \tag{4.53}$$

for all $\big((\boldsymbol{v}_h^{\mathrm{f}}, \boldsymbol{v}_h^{\mathrm{s}}), q_h\big) \in \boldsymbol{W}_h \times Q_h$. The existence and uniqueness of the solution $\big((\boldsymbol{x}_h^{\mathrm{f}}, \boldsymbol{x}_h^{\mathrm{s}}), y_h\big)$ results from Lemma 4.3.3. Since $\operatorname{div} \boldsymbol{u} = 0$ in Ω^{f}, owing to $(4.53)_2$ we have that $\big((\boldsymbol{x}_h^{\mathrm{f}} + \boldsymbol{z}_h^{\mathrm{f}}, \boldsymbol{x}_h^{\mathrm{s}} + \boldsymbol{z}_h^{\mathrm{s}}), y_h + r_h\big) \in \boldsymbol{Z}_h$. Therefore,

$$\begin{aligned}&\inf_{\big((\hat{\boldsymbol{v}}_h^{\mathrm{f}}, \hat{\boldsymbol{v}}_h^{\mathrm{s}}), \hat{p}_h\big) \in \boldsymbol{Z}_h} \Big\{ \|\boldsymbol{u} - \hat{\boldsymbol{v}}_h^{\mathrm{f}}\|_{\boldsymbol{V}} + \alpha_1^{\frac{1}{2}} \|\dot{\boldsymbol{d}} - \hat{\boldsymbol{v}}_h^{\mathrm{s}}\|_{\mathrm{e}} + \|\hat{p}_h\|_Q + |\hat{p}_h|_{s_h} \Big\} \\ &\qquad \leq \|\boldsymbol{u} - (\boldsymbol{x}_h^{\mathrm{f}} + \boldsymbol{z}_h^{\mathrm{f}})\|_{\boldsymbol{V}} + \alpha_1^{\frac{1}{2}} \|\dot{\boldsymbol{d}} - (\boldsymbol{x}_h^{\mathrm{s}} + \boldsymbol{z}_h^{\mathrm{s}})\|_{\mathrm{e}} + \|y_h + r_h\|_Q + |y_h + r_h|_{s_h} \\ &\leq \|\boldsymbol{u} - \boldsymbol{z}_h^{\mathrm{f}}\|_{\boldsymbol{V}} + \alpha_1^{\frac{1}{2}} \|\dot{\boldsymbol{d}} - \boldsymbol{z}_h^{\mathrm{s}}\|_{\mathrm{e}} + \|r_h\|_Q + |r_h|_{s_h} + \|\boldsymbol{x}_h^{\mathrm{f}}\|_{\boldsymbol{V}} + \alpha_1^{\frac{1}{2}} \|\boldsymbol{x}_h^{\mathrm{s}}\|_{\mathrm{e}} + \|y_h\|_Q + |y_h|_{s_h}.\end{aligned} \tag{4.54}$$

In order to control the last four terms, we take $(\boldsymbol{v}_h^{\mathrm{f}}, \boldsymbol{v}_h^{\mathrm{s}}) = (\boldsymbol{x}_h^{\mathrm{f}}, \boldsymbol{x}_h^{\mathrm{s}})$ and $q_h = y_h$ in (4.53), which yields

$$\|\boldsymbol{x}_h^{\mathrm{f}}\|_{\boldsymbol{V}} + \alpha_1^{\frac{1}{2}} \|\boldsymbol{x}_h^{\mathrm{s}}\|_{\mathrm{e}} + |y_h|_{s_h} \lesssim \|\boldsymbol{u} - \boldsymbol{z}_h^{\mathrm{f}}\|_{\boldsymbol{V}} + \|y_h\|_Q + |r_h|_{s_h}. \tag{4.55}$$

Furthermore, using the generalized inf-sup condition of Lemma 4.3.3, we infer that

$$\|y_h\|_Q \lesssim |y_h|_{s_h} + \|\boldsymbol{x}_h^{\mathrm{f}}\|_{\boldsymbol{V}} + \alpha_1^{\frac{1}{2}} \|\boldsymbol{x}_h^{\mathrm{s}}\|_{\mathrm{e}}. \tag{4.56}$$

We hence conclude by inserting (4.55) and (4.56) into (4.54) and using the arbitrariness of $\big((\boldsymbol{z}_h^{\mathrm{f}}, \boldsymbol{z}_h^{\mathrm{s}}), r_h\big) \in \boldsymbol{W}_h \times Q_h$. □

Finally, the error estimate (4.31) follows from Lemma 4.3.5, by taking $\boldsymbol{z}_h^{\mathrm{f}}$ and $\boldsymbol{z}_h^{\mathrm{s}}$ as the Lagrange interpolants of $\boldsymbol{u}$ and $\dot{\boldsymbol{d}}$, respectively, and $r_h = 0$. Note that, since $(\boldsymbol{u}, \dot{\boldsymbol{d}}) \in \boldsymbol{W}$, we do have $(\boldsymbol{z}_h^{\mathrm{f}}, \boldsymbol{z}_h^{\mathrm{f}}) \in \boldsymbol{W}_h$.

4.3.6 Proof of Theorem 4.3.1

Basically, the proof follows the same steps as in the case of a thin-walled structure (Section 2.6.2 of Chapter 2), but with the additional technicalities related to:

- the lumped-mass approximation in the solid;
- the new velocity projection-operator;
- the distributed nature of the solid velocity (i.e. we cannot control the solid velocity terms within the fluid via a trace inequality).

From (4.1) and (4.12) we get the following modified Galerkin orthogonality

$$\begin{aligned}
&\rho^{\mathrm{f}}\big(\partial_\tau(\boldsymbol{u}(t_n) - \boldsymbol{u}_h^n), \boldsymbol{v}_h^{\mathrm{f}}\big)_{\Omega^{\mathrm{f}}} + a(\boldsymbol{u}(t_n) - \boldsymbol{u}_h^n, \boldsymbol{v}_h^{\mathrm{f}}) + b(p(t_n) - p_h^n, \boldsymbol{v}_h^{\mathrm{f}}) - b(q_h, \boldsymbol{u}(t_n) - \boldsymbol{u}_h^n) \\
&+ \rho^{\mathrm{s}}\big(\partial_\tau\dot{\boldsymbol{d}}(t_n), \boldsymbol{v}_h^{\mathrm{s}}\big)_{\Omega^{\mathrm{s}}} - \rho^{\mathrm{s}}\big(\partial_\tau\dot{\boldsymbol{d}}_h^n, \boldsymbol{v}_h^{\mathrm{s}}\big)_* + a^{\mathrm{e}}(\boldsymbol{d}(t_n) - \boldsymbol{d}_h^n, \boldsymbol{v}_h^{\mathrm{s}}) + a^{\mathrm{v}}(\dot{\boldsymbol{d}}(t_n), \boldsymbol{v}_h^{\mathrm{s}}) - a_*^{\mathrm{v}}(\dot{\boldsymbol{d}}_h^n, \boldsymbol{v}_h^{\mathrm{s}}) \\
&\qquad = -\rho^{\mathrm{f}}\big((\partial_t - \partial_\tau)\boldsymbol{u}(t_n), \boldsymbol{v}_h^{\mathrm{f}}\big)_{\Omega^{\mathrm{f}}} - \rho^{\mathrm{s}}\big((\partial_t - \partial_\tau)\dot{\boldsymbol{d}}(t_n), \boldsymbol{v}_h^{\mathrm{s}}\big)_{\Omega^{\mathrm{s}}} + s_h(p_h^n, q_h) \qquad (4.57)
\end{aligned}$$

for all $\big((\boldsymbol{v}_h^{\mathrm{f}}, \boldsymbol{v}_h^{\mathrm{s}}), q_h\big) \in \boldsymbol{W}_h \times Q_h$ and $n > r$. In addition, using $(4.32)_2$, we have

$$\begin{aligned}
\big(\partial_\tau\dot{\boldsymbol{d}}(t_n), \boldsymbol{v}_h^{\mathrm{s}}\big)_{\Omega^{\mathrm{s}}} - \big(\partial_\tau\dot{\boldsymbol{d}}_h^n, \boldsymbol{v}_h^{\mathrm{s}}\big)_* =& \big(\partial_\tau\dot{\boldsymbol{\xi}}_h^n, \boldsymbol{v}_h^{\mathrm{s}}\big)_* + \big(\partial_\tau\dot{\boldsymbol{\xi}}_\pi^n, \boldsymbol{v}_h^{\mathrm{s}}\big)_{\Omega^{\mathrm{s}}} \\
&+ \delta_h\big(\partial_\tau\boldsymbol{P}_h^{\mathrm{s}}(\boldsymbol{u}(t_n), \dot{\boldsymbol{d}}(t_n)), \boldsymbol{v}_h^{\mathrm{s}}\big), \\
a^{\mathrm{v}}(\dot{\boldsymbol{d}}(t_n), \boldsymbol{v}_h^{\mathrm{s}}) - a_*^{\mathrm{v}}(\dot{\boldsymbol{d}}_h^n, \boldsymbol{v}_h^{\mathrm{s}}) =& a_*^{\mathrm{v}}(\dot{\boldsymbol{\xi}}_h^n, \boldsymbol{v}_h^{\mathrm{s}}) + a^{\mathrm{v}}\big(\dot{\boldsymbol{\xi}}_\pi^n, \boldsymbol{v}_h^{\mathrm{s}}\big) \\
&+ \alpha_0\rho^{\mathrm{s}}\delta_h\big(\boldsymbol{P}_h^{\mathrm{s}}(\boldsymbol{u}(t_n), \dot{\boldsymbol{d}}(t_n)), \boldsymbol{v}_h^{\mathrm{s}}\big)
\end{aligned}$$

for all $\boldsymbol{v}_h^{\mathrm{s}} \in \boldsymbol{V}_h^{\mathrm{s}}$. Hence, by inserting this expressions into (4.57) and using the remaining error decompositions (4.27), $(4.32)_1$ and (4.33), we infer that

$$\begin{aligned}
&\rho^{\mathrm{f}}\big(\partial_\tau\boldsymbol{\theta}_h^n, \boldsymbol{v}_h^{\mathrm{f}}\big)_{\Omega^{\mathrm{f}}} + a(\boldsymbol{\theta}_h^n, \boldsymbol{v}_h^{\mathrm{f}}) + b(y_h^n, \boldsymbol{v}_h^{\mathrm{f}}) - b(q_h, \boldsymbol{\theta}_h^n) + s_h(y_h^n, q_h) + \rho^{\mathrm{s}}\big(\partial_\tau\dot{\boldsymbol{\xi}}_h^n, \boldsymbol{v}_h^{\mathrm{s}}\big)_* \\
&\quad + a^{\mathrm{e}}(\boldsymbol{\xi}_h^n, \boldsymbol{v}_h^{\mathrm{s}}) + a_*^{\mathrm{v}}(\dot{\boldsymbol{\xi}}_h^n, \boldsymbol{v}_h^{\mathrm{s}}) = \underbrace{-\rho^{\mathrm{f}}\big((\partial_t - \partial_\tau)\boldsymbol{u}(t_n), \boldsymbol{v}_h^{\mathrm{f}}\big)_{\Omega^{\mathrm{f}}} - \rho^{\mathrm{f}}\big(\partial_\tau\boldsymbol{\theta}_\pi^n, \boldsymbol{v}_h^{\mathrm{f}}\big)_{\Omega^{\mathrm{f}}}}_{T_1(\boldsymbol{v}_h^{\mathrm{f}})} \\
&\quad \underbrace{-\rho^{\mathrm{s}}\big((\partial_t - \partial_\tau)\dot{\boldsymbol{d}}(t_n), \boldsymbol{v}_h^{\mathrm{s}}\big)_{\Omega^{\mathrm{s}}} - \rho^{\mathrm{s}}\big(\partial_\tau\dot{\boldsymbol{\xi}}_\pi^n, \boldsymbol{v}_h^{\mathrm{s}}\big)_{\Omega^{\mathrm{s}}}}_{T_2(\boldsymbol{v}_h^{\mathrm{s}})} \qquad (4.58) \\
&\quad \underbrace{-a\big(\boldsymbol{\theta}_\pi^n, \boldsymbol{v}_h^{\mathrm{f}}\big) - a^{\mathrm{v}}\big(\dot{\boldsymbol{\xi}}_\pi^n, \boldsymbol{v}_h^{\mathrm{s}}\big) - b\big(y_\pi^n, \boldsymbol{v}_h^{\mathrm{f}}\big) + b\big(q_h, \boldsymbol{\theta}_\pi^n\big) + s_h\big(\Pi_h p(t_n), q_h\big)}_{T_3(\boldsymbol{v}_h^{\mathrm{f}}, q_h, \boldsymbol{v}_h^{\mathrm{s}})} \\
&\quad + \underbrace{\rho^{\mathrm{s}}\delta_h\big((\partial_\tau + \alpha_0)\boldsymbol{P}_h^{\mathrm{s}}(\boldsymbol{u}(t_n), \dot{\boldsymbol{d}}(t_n)), \boldsymbol{v}_h^{\mathrm{s}}\big)}_{T_4(\boldsymbol{v}_h^{\mathrm{s}})} + \underbrace{a^{\mathrm{e}}\left(\boldsymbol{\xi}_\pi^n, \boldsymbol{v}_h^{\mathrm{s}}\right)}_{=0}
\end{aligned}$$

for all $\big((\boldsymbol{v}_h^{\mathrm{f}}, \boldsymbol{v}_h^{\mathrm{s}}), q_h\big) \in \boldsymbol{W}_h \times Q_h$ and $n > r$.

At this point, it is worth noting that the quantities $\boldsymbol{\theta}_h^n$ and $\dot{\boldsymbol{\xi}}_h^n$ do not match at the interface and, therefore, the couple $(\boldsymbol{\theta}_h^n, \dot{\boldsymbol{\xi}}_h^n)$ cannot be used as valid test functions in (4.58). The next lemma is devoted to the construction of an appropriate solid test function that correctly matches $\boldsymbol{\theta}_h^n$ on Σ.

Lemma 4.3.6. *Let $\dot{\boldsymbol{\xi}}_h^{n-\frac{1}{2}} \in \boldsymbol{V}_h^{\mathrm{s}}$ be defined as*

$$\begin{aligned}\dot{\boldsymbol{\xi}}_h^{n-\frac{1}{2}} \overset{\text{def}}{=} \dot{\boldsymbol{\xi}}_h^n &+ \frac{\tau}{\rho^{\mathrm{s}}}\left[\boldsymbol{L}_h^{\mathrm{e}}\big(\boldsymbol{\xi}_h^n - \boldsymbol{\xi}_h^\star\big) + \boldsymbol{L}_h^{\mathrm{v}}\big(\dot{\boldsymbol{\xi}}_h^n - \dot{\boldsymbol{\xi}}_h^\star\big)\right] \\ &- \frac{\tau}{\rho^{\mathrm{s}}}\left[\boldsymbol{L}_h^{\mathrm{e}}\big(\boldsymbol{d}(t_n) - \boldsymbol{d}^\star\big) + \boldsymbol{L}_h^{\mathrm{v}}\boldsymbol{P}_h^{\mathrm{s}}(\boldsymbol{u}(t_n) - \boldsymbol{u}^\star, \dot{\boldsymbol{d}}(t_n) - \dot{\boldsymbol{d}}^\star)\right].\end{aligned} \tag{4.59}$$

Then, we have

$$\boldsymbol{\theta}_h^n = \dot{\boldsymbol{\xi}}_h^{n-\frac{1}{2}} \quad \text{on} \quad \Sigma.$$

Proof. The equality on the interface follows from (4.11), (4.27), (4.29) and (4.32). □

Even though we have $\dot{\boldsymbol{d}}_h^n = \partial_\tau \boldsymbol{d}_h^n$, a similar relation does not holds with the discrete errors $\dot{\boldsymbol{\xi}}_h^n$ and $\boldsymbol{\xi}_h^n$. This is due to the fact that different projection operators are considered for the solid displacement and velocity. More precisely, we have the following result.

Lemma 4.3.7. *Let $\boldsymbol{z}_h^n \in \boldsymbol{V}_h^{\mathrm{s}}$ be defined as $\boldsymbol{z}_h^n \overset{\text{def}}{=} \dot{\boldsymbol{\xi}}_h^n - \partial_\tau \boldsymbol{\xi}_h^n$. Then, we have*

$$\boldsymbol{z}_h^n = \boldsymbol{P}_h^{\mathrm{s}}(\boldsymbol{u}(t_n), \dot{\boldsymbol{d}}(t_n)) - \boldsymbol{\pi}_h^{\mathrm{e}} \partial_\tau \boldsymbol{d}(t_n)$$

and

$$\|\boldsymbol{z}_h^n\|_{\mathrm{e}} \lesssim h\left((\beta_{\mathrm{e}})^{\frac{1}{2}} + \left(\frac{\mu}{\alpha_1}\right)^{\frac{1}{2}}\right)\|\dot{\boldsymbol{d}}(t_n)\|_{2,\Omega^{\mathrm{s}}} + \tau^{\frac{1}{2}}(\beta_{\mathrm{e}})^{\frac{1}{2}}\|\partial_t \dot{\boldsymbol{d}}\|_{L^2(t_{n-1},t_n,H^1(\Omega^{\mathrm{s}}))}. \tag{4.60}$$

Proof. We first note that

$$\|\boldsymbol{z}_h^n\|_{\mathrm{e}} \le \|\boldsymbol{P}_h^{\mathrm{s}}(\boldsymbol{u}(t_n), \dot{\boldsymbol{d}}(t_n)) - \dot{\boldsymbol{d}}(t_n)\|_{\mathrm{e}} + \|\dot{\boldsymbol{d}}(t_n) - \boldsymbol{\pi}_h^{\mathrm{e}}\dot{\boldsymbol{d}}(t_n)\|_{\mathrm{e}} + \|\boldsymbol{\pi}_h^{\mathrm{e}}(\partial_t - \partial_\tau)\boldsymbol{d}(t_n)\|_{\mathrm{e}}.$$

Then, we estimate each term separately using (4.26), (4.31) and a Taylor expansion. □

We resume the proof of Theorem 4.3.1. Owing to Lemma 4.3.6, we can safely test (4.58) with $\boldsymbol{v}_h^{\mathrm{f}} = \tau\boldsymbol{\theta}_h^n$, $q_h = \tau y_h^n$ and $\boldsymbol{v}_h^{\mathrm{s}} = \tau\dot{\boldsymbol{\xi}}^{n-\frac{1}{2}}$, to get

$$\begin{aligned}&\frac{\rho^{\mathrm{f}}}{2}\left(\|\boldsymbol{\theta}_h^n\|_{0,\Omega^{\mathrm{f}}}^2 - \|\boldsymbol{\theta}_h^{n-1}\|_{0,\Omega^{\mathrm{f}}}^2 + \tau\|\partial_\tau\boldsymbol{\theta}_h^n\|_{0,\Omega^{\mathrm{f}}}^2\right) + 2\mu\tau\|\boldsymbol{\epsilon}(\boldsymbol{\theta}_h^n)\|_{0,\Omega^{\mathrm{f}}}^2 + \tau|y_h^n|_{\mathrm{s},h}^2 \\ &+ \frac{\rho^{\mathrm{s}}}{2}\left(\|\dot{\boldsymbol{\xi}}_h^n\|_*^2 - \|\dot{\boldsymbol{\xi}}_h^{n-1}\|_*^2 + \tau\|\partial_\tau\dot{\boldsymbol{\xi}}_h^n\|_*^2\right) + \frac{1}{2}\left(\|\boldsymbol{\xi}_h^n\|_{\mathrm{e}}^2 - \|\boldsymbol{\xi}_h^{n-1}\|_{\mathrm{e}}^2 + \tau\|\partial_\tau\boldsymbol{\xi}_h^n\|_{\mathrm{e}}^2\right) + \tau\|\dot{\boldsymbol{\xi}}_h^n\|_{\mathrm{v},*}^2 \\ &+ T_{5,1} + T_{5,2} = T_1(\boldsymbol{v}_h^{\mathrm{f}}) + T_2(\boldsymbol{v}_h^{\mathrm{s}}) + T_3(\boldsymbol{v}_h^{\mathrm{f}}, q_h, \boldsymbol{v}_h^{\mathrm{s}}) + T_4(\boldsymbol{v}_h^{\mathrm{s}}) + T_{6,1} + T_{6,2} - \underbrace{\tau a^{\mathrm{e}}(\boldsymbol{\xi}_h^n, \boldsymbol{z}_h^n)}_{T_7}.\end{aligned} \tag{4.61}$$

The terms $T_{5,1}, T_{5,2}$ and $T_{6,1}, T_{6,2}$ come from the last two contributions of $\dot{\boldsymbol{\xi}}_h^{n-\frac{1}{2}}$ in (4.59). More precisely, we have

$$
\begin{aligned}
T_{5,1} &\stackrel{\text{def}}{=} \tau \left(\dot{\boldsymbol{\xi}}_h^n - \dot{\boldsymbol{\xi}}_h^{n-1}, \boldsymbol{L}_h^{\mathrm{e}}\big(\boldsymbol{\xi}_h^n - \boldsymbol{\xi}_h^\star\big) + \boldsymbol{L}_h^{\mathrm{v}}\big(\dot{\boldsymbol{\xi}}_h^n - \dot{\boldsymbol{\xi}}_h^\star\big) \right)_*, \\
T_{5,2} &\stackrel{\text{def}}{=} \frac{\tau^2}{\rho^{\mathrm{s}}} \left(\boldsymbol{L}_h^{\mathrm{e}} \boldsymbol{\xi}_h^n + \boldsymbol{L}_h^{\mathrm{v}} \dot{\boldsymbol{\xi}}_h^n, \boldsymbol{L}_h^{\mathrm{e}}\big(\boldsymbol{\xi}_h^n - \boldsymbol{\xi}_h^\star\big) + \boldsymbol{L}_h^{\mathrm{v}}\big(\dot{\boldsymbol{\xi}}_h^n - \dot{\boldsymbol{\xi}}_h^\star\big) \right)_*, \\
T_{6,1} &\stackrel{\text{def}}{=} \tau \left(\dot{\boldsymbol{\xi}}_h^n - \dot{\boldsymbol{\xi}}_h^{n-1}, \boldsymbol{L}_h^{\mathrm{e}}\left(\boldsymbol{d}(t_n) - \boldsymbol{d}^\star\right) + \boldsymbol{L}_h^{\mathrm{v}} \boldsymbol{P}_h^{\mathrm{s}}(\boldsymbol{u}(t_n) - \boldsymbol{u}^\star, \dot{\boldsymbol{d}}(t_n) - \dot{\boldsymbol{d}}^\star) \right)_*, \\
T_{6,2} &\stackrel{\text{def}}{=} \frac{\tau^2}{\rho^{\mathrm{s}}} \left(\boldsymbol{L}_h^{\mathrm{e}} \boldsymbol{\xi}_h^n + \boldsymbol{L}_h^{\mathrm{v}} \dot{\boldsymbol{\xi}}_h^n, \boldsymbol{L}_h^{\mathrm{e}}\left(\boldsymbol{d}(t_n) - \boldsymbol{d}^\star\right) + \boldsymbol{L}_h^{\mathrm{v}} \boldsymbol{P}_h^{\mathrm{s}}(\boldsymbol{u}(t_n) - \boldsymbol{u}^\star, \dot{\boldsymbol{d}}(t_n) - \dot{\boldsymbol{d}}^\star) \right)_*.
\end{aligned}
\tag{4.62}
$$

The estimation of T_1, T_2, T_3, T_4 and T_7 in (4.61) does not depend on the extrapolation order r, whereas the other terms will be treated separately for each choice of r. We start by estimating T_1, T_2, T_3, T_4 and T_7. The treatment of the terms T_1, T_2 and T_3 is similar to the proof of Theorem 2.6.1 in Chapter 2, except that the fluid-solid velocity projector is different, yielding modified estimates. Besides, the term T_4 coming from the mass lumping approximation requires a specific case.

We use the Poincaré inequality with constant C_{P} and a Taylor expansion for the estimation of the standard term T_1:

$$
\begin{aligned}
|T_1(\tau \boldsymbol{\theta}_h^n)| &\leq \rho^{\mathrm{f}} \tau \left(\|(\partial_t - \partial_\tau)\, \boldsymbol{u}^n\|_{0,\Omega^{\mathrm{f}}} + \|\partial_\tau \boldsymbol{\theta}_\pi^n\|_{0,\Omega^{\mathrm{f}}} \right) \|\boldsymbol{\theta}_h^n\|_{0,\Omega^{\mathrm{f}}} \\
&\leq \rho^{\mathrm{f}} \tau \left(\tau^{\frac{1}{2}} \|\partial_{tt} \boldsymbol{u}\|_{L^2(t_{n-1},t_n;L^2(\Omega^{\mathrm{f}}))} + \tau^{-\frac{1}{2}} \|\partial_t \boldsymbol{\theta}_\pi\|_{L^2(t_{n-1},t_n;L^2(\Omega^{\mathrm{f}}))} \right) \|\boldsymbol{\theta}_h^n\|_{0,\Omega^{\mathrm{f}}} \\
&\leq \frac{(\tau \rho^{\mathrm{f}} C_{\mathrm{P}})^2}{4\epsilon_1 \mu} \|\partial_{tt} \boldsymbol{u}\|^2_{L^2(t_{n-1},t_n;L^2(\Omega^{\mathrm{f}}))} + \frac{(\rho^{\mathrm{f}} C_{\mathrm{P}})^2}{4\epsilon_1 \mu} \|\partial_t \boldsymbol{\theta}_\pi\|^2_{L^2(t_{n-1},t_n;L^2(\Omega^{\mathrm{f}}))} \\
&\quad + \epsilon_1 \mu \tau \|\boldsymbol{\theta}_h^n\|^2_{1,\Omega^{\mathrm{f}}}.
\end{aligned}
\tag{4.63}
$$

In this estimate, the last term will be absorbed in the left-hand side of (4.61), for $\epsilon_1 > 0$ small enough. The second term involving $\|\partial_t \boldsymbol{\theta}_\pi\|^2_{L^2(t_{n-1},t_n;L^2(\Omega^{\mathrm{f}}))}$ is bounded by combining the Poincaré inequality with estimate (4.31), which yields

$$
\begin{aligned}
\|\partial_t \boldsymbol{\theta}_\pi\|^2_{L^2(t_{n-1},t_n;L^2(\Omega^{\mathrm{f}}))} &\leq C_{\mathrm{P}}^2 \|\partial_t \boldsymbol{\theta}_\pi\|^2_{L^2(t_{n-1},t_n;H^1(\Omega^{\mathrm{f}}))} \\
&\lesssim h^2 C_{\mathrm{P}}^2 \left(\|\partial_t \boldsymbol{u}\|^2_{L^2(t_{n-1},t_n;H^2(\Omega^{\mathrm{f}}))} + \frac{\alpha_1 \beta_{\mathrm{e}}}{\mu} \|\partial_t \dot{\boldsymbol{d}}\|^2_{L^2(t_{n-1},t_n;H^2(\Omega^{\mathrm{f}}))} \right).
\end{aligned}
$$

For the solid term T_2, we have

$$
\begin{aligned}
|T_2(\tau\dot{\boldsymbol{\xi}}^{n-\frac{1}{2}})| &\le \rho^{\mathrm{s}}\tau\left(\|(\partial_t-\partial_\tau)\,\dot{\boldsymbol{d}}(t_n)\|_{0,\Omega^{\mathrm{s}}}+\|\partial_\tau\dot{\boldsymbol{\xi}}_\pi^n\|_{0,\Omega^{\mathrm{s}}}\right)\|\dot{\boldsymbol{\xi}}^{n-\frac{1}{2}}\|_{0,\Omega^{\mathrm{s}}}\\
&\le \rho^{\mathrm{s}}\tau\left(\tau^{\frac{1}{2}}\|\partial_{tt}\dot{\boldsymbol{d}}\|_{L^2(t_{n-1},t_n;L^2(\Omega^{\mathrm{s}}))}+\tau^{-\frac{1}{2}}\|\partial_t\dot{\boldsymbol{\xi}}_\pi\|_{L^2(t_{n-1},t_n;L^2(\Omega^{\mathrm{s}}))}\right)\|\dot{\boldsymbol{\xi}}^{n-\frac{1}{2}}\|_{0,\Omega^{\mathrm{s}}}\\
&\le \frac{\rho^{\mathrm{s}}T\tau^2}{\epsilon_2}\|\partial_{tt}\dot{\boldsymbol{d}}\|^2_{L^2(t_{n-1},t_n;L^2(\Omega^{\mathrm{s}}))}+\frac{\rho^{\mathrm{s}}T}{\epsilon_2}\|\partial_t\dot{\boldsymbol{\xi}}_\pi\|^2_{L^2(t_{n-1},t_n;L^2(\Omega^{\mathrm{s}}))}\\
&\quad+\epsilon_2\frac{\rho^{\mathrm{s}}\tau}{T}\|\dot{\boldsymbol{\xi}}^{n-\frac{1}{2}}\|^2_{0,\Omega^{\mathrm{s}}}.
\end{aligned}
\tag{4.64}
$$

The last term will be controlled below, for some $\epsilon_2>0$ small enough, with the additional dissipation provided by the stability analysis. This will be done later in the proof. The second term, involving $\|\partial_t\dot{\boldsymbol{\xi}}_\pi\|^2_{L^2(t_{n-1},t_n;L^2(\Omega^{\mathrm{s}}))}$ can be estimated thanks to (4.31) and to the H^1-coercivity of the elastic bilinear form a^{e} stated in (4.24), namely,

$$
\begin{aligned}
\|\partial_t\dot{\boldsymbol{\xi}}_\pi\|^2_{L^2(t_{n-1},t_n;L^2(\Omega^{\mathrm{s}}))} &\le C_{\mathrm{P}}^2\|\partial_t\dot{\boldsymbol{\xi}}_\pi\|^2_{L^2(t_{n-1},t_n;H^1(\Omega^{\mathrm{f}}))}\\
&\lesssim \frac{h^2C_{\mathrm{P}}^2}{\alpha_{\mathrm{e}}}\left(\frac{\mu}{\alpha_1}\|\partial_t\boldsymbol{u}\|^2_{L^2(t_{n-1},t_n;H^2(\Omega^{\mathrm{f}}))}+\beta_{\mathrm{e}}\|\partial_t\dot{\boldsymbol{d}}\|^2_{L^2(t_{n-1},t_n;H^2(\Omega^{\mathrm{f}}))}.\right)
\end{aligned}
$$

As regards T_3, using the particular form of the fluid velocity projector (4.28) and the fact that $\operatorname{div}\boldsymbol{u}(t_n)=0$ in Ω^{f}, we have

$$
\begin{aligned}
|\tau T_3(\boldsymbol{\theta}_h^n,y_h^n,\dot{\boldsymbol{\xi}}^{n-\frac{1}{2}})| \le& |b\big(R_h(\boldsymbol{u}(t_n),\dot{\boldsymbol{d}}(t_n)),\tau\boldsymbol{\theta}_h^n\big)|+|b\big(y_\pi^n,\tau\boldsymbol{\theta}_h^n\big)|\\
&+|s_h(\Pi_hp(t_n),\tau y_h^n)|+|s_h(R_h(\boldsymbol{u}(t_n),\dot{\boldsymbol{d}}(t_n)),\tau y_h^n)|\\
&+\alpha_0\rho^{\mathrm{s}}\left|\left(\dot{\boldsymbol{\xi}}_\pi^n,\tau\dot{\boldsymbol{\xi}}_h^{n-\frac{1}{2}}\right)_\star\right|\\
\le&\tau\|\boldsymbol{\theta}_h^n\|_{1,\Omega^{\mathrm{f}}}\left(\|R_h(\boldsymbol{u}(t_n),\dot{\boldsymbol{d}}(t_n))\|_{0,\Omega^{\mathrm{f}}}+\|y_\pi^n\|_{0,\Omega^{\mathrm{f}}}\right)\\
&+\tau|y_h^n|_{s_h}\left(|\Pi_hp(t_n)|_{s_h}+|R_h(\boldsymbol{u}(t_n),\dot{\boldsymbol{d}}(t_n))|_{s_h}\right)\\
&+\alpha_0\rho^{\mathrm{s}}\tau\|\dot{\boldsymbol{\xi}}_\pi^n\|_*\|\dot{\boldsymbol{\xi}}_h^{n-\frac{1}{2}}\|_*\\
\le&\frac{(\epsilon_3+\epsilon_4)\mu\tau}{2}\|\boldsymbol{\theta}_h^n\|^2_{1,\Omega^{\mathrm{f}}}+\frac{\tau}{2}|y_h^n|^2_{s_h}\\
&+\frac{\tau}{2\epsilon_3}\|R_h(\boldsymbol{u}(t_n),\dot{\boldsymbol{d}}(t_n))\|^2_Q+\frac{\tau}{2\epsilon_4}\|y_\pi^n\|^2_Q\\
&+\frac{\tau}{2}\left(|\Pi_hp(t_n)|^2_{s_h}+|R_h(\boldsymbol{u}(t_n),\dot{\boldsymbol{d}}(t_n))|^2_{s_h}\right)\\
&+\epsilon_5\alpha_0\rho^{\mathrm{s}}\tau\|\dot{\boldsymbol{\xi}}_h^{n-\frac{1}{2}}\|^2_*+\frac{\alpha_0\rho^{\mathrm{s}}\tau}{4\epsilon_5}\|\dot{\boldsymbol{\xi}}_\pi^n\|^2_*.
\end{aligned}
\tag{4.65}
$$

If ϵ_3 and ϵ_4 are small enough, the first part of the right hand side can be absorbed by positive terms of the left hand side of (4.61). As regards the last part and thanks to

estimate (4.31) and (4.34), we have

$$\frac{\tau}{2\epsilon_3}\|R_h(\boldsymbol{u}(t_n),\dot{\boldsymbol{d}}(t_n))\|_Q^2+\frac{\tau}{2}|R_h(\boldsymbol{u}(t_n),\dot{\boldsymbol{d}}(t_n))|_{s_h}^2 \lesssim \tau h^2\left(\mu\|\boldsymbol{u}(t_n)\|_{2,\Omega^{\mathrm{f}}}^2+\alpha_1\beta_{\mathrm{e}}\|\dot{\boldsymbol{d}}(t_n)\|_{2,\Omega^{\mathrm{s}}}^2\right)$$

$$\frac{\tau}{2\epsilon_4}\|y_\pi^n\|_Q^2+\frac{\tau}{2}|\Pi_h p(t_n)|_{s_h}^2 \lesssim \frac{\tau h^2}{\mu}\left(h^2\|p(t_n)\|_{2,\Omega^{\mathrm{f}}}^2+\|p(t_n)\|_{1,\Omega^{\mathrm{f}}}^2\right)$$

Then, for the term involving $\|\dot{\boldsymbol{\xi}}_\pi^n\|_*^2$, we need Poincaré inequality, (4.24) and estimate (4.31) to write

$$\frac{\alpha_0\rho^{\mathrm{s}}\tau}{4\epsilon_5}\|\dot{\boldsymbol{\xi}}_\pi^n\|_*^2 \lesssim \frac{\alpha_0\rho^{\mathrm{s}}C_{\mathrm{P}}^2\tau}{4\epsilon_5}\|\dot{\boldsymbol{\xi}}_\pi^n\|_{1,\Omega^{\mathrm{s}}}^2 \lesssim \tau h^2\frac{\alpha_0\rho^{\mathrm{s}}C_{\mathrm{P}}^2}{4\epsilon_5\alpha_{\mathrm{e}}}\left(\frac{\mu}{\alpha_1}\|\boldsymbol{u}(t_n)\|_{2,\Omega^{\mathrm{f}}}^2+\beta_{\mathrm{e}}\|\dot{\boldsymbol{d}}(t_n)\|_{2,\Omega^{\mathrm{s}}}^2\right)$$

At last, the term $\epsilon_5\alpha_0\rho^{\mathrm{s}}\tau\|\dot{\boldsymbol{\xi}}_h^{n-\frac{1}{2}}\|_*^2$ remains to be controlled. This will be done below in the proof as for the last term of (4.64) using the numerical dissipation of the scheme.

For the mass-lumping term T_4, using Poincaré inequality and the estimates (4.23) and (4.30), we have:

$$\begin{aligned}|T_4(\tau\dot{\boldsymbol{\xi}}^{n-\frac{1}{2}})| &\lesssim h\tau\rho^{\mathrm{s}}\|(\partial_\tau+\alpha_0)\boldsymbol{P}_h^{\mathrm{s}}(\boldsymbol{u}(t_n),\dot{\boldsymbol{d}}(t_n))\|_{1,\Omega^{\mathrm{s}}}\|\dot{\boldsymbol{\xi}}^{n-\frac{1}{2}}\|_{0,\Omega^{\mathrm{s}}}\\ &\lesssim \frac{\rho^{\mathrm{s}}T\tau h^2}{\epsilon_6}\|(\partial_\tau+\alpha_0)\boldsymbol{P}_h^{\mathrm{s}}(\boldsymbol{u}(t_n),\dot{\boldsymbol{d}}(t_n))\|_{1,\Omega^{\mathrm{s}}}^2+\frac{\epsilon_6\rho^{\mathrm{s}}\tau}{T}\|\dot{\boldsymbol{\xi}}^{n-\frac{1}{2}}\|_{0,\Omega^{\mathrm{s}}}^2\end{aligned} \tag{4.66}$$

Notice that this term was not present in Chapter 2 when dealing with thin-walled structures. As for the previous terms T_2 and T_3, the last part involving $\dot{\boldsymbol{\xi}}^{n-\frac{1}{2}}$ remains to be controlled for some $\epsilon_6>0$ with other terms coming from the stability analysis. The first term is controlled with the estimates (4.24) and (4.30).

$$\|\boldsymbol{P}_h^{\mathrm{s}}(\boldsymbol{u}(t_n),\dot{\boldsymbol{d}}(t_n))\|_{1,\Omega^{\mathrm{s}}}^2 \le \frac{1}{\alpha_{\mathrm{e}}}\left(\frac{\mu}{\alpha_1}\|\boldsymbol{u}(t_n)\|_{1,\Omega^{\mathrm{f}}}^2+\beta_{\mathrm{e}}\|\dot{\boldsymbol{d}}(t_n)\|_{1,\Omega^{\mathrm{s}}}^2\right)$$

For T_7 and thanks to the continuity of the form a^{e}, we have:

$$|T_7| \le \tau\|\boldsymbol{\xi}_h^n\|_{\mathrm{e}}\|\boldsymbol{z}_h^n\|_{\mathrm{e}} \le \frac{\tau}{2T}\|\boldsymbol{\xi}_h^n\|_{\mathrm{e}}^2+\frac{T\tau}{2}\|\boldsymbol{z}_h^n\|_{\mathrm{e}}^2 \tag{4.67}$$

In this last estimate, the first term $\|\boldsymbol{\xi}_h^n\|_{\mathrm{e}}^2$ will remain on the left hand side and will be treated thanks to a discrete Gronwall lemma. The last term is controlled thanks to (4.60).

We keep in mind that we need a control for the term $\rho^{\mathrm{s}}\epsilon\tau(\alpha_0+1/T)\|\dot{\boldsymbol{\xi}}^{n-\frac{1}{2}}\|_{0,\Omega^{\mathrm{s}}}^2$ for *epsilon* >0 small enough. Notice that, owing to (4.59), this term can be split into three parts as:

$$\begin{aligned}\rho^{\mathrm{s}}\epsilon\tau\left(\alpha_0+\frac{1}{T}\right)\|\dot{\boldsymbol{\xi}}^{n-\frac{1}{2}}\|_{0,\Omega^{\mathrm{s}}}^2 \le{}& \rho^{\mathrm{s}}\epsilon\tau\left(\alpha_0+\frac{1}{T}\right)\|\dot{\boldsymbol{\xi}}_h^n\|_{0,\Omega^{\mathrm{s}}}^2\\ &+\frac{\epsilon\tau^3}{\rho^{\mathrm{s}}}\left(\alpha_0+\frac{1}{T}\right)\|\boldsymbol{L}_h^{\mathrm{e}}(\boldsymbol{\xi}_h^n-\boldsymbol{\xi}_h^\star)+\boldsymbol{L}_h^{\mathrm{v}}\left(\dot{\boldsymbol{\xi}}_h^n-\dot{\boldsymbol{\xi}}_h^\star\right)\|_{0,\Omega^{\mathrm{s}}}^2\\ &+\frac{\epsilon\tau^3}{\rho^{\mathrm{s}}}\left(\alpha_0+\frac{1}{T}\right)\|\boldsymbol{L}_h^{\mathrm{e}}(\boldsymbol{d}(t_n)-\boldsymbol{d}^\star)+\boldsymbol{L}_h^{\mathrm{v}}\boldsymbol{P}_h^{\mathrm{s}}(\boldsymbol{u}(t_n)-\boldsymbol{u}^\star,\dot{\boldsymbol{d}}(t_n)-\dot{\boldsymbol{d}}^\star)\|_{0,\Omega^{\mathrm{s}}}^2\end{aligned}$$

The first part will be left in the left-hand side and will be treated with the discrete Gronwall lemma. The last part will be left in the right hand side and its control depends on the value of r and also on regularity assumptions for the exact solution. Therefore, it only remains to control, for each choice of r, the second part of this term, that is

$$T_8 \overset{\text{def}}{=} \frac{\epsilon\tau^3}{\rho^{\mathrm{s}}}\left(\alpha_0+\frac{1}{T}\right)\|\boldsymbol{L}_h^{\mathrm{e}}\left(\boldsymbol{\xi}_h^n-\boldsymbol{\xi}_h^\star\right)+\boldsymbol{L}_h^{\mathrm{v}}\left(\dot{\boldsymbol{\xi}}_h^n-\dot{\boldsymbol{\xi}}_h^\star\right)\|_{0,\Omega^{\mathrm{s}}}^2.$$

This will be treated with the numerical dissipation provided by the splitting. We now estimate the other terms T_5 and T_6 for each choice of the extrapolation order r. For the sake of clarity, The estimates of $T_{5,1}+T_{5,2}$ for each choice of r will be simply recalled from the stability analysis without proof. Details are available in Section 3.4.2.

For $\boldsymbol{r=0}$, the stability analysis gives:

$$T_{5,1}+T_{5,2}\geq-\frac{\rho^{\mathrm{s}}}{3}\|\dot{\boldsymbol{\xi}}_h^n-\dot{\boldsymbol{\xi}}_h^{n-1}\|_*^2+\frac{\tau^2}{4\rho^{\mathrm{s}}}\|\boldsymbol{L}_h^{\mathrm{e}}\boldsymbol{\xi}_h^n+\boldsymbol{L}_h^{\mathrm{v}}\dot{\boldsymbol{\xi}}_h^n\|_*^2. \tag{4.68}$$

In the last estimate, the first part is absorbed by the numerical diffusion of the solid inertia and the second yields a positive term. Since $(\alpha_0+1/T)\tau<1$, (4.68) also provides a control of the term T_8.

The term T_5 is then treated as follows:

$$\begin{aligned}T_{6,1}+T_{6,2}\leq{}&\frac{\rho^{\mathrm{s}}}{6}\|\dot{\boldsymbol{\xi}}_h^n-\dot{\boldsymbol{\xi}}_h^{n-1}\|_*^2+\frac{\tau^2}{8\rho^{\mathrm{s}}}\|\boldsymbol{L}_h^{\mathrm{e}}\boldsymbol{\xi}_h^n+\boldsymbol{L}_h^{\mathrm{v}}\dot{\boldsymbol{\xi}}_h^n\|_*^2\\&+\frac{7\tau^2}{2\rho^{\mathrm{s}}}\|\boldsymbol{L}_h^{\mathrm{e}}\boldsymbol{d}(t_n)+\boldsymbol{L}_h^{\mathrm{v}}\boldsymbol{P}_h^{\mathrm{s}}(\boldsymbol{u}(t_n),\dot{\boldsymbol{d}}(t_n))\|_*^2,\end{aligned} \tag{4.69}$$

and we have

$$\frac{7\tau^2}{2\rho^{\mathrm{s}}}\|\boldsymbol{L}_h^{\mathrm{e}}\boldsymbol{d}(t_n)+\boldsymbol{L}_h^{\mathrm{v}}\boldsymbol{P}_h^{\mathrm{s}}(\boldsymbol{u}(t_n),\dot{\boldsymbol{d}}(t_n))\|_*^2\lesssim\frac{\tau}{\rho^{\mathrm{s}}}\|\boldsymbol{L}_h^{\mathrm{e}}\boldsymbol{d}+\boldsymbol{L}_h^{\mathrm{v}}\boldsymbol{P}_h^{\mathrm{s}}(\boldsymbol{u},\dot{\boldsymbol{d}})\|_{L^2(t_{n-1},t_n;L^2(\Omega^{\mathrm{s}}))}^2.$$

Finally, estimate (4.37) follows by inserting (4.63)-(4.67) and (4.68)-(4.69) in (4.61), summing over n and applying the discrete Gronwall lemma.

For $\boldsymbol{r=1}$, the stability analysis gives:

$$\begin{aligned}T_{5,1}+T_{5,2}={}&\frac{\tau^2}{2}\left(\|\dot{\boldsymbol{\xi}}_h^n\|_{\mathrm{e}}^2-\|\dot{\boldsymbol{\xi}}_h^{n-1}\|_{\mathrm{e}}^2+\|\dot{\boldsymbol{\xi}}_h^n-\dot{\boldsymbol{\xi}}_h^{n-1}\|_{\mathrm{e}}^2\right)+\tau\|\dot{\boldsymbol{\xi}}_h^n-\dot{\boldsymbol{\xi}}_h^{n-1}\|_{\mathrm{v}}^2\\&+\frac{\tau^2}{2\rho^{\mathrm{s}}}\left(\|\boldsymbol{L}_h^{\mathrm{e}}\boldsymbol{\xi}_h^n+\boldsymbol{L}_h^{\mathrm{v}}\dot{\boldsymbol{\xi}}_h^n\|_*^2-\|\boldsymbol{L}_h^{\mathrm{e}}\boldsymbol{\xi}_h^{n-1}+\boldsymbol{L}_h^{\mathrm{v}}\dot{\boldsymbol{\xi}}_h^{n-1}\|_*^2\right)\\&+\frac{\tau^2}{2\rho^{\mathrm{s}}}\|\boldsymbol{L}_h^{\mathrm{e}}(\boldsymbol{\xi}_h^n-\boldsymbol{\xi}_h^{n-1})+\boldsymbol{L}_h^{\mathrm{v}}(\dot{\boldsymbol{\xi}}_h^n-\dot{\boldsymbol{\xi}}_h^{n-1})\|_*^2-\tau^2a^{\mathrm{e}}(\dot{\boldsymbol{\xi}}_h^n-\dot{\boldsymbol{\xi}}_h^{n-1},\boldsymbol{z}_h^n).\end{aligned} \tag{4.70}$$

In the last line, the numerical dissipation will be used to control the term T_8 under the hypothesis $(\alpha_0+1/T)\tau<1$, and the last term is controlled with (4.60) and

$$\tau^2|a^{\mathrm{e}}(\dot{\boldsymbol{\xi}}_h^n-\dot{\boldsymbol{\xi}}_h^{n-1},\boldsymbol{z}_h^n)|\leq\frac{\tau^2}{4}\|\dot{\boldsymbol{\xi}}_h^n-\dot{\boldsymbol{\xi}}_h^{n-1}\|_{\mathrm{e}}^2+\tau^2\|\boldsymbol{z}_h^n\|_{\mathrm{e}}^2.$$

Then we have:

$$T_{6,1}+T_{6,2}\leq\frac{\rho^{\mathrm{s}}}{4}\|\dot{\boldsymbol{\xi}}_h^n-\dot{\boldsymbol{\xi}}_h^{n-1}\|_*^2+\frac{\tau^3}{2T\rho^{\mathrm{s}}}\|\boldsymbol{L}_h^{\mathrm{e}}\boldsymbol{\xi}_h^n+\boldsymbol{L}_h^{\mathrm{v}}\dot{\boldsymbol{\xi}}_h^n\|_*^2 \\ +\frac{\tau^3(T+\tau)}{2\rho^{\mathrm{s}}}\|\partial_\tau\left(\boldsymbol{L}_h^{\mathrm{e}}\boldsymbol{d}(t_n)+\boldsymbol{L}_h^{\mathrm{v}}\boldsymbol{P}_h^{\mathrm{s}}(\boldsymbol{u}(t_n),\dot{\boldsymbol{d}}(t_n))\right)\|_*^2. \tag{4.71}$$

The first term will be absorbed by the left hand side of (4.61), the second term will be controlled with (4.70) and the discrete Gronwall lemma and the last term will be kept in the right-hand side. Besides, we have

$$\frac{\tau^3(T+\tau)}{2\rho^{\mathrm{s}}}\|\partial_\tau\left(\boldsymbol{L}_h^{\mathrm{e}}\boldsymbol{d}^n+\boldsymbol{L}_h^{\mathrm{v}}\boldsymbol{P}_h^{\mathrm{s}}(\boldsymbol{u}^n,\dot{\boldsymbol{d}}^n)\right)\|_*^2 \\ \lesssim\frac{\tau^2T}{\rho^{\mathrm{s}}}\|\partial_t\left(\boldsymbol{L}_h^{\mathrm{e}}\boldsymbol{d}+\boldsymbol{L}_h^{\mathrm{v}}\boldsymbol{P}_h^{\mathrm{s}}(\boldsymbol{u},\dot{\boldsymbol{d}})\right)\|_{L^2(t_{n-1},t_n;L^2(\Omega^{\mathrm{s}}))}^2 \tag{4.72}$$

Finally, estimate (4.37) follows by inserting (4.63)-(4.67) and (4.70)-(4.71) in (4.61), summing over n and applying the discrete Gronwall lemma.

At last, **for $r=2$** and under the stability conditions (3.43), the stability analysis gives:

$$T_{5,1}=\tau^2\|\dot{\boldsymbol{\xi}}_h^n-\dot{\boldsymbol{\xi}}_h^{n-1}\|_{\mathrm{e}}^2-\tau^2a^{\mathrm{e}}(\dot{\boldsymbol{\xi}}_h^n-\dot{\boldsymbol{\xi}}_h^{n-1},\boldsymbol{z}_h^n-\boldsymbol{z}_h^{n-1}) \\ +\frac{\tau}{2}\left(\|\dot{\boldsymbol{\xi}}_h^n-\dot{\boldsymbol{\xi}}_h^{n-1}\|_{\mathrm{v}}^2-\|\dot{\boldsymbol{\xi}}_h^{n-1}-\dot{\boldsymbol{\xi}}_h^{n-2}\|_{\mathrm{v}}^2+\|\dot{\boldsymbol{\xi}}_h^n-2\dot{\boldsymbol{\xi}}_h^{n-1}+\dot{\boldsymbol{\xi}}_h^{n-2}\|_{\mathrm{v}}^2\right),$$

$$\begin{aligned}T_{5,2}=&\frac{\tau^3}{\rho^{\mathrm{s}}}a^{\mathrm{e}}(\boldsymbol{L}_h^{\mathrm{e}}\boldsymbol{\xi}_h^n,\dot{\boldsymbol{\xi}}_h^n-\dot{\boldsymbol{\xi}}_h^{n-1})-\frac{\tau^3}{\rho^{\mathrm{s}}}a^{\mathrm{e}}(\boldsymbol{L}_h^{\mathrm{e}}\boldsymbol{\xi}_h^n,\boldsymbol{z}_h^n-\boldsymbol{z}_h^{n-1}) \\ &+\frac{\tau^2}{\rho^{\mathrm{s}}}a^{\mathrm{v}}(\boldsymbol{L}_h^{\mathrm{e}}\boldsymbol{\xi}_h^n+\boldsymbol{L}_h^{\mathrm{v}}\dot{\boldsymbol{\xi}}_h^n,\dot{\boldsymbol{\xi}}_h^n-2\dot{\boldsymbol{\xi}}_h^{n-1}+\dot{\boldsymbol{\xi}}_h^{n-2}) \\ &+\frac{\alpha_0\tau^3}{2}\left(\|\dot{\boldsymbol{\xi}}_h^n\|_{\mathrm{e}}^2-\|\dot{\boldsymbol{\xi}}_h^{n-1}\|_{\mathrm{e}}^2+\tau\|\partial_\tau\dot{\boldsymbol{\xi}}_h^n\|_{\mathrm{e}}^2\right) \\ &+\frac{\alpha_1\tau^3}{2\rho^{\mathrm{s}}}\left(\|\boldsymbol{L}_h^{\mathrm{e}}\dot{\boldsymbol{\xi}}_h^n\|_*^2-\|\boldsymbol{L}_h^{\mathrm{e}}\dot{\boldsymbol{\xi}}_h^{n-1}\|_*^2+\tau\|\boldsymbol{L}_h^{\mathrm{e}}\partial_\tau\dot{\boldsymbol{\xi}}_h^n\|_*^2\right)\end{aligned} \tag{4.73}$$

We now estimate each term separately:

$$\tau^2|a^{\mathrm{e}}(\dot{\boldsymbol{\xi}}_h^n-\dot{\boldsymbol{\xi}}_h^{n-1},\boldsymbol{z}_h^n-\boldsymbol{z}_h^{n-1})|\leq\tau^2\|\dot{\boldsymbol{\xi}}_h^n-\dot{\boldsymbol{\xi}}_h^{n-1}\|_{\mathrm{e}}\|\boldsymbol{z}_h^n-\boldsymbol{z}_h^{n-1}\|_{\mathrm{e}} \\ \leq\frac{\tau^2}{4}\|\dot{\boldsymbol{\xi}}_h^n-\dot{\boldsymbol{\xi}}_h^{n-1}\|_{\mathrm{e}}^2+\tau^2\|\boldsymbol{z}_h^n-\boldsymbol{z}_h^{n-1}\|_{\mathrm{e}}^2. \tag{4.74}$$

Then we have

$$\frac{\tau^3}{\rho^{\mathrm{s}}}|a^{\mathrm{e}}(\boldsymbol{L}_h^{\mathrm{e}}\boldsymbol{\xi}_h^n,\dot{\boldsymbol{\xi}}_h^n-\dot{\boldsymbol{\xi}}_h^{n-1})|\leq\frac{\tau^3}{\rho^{\mathrm{s}}}\|\boldsymbol{L}_h^{\mathrm{e}}\boldsymbol{\xi}_h^n\|_{\mathrm{e}}\|\dot{\boldsymbol{\xi}}_h^n-\dot{\boldsymbol{\xi}}_h^{n-1}\|_{\mathrm{e}} \\ \leq\frac{\tau^3\beta_{\mathrm{e}}^{3/2}C_{\mathrm{inv}}^3}{\rho^{\mathrm{s}}h^3}\|\boldsymbol{\xi}_h^n\|_{\mathrm{e}}\|\dot{\boldsymbol{\xi}}_h^n-\dot{\boldsymbol{\xi}}_h^{n-1}\|_* \\ \leq\frac{\gamma\tau}{2}\|\boldsymbol{\xi}_h^n\|_{\mathrm{e}}^2+\frac{\rho^{\mathrm{s}}}{2}\|\dot{\boldsymbol{\xi}}_h^n-\dot{\boldsymbol{\xi}}_h^{n-1}\|_*^2.$$

The first term will be treated with the discrete Gronwall lemma and the last term is absorbed by the left-hand side numerical dissipation in the solid inertia. The next term is treated similarly:

$$\begin{aligned}\frac{\tau^3}{\rho^{\mathrm{s}}}|a^{\mathrm{e}}(\boldsymbol{L}_h^{\mathrm{e}}\boldsymbol{\xi}_h^n, \boldsymbol{z}_h^n - \boldsymbol{z}_h^{n-1})| &\leq \frac{\tau^3}{\rho^{\mathrm{s}}}\|\boldsymbol{L}_h^{\mathrm{e}}\boldsymbol{\xi}_h^n\|_{\mathrm{e}}\|\boldsymbol{z}_h^n - \boldsymbol{z}_h^{n-1}\|_{\mathrm{e}} \\ &\leq \gamma\tau\|\boldsymbol{\xi}_h^n\|_{\mathrm{e}}^2 + \frac{4\tau^{5/3}}{\gamma^{1/3}}\|\boldsymbol{z}_h^n - \boldsymbol{z}_h^{n-1}\|_{\mathrm{e}}^2.\end{aligned}$$

Once again, the first tem will be treated with the discrete Gronwall lemma. The control of the last term comes from (4.60). Then, owing to the stability condition (4.18), we have

$$\begin{aligned}\frac{\tau^2}{\rho^{\mathrm{s}}}|a^{\mathrm{v}}(\boldsymbol{L}_h^{\mathrm{e}}\boldsymbol{\xi}_h^n + \boldsymbol{L}_h^{\mathrm{v}}\dot{\boldsymbol{\xi}}_h^n, \dot{\boldsymbol{\xi}}_h^n - 2\dot{\boldsymbol{\xi}}_h^{n-1} + \dot{\boldsymbol{\xi}}_h^{n-2})| &\leq \frac{\tau^2}{\rho^{\mathrm{s}}}\|\boldsymbol{L}_h^{\mathrm{e}}\boldsymbol{\xi}_h^n + \boldsymbol{L}_h^{\mathrm{v}}\dot{\boldsymbol{\xi}}_h^n\|_{\mathrm{v}}\|\dot{\boldsymbol{\xi}}_h^n - 2\dot{\boldsymbol{\xi}}_h^{n-1} + \dot{\boldsymbol{\xi}}_h^{n-2}\|_{\mathrm{v}} \\ &\leq \frac{\tau^3}{4(\rho^{\mathrm{s}})^2}\|\boldsymbol{L}_h^{\mathrm{e}}\boldsymbol{\xi}_h^n\|_{\mathrm{v}}^2 + \frac{\tau^3}{4\rho^{\mathrm{s}2}}\|\boldsymbol{L}_h^{\mathrm{v}}\dot{\boldsymbol{\xi}}_h^n\|_{\mathrm{v}}^2 \\ &\quad + \frac{\tau}{4}\|\dot{\boldsymbol{\xi}}_h^n - 2\dot{\boldsymbol{\xi}}_h^{n-1} + \dot{\boldsymbol{\xi}}_h^{n-2}\|_{\mathrm{v}}^2 \\ &\leq \gamma\tau\|\boldsymbol{\xi}_h^n\|_{\mathrm{e}}^2 + \tau\delta^2\|\dot{\boldsymbol{\xi}}_h^n\|_{\mathrm{v}}^2 \\ &\quad + \frac{\tau}{4}\|\dot{\boldsymbol{\xi}}_h^n - 2\dot{\boldsymbol{\xi}}_h^{n-1} + \dot{\boldsymbol{\xi}}_h^{n-2}\|_{\mathrm{v}}^2.\end{aligned}$$

We now justify why the quantity T_8 is controlled in this case. Thanks to estimates (4.25) and to the stability condition (4.18), we have

$$\begin{aligned}T_8 &\leq \frac{2\epsilon\tau^5}{\rho^{\mathrm{s}}}\left(\alpha_0 + \frac{1}{T}\right)\|\boldsymbol{L}_h^{\mathrm{e}}(\dot{\boldsymbol{\xi}}_h^n - \dot{\boldsymbol{\xi}}_h^{n-1} + \boldsymbol{z}_h^n - \boldsymbol{z}_h^{n-1})\|_{0,\Omega^{\mathrm{s}}}^2 \\ &\quad + \frac{2\epsilon\tau^3}{\rho^{\mathrm{s}}}\left(\alpha_0 + \frac{1}{T}\right)\|\boldsymbol{L}_h^{\mathrm{v}}(\dot{\boldsymbol{\xi}}_h^n - 2\dot{\boldsymbol{\xi}}_h^{n-1} + \dot{\boldsymbol{\xi}}_h^{n-2})\|_{0,\Omega^{\mathrm{s}}}^2 \\ &\leq 4\epsilon\tau^3(\gamma\tau)^{1/3}\left(\alpha_0 + \frac{1}{T}\right)\left(\|\dot{\boldsymbol{\xi}}_h^n - \dot{\boldsymbol{\xi}}_h^{n-1}\|_{\mathrm{e}}^2 + \|\boldsymbol{z}_h^n - \boldsymbol{z}_h^{n-1}\|_{\mathrm{e}}^2\right) \\ &\quad + 2\epsilon\tau^2\delta\left(\alpha_0 + \frac{1}{T}\right)\|(\dot{\boldsymbol{\xi}}_h^n - 2\dot{\boldsymbol{\xi}}_h^{n-1} + \dot{\boldsymbol{\xi}}_h^{n-2})\|_{\mathrm{v}}^2.\end{aligned} \tag{4.75}$$

The first and the last term can be absorbed into $T_{5,1}$ and $T_{5,2}$ for ϵ small enough. The second term involving $\|\boldsymbol{z}_h^n - \boldsymbol{z}_h^{n-1}\|_{\mathrm{e}}^2$ is controlled via (4.60). Now we go on to the right hand side terms $T_{6,1}$ and $T_{6,2}$. Assuming that the stability condition (3.43) is satisfied, we get:

$$\begin{aligned}T_{6,1} + T_{6,2} \leq \frac{\rho^{\mathrm{s}}}{4}\|\dot{\boldsymbol{\xi}}_h^n - \dot{\boldsymbol{\xi}}_h^{n-1}\|_*^2 + \frac{\tau^5(\tau + T/\varepsilon)}{\rho^{\mathrm{s}}}\|\partial_\tau^2\left(\boldsymbol{L}_h^{\mathrm{e}}\boldsymbol{d}(t_n) + \boldsymbol{L}_h^{\mathrm{v}}\boldsymbol{P}_h^{\mathrm{s}}(\boldsymbol{u}(t_n), \dot{\boldsymbol{d}}(t_n))\right)\|_*^2 \\ + \frac{\varepsilon\tau\,(\gamma\tau)^{1/3}}{4T}\|\boldsymbol{\xi}_h^n\|_{\mathrm{e}}^2 + \frac{\varepsilon\tau^2\delta}{4T}\|\dot{\boldsymbol{\xi}}_h^n\|_{\mathrm{v}}^2\end{aligned} \tag{4.76}$$

for all $\varepsilon > 0$. We then set ε small enough to ensure that the last term is absorbed into the left-hand side. At last, a Taylor expansion gives

$$\frac{\tau^5(\tau+\frac{T}{\varepsilon})}{\rho^{\mathrm{s}}}\|\partial_\tau^2\left(\boldsymbol{L}_h^{\mathrm{e}}\boldsymbol{d}(t_n)+\boldsymbol{L}_h^{\mathrm{v}}\boldsymbol{P}_h^{\mathrm{s}}(\boldsymbol{u}(t_n),\dot{\boldsymbol{d}}(t_n))\right)\|_*^2 \lesssim \frac{\tau^4 T}{\rho^{\mathrm{s}}}\|\partial_t^2\left(\boldsymbol{L}_h^{\mathrm{e}}\boldsymbol{d}+\boldsymbol{L}_h^{\mathrm{v}}\boldsymbol{P}_h^{\mathrm{s}}(\boldsymbol{u},\dot{\boldsymbol{d}})\right)\|^2_{L^2(t_{n-1},t_n;L^2(\Omega^{\mathrm{s}}))}.$$

Finally, estimate (4.37) follows by inserting (4.63)-(4.67) and (4.73)-(4.76) in (4.61), summing over n and applying the discrete Gronwall lemma.

4.3.7 Proof of Theorem 4.3.2

Here we treat the case $\alpha_1 = 0$. The modified Galerkin orthogonality (4.58) now writes

$$\begin{aligned}
&\rho^{\mathrm{f}}\big(\partial_\tau\boldsymbol{\theta}_h^n,\boldsymbol{v}_h^{\mathrm{f}}\big)_{\Omega^{\mathrm{f}}}+a(\boldsymbol{\theta}_h^n,\boldsymbol{v}_h^{\mathrm{f}})+b(y_h^n,\boldsymbol{v}_h^{\mathrm{f}})-b(q_h,\boldsymbol{\theta}_h^n)+s_h(y_h^n,q_h)+\rho^{\mathrm{s}}\big(\partial_\tau\dot{\boldsymbol{\xi}}_h^n,\boldsymbol{v}_h^{\mathrm{s}}\big)_*\\
&\quad+a^{\mathrm{e}}(\boldsymbol{\xi}_h^n,\boldsymbol{v}_h^{\mathrm{s}})+a_*^{\mathrm{v}}(\dot{\boldsymbol{\xi}}_h^n,\boldsymbol{v}_h^{\mathrm{s}})=\underbrace{-\rho^{\mathrm{f}}\big((\partial_t-\partial_\tau)\boldsymbol{u}(t_n),\boldsymbol{v}_h^{\mathrm{f}}\big)_{\Omega^{\mathrm{f}}}-\rho^{\mathrm{f}}\big(\partial_\tau\boldsymbol{\theta}_\pi^n,\boldsymbol{v}_h^{\mathrm{f}}\big)_{\Omega^{\mathrm{f}}}}_{T_1(\boldsymbol{v}_h^{\mathrm{f}})}\\
&\underbrace{-\rho^{\mathrm{s}}\big((\partial_t-\partial_\tau)\dot{\boldsymbol{d}}(t_n),\boldsymbol{v}_h^{\mathrm{s}}\big)_{\Omega^{\mathrm{s}}}-\rho^{\mathrm{s}}\big(\partial_\tau\dot{\boldsymbol{\xi}}_\pi^n,\boldsymbol{v}_h^{\mathrm{s}}\big)_{\Omega^{\mathrm{s}}}}_{T_2(\boldsymbol{v}_h^{\mathrm{s}})}\\
&\underbrace{-a\big(\boldsymbol{\theta}_\pi^n,\boldsymbol{v}_h^{\mathrm{f}}\big)-b\big(y_\pi^n,\boldsymbol{v}_h^{\mathrm{f}}\big)+b\big(q_h,\boldsymbol{\theta}_\pi^n\big)+s_h\big(\Pi_h p(t_n),q_h\big)}_{T_3(\boldsymbol{v}_h^{\mathrm{f}},q_h,\boldsymbol{v}_h^{\mathrm{s}})}\\
&+\underbrace{\rho^{\mathrm{s}}\delta_h\big((\partial_\tau+\alpha_0)\boldsymbol{P}_h^{\mathrm{s}}(\boldsymbol{u}(t_n),\dot{\boldsymbol{d}}(t_n)),\boldsymbol{v}_h^{\mathrm{s}}\big)}_{T_4(\boldsymbol{v}_h^{\mathrm{s}})}+\underbrace{a^{\mathrm{e}}\left(\boldsymbol{\xi}_\pi^n,\boldsymbol{v}_h^{\mathrm{s}}\right)}_{=0}+\underbrace{a^{\mathrm{v}}\big(\dot{\boldsymbol{\xi}}_\pi^n,\boldsymbol{v}_h^{\mathrm{s}}\big)}_{T_5(\boldsymbol{v}_h^{\mathrm{s}})}
\end{aligned}\tag{4.77}$$

for all $\big((\boldsymbol{v}_h^{\mathrm{f}},\boldsymbol{v}_h^{\mathrm{s}}),q_h\big)\in\boldsymbol{W}_h\times Q_h$ and $n>r$. In addition, the term T_5 reduces to

$$T_5(\boldsymbol{v}_h^{\mathrm{s}})=\alpha_0\rho^{\mathrm{s}}\left(\dot{\boldsymbol{\xi}}_\pi^n,\boldsymbol{v}_h^{\mathrm{s}}\right)_{\Omega^{\mathrm{s}}}.$$

It is worth noting that the choice of the Lagrange interpolant and (4.38) as fluid-solid velocity projector was not appropriate if $\alpha_1 > 0$. Indeed, in this case, the term T_5 would include the full solid viscous contribution, leading to the term $\tau a^{\mathrm{v}}(\dot{\boldsymbol{\xi}}_\pi^n,\dot{\boldsymbol{\xi}}_h^{n-\frac{1}{2}})$.

We now recall, without proof, the counterparts of lemma 4.3.7 and 4.3.6:

Lemma 4.3.8. *Let $\boldsymbol{z}_h^n\in\boldsymbol{V}_h^{\mathrm{s}}$ be defined as $\boldsymbol{z}_h^n\overset{\mathrm{def}}{=}\dot{\boldsymbol{\xi}}_h^n-\partial_\tau\boldsymbol{\xi}_h^n$. Then, we have*

$$\boldsymbol{z}_h^n=\boldsymbol{\mathcal{I}}_h^{\Omega^{\mathrm{s}}}\dot{\boldsymbol{d}}(t_n)-\boldsymbol{\pi}_h^{\mathrm{e}}\partial_\tau\boldsymbol{d}(t_n)$$

and

$$\|\boldsymbol{z}_h^n\|_{\mathrm{e}}\lesssim h\,(\beta_{\mathrm{e}})^{\frac{1}{2}}\,\|\dot{\boldsymbol{d}}(t_n)\|_{2,\Omega^{\mathrm{s}}}+(\tau\beta_{\mathrm{e}})^{\frac{1}{2}}\,\|\partial_t\dot{\boldsymbol{d}}\|_{L^2((t^{n-1},t^n),H^1(\Omega^{\mathrm{s}}))}.\tag{4.78}$$

Lemma 4.3.9. *Let* $\dot{\boldsymbol{\xi}}_h^{n-\frac{1}{2}} \in \boldsymbol{V}_h^{\mathrm{s}}$ *be defined as*

$$\begin{aligned}\dot{\boldsymbol{\xi}}_h^{n-\frac{1}{2}} \overset{\text{def}}{=} & \dot{\boldsymbol{\xi}}_h^{n} + \frac{\tau}{\rho^{\mathrm{s}}}\left[\boldsymbol{L}_h^{\mathrm{e}}\big(\boldsymbol{\xi}_h^n - \boldsymbol{\xi}_h^\star\big) + \alpha_0\rho^{\mathrm{s}}\big(\dot{\boldsymbol{\xi}}_h^n - \dot{\boldsymbol{\xi}}_h^\star\big)\right] \\ & - \frac{\tau}{\rho^{\mathrm{s}}}\left[\boldsymbol{L}_h^{\mathrm{e}}\big(\boldsymbol{d}(t_n) - \boldsymbol{d}^\star\big) + \alpha_0\rho^{\mathrm{s}}\boldsymbol{\mathcal{I}}_h^{\Omega^{\mathrm{s}}}\left(\dot{\boldsymbol{d}}(t_n) - \dot{\boldsymbol{d}}^\star\right)\right].\end{aligned} \tag{4.79}$$

Then, we have

$$\boldsymbol{\theta}_h^n = \dot{\boldsymbol{\xi}}_h^{n-\frac{1}{2}} \quad on \quad \Sigma.$$

We now test (4.77) with $\boldsymbol{v}_h^{\mathrm{f}} = \tau\boldsymbol{\theta}_h^n$, $q_h = \tau y_h^n$ and $\boldsymbol{v}_h^{\mathrm{s}} = \tau\dot{\boldsymbol{\xi}}^{n-\frac{1}{2}}$. We report here the estimates of T_2, T_3 and T_4 that are different from those in Section 4.3.6:

$$\begin{aligned}|T_2(\tau\dot{\boldsymbol{\xi}}^{n-\frac{1}{2}})| \leq & \frac{\rho^{\mathrm{s}}T\tau^2}{\epsilon_2}\|\partial_{tt}\dot{\boldsymbol{d}}\|^2_{L^2(t_{n-1},t_n;L^2(\Omega^{\mathrm{s}}))} + \frac{\rho^{\mathrm{s}}TC_{\mathrm{P}}^2}{\epsilon_2}\|\partial_t\dot{\boldsymbol{d}}\|^2_{L^2(t_{n-1},t_n;H^2(\Omega^{\mathrm{s}}))} \\ & + \epsilon_2\frac{\rho^{\mathrm{s}}\tau}{T}\|\dot{\boldsymbol{\xi}}^{n-\frac{1}{2}}\|^2_{0,\Omega^{\mathrm{s}}},\end{aligned}$$

$$\begin{aligned}|\tau T_3(\boldsymbol{\theta}_h^n, y_h^n, \dot{\boldsymbol{\xi}}^{n-\frac{1}{2}})| \lesssim & \frac{(\epsilon_3+\epsilon_4)\mu\tau}{2}\|\boldsymbol{\theta}_h^n\|^2_{1,\Omega^{\mathrm{f}}} + \frac{\tau}{2}|y_h^n|^2_{s_h} \\ & + \frac{\tau h^2\mu}{2\epsilon_3}\|\boldsymbol{u}(t_n)\|^2_{2,\Omega^{\mathrm{f}}} + \frac{\tau h^2}{\mu\epsilon_4}\left(h^2\|p(t_n)\|^2_{2,\Omega^{\mathrm{f}}} + \|p(t_n)\|^2_{1,\Omega^{\mathrm{f}}}\right),\end{aligned} \tag{4.80}$$

$$|T_4(\tau\dot{\boldsymbol{\xi}}^{n-\frac{1}{2}})| \lesssim \frac{\rho^{\mathrm{s}}T\tau h^2}{\epsilon_6}\|(\partial_\tau + \alpha_0)\dot{\boldsymbol{d}}(t_n))\|^2_{1,\Omega^{\mathrm{s}}} + \frac{\epsilon_6\rho^{\mathrm{s}}\tau}{T}\|\dot{\boldsymbol{\xi}}_h^{n-\frac{1}{2}}\|^2_{0,\Omega^{\mathrm{s}}}. \tag{4.81}$$

At last, we control the new term T_5 as

$$\begin{aligned}|T_5(\tau\dot{\boldsymbol{\xi}}^{n-\frac{1}{2}})| & \leq \alpha_0\rho^{\mathrm{s}}\tau\|\dot{\boldsymbol{\xi}}_h^{n-\frac{1}{2}}\|_{0,\Omega^{\mathrm{s}}}\|\dot{\boldsymbol{\xi}}_\pi^n\|_{0,\Omega^{\mathrm{s}}} \\ & \leq \epsilon_7\alpha_0\rho^{\mathrm{s}}\tau\|\dot{\boldsymbol{\xi}}_h^{n-\frac{1}{2}}\|^2_{0,\Omega^{\mathrm{s}}} + \frac{\alpha_0\rho^{\mathrm{s}}\tau h^2}{4\epsilon_7}\|\dot{\boldsymbol{d}}^n\|^2_{2,\Omega^{\mathrm{s}}}.\end{aligned} \tag{4.82}$$

and this last term is controlled as T_8 in the proof of Theorem 4.3.1, under the condition $(\alpha_0 + 1/T)\tau < 1$. All the other terms are treated as in the proof of Theorem 4.3.1.

4.4 Numerical experiments

Numerical evidence on the convergence rates of Algorithm 4.2 has been reported in Section 3.6.1.1. The objective of this numerical section is threefold:

- The first target is to illustrate that, as predicted by the above error analysis, Algorithms 4.1 and 4.2 deliver the same convergence rate. In order words, the mass-lumping approximation does not affect the accuracy of the splitting.

- The second is to highlight the $h^{-\frac{1}{2}}$ perturbation in the error through different scalings : $\tau = \mathcal{O}(h)$, $\tau = \mathcal{O}(h^{3/2})$ and $\tau = \mathcal{O}(h^2)$.
- The third purpose consists in demonstrating that that Algorithm 4.3 suffers from similar non-uniformity convergence issues.

To this purpose we consider the numerical experiment of Section 3.6.1.1. For the sake of simplicity, a purely elastic solid is considered ($\alpha_0 = \alpha_1 = 0$). Hence the results of Theorem 4.3.4 apply.

We have reported the relative displacement error $\|\boldsymbol{d}_h^N - \boldsymbol{d}(T)\|_{\mathrm{e}} / \|\boldsymbol{d}(T)\|_{\mathrm{e}}$ at the final time $T = 0.015$ for the different schemes and several choices of scaling for the couple (h, τ). We also present the rate of convergence to illustrate the global accuracy of the schemes. Relative errors are calculated with a reference solution obtained with an implicit coupling scheme with $h = 0.003125$ and $\tau = 10^{-6}$.

Table 4.1 reports the convergence results for Algorithm 4.2 with $\tau = \mathcal{O}(h)$. We clearly see that the scheme with $r = 0$ does not converge and that the scheme with $r = 1$ exhibits a sub-optimal convergence rate. As shown in Table 4.2, same phenomena are observed with Algorithms 4.1. This points out the fact the mass-lumping approximation has nothing to do with the non-uniformity in h of the splitting. Table 4.3 demonstrates that Algorithm 4.3 with $\beta = 1$ also suffers from this issue.

		$r = 0$		$r = 1$	
h	τ	rel. error	h-rate	rel. error	h-rate
0.1	3.75×10^{-4}	1.00	–	0.96	–
0.05	1.875×10^{-4}	1.00	0	0.83	0.22
0.025	9.375×10^{-5}	1.00	0	0.57	0.54
0.0125	4.6875×10^{-5}	1.01	0	0.33	0.77
0.00625	2.34375×10^{-5}	1.01	0	0.18	0.88

Table 4.1: Algorithm 4.2 with $\tau = \mathcal{O}(h)$.

		$r = 0$		$r = 1$	
h	τ	rel. error	h-rate	rel. error	h-rate
0.1	3.75×10^{-4}	1.00	–	1.11	–
0.05	1.875×10^{-4}	1.00	0	1.07	0.05
0.025	9.375×10^{-5}	1.00	0	0.83	0.37
0.0125	4.6875×10^{-5}	1.00	0	0.52	0.67
0.00625	2.34375×10^{-5}	1.00	0	0.29	0.83

Table 4.2: Algorithm 4.1 with $\tau = \mathcal{O}(h)$.

We now consider a different scaling for the couple of discretization parameters. Table 4.4 reports the results obtained with Algorithms 4.1 and 4.2 with $r = 1$ and $\tau = \mathcal{O}(h^{\frac{3}{2}})$. In both cases we recover an optimal fist-order convergence rate.

h	τ	rel. error	h-rate
0.1	3.75×10^{-4}	1.06899	–
0.05	1.875×10^{-4}	1.01822	0.07
0.025	9.375×10^{-5}	0.79880	0.35
0.0125	4.6875×10^{-5}	0.51719	0.64
0.00625	2.34375×10^{-5}	0.29598	0.82

Table 4.3: Algorithm 4.3 with $\beta = 1$ and $\tau = \mathcal{O}(h)$.

		Algorithm 4.1		Algorithm 4.2	
h	τ	rel. error	h-rate	rel. error	h-rate
0.1	3.75×10^{-4}	0.96	–	1.11	–
0.05	1.60×10^{-4}	0.70	0.47	0.92	0.03
0.025	6.87×10^{-5}	0.36	0.95	0.52	0.83
0.0125	2.93749×10^{-5}	0.16	1.21	0.23	1.18

Table 4.4: Algorithm 4.1 and 4.2 with $r = 1$ and $\tau = \mathcal{O}(h^{\frac{3}{2}})$.

In Table 4.5 we report the convergence results for Algorithms 4.1 and 4.2 with $r = 2$ and $\tau = \mathcal{O}(h^{6/5})$. Note that, in this case, the scaling $\tau = \mathcal{O}(h)$ is inappropriate since the stability condition (4.18) is not fulfilled. We clearly see that both schemes deliver the same accuracy. Note that with the finest discretization we obtain a convergence rate larger than one. This is certainly due to the fact that we are too close to the resolution with which the reference solution has been generated.

		Algorithm 4.1		Algorithm 4.2	
h	τ	rel. error	h-rate	rel. error	h-rate
0.1	3×10^{-5}	0.73496	–	0.73546	–
0.05	1.40×10^{-5}	0.38805	0.92	0.38978	0.92
0.025	6.57×10^{-6}	0.14419	1.42	0.14578	1.42
0.0125	3.07×10^{-6}	0.04197	1.78	0.04255	1.78

Table 4.5: Algorithm 4.1 and 4.2 with $r = 2$ and $\tau = \mathcal{O}(h^{6/5})$.

4.5 Conclusion

In this chapter, we have presented an a priori error analysis for the generalized Robin-Neumann explicit coupling schemes introduced in Chapter 3. This schemes have been derived within a fractional-step splitting framework in which both the case with and without mass-lumping are considered. In both cases, the analysis confirms the $\mathcal{O}(\tau^{2^{r-1}}/h^{\frac{1}{2}})$ error perturbation anticipated by the numerical evidence of Chapter 3.

Another fundamental result of this chapter is that the h-non-uniformity of the splitting error is not a consequence of the mass-lumping approximation (which simply dictates the explicit or semi-implicit nature of the coupling scheme). The analysis indicates that the genesis of the $\mathcal{O}(h^{-\frac{1}{2}})$ is the non-uniformity of discrete viscoelastic operator, which is a consequence of thick-walled character of the solid.

General conclusion and perspectives

The design and the analysis of stable and accurate explicit coupling schemes for incompressible fluid-structure interaction problem is a challenging problem. Stability in explicit coupling has been an open problem for years. It appears, however, that the most intricate issue is accuracy.

In this thesis, we have developed and analyzed a class of Robin-Neumann explicit coupling schemes for the interaction of a viscous incompressible fluid and a general (thin- or thick-walled) structure. The basic ingredients of these methods are the following:

- *The interface Robin consistency.* This is an intrinsic feature of the continuous problem in the case of the coupling with a thin-walled structure (Chapter 2). We have extended this notion to the case of the coupling with thick-walled structures, by considering the space semi-discrete formulation with a mass-lumping approximation in the solid (Chapter 3). This (generalized) Robin condition involves a new interface operator which consistently integrates the solid inertial effects on the interface.

- *Implicit treatment of the sole interface solid inertia within the fluid.* After time-discretization of the interface Robin consistency relation, we can derive an explicit Robin interface condition for the fluid, which combines (explicit) extrapolations of the solid velocity and stresses with an implicit treatment of the solid inertia. We have shown that this is enough to guarantee (added-mass free) stability.

- *Appropriate extrapolations of the interface solid velocity and stress.* The methods proposed can be viewed as kinematic perturbation of an implicit coupling scheme. The size of this perturbation, which depends on the extrapolated quantities on the interface, dictates the accuracy of the splitting. In the case of the coupling with a thin-walled structure (Chapter 2), the method with first-order extrapolation simultaneously delivers unconditional stability and optimal first-order accuracy. For thick-walled structures (Chapters 3 and 4) we retrieve the same accuracy in time, but the constant in front of the splitting error is not uniform with respect to the spatial grid step h. As a result, we loose the optimally of the overall accuracy. The genesis of this issue is the stability of the discrete viscoelastic operator which, in the thick-walled case, scales as $\mathcal{O}(h^{\frac{1}{2}})$. It is worth noting that this non-uniformity is not specific feature of the Robin-Neumann methods proposed. Other splitting methods proposed in the literature also suffer from this issue: for instance, the Nitsche based explicit coupling reported in [18, 20] and, as shown in Section 4.4, the semi-implicit scheme recently reported in [14]. In this respect, a salient feature of the method with first-order extrapolation introduced in Chapter 3 is that it simultaneously yields unconditional stability

and convergence under a standard hyperbolic-CFL constraint whiteout the need of correction iterations.

The proposed explicit coupling schemes have been interpreted as single iterations, with appropriate initialization, of a parameter-free Robin-Neumann iterative solution procedures for strong coupling. In the case of the coupling with thick-walled solids these methods are new. Original results on the convergence of these procedures have been derived. A salient consequence of the analysis is that there is a close relation between stable and accurate explicit coupling schemes and efficient iterative methods for the solution of strong coupling.

Extensions of this work can explore various research directions. We list and discuss below some of them together with some open problems:

- A fundamental problem not addressed in this thesis is the case of the coupling with unfitted fluid and solid meshes or discretizations (see, e.g., [19]). In fact, a key assumption in the derivation of the methods introduced in Chapters 2 and 3 is that the fluid and solid discretization match at the interface. This is natural for fluid-structure systems with moderate interface displacements, but it rapidly becomes unfeasible for problems involving complex interface motions (e.g., immersed interfaces such as vesicles and heart valves [30, 2]). Some preliminary results in this direction can be found in [52, 83]. Interestingly, the explicit or semi-implicit nature of the coupling scheme depends on the order in which the spatial discretization and the Robin-Neumann splitting are performed. In fact, these operations do not commute in the case of unfitted spatial discretizations.

- The analysis reported in Chapters 2-4 has been carried out within a linear framework. This is justified by the fact that: (i) the explicit treatment of the geometrical nonlinearities (i.e., fluid domain motion) is known to not compromise stability (see, e.g., [96, 108, 94, 93]); and (ii) the linear setting considered (i.e, Stokesian flow coupled with a linearly viscoelastic solid) is resentative of added-mass stability issues in explicit coupling. In spite of that, we think the generalization of at least some ingredients of the present analysis (e.g., stability) to the nonlinear case is of major interest.

- Although not addressed herein, the coupling schemes proposed can also be used to consider the case of structures with constraints enforced via Lagrange multipliers, such as inextensibility and incompressibility (as is often the case for problems in bio-engineering). Due to intrinsic partitioned nature of the Robin-Neumann splitting, the incorporation of this additional solid features requires minor modification in the scheme, but the analysis can be more intricate (particularly for the second-order extrapolations).

- Another interesting problem not considered in this thesis is the formulation of the Robin-Neumann schemes with a fractional-step time marching in the fluid.

In fact, fractional-step methods are certainly the most widespread technique for the time-discretization of the incompressible Navier-Stokes equations (see, e.g., [66]). The key difficulty here is how to preserve the stability and accuracy of the fluid-solid splitting without compromising the velocity/pressure uncoupling of the fluid time-marching. Some results in this direction can be found in [49, 50].

- The design and analysis of an explicit coupling method delivering second-order accuracy remains an open problem. In the framework of the coupling with thin-walled structures, a first approach in this direction can be to combine second-order fluid and solid time-marchings with the Robin-Neumann paradigm of Chapter 2 and appropriate second-order extrapolations. Formally, a neutrally stable second-order Newmark's scheme could be employed in the solid, but the stability properties of the resulting coupling scheme requires further investigation, both from the numerical and analysis standpoint. An alternative approach can be the combination of a first-order extrapolation which enhances stability, with a defect-correction iteration to achieve second-order consistency in the perturbed kinematic relation. We refer to [51] for a study in this direction.

- Though significant advances have been obtained with the results of Chapters 3 and 4, achieving optimal first-order accuracy in the case of the coupling with thick-walled structures appears to be an open problem. A promising approach is the use a non-symmetric penalty-free formulation at the space semi-discrete level (see [20, Section 4.3]), but the rigorous stability analysis of the resulting method remains open.

Bibliography

[1] M. Astorino, F. Chouly, and M.A. Fernández. Robin based semi-implicit coupling in fluid-structure interaction: Stability analysis and numerics. *SIAM J. Sci. Comput.*, 31(6):4041–4065, 2009.

[2] M. Astorino, J.-F. Gerbeau, O. Pantz, and K.-F. Traoré. Fluid-structure interaction and multi-body contact: application to aortic valves. *Comput. Methods Appl. Mech. Engrg.*, 198(45-46):3603–3612, 2009.

[3] S. Badia, F. Nobile, and C. Vergara. Fluid-structure partitioned procedures based on Robin transmission conditions. *J. Comp. Phys.*, 227:7027–7051, 2008.

[4] S. Badia, A. Quaini, and A. Quarteroni. Modular vs. non-modular preconditioners for fluid-structure systems with large added-mass effect. *Comput. Methods Appl. Mech. Engrg.*, 197(49-50):4216–4232, 2008.

[5] S. Badia, A. Quaini, and A. Quarteroni. Splitting methods based on algebraic factorization for fluid-structure interaction. *SIAM J. Sci. Comput.*, 30(4):1778–1805, 2008.

[6] H. Baek and G.E. Karniadakis. A convergence study of a new partitioned fluid-structure interaction algorithm based on fictitious mass and damping. *J. Comput. Phys.*, 231(2):629–652, 2012.

[7] Y. Bazilevs, V.M. Calo, T.J.R. Hughes, and Y. Zhang. Isogeometric fluid-structure interaction: theory, algorithms, and computations. *Comput. Mech.*, 43(1):3–37, 2008.

[8] R. Becker and M. Braack. A finite element pressure gradient stabilization for the Stokes equations based on local projections. *Calcolo*, 38(4):173–199, 2001.

[9] C. Bertoglio, P. Moireau, and J.-F. Gerbeau. Sequential parameter estimation for fluid–structure problems: application to hemodynamics. *Int. J. Numer. Methods Biomed. Eng.*, 28(4):434–455, 2012.

[10] M. Bischoff, K.-U. Bletzinger, W.A. Wall, and E. Ramm. *Models and Finite Elements for Thin-Walled Structures*, chapter 3. John Wiley & Sons, Ltd, 2004.

[11] D. Boffi, L. Gastaldi, and L. Heltai. Numerical stability of the finite element immersed boundary method. *Math. Models Methods Appl. Sci.*, 17(10):1479–1505, 2007.

[12] S.C. Brenner and L.R. Scott. *The mathematical theory of finite element methods*, volume 15 of *Texts in Applied Mathematics*. Springer, New York, 2008.

[13] F. Brezzi and J. Pitkäranta. On the stabilization of finite element approximations of the Stokes equations. volume 10 of *Notes Numer. Fluid Mech.*, pages 11–19. Vieweg, 1984.

[14] M. Bukač, S. Čanić, R. Glowinski, B. Muha, and A. Quaini. A modular, operator-splitting scheme for fluid-structure interaction problems with thick structures. *Int. J. Numer. Meth. Fluids.*, 74(8):577–604, 2014.

[15] M. Bukač, S. Čanić, R. Glowinski, J. Tambača, and A. Quaini. Fluid-structure interaction in blood flow capturing non-zero longitudinal structure displacement. *J. Comput. Phys.*, 235:515–541, 2013.

[16] E. Burman and M.A. Fernández. Stabilized explicit coupling for fluid-structure interaction using Nitsche's method. *C. R. Math. Acad. Sci. Paris*, 345(8):467–472, 2007.

[17] E. Burman and M.A. Fernández. Galerkin finite element methods with symmetric pressure stabilization for the transient Stokes equations: stability and convergence analysis. *SIAM J. Numer. Anal.*, 47(1):409–439, 2008.

[18] E. Burman and M.A. Fernández. Stabilization of explicit coupling in fluid-structure interaction involving fluid incompressibility. *Comput. Methods Appl. Mech. Engrg.*, 198(5-8):766–784, 2009.

[19] E. Burman and M.A. Fernández. An unfitted Nitsche method for incompressible fluid-structure interaction using overlapping meshes. *Comput. Methods Appl. Mech. Engrg.*, 2014. To appear. `http://hal.inria.fr/hal-00918272`.

[20] E. Burman and M.A. Fernández. Explicit strategies for incompressible fluid-structure interaction problems: Nitsche type mortaring versus Robin-Robin coupling. *Internat. J. Numer. Methods Engrg.*, 97(10):739–758, 2014.

[21] E. Burman and M.A. Fernández. Explicit strategies for incompressible fluid-structure interaction problems: Nitsche type mortaring versus Robin–Robin coupling. *Int. J. Num. Meth. Engrg.*, 97(10):739–758, 2014.

[22] E. Burman, M.A. Fernández, and P. Hansbo. Continuous interior penalty finite element method for Oseen's equations. *SIAM J. Numer. Anal.*, 44(3):1248–1274, 2006.

[23] E. Burman and P. Hansbo. Edge stabilization for the generalized Stokes problem: a continuous interior penalty method. *Comput. Methods Appl. Mech. Engrg.*, 195(19-22):2393–2410, 2006.

[24] S. Čanić, J. Tambača, G. Guidoboni, A. Mikelić, C.J. Hartley, and D. Rosenstrauch. Modeling viscoelastic behavior of arterial walls and their interaction with pulsatile blood flow. *SIAM J. Appl. Math.*, 67(1):164–193, 2006.

[25] P. Causin, J.-F. Gerbeau, and F. Nobile. Added-mass effect in the design of partitioned algorithms for fluid-structure problems. *Comput. Methods Appl. Mech. Engrg.*, 194(42–44):4506–4527, 2005.

[26] D. Chapelle and K.J. Bathe. *The Finite Element Analysis of Shells - Fundamentals*. Springer, 2011.

[27] D. Chapelle and A. Ferent. Modeling of the inclusion of a reinforcing sheet within a 3D medium. *Math. Models Methods Appl. Sci.*, 13(4):573–595, 2003.

[28] Ph. Clément. Approximation by finite element functions using local regularization. *Rev. Française Automat. Informat. Recherche Opérationnelle Sér. RAIRO Analyse Numérique*, 9(R-2):77–84, 1975.

[29] R. Codina and J. Blasco. A finite element formulation for the Stokes problem allowing equal velocity-pressure interpolation. *Comput. Methods Appl. Mech. Engrg.*, 143(3-4):373–391, 1997.

[30] G.-H. Cottet, E. Maitre, and T. Milcent. Eulerian formulation and level set models for incompressible fluid-structure interaction. *M2AN Math. Model. Numer. Anal.*, 42(3):471–492, 2008.

[31] P. Crosetto, S. Deparis, G. Fourestey, and A. Quarteroni. Parallel algorithms for fluid-structure interaction problems in haemodynamics. *SIAM J. Sci. Comput.*, 33(4):1598–1622, 2011.

[32] J. Degroote. On the similarity between Dirichlet-Neumann with interface artificial compressibility and Robin-Neumann schemes for the solution of fluid-structure interaction problems. *J. Comput. Phys.*, 230(17):6399–6403, 2011.

[33] J. Degroote, R. Haelterman, S. Annerel, P. Bruggeman, and J. Vierendeels. Performance of partitioned procedures in fluid-structure interaction. *Comp. & Struct.*, 88(7-8):446–457, 2010.

[34] J. Degroote, A. Swillens, P. Bruggeman, R. Haelterman, P. Segers, and J. Vierendeels. Simulation of fluid-structure interaction with the interface artificial compressibility method. *Int. J. Numer. Meth. Biomed. Engng.*, 26(3-4):276–289, 2010.

[35] P. Degroote, J. Bruggeman, R. Haelterman, and J. Vierendeels. Stability of a coupling technique for partitioned solvers in FSI applications. *Comp. & Struct.*, 86(23-24):2224–2234, 2008.

[36] S. Deparis, M. Discacciati, G. Fourestey, and A. Quarteroni. Fluid-structure algorithms based on Steklov-Poincaré operators. *Comput. Methods Appl. Mech. Engrg.*, 195(41-43):5797–5812, 2006.

[37] W. Dettmer and D. Perić. A computational framework for fluid-rigid body interaction: finite element formulation and applications. *Comput. Methods Appl. Mech. Engrg.*, 195(13-16):1633–1666, 2006.

[38] V. Domínguez and F.J. Sayas. Stability of discrete liftings. *C. R. Math. Acad. Sci. Paris*, 337(12):805–808, 2003.

[39] Q. Du, M. D. Gunzburger, L. S. Hou, and J. Lee. Analysis of a linear fluid-structure interaction problem. *Discrete Contin. Dyn. Syst.*, 9(3):633–650, 2003.

[40] A. Ern and J.-L. Guermond. *Theory and practice of finite elements*. Springer, 2004.

[41] M. Eswaran, U.K. Saha, and D. Maity. Effect of baffles on a partially filled cubic tank: Numerical simulation and experimental validation. *Computers & Structures*, 87(3–4):198–205, 2009.

[42] C. Farhat, K. van der Zee, and Ph. Geuzaine. Provably second-order time-accurate loosely-coupled solution algorithms for transient nonlinear aeroelasticity. *Comput. Methods Appl. Mech. Engrg.*, 195(17–18):1973–2001, 2006.

[43] M.A. Fernández. Coupling schemes for incompressible fluid-structure interaction: implicit, semi-implicit and explicit. *SEMA J.*, (55):59–108, 2011.

[44] M.A. Fernández. Incremental displacement-correction schemes for the explicit coupling of a thin structure with an incompressible fluid. *C. R. Math. Acad. Sci. Paris*, 349(7-8):473–477, 2011.

[45] M.A. Fernández. Incremental displacement-correction schemes for incompressible fluid-structure interaction: stability and convergence analysis. *Numer. Math.*, 123(1):21–65, 2013.

[46] M.A. Fernández and J.-F. Gerbeau. Algorithms for fluid-structure interaction problems. In *Cardiovascular mathematics*, volume 1 of *MS&A. Model. Simul. Appl.*, pages 307–346. Springer, 2009.

[47] M.A. Fernández, J.-F. Gerbeau, and C. Grandmont. A projection algorithm for fluid-structure interaction problems with strong added-mass effect. *C. R. Math. Acad. Sci. Paris*, 342(4):279–284, 2006.

[48] M.A. Fernández, J.F. Gerbeau, and C. Grandmont. A projection semi-implicit scheme for the coupling of an elastic structure with an incompressible fluid. *Int. J. Num. Meth. Engrg.*, 69(4):794–821, 2007.

[49] M.A. Fernández and M. Landajuela. A fully decoupled scheme for the interaction of a thin-walled structure with an incompressible fluid. *C. R. Math. Acad. Sci. Paris*, 351(3-4):161–164, 2013.

[50] M.A. Fernández and M. Landajuela. Fully decoupled time-marching schemes for incompressible fluid/thin-walled structure interaction. Research Report RR-8425, INRIA, 2013. `http://hal.inria.fr/hal-00918498`.

[51] M.A. Fernández and M. Landajuela. Second-order time-accurate explicit schemes for the interaction of a thin-walled structure with an incompressible fluid. In *WCCM XI*, Barcelona, 2014.

[52] M.A. Fernández and M. Landajuela. Splitting schemes for fluid/thin-walled structure interaction with unfitted meshes. *C. R. Math. Acad. Sci. Paris*, 2014. Submitted.

[53] M.A. Fernández and M. Moubachir. A Newton method using exact Jacobians for solving fluid-structure coupling. *Comp. & Struct.*, 83:127–142, 2005.

[54] M.A. Fernández and J. Mullaert. Displacement-velocity correction schemes for incompressible fluid-structure interaction. *C. R. Math. Acad. Sci. Paris*, 349(17-18):1011–1015, 2011.

[55] M.A. Fernández, J. Mullaert, and Y. Maday. Préconditionnement d'algorithmes d'interaction fluide-structure. In *10e colloque national en calcul des structures*, Giens, France, 2011. `http://hal.archives-ouvertes.fr/hal-00592797`.

[56] M.A. Fernández, J. Mullaert, and M. Vidrascu. Explicit Robin-Neumann schemes for the coupling of incompressible fluids with thin-walled structures. *Comput. Methods Appl. Mech. Engrg.*, 267:566–593, 2013.

[57] M.A. Fernández, J. Mullaert, and M. Vidrascu. Generalized Robin-Neumann explicit coupling schemes for incompressible fluid-structure interaction: stability analysis and numerics. *Internat. J. Numer. Methods Engrg.*, 2014. DOI: 10.1002/nme.4785.

[58] C.A. Figueroa, I.E. Vignon-Clementel, K.E. Jansen, T.J.R. Hughes, and C.A. Taylor. A coupled momentum method for modeling blood flow in three-dimensional deformable arteries. *Comput. Methods Appl. Mech. Engrg.*, 195(41-43):5685–5706, 2006.

[59] L. Formaggia, J.-F. Gerbeau, F. Nobile, and A. Quarteroni. On the coupling of 3D and 1D Navier-Stokes equations for flow problems in compliant vessels. *Comp. Meth. Appl. Mech. Engrg.*, 191(6-7):561–582, 2001.

[60] L. Formaggia, A. Quarteroni, and A. Veneziani, editors. *Cardiovascular Mathematics. Modeling and simulation of the circulatory system*, volume 1 of *Modeling, Simulation and Applications*. Springer, 2009.

[61] C. Förster, W.A. Wall, and E. Ramm. Artificial added mass instabilities in sequential staggered coupling of nonlinear structures and incompressible viscous flows. *Comput. Methods Appl. Mech. Engrg.*, 196(7):1278–1293, 2007.

[62] M. Gee, E. Ramm, and W.-A. Wal. Parallel multilevel solution of nonlinear shell structures. *Comput. Methods Appl. Mech. Engrg.*, 194(21-24):2513–2533, 2005.

[63] M.W. Gee, U. Küttler, and W. Wall. Truly monolithic algebraic multigrid for fluid-structure interaction. *Int. J. Numer. Meth. Engng.*, 85(8):987–1016, 2011.

[64] J.-F. Gerbeau and M. Vidrascu. A quasi-Newton algorithm based on a reduced model for fluid-structure interactions problems in blood flows. *Math. Model. Num. Anal.*, 37(4):631–648, 2003.

[65] V. Girault and P.-A. Raviart. *Finite element methods for Navier-Stokes equations*. Springer, 1986.

[66] J. L. Guermond, P. Minev, and J. Shen. An overview of projection methods for incompressible flows. *Comput. Methods Appl. Mech. Engrg.*, 195(44-47):6011–6045, 2006.

[67] G. Guidoboni, R. Glowinski, N. Cavallini, and S. Canic. Stable loosely-coupled-type algorithm for fluid-structure interaction in blood flow. *J. Comp. Phys.*, 228(18):6916–6937, 2009.

[68] M.D. Gunzburger and S.L. Hou. Treating inhomogeneous essential boundary conditions in finite element methods and the calculation of boundary stresses. *SIAM J. Numer. Anal.*, 29(2):390–424, 1992.

[69] P. Hansbo. Nitsche's method for interface problems in computational mechanics. *GAMM-Mitt.*, 28(2):183–206, 2005.

[70] F. Hecht. New development in FreeFem++. *J. Numer. Math.*, 20(3-4):251–265, 2012.

[71] M. Heil. An efficient solver for the fully coupled solution of large-displacement fluid-structure interaction problems. *Comput. Methods Appl. Mech. Engrg.*, 193(1-2):1–23, 2004.

[72] M. Heil and A.L. Hazel. Fluid-structure interaction in internal physiological flows. *Annu. Rev. Fluid Mech.*, 43:141–162, 2011.

[73] J.G. Heywood and R. Rannacher. Finite-element approximation of the nonstationary Navier-Stokes problem. IV. Error analysis for second-order time discretization. *SIAM J. Numer. Anal.*, 27(2):353–384, 1990.

[74] G.A. Holzapfel. *Nonlinear solid mechanics*. John Wiley & Sons, Ltd., Chichester, 2000.

[75] G. Hou, J. Wang, and A. Layton. Numerical methods for fluid-structure interaction—a review. *Commun. Comput. Phys.*, 12(2):337–377, 2012.

[76] T.J.R. Hughes. *The finite element method*. Prentice Hall, 1987.

[77] E. Järvinen, P. Råback, M. Lyly, and J.-P. Salenius. A method for partitioned fluid-structure interaction computation of flow in arteries. *Medical Engineering & Physics*, 30(7):917–923, 2008.

[78] P. Joly. Variational methods for time-dependent wave propagation problems. In M. Ainsworth, P. Davies, D. Duncan, B. Rynne, and P. Martin, editors, *Topics in Computational Wave Propagation*, volume 31 of *Lecture Notes in Computational Science and Engineering*, pages 201–264. Springer Berlin Heidelberg, 2003.

[79] P. Kalita and R. Schaefer. Mechanical models of artery walls. *Arch. Comput. Methods Eng.*, 15(1):1–36, 2008.

[80] U. Küttler, C. Förster, and W.A. Wall. A solution for the incompressibility dilemma in partitioned fluid-structure interaction with pure Dirichlet fluid domains. *Comput. Mech.*, 38:417–429, 2006.

[81] U. Küttler and W.A. Wall. Fixed-point fluid-structure interaction solvers with dynamic relaxation. *Comp. Mech.*, 43(1):61–72, 2008.

[82] J.F. LaDisa, I. Guler, L.E. Olson, D.A. Hettrick, J.R. Kersten, D.C. Warltier, and P.S. Pagel. Three-dimensional computational fluid dynamics modeling of alterations in coronary wall shear stress produced by stent implantation. *Ann. Biomed. Eng.*, 31:972–980, 2003.

[83] M. Landajuela. *Coupling schemes and unfitted mesh methods for fluid-structure interaction*. PhD thesis, Université Paris VI, In preparation.

[84] P. Le Tallec. Numerical methods for nonlinear three-dimensional elasticity. In *Handbook of numerical analysis, Vol. III*, pages 465–622. North-Holland, 1994.

[85] P. Le Tallec and J. Mouro. Fluid structure interaction with large structural displacements. *Comput. Meth. Appl. Mech. Engrg.*, 190:3039–3067, 2001.

[86] P. Le Tallec, C. Rahier, and A. Kaiss. Three-dimensional incompressible viscoelasticity in large strains: formulation and numerical approximation. *Comput. Methods Appl. Mech. Engrg.*, 109(3-4):233–258, 1993.

[87] M. Lombardi, N. Parolini, A. Quarteroni, and G. Rozza. Numerical simulation of sailing boats: Dynamics, FSI, and shape optimization. In G. Buttazzo and A. Frediani, editors, *Variational Analysis and Aerospace Engineering: Mathematical Challenges for Aerospace Design*, Springer Optimization and Its Applications, pages 339–377. Springer, 2012.

[88] M. Lukáčová, G. Rusnáková, and A. Hundertmark. Kinematic splitting algorithm for fluid–structure interaction in hemodynamics. *Comput. Methods Appl. Mech. Engrg.*, 265(1):83–106, 2013.

[89] Y. Maday. Analysis of coupled models for fluid-structure interaction of internal flows. In *Cardiovascular mathematics*, volume 1 of *MS&A. Model. Simul. Appl.*, pages 279–306. Springer, 2009.

[90] P. Moireau, N. Xiao, M. Astorino, C.A. Figueroa, D. Chapelle, C. A. Taylor, and J-F. Gerbeau. External tissue support and fluid-structure simulation in blood flows. *Biomech. Model. Mechanobiol.*, 11:1–18, 2012.

[91] J. Mouro. *Interactions fluide structure en grands déplacements. Résolution numérique et application aux composants hydrauliques automobiles.* PhD thesis, Ecole Polytechnique, France, 1996.

[92] R.L. Muddle, M. Mihajlović, and M. Heil. An efficient preconditioner for monolithically-coupled large-displacement fluid-structure interaction problems with pseudo-solid mesh updates. *J. Comput. Phys.*, 231(21):7315–7334, 2012.

[93] B. Muha and S. Čanić. Existence of a weak solution to a nonlinear fluid–structure interaction problem modeling the flow of an incompressible, viscous fluid in a cylinder with deformable walls. *Arch. Rational Mech. Anal.*, 207:919–968, 2013.

[94] C.M. Murea and S. Sy. A fast method for solving fluid-structure interaction problems numerically. *Internat. J. Numer. Methods Fluids*, 60(10):1149–1172, 2009.

[95] J. Nitsche. Über ein Variationsprinzip zur Lösung von Dirichlet-Problemen bei Verwendung von Teilräumen, die keinen Randbedingungen unterworfen sind. *Abh. Math. Sem. Univ. Hamburg*, 36:9–15, 1971.

[96] F. Nobile. *Numerical approximation of fluid-structure interaction problems with application to haemodynamics.* PhD thesis, EPFL, Switzerland, 2001.

[97] F. Nobile and C. Vergara. An effective fluid-structure interaction formulation for vascular dynamics by generalized Robin conditions. *SIAM J. Sci. Comput.*, 30(2):731–763, 2008.

[98] F. Nobile and C. Vergara. Partitioned Algorithms for Fluid-Structure Interaction Problems in Haemodynamics. *Milan J. Math.*, 80(2):443–467, 2012.

[99] M.P. Païdoussis, S.J. Price, and E. de Langre. *Fluid-structure interactions: cross-flow-induced instabilities.* Cambridge University Press, 2011.

[100] K.C. Park, C.A. Felippa, and J.A. Deruntz. Stabilization of staggered solution procedures for fluid-structure interaction analysis. In Belytschko. T. and T.L. Geers, editors, *Computational Methods for Fluid-Structure Interaction Problems*, volume 26, pages 95–124. American Society of Mechanical Engineers, 1977.

[101] M. Perego, A. Veneziani, and C. Vergara. A variational approach for estimating the compliance of the cardiovascular tissue. An inverse fluid-structure interaction problem. *SIAM J. Sci. Comput.*, 33(3):1181–1211, 2011.

[102] C.S. Peskin. The immersed boundary method. *Acta Numer.*, 11:479–517, 2002.

[103] S. Piperno. Explicit/implicit fluid/structure staggered procedures with a structural predictor and fluid subcycling for 2D inviscid aeroelastic simulations. *Internat. J. Numer. Methods Fluids*, 25(10):1207–1226, 1997.

[104] A. Quaini and A. Quarteroni. A semi-implicit approach for fluid-structure interaction based on an algebraic fractional step method. *Math. Models Methods Appl. Sci.*, 17(6):957–983, 2007.

[105] A.-V. Salsac, S.R. Sparks, J.M. Chomaz, and J.C. Lasheras. Evolution of the wall shear stresses during the progressive enlargement of symmetric abdominal aortic aneurysms. *J. Fluid Mech.*, 550:19–51, 2006.

[106] H.J. Stetter. The defect correction principle and discretization methods. *Numer. Math.*, 29:425–443, 1978.

[107] G.R. Stuhne and D.A. Steinman. Finite-element modeling of the hemodynamics of stented aneurysms. *J. Biomech. Engng.*, 126(3):382–387, 2004.

[108] E. W. Swim and P. Seshaiyer. A nonconforming finite element method for fluid-structure interaction problems. *Comput. Methods Appl. Mech. Engrg.*, 195(17-18):2088–2099, 2006.

[109] M. Szopos, N. Poussineau, Y. Maday, C. Canniffe, D.S. Celermajer, D. Bonnet, and P. Ou. Computational modeling of blood flow in the aorta—insights into eccentric dilatation of the ascending aorta after surgery for coarctation. *The Journal of Thoracic and Cardiovascular Surgery*, 2013. DOI: 10.1016/j.jtcvs.2013.11.055.

[110] K. Takizawa and T.E. Tezduyar. Computational methods for parachute fluid-structure interactions. *Arch. Comput. Methods Eng.*, 19:125–169, 2012.

[111] T.E. Tezduyar. Finite element methods for fluid dynamics with moving boundaries and interfaces. *Arch. Comput. Methods Engrg.*, 8:83–130, 2001.

[112] V. Thomée. *Galerkin finite element methods for parabolic problems.* Springer, 2006.

[113] C. Tu and C.S. Peskin. Stability and instability in the computation of flows with moving immersed boundaries: a comparison of three methods. *SIAM J. Sci. Statist. Comput.*, 13(6):1361–1376, 1992.

[114] S. Turek and J. Hron. Proposal for numerical benchmarking of fluid-structure interaction between an elastic object and laminar incompressible flow. In *Fluid-structure interaction*, volume 53 of *Lect. Notes Comput. Sci. Eng.*, pages 371–385. Springer, Berlin, 2006.

[115] D. Valdez-Jasso, H.T. Banks, M.A. Haider, D. Bia, Y. Zocalo, R.L. Armentano, and M.S. Olufsen. Viscoelastic models for passive arterial wall dynamics. *Adv. Appl. Math. Mech.*, 1(2):151–165, 2009.